DIGITAL RADIOLOGY: A CRITICAL APPRAISAL OF CARDIOVASCULAR SUBTRACTION ANGIOGRAPHY AND MEASUREMENT OF BLOOD FLOW

by

George Joseph Stephen Hunter

The Middlesex Hospital

Thesis submitted for the degree of M.D. in
The University of London, 2000.

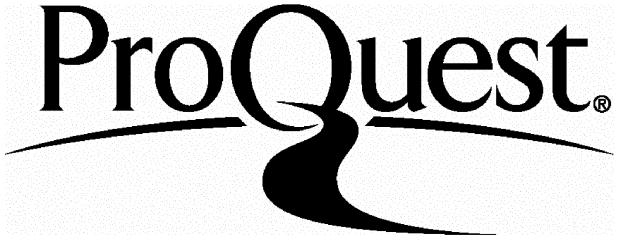

Purpose of thesis and statement of original work

Throughout the 1970's, the integration of computers with radiological instruments was used to improve the ability of these instruments to visualize cardiovascular anatomy. Prototype machines that relied on computer technology came to fruition as usable commercial units circa 1982. For many years prior to this commercial availability, however, the measurement of absolute arterial blood flow had been possible with the aid of computer-assisted cine film and videodensitometric time–of–flight methods. The advent of digital subtraction angiography (DSA), as computerized fluoroscopy came to be known, allowed the feasibility of routine applications of videodensitometry to be re-evaluated for the case of a DSA image series used as the source of both timing and spatial information.

Anatomical imaging of some arterial structures is usually adequate following intravenous injection and of highest quality after the direct arterial injection of contrast material. Simultaneously with anatomical data, timing information can be extracted from the known time of image exposure and its acquisition. This allows functional or physiological imaging to be coupled with anatomical data. In this thesis, two principle applications of DSA are discussed, i) absolute volume blood flow and ii) relative blood flow and organ perfusion.

Fourier transform methods are described for the measurement of time-of-flight and compared with existing curve fitting algorithms. The methods are analysed by using statistical modelling techniques (Monte-Carlo theory), and then validated in an animal model by using calibrated electromagnetic flow probes as the Gold Standard of volume blood flow.

Clinical applicability of this technique is described and discussed in the context of relative organ perfusion and contrasted with methods of absolute flow estimation. The principal conclusion, supported by the animal validation, is that the Fourier method is more accurate than existing techniques in the presence of noisy data. Nevertheless, the much simpler relative flow techniques have a useful role in routine clinical practice, as exemplified by the parametric assessment of myocardial perfusion reserve.

CONTENTS

Tables

Figures

ACKNOWLEDGEMENTS

The clinical work reported was performed in the Department of Diagnostic Imaging, The Middlesex Hospital. Financial support was provided by the Special Trustees of The Middlesex Hospital and Medical School. The animal work was performed at the Center for Imaging and Pharmaceutical Research, Massachusetts General Hospital, USA.

None of this work would have been possible without the foresight of Dr. Richard Mason, who suggested the area of study. I would like to recognise the tremendous encouragement and advice offered me throughout by Dr. Maurice Raphael, whose constructive criticism drove me to higher standards of experimental technique. I would like to thank Dr. Malcolm Chapman, who allowed me to use the DSA equipment in his department at all hours of the day and night, and the radiographers and nursing staff at the Middlesex Hospital, who tolerated my requests without a murmur. In no less a manner I wish to thank Dr. R.H. Swanton, Dr. W. Walton, Dr. R. Hayward and Mr. T. Treasure, who sent me their patients to study. I am grateful to Professor Wolf for granting me time and access to the facilities at CIPR to perform the animal studies. My thanks go to Mrs. P. Vecchi, who typed the manuscript. Grateful thanks go to Joanne Fordham who corrected my grammar and punctuation patiently throughout the process. Final thanks go to Dr. Leena Hamberg who constantly encouraged me to finish this work, and without whom it would never have been completed.

CHAPTER 1

HISTORICAL PERSPECTIVES AND AN OVERVIEW OF THE BASIC THEORY OF X-RAY IMAGING

1.1 Historical Introduction

In 1895, Roentgen published his discovery of "rays with unexpected penetrating power" - x-rays (Roentgen, W.C. 1895). This discovery very rapidly led to many applications of static imaging. Dynamic imaging of the heart and circulation by radiological means, however, was not to come about until much later. In addition to routine techniques of plain film radiology, contrast examinations of the circulation were employed in early, exploratory efforts to image the circulatory system. The first arteriogram was performed in 1896 in Vienna by Haschek and Lindenthal, when they injected contrast material into the vessels of an amputated hand and obtained radiographs of opacified vessels (Haschek, E. and Lindenthal, O. 1896). In 1910 Franck and Alwens introduced a suspension of bismuth and oil into the hearts of dogs and rabbits through large veins in order to look at the heart and pulmonary circulation in life (Franck, O. and Alwens, W. 1910). Further progress with cardiovascular studies was made in 1923 with the injection of lipiodol into femoral veins to permit observation of the passage of contrast through the heart and lungs (Sicard, J.A. and Forestier, J. 1923). In 1929, the first account of catheterization in humans was published (Forssmann, W. 1929). Under fluoroscopic control, Forssman introduced a ureteric catheter into his own heart from an arm vein. Two years later, he was able to extend this procedure by injecting Uroselectan and sodium iodide through such a catheter, and so obtained one of the first contrast studies of the human vasculature (Forssmann, W. 1931). Despite the potential of this work, it remained in obscurity and Forssman abandoned his experiments.

There were two reasons why contrast studies were not an immediate success. Firstly, the technology for the production of rapid serial cut films or cine films at an acceptable radiation dose had not been developed and, secondly, contrast media were too toxic. The first really practical and useful cine-radiographic equipment was developed by Reynolds in 1935 (Reynolds, R.J. 1935), with the first record of a satisfactory angiographic demonstration of the heart and pulmonary artery

appearing in 1936 (Ameuille, P., Ronneaux, G., et al., 1936). It was not until the following year, however, that Castellanos and colleagues reported the first truly successful contrast studies (Castellanos, A., Pereiras, R., et al., 1937). The final seal of approval came as a result of work published by Robb and Steinberg in 1938 and 1939, which demonstrated the chambers of the human heart, pulmonary circulation, and great vessels, both in health and disease (Robb, J.P. and Steinberg, I. 1938; Robb, J.P. and Steinberg, I. 1939a; Robb, J.P. and Steinberg, I. 1939b).

Over the next decade, the introduction of selective intracardiac injection of contrast allowed much progress to be achieved in technique, with subsequent improvements in image quality (Cournand, A. and Ranges, H.A. 1941; Cellis, A.S. 1946). Most angiography was recorded on serial film changers. These were usually manually operated and consisted of various designs of home-made vertical and horizontal cassette tunnels and changers with rotary drums and wheels. In 1943, a changer for a maximum of twelve 10" x 12" cassettes was described by Sanchez-Perez (Sanchez, P.J. 1943) and adapted from its original neuroradiological use to more widespread cardiac and thoracic angiography. In 1948 and 1949, further advances in technology led to a roll film changer design (Dotter, C., Steinberg, I., et al., 1949; Gidlund, A. 1949). By 1951, up to 20 cassettes (30 cm x 40 cm) could be consecutively exposed at the rate of 3 cassettes every 2 seconds. This development led to the familiar cassette-free cut film changer - the AOT, an acronym for AngiO-Table (Sjogren, S.E. and Fredzell, G. 1953). The maximum changing rate for an AOT is 6 frames per second. In parallel, the Gidlund roll film changer was developed into the Elema biplane roll film changer (Magni, G.A. 1954), with a maximum of 12.5 frames per second exposure rate. Control of these items of equipment was electromechanical.

Fluoroscopy was a major problem in the early days of angiography. For an image to be seen, it was necessary to perform the entire procedure in a blacked-out room, clearly a suboptimal situation. With the development of the image intensifier, this was no longer necessary, and the devices were immediately incorporated into the equipment of the angiographic suite. Subsequently, cine-film cameras were attached to the image intensifiers, but it was not until the end of the 1960's that adequate image quality could be attained through this combination. By the mid-1970's, cine film had become the premier and routine medium on which to store anatomical information gained from cardiac chamber catheterization and selective

coronary arteriography. After many trials, a speed of 50 frames/s in adults and 90 frames/s in children was established for routine work. Outside the study of the heart, cut film, exposed at typical framing rates under 3 frames/s, remained the norm.

In parallel with advances in radiographic equipment were developments in contrast material. Early studies made use of sodium iodide, a rather toxic agent. In 1929, Uroselectan, an organic iodide, was developed and used clinically (Von Lichtenberg, A. and Swick, M. 1929). Thorotrast, a compound of radioactive thorium, became available in 1931, and was used for peripheral angiography (Dos Santos, R., Lamas, A.C., et al., 1931). It was not widely introduced because of its long half life, as well as the agent's uptake by the reticuloendothelial system. During the 1930's Uroselectan B, mixed with sodium iodide, was available for vascular visualization; it was quite adequate for this purpose, but the sodium iodide in particular was toxic. In 1939, diodrast (Sterling-Winthrop) was used in cardiovascular imaging by Robb and Steinberg (Robb, J.P. and Steinberg, I. 1939a; Robb, J.P. and Steinberg, I. 1939b). In its original 35% concentration, used for intravenous pyelography, this agent did not provide sufficient contrast for good cardiovascular visualization. Robb and Steinberg therefore boiled the agent to achieve a 70% concentration. Attention was simultaneously paid to the method by which the contrast agent was introduced, leading to the design of the Robb & Steinberg needle. This was a 12 gauge device, intended to be percutaneously inserted into the basilic vein of the arm. Fifty millilitres of contrast could be injected through it in two seconds. By 1954, Renografin, a safe, relatively non-toxic, ionic, organic iodide, had been developed (Schering AG). Power-assisted injections became commonplace and, with other refinements, better visualization of vascular structures was made possible (Finby, N. 1964). Further advances in contrast materials led to two groups of ionic media, iodinated molecules of triiododiamino benzoic acid (1952, Schering, diatrizoate) and triiodoisophthalamic acid (1961, Mallinckrodt, iothalamates). The connection between lipophilicity and toxicity of contrast material was recognized early in the development of these agents (Knoefel, P.K. and Huang, K.C. 1956), leading to reduction of toxicity to tolerable levels by the addition of hydrophilic side chains to the molecules, as in iothalamate .

By the early 1970's, therefore, state of the art angiography involved the selective injection of ionic contrast into the vessel(s) under investigation, followed by the acquisition of images of the arterial tree through an image intensifier (to produce cine images), or directly onto cut film. It was into this process that computer technology was introduced, eventually leading to digital subtraction angiography (DSA).

1.2 Physics of Image Production

1.2.1 x-ray generation and the nature of an x-ray beam

Roentgen reported in his original paper that x-rays are produced where cathode rays strike some material object. As cathode rays are high velocity electrons, this is usually restated as "x-rays are produced when high velocity electrons abruptly lose a significant portion of their energy".

Most of the electrons which interact with matter undergo multiple glancing collisions and, in the course of these, lose their energy a little at a time, merely increasing the average kinetic energy of the particles in the material. This results in a temperature rise of the target material. It is found that most of the energy of the electron beam goes into heating the target.

Some of the bombarding electrons, however, make solid hits and lose most or all of their energy in just one collision. These electrons are rapidly decelerated. It is now known that radiation results when a charged body is accelerated. Therefore, when an electron loses a large amount of energy by deceleration, an energetic pulse of electromagnetic radiation is produced. This is an inverse photoelectric effect, through which an electron produces a photon. Electrons of a given energy produce x-ray photons with a certain maximum energy. According to classical electromagnetic theory, there is no lower limit to the wavelength of the radiation that a moving electron can produce when stopped suddenly. There is, however, a quantum limit. The energy (E) of a photon can be expressed by the equation:

$$\mathrm{E}\,(eV) = \frac{1.24 * 10^3}{\lambda} \qquad 1.1$$

where λ = wavelength of radiation in nanometres, and eV = electron-volts. If an electron loses all its energy in a single encounter, the minimum wavelength of the ensuing electromagnetic radiation is given by:

$$\lambda_{\min}(nM) = \frac{1240}{V} \qquad 1.2$$

where V is the accelerating potential of the electron in volts. This is a minimum, since no electron can lose more energy than it possesses. There is a continuous distribution of radiation towards the longer wavelengths, since not all collisions result in total energy loss. The glancing collisions account for the continuous spectrum of x-rays from any target material and also for the inefficiency of the conversion of electron kinetic energy into x-ray energy. The Germans named this continuous radiation "Bremsstrahlung," meaning literally, breaking radiation.

By examining the collision process more closely, it is found that there exists another, very important, exchange of collision energy. This consists of the transfer of energy to bound electrons in the target atoms. If enough energy is transferred, these bound electrons may become free, and ions produced. Such an event may occur because electrons capable of producing x-ray radiation have energies of the order of many thousands of electron volts, sufficient to remove outer shell electrons. x-ray producing electrons may also have enough energy to produce ions by removing inner, K & L shell electrons. Such an ion has a low-energy hole in its electronic structure, a vacancy promptly filled when an electron from a higher energy state falls to this low-energy level.

Although the energy required to ionize an atom by removal of an outer electron is much less than 100 eV, the energy required to ionize by removal of an inner electron may be as high as 120 KeV. When an outer electron falls into such a vacancy, it will radiate a photon with this high energy. These photons are in the x-ray region of the electromagnetic spectrum, and have wavelengths of the order of fractions of a nanometre. This mechanism, which accounts for a significant part of x-ray production, produces x-rays having particular wavelengths which are characteristic of the target material - for example the K excitation energy for tungsten is 69.55 KeV, whilst for molybdenum it is 20.1 KeV. This characteristic radiation, as it is called, is superimposed on the Bremsstrahlung to give the familiar x-ray spectrum, illustrated in Figure 1 for molybdenum. Note that at a 20 kV accelerating voltage, no

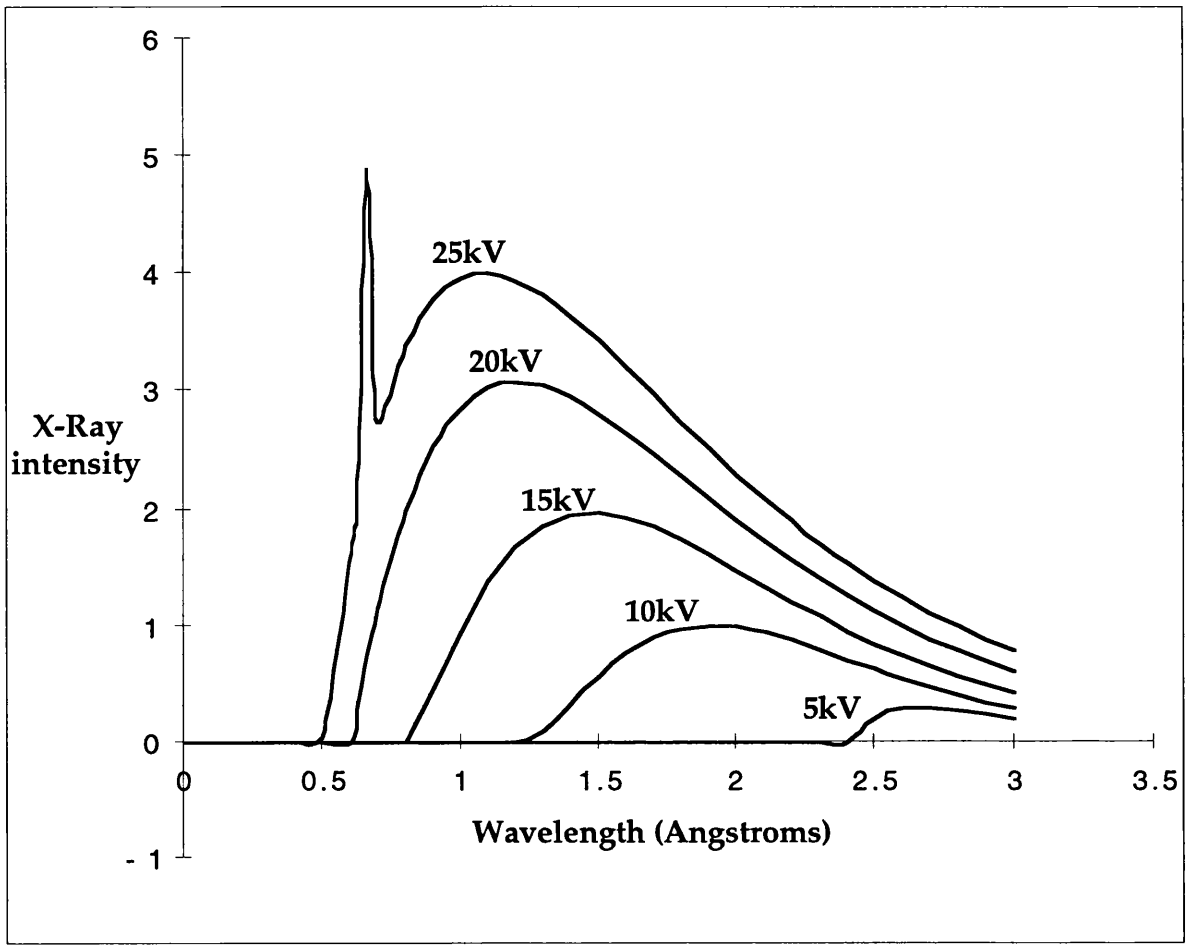

Figure 1. x-ray spectra of molybdenum as a function of the voltage applied to the accelerated, bombarding electrons. The K-edge of this element is at 20.1 keV. Therefore, characteristic radiation only appears on the spectra of radiation obtained from bombarding electrons which have been accelerated to energies above this value. Five energy spectra are shown, generated by electrons which have been accelerated from 5 to 25 kV, in steps of 5 kV.

electron will have enough energy to initiate a K-edge event, and therefore the spectrum does not contain characteristic radiation. The important point to take forward from this section is that, in real life, an x-ray beam is polychromatic, with many wavelengths contributing to its intensity. This imposes practical limitations on some aspects of the subtraction process utilized to produce high conspicuity images in DSA.

1.2.2 x-ray absorption

The most spectacular property of x-rays is their ability to penetrate materials which are opaque to less energetic radiation. The basic mechanism of the absorption of ultraviolet, visible and infrared radiation is the transfer of photon energy to the vibrational energy states of the material that is doing the absorbing. In the case of an

x-ray photon with energy in the range used for diagnostic purposes, ie. several orders of magnitude greater than visible light, an x-ray photon has only a very low probability of participating in this low energy process. In its passage through matter, an x-ray photon is more likely to interact with electrons in the atoms comprising the irradiated material, however, since the probability of this interaction is relatively small, any individual x-rays photon is likely to pass through the material.

Given an intensity of I_0 of incident monochromatic x-radiation, the radiation transmitted through an homogenous attenuator may be described by the differential equation:

$$dI_x = -\mu_l I_x dx. \qquad 1.3$$

where dx is a small thickness of the attenuator at x, dI is the amount of attenuation afforded by dx, μ_1 is a constant, I_x is the amount of radiation incident on the element dx at position x within an homogenous object, and the whole is considered to be in a vacuum. Integrating Eq. 1.3 and applying boundary conditions yields:

$$I_x = I_0 \, e^{-\mu_1 x} \qquad 1.4$$

μ_1, the linear attenuation coefficient, is equal to the fractional decrease in radiation intensity per unit thickness of the absorber, and has dimensions of reciprocal length. It should be noted that μ_1 depends strongly on the density of the absorbing material; a quantity μ_1/ρ may be defined as the mass attenuation coefficient, where ρ is the density of the material concerned:

$$\mu_m = \mu_1/\rho. \qquad 1.5$$

μ_m has units of area/mass m^2/kg, and is independent of density. It follows from Eq. 1.5 by substitution that:

$$\mu_1 x = \frac{\mu_1(x\rho)}{\rho} \qquad 1.6$$

which when re-arranged yields:

$$\mu_1 x = \mu_m(x\rho) \qquad 1.7$$

where $(x\rho)$ is the mass per unit area of the absorber and is usually denoted m_a. Therefore Eq. 1.4 can now be re-written

$$I_x = I_o\, e^{-\mu_m m_a}. \qquad 1.8$$

μ_m in turn may be expressed in more fundamental terms by

$$\mu_m = \frac{\sigma_{tot}\, N_a}{M} \qquad 1.9$$

where σ_{tot} is the total atomic interaction cross section, N_a is Avogadro's number and M is the atomic weight of the absorber. It can be seen that μ_m has a dependency on the atomic number of the attenuating material. Now σ_{tot} is in fact a linear sum of several factors that contribute to x-ray absorption. In the range of energies that comprise the common diagnostic x-ray beams (20 – 100 *keV*) there are two principle components contributing to σ_{tot}. These are the photoelectric effect and Compton scattering.

Let σ_τ be the photoelectric effect component and σ_c be the Compton scattering component. Then:

$$\sigma_{tot} = \sigma_\tau + \sigma_c \qquad 1.10$$

which, by applying Eq. 1.9 and rearranging, leads to:

$$\mu_m = \mu_\tau + \mu_c. \qquad 1.11$$

This is valid within the range of x-ray energies 10*keV* to 1.02*MeV*. These are tabulated as a function of energy for air, water, muscle, bone, and contrast in tables 1-6. (White-Grodstein, G. 1957; Davisson, C.M. 1965; Evans, R.D. 1968) The two important points to carry forward from this analysis are that μ_m varies both with each element in the periodic table and with the energy of the incident x-ray beam.

1.2.3 Tissue contrast and production of an image

From section 1.2.2 it will be appreciated that as there are differences in the ability of diverse tissues and compounds to attenuate x-rays, so there is a mechanism for production of an image based on these differences. The ability to distinguish between two adjacent tissues based on such attenuation differences is termed tissue

Table 1

Composite mass attenuation coefficient (μ_m) and its components due to the photoelectric effect and Compton scattering for air.

keV	Photoelectric Effect μ_t (cm ^{2}/gm)	Compton Scattering μ_c (cm ^{2}/gm)	Total μ_m (cm ^{2}/gm)
10	4.6300	0.193	4.820
15	1.2700	0.189	1.450
20	0.5050	0.186	0.690
30	0.1390	0.180	0.320
40	0.5550	0.174	0.230
50	0.0270	0.169	0.196
60	0.0150	0.164	0.179
80	0.0060	0.156	0.162
100	0.0030	0.148	0.151
150	0.0008	0.133	0.134

Table 2

Composite mass attenuation coefficient (μ_m) and its components due to the photoelectric effect and Compton scattering for water.

keV	Photoelectric Effect μ_t (cm ^{2}/gm)	Compton Scattering μ_c (cm ^{2}/gm)	Total μ_m (cm ^{2}/gm)
10	4.7800	0.214	4.990
15	1.2700	0.210	1.480
20	0.5050	0.207	0.711
30	0.1380	0.200	0.338
40	0.0550	0.193	0.248
50	0.0270	0.188	0.214
60	0.0150	0.182	0.197
80	0.0060	0.173	0.179
100	0.0030	0.165	0.168
150	0.0008	0.148	0.149

Table 3

Composite mass attenuation coefficient (μ_m) and its components due to the photoelectric effect and Compton scattering for muscle.

keV	Photoelectric Effect μ_t (cm ^{2}/gm)	Compton Scattering μ_c (cm ^{2}/gm)	Total μ_m (cm ^{2}/gm)
10	4.8800	0.212	5.090
15	1.3200	0.208	1.530
20	0.5260	0.205	0.731
30	0.1440	0.198	0.342
40	0.0570	0.192	0.249
50	0.0280	0.186	0.214
60	0.0160	0.181	0.197
80	0.0060	0.171	0.178
100	0.0030	0.163	0.166
150	0.0008	0.147	0.148

Table 4

Composite mass attenuation coefficient (μ_m) and its components due to the photoelectric effect and Compton scattering for bone.

keV	Photoelectric Effect μ_t (cm ^{2}/gm)	Compton Scattering μ_c (cm ^{2}/gm)	Total μ_m (cm ^{2}/gm)
10	19.8000	0.205	20.000
15	5.9500	0.201	6.150
20	2.4900	0.197	2.680
30	0.7160	0.191	0.910
40	0.2930	0.185	0.478
50	0.1470	0.179	0.327
60	0.0840	0.174	0.258
80	0.0350	0.165	0.200
100	0.0170	0.157	0.174
150	0.0050	0.142	0.147

Table 5

Composite mass attenuation coefficient (μ_m) and its components due to the photoelectric effect and Compton scattering for iodine contrast material (Iopamidol, E. Merck).

keV	Photoelectric Effect μ_t (cm ^{2}/gm)	Compton Scattering μ_c (cm ^{2}/gm)	Total μ_m (cm ^{2}/gm)
10	79.07	0.178	79.260
15	26.49	0.179	26.670
20	12.22	0.176	12.390
30	3.88	0.170	4.050
40	10.86	0.165	11.030
50	5.99	0.160	6.150
60	3.64	0.155	3.790
80	1.66	0.147	1.810
100	0.88	0.140	1.018
150	0.27	0.126	0.401

Table 6

Composite mass attenuation coefficient (μ_m) of the elements comprising Iopamidol ($C_{17}H_{22}N_3O_2I_3$)

keV	Total μ_m (cm ^{2}/gm)				
	C	H	N	O	I
10	2.14	0.39	3.57	5.57	158.20
15	0.72	0.38	1.09	1.62	53.31
20	0.39	0.37	0.54	0.75	24.74
30	0.23	0.36	0.28	0.34	7.98
40	0.19	0.35	0.21	0.24	22.26
50	0.18	0.34	0.19	0.20	12.34
60	0.17	0.33	0.17	0.18	7.54
80	0.16	0.31	0.16	0.16	3.52
100	0.15	0.30	0.15	0.15	1.91

contrast. Given a single beam of x-rays irradiating a patient, the radiographic image is a map of the residual photon flux after each part of the original beam has been attenuated by tissues in its path.

A biological specimen has a limited number of tissue constituents, so that for practical purposes a body may be considered to consist of air (eg. lung), bone, water (eg. soft tissue, blood) and fat. There is thus a limited amount of inherent tissue contrast present in a plain radiograph. The ability of a system to distinguish between tissues based on x-ray attenuation leads to the concept of conspicuity. Conspicuity is the perceived ease of distinguishing between tissue contrasts of similar value. An image with high conspicuity has a high perceived contrast between similar tissues.

1.2.4 Visualization and storage of an image

When a uniform beam of x-rays passes through a patient, as discussed in section 1.2.3, differential attenuation takes place. This pattern of intensity created within the x-ray beam depends entirely on the nature and position of the anatomical structures in the patient through which the beam has passed. Although this pattern is actually present in the emerging x-ray beam, it cannot be directly discerned because the human eye is not visually sensitive to x-radiation. It is necessary to render the pattern visible, which can be accomplished by two principal methods.

1.2.4.1 *Radiography*

In this method, the pattern of x-rays is allowed to fall onto a photographic film, contained in a light tight cassette and placed in the path of an emerging x-ray beam. After exposure, the film is photographically processed to produce a stable visual representation of whites, greys and blacks, corresponding to low or absent, intermediate, and high x-ray photon flux. These tonal ranges correspond to areas of high attenuation, medium attenuation, and little or no attenuation. The film is therefore viewed as a series of grey levels.

1.2.4.2 *Fluoroscopy*

Instead of allowing the modified, transmitted x-ray beam to fall onto film, it may instead fall onto a fluorescent screen. The main property of such a screen is to convert the very high energy x-ray photons into low energy visible light, in proportion to the incident x-ray intensity. However, the resulting visible image is quite dim and requires further amplification, which can be achieved by an image-intensifier. Thus the image is made brighter, and thereby rendered easier to see. Furthermore, the output of the image intensifier may be photographed by using $35mm$ cine film, or with a standard television camera. If a television camera is used, its analogue output is usually transmitted to closed circuit TV monitors for convenient viewing, and possibly video tape storage. Cine film provides a dynamic record of a series of events.

1.3 Altering Inherent Tissue Contrast

From examination of the attenuation coefficients at varying x-ray beam energies (tables 1-6), it can be deduced that a judicious choice of irradiating energy can maximise the rather small differences in attenuation coefficient. In general, the lower the keV of the x-ray photon beam, the greater the tissue contrast generated. However, there are several drawbacks. Enough x-rays have to penetrate without attenuation in order to produce an image in the first place. In addition the biological effects of x-rays on tissue are more pronounced at lower energies. This means that there is a limited range of peak energies which can be used in generating x-rays. Fortunately photographic film has a very wide dynamic range and is relatively forgiving of errors in the choice of x-ray exposure factors. The upper limits of peak energies are governed by the scatter produced within tissue. At high energies ($> 80kVp$), a significant proportion of the scattered radiation will fall onto the film and create a background fogging effect. This in itself will reduce apparent tissue contrast.

1.3.1 Introduction of iodine contrast material

Since manipulation of the x-ray equipment did not yield major improvement in visualization of tissue structures, the obverse approach was adopted and various tissue structures had their inherent contrast altered, albeit temporarily, by the

introduction of some form of dense, yet non-toxic material. A suspension of barium was adopted for the alimentary tract, and in the vascular tree a solution of an organic iodine based molecule was used. The present discussion will be limited to the use of iodinated contrast material.

Consider a volume element of tissue (voxel) with a square cross-section measuring 1 cm, and of length x cm. Let the tissue be homogenous, with a mass attenuation coefficient of μ_t. Then, by application of Eq. 1.8, we get:

$$I_t = I_o\, e^{-\mu_t (m_t/x)x} \qquad 1.12$$

where m_t is the mass per unit area of tissue, and $m_t/x = \rho$, the density of the material. Now introduce a volume element of rectangular cross section $1cm^2$ and thickness δx into the path of the beam. By replacing part of the tissue with iodinated contrast material (here represented as μ_i and m_i) as the attenuation coefficient and mass of material per unit area, respectively, Eq. 1.12 gives:

$$I_t' = I_o\, e^{-\mu_t (m_t/x)(x-\delta x)}\, e^{-\mu_i (m_i/\delta x)\delta x}. \qquad 1.13$$

If $\delta x << x$, this is usually approximated by:

$$I_t' = I_o\, e^{-\mu_t (m_t/x)x}\, e^{-\mu_i (m_i/\delta x)\delta x}. \qquad 1.14$$

Subtracting Eq. 1.14 from Eq. 1.12 gives

$$\Delta I = I_o\, e^{-\mu_t (m_t/x)x} \{1 - e^{-\mu_i (m_i/\delta x)\delta x}\} \qquad 1.15$$

This equation represents the decrease in intensity of the transmitted beam, caused by the introduction of iodine into its path. For the purposes of derivation of Eq. 1.15, the element δx was considered to consist of solid iodine. Clearly this is not the case in reality. One cm^3 of solid iodine would contain 4.94 gm of the element $(\rho = 4.94\, gm/cm^3)$. A typical modern contrast agent, such as Iopamidol 370 (E. Merck Ltd.), contains 0.37 gm/cm^3 of iodine.

Equation 1.15 may be re-written in a slightly more useful form, by removing the dependence on m_i and generalizing to a concentration of achieved contrast material within the path of the x-ray beam. This removes the constraint of a known area of cross-section of the beam and/or voxel under question. μ_i has units of cm^2/gm, and

m_i has units of gm/cm^2. Consider a voxel with volume $V = a\delta x$, where a is the area of the face of the voxel on which radiation is incident. Then:

$$m_i = (\text{mass of iodine in } V)/a. \qquad 1.15a$$

Now the concentration of iodine in the volume is given by:

$$[I] = \frac{\text{mass of iodine}}{V}. \qquad 1.15b$$

$$\therefore\ m_i = \frac{[I]\,V}{a} \qquad 1.15c$$

but $\frac{V}{a} = \delta x$:

$$\therefore\ m_i = [I]\delta x. \qquad 1.15d$$

and

$$\Delta I = I_0\, e^{-\mu_i m_i x}\{1 - e^{-\mu_i [I]\delta x}\}. \qquad 1.16$$

Expressed as a ratio, the fractional increase in tissue contrast (T_c) accruing as a result of injection of an iodinated agent into a blood vessel can thus be given by:

$$T_c = 1 - e^{-\mu_i [I]\delta x}. \qquad 1.17$$

The assumptions inherent in this equation are:

a) $\delta x \ll$ total path of tissue traversed by the beam, ignoring attenuation due to air;

b) μ_i is dominated by the iodine molecules in the contrast agent.

In the situation that exists clinically, the first of these assumptions is acceptable, as δx is typically in the range $0.1\ cm < \delta x < 5\ cm$, and x is typically 30-40cm (including tissue equivalents due to inherent tube filtration and the apparatus to support the patient). The second assumption, b, is also acceptable. This can be appreciated by looking at table 6, where it can be seen that at 60 keV, the ratio of μ caused by iodine to the rest of the molecule per atom of iodine is 7.54:0.85. With respect to water (table 2), this ratio is 7.54:0.197, ie., 40:1 overall. In summary, as long as δx is relatively small, the generated extra tissue contrast is related to the concentration of iodine in the beam path and the thickness of the iodine containing tissues.

1.3.2 Film Subtraction

In angiography, a loss of radiographic contrast may occur due to the superimposition of bone and other structures upon the vascular pattern demonstrated by iodinated contrast material. In these instances, retrieval of the radiographic information is made possible by the technique of photographic subtraction. This was first described in 1935 and has been an invaluable tool, particularly in neuroradiology (Ziedses Des Plantes, B.G. 1935).

The technique involves making two radiographic exposures as well as an intermediate positive transparency. Initially, the part of the patient to be radiographed is immobilized and a preliminary radiograph obtained prior to injection; this is the mask film. During the injection of contrast material, a second film is obtained with the same exposure factors as used for the mask film. This film contains new information, resulting from the presence of iodinated contrast material in the tissue, as well as the information previously seen in the mask film; this is the data film. A photographic contact transparency is made of the mask film. This intermediate film is then superimposed on the data film, and a final subtracted transparency is made. This final film is a totally reversed version of the data film, with bone and soft tissue detail removed, leaving behind only the information resulting from the presence of iodinated contrast material in the tissue. However, this procedure is both tedious and time consuming .

The automated combination of these two methods of altering inherent contrast to make the vasculature more conspicuous is the technique of digital subtraction angiography.

CHAPTER 2

DIGITAL SUBTRACTION: PHYSICS

2.1 Components of the Equipment

The commercial digital unit on which the bulk of this research was carried out is shown schematically in Figure 2. The principal components are a primary switched x-ray generator with a high heat capacity tube mounted on one side of an L-U arm system, the image intensifier and plumbicon camera being mounted on the opposite side. The analogue-to-digital converter, computerized frame grabber and array processor are connected by shielded cabling to the plumbicon tube, and are physically located in a separate computer room. The computer controlling all the functions of the system is operated in tandem with an x-ray setup console. The components of this system that make the whole technique possible are i) the image intensifier, ii) the analogue-to-digital converter and iii) the high speed frame grabber.

2.2 The Theory and Practice of Operation

2.2.1 x-ray Production

As with any procedure requiring multiple rapid exposures and a high photon flux, the design and implementation of the generator and tube combination are important. A high heat capacity, heavy-duty tube is necessary in order to produce a sufficiently high photon flux. As the use of a 0.3 mm focal spot results in unacceptable levels of heat generation, a 0.6 mm or 1.2 mm spot must be implemented. Since digital subtraction angiography is a relatively low resolution system, the use of a 1.2 mm focal spot incurs very little penalty (Kruger, R.A. 1982). A constant potential generator would be ideal. Implementation of such a generator in a rapid-switching situation, however, is expensive and, generally, a 3 phase, 12 pulse primary switched and smoothed generator produces good images. The tube and generator are not usually considered to be the critical or limiting parts of the imaging process.

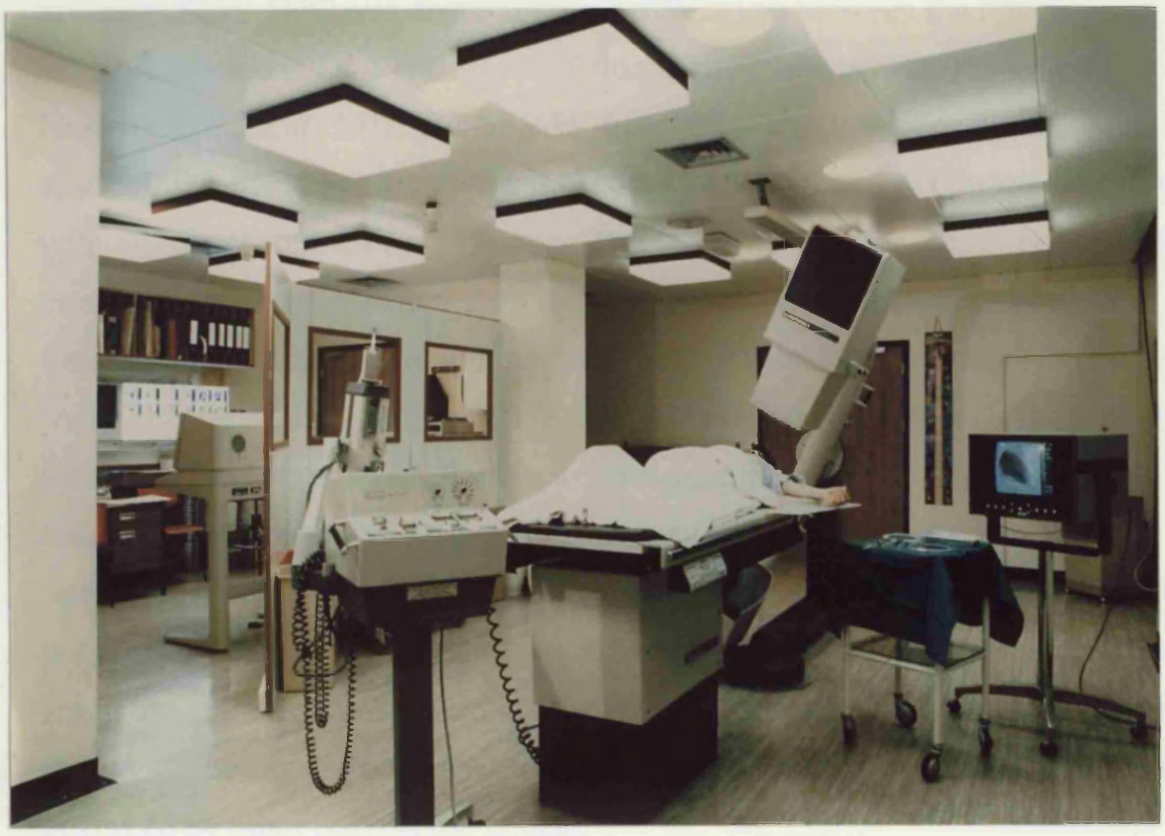

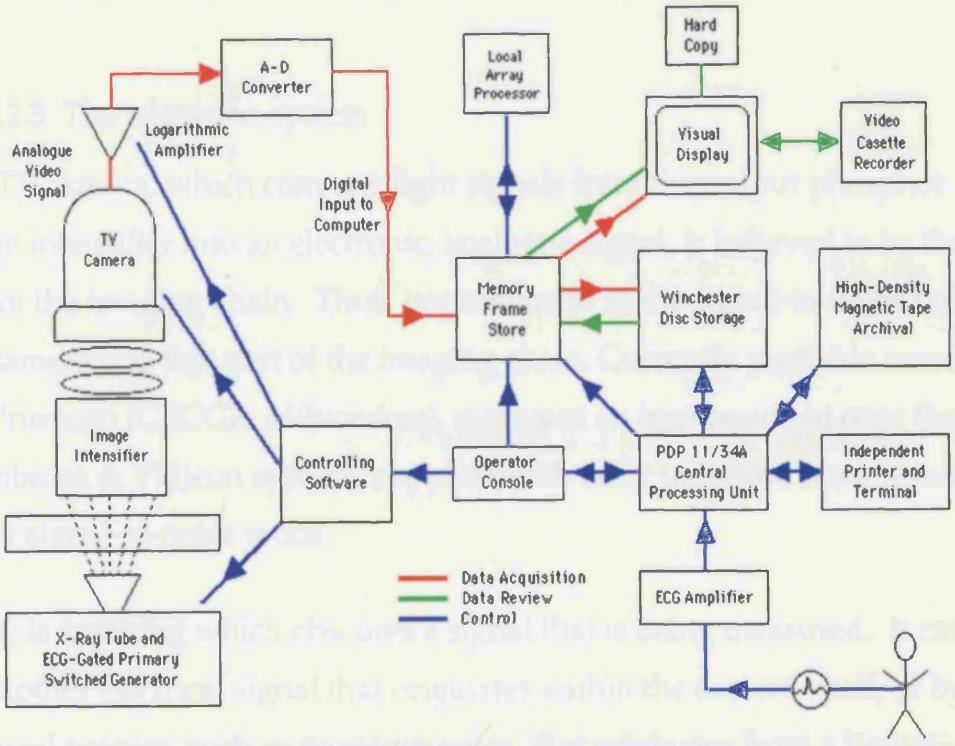

Figure 2. The inter-relationships of the components of a commercial digital subtraction system are shown.

2.2.2 The Image Intensifier

The modern caesium iodide intensifier is one of the strongest links in the DSA imaging chain. However, there are some differences between the image intensifiers used in DSA and standard fluoroscopic intensifiers (Roehrig, H., Nudelman, S., et al., 1977; Roehrig, H., Lum, B., et al., 1979). For digital applications, the image intensifier must operate at a 1-2 mR per image exposure without loss of contrast or resolution. This is higher than for conventional work, or even for cine-fluoroscopy. This requirement alone can lead to pulse change defocusing, or saturation of the output phosphor in a standard image intensifier (Arnold, V., Eisenberg, H., et al., 1981). One further consideration is that at high (relatively) radiation levels, there is a correspondingly high gain in light level output. This necessitates proper aperture control of the TV camera to allow optimal response (Arnold, V., Eisenberg, H., et al., 1981). The caesium iodide unit is a standard for digital systems, and currently intensifiers up to 40 cm in diameter are in use. However, whilst these offer superior contrast resolution, a decrease in spatial resolution also occurs with their use because of the fixed acquisition matrix governed by other parts of the system.

2.2.3 The television system

The TV camera, which converts light signals from the output phosphor of the image intensifier into an electronic, analogue signal, is believed to be the weakest link in the imaging chain. Thus, improvement in the signal-to-noise ratio (SNR) is fundamental to this part of the imaging chain. Currently available cameras, such as the Primicon (GECGR, Milwaukee), represent an improvement over the initial Plumbicon & Vidicon systems supplied with early units and have resulted in better signal-to-noise ratios.

Noise is anything which obscures a signal that is being measured. It can be caused by another electrical signal that originates within the camera itself, or by some physical process, such as quantum noise, that originates from a limitation in the number of x-ray photons per image, or from the digitization noise associated with the uncertainties of quantizing a video signal into a finite number of digital levels (Kruger, R.A. 1982). The SNR can be considered to consist of two dominant components. One results from the quantum nature of the x-ray beam and is

proportional to the number of photons *(N)* travelling through the tissue. The second is introduced by the electronics of the video system and may be represented by SNR_{tv}. Together they produce a total SNR given by:

$$SNR = \frac{1}{(1/N + 1/SNR_{tv})} \qquad 2.1$$

Further consideration of this problem has been undertaken by Pullan. Summarizing from that source, at current levels of SNR (of the order of 800:1), a final subtracted image signal-to-noise ratio of 5:1 can be readily achieved in a $1\,mm$ x $1\,mm$ vessel by using standard methods of contrast introduction (Pullan, B.R. 1981).

The crucial point to be gained here is that in practice, as long as an adequate exposure is obtained, the SNR of cameras in current use is not a limiting factor in the acquisition and storage of a digital image.

2.2.4 The analogue-to-digital converter

The process of changing an analogue TV signal into a stream of digital information is performed by an analogue-to-digital converter (ADC). The efficiency of the process can be defined by the rate and depth of digitization. The necessary rate of digitization is governed by the scan rate of the TV camera and the fineness of spatial separation between successively digitized parts of the image. In general, the digitization rate is not a limiting factor in the imaging chain. The depth of digitization is, however, important because it is related to the number of shades of grey in the final image. In terms of visual perception, the human eye has a surprisingly narrow bandwidth, and only some 32 to 64 grey levels can be simultaneously distinguished. This conforms to 5 or 6 bit levels of digitization. Therefore, allowing for noise, a perfectly adequate compromise between the desire for ultimate contrast resolution and visual appreciation of the final image is digitization to 8 bits, or 256 grey levels. No system works well at its limit, and this applies equally to an ADC. Commercial DSA systems digitize to at least 10 bits; and the very best machines routinely digitize to 16 bits. This extra, internal resolution allows signal averaging to occur and permits a final 8 bit image to have

a linear response across the range of grey levels. In modern systems, the ADC, like the TV camera, is not a limiting factor in the imaging chain.

2.2.5 The logarithmic amplifier

If Eq. 1.12 and Eq. 1.14 are written in terms of linear attenuation coefficients, then:

$$I_t = I_o\, e^{-\mu_{It}x} \qquad 2.2$$

$$I'_t = I_o\, e^{-\mu_{It}x}\, e^{-\mu_{Ii}\delta x} \qquad 2.3$$

where μ_{It} and μ_{Ii} are the linear attenuation coefficients of tissue and iodine respectively. Taking logarithms of both sides of Eq. 2.2 and Eq. 2.3 gives:

$$Ln(I_t) = Ln(I_o) + (-\mu_{It}x) \qquad 2.4$$

$$Ln(I'_t) = Ln(I_o) + (-\mu_{It}x) + (-\mu_{Ii}\delta x). \qquad 2.5$$

Subtracting Eq. 2.4 from Eq. 2.5 and rearranging them gives:

$$Ln(I_t) - Ln(I'_t) = \mu_{Ii}\delta x. \qquad 2.6$$

Thus, a rather unwieldy equation has been transformed into a simple relationship which states that after logarithmic transformation, the difference between two signals is due solely to the thickness of iodine added into the path of the beam. Thus, DSA counts the number of molecules of iodine in the path of the x-ray beam.

Logarithmic amplification can be achieved by a hardwired system or in software. In either case, the net result is the same. Figure 3 shows a typical logarithmic transform function on an 8 bit 256 grey level image.

2.2.6 The Digital Storage Device

The x-ray beam is mapped onto a two dimensional rectangular array of points, the image matrix. The matrix size is defined by the number of these array points or pixels (short for picture elements) on each side of the image. Typical matrix sizes are 256 x 256, 512 x 512 and, more recently, 1024 x 1024 pixels. As the pixel is the smallest element in the picture, the resolution of the system is defined by the pixel size. The in-plane resolution of an individual pixel is 0.19 mm if a 512 x 512 matrix

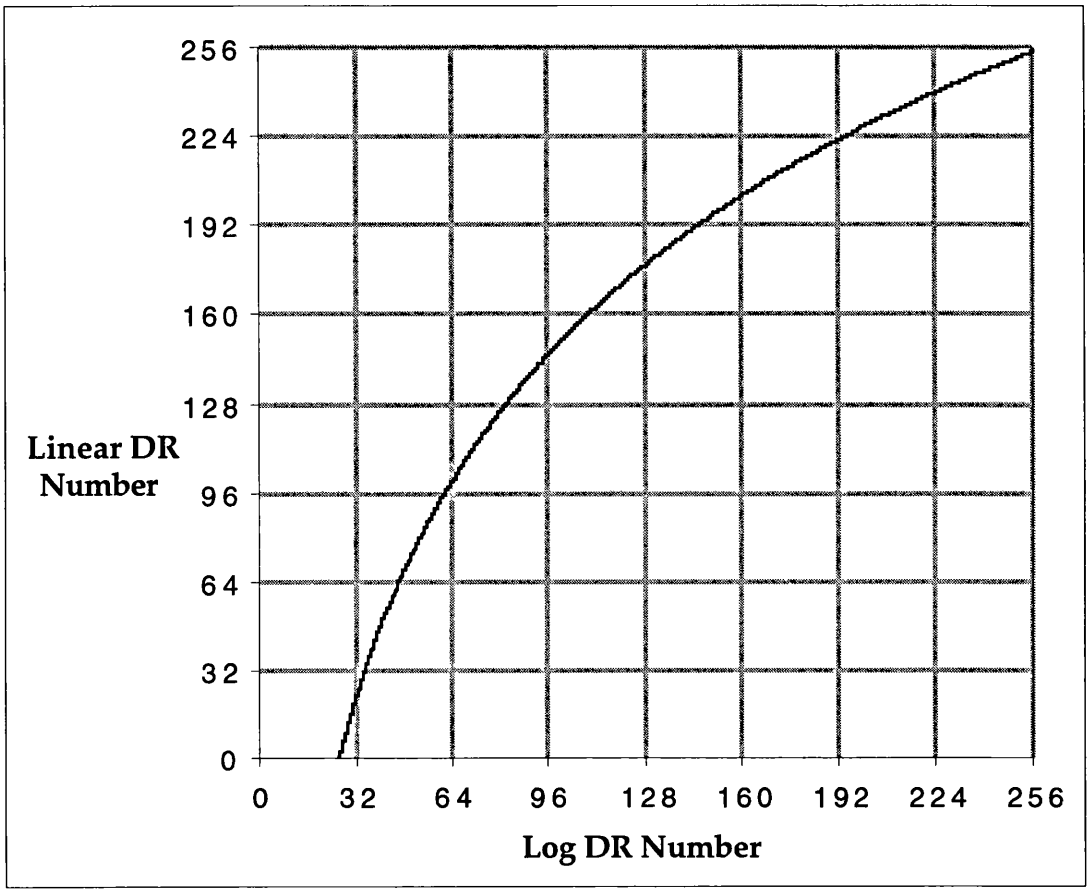

Figure 3. This is a graphical representation of a logarithmic transformation. The linear value of attenuation is transformed logarithmically along the curve shown. Thus, if the raw attenuation number is 153, it will be transformed into the value 102 and stored in digital form as 102. Subtraction between logarithmically transformed numbers yields a value linearly related to the iodine content introduced into the path of the x-ray beam.

is mapped onto a 10 cm field-of-view (fov). More commonly though, a field-of-view of 22 cm or 30 cm is used, which leads even with a 1024 x 1024 matrix to an in-plane pixel dimension of some 0.3 mm, or 1.5 line pairs/mm resolution. Under all but the most demanding circumstances, a 512 x 512 matrix on a 30 cm field-of-view is indistinguishable from a 1024 x 1024 matrix on the same field-of-view, as long as interpretation or analysis is purely visual. In most cases, even a 256 x 256 image is perfectly adequate. Figure 4 demonstrates this point by using a well-known household object as a phantom. There are benefits in terms of both storage space and acquisition rate in using a smaller matrix size, since at 8 bits per pixel, a 256 x 256 image will need 65536 bytes of storage, whereas a 1024 x 1024 image will need 1,048,576 bytes of storage (1024K). Clearly, a 16 fold increase in both transfer rate and data storage may not be justifiable in terms of cost and space.

Figure 4. Three images of a telephone showing the effect of matrix size on the final picture. Top = 512*512, middle = 256*256, and bottom = 128*128. Note how it is very difficult to distinguish between the top and middle images, whilst the bottom image is quite obviously made up of discrete pixels, particularly seen around the highlights.

2.3 The Limitations of a Real System

Ideally in DSA there should be a linear relationship between the subtraction image and the thickness of iodine as outlined above. In practice, the relationship is non-linear due to the presence of beam hardening, veiling glare and radiation scatter. Beam hardening occurs as a consequence of the polychromatic nature of the x-ray beam and the differential attenuation at various energies. Scatter is also variable, depending on energy. Veiling glare is a feature of the image intensifier, whereby blooming of the electron beam occurs due to imperfect focusing in areas of high electron density (electrons repel each other). In addition, there are problems of image distortion due either to pincushion effects, or barrel distortion inherent to image intensifiers. The contribution to the iodine signal in these cases has been discussed in detail by Shaw (Shaw, C.G., Ergun, D.L., et al., 1982). In clinical terms, if DSA is being used purely as a superior method for demonstrating anatomy, then no attention need be paid to these effects. If some form of absolute iodine measurement is being inferred from the images, then significant errors may result if these effects are not considered. This latter situation has major implications for the discussion of blood flow measurement by existing methods and will be considered in detail in part two of this thesis.

The problems of radiation scatter can be minimized by the use of a fixed grid (16:1 ratio) and the presence of a small air gap. Veiling glare is minimized by careful choice of exposure factors, and pincushion or barrel distortion can be ignored, as long as the region of interest is not at the very edge of the intensifier image (Shaw, C.G., Ergun, D.L., et al., 1982).

In summary, of the possible problems which could seriously alter the true representation of image data, only beam hardening remains significant. Figure 5 demonstrates the effects of beam hardening in the subtraction process, where incomplete subtraction of the vertebral body can be seen projecting through an area of very high iodinated contrast concentration.

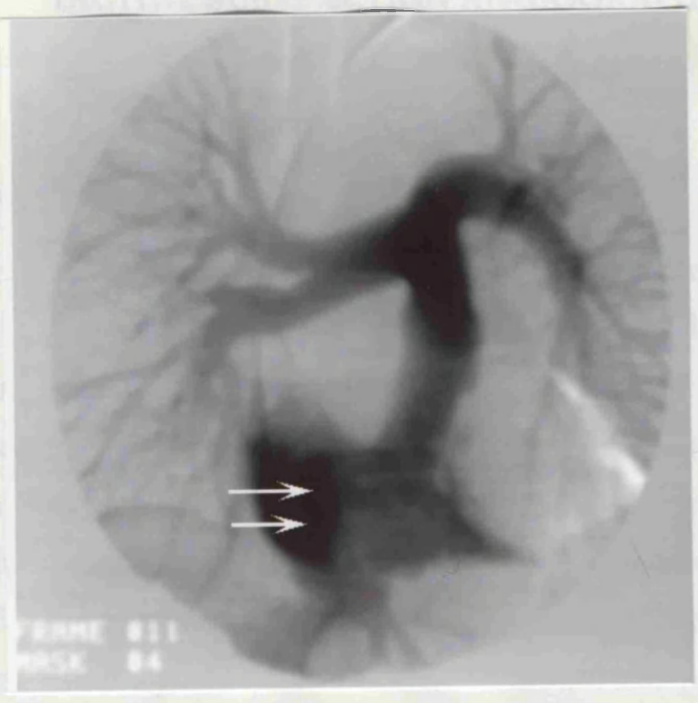

Figure 5. An injection of contrast (350 mg/ml) has been made into the right atrium; note how the vertebral bodies are seen overlying the dense part of the image due to imperfect subtraction. They have subtracted out perfectly over the areas of low iodine contrast density. This imperfect subtraction of the vertebral bodies is a manifestation of beam hardening. The partially subtracted vertebral body is indicated by arrows.

2.4 Summary of Working Assumptions

The polychromatic x-ray beam can be considered as a single energy entity, unless the iodine concentration rises above 2% (20 mg/ml). Pincushion and other distortions originating within the image intensifier may be ignored if the region of interest is in the central part of the image intensifier, where these effects are minimal. Scatter may be controlled by a grid, and veiling glare may be controlled by judicious choice of exposure factors.

CHAPTER 3

DIGITAL SUBTRACTION ANGIOGRAPHY: THE CLINICAL ENVIRONMENT

3.1 Advantages Over Conventional Acquisition

As has been previously discussed, technology prior to 1970 made adequate augmentation of arterial injection angiography possible, but could not be used to define arterial anatomy in conjunction with intravenous contrast injection because its sensitivity was insufficient. With the advent of improvements in computer technology, image intensifiers, and TV cameras in general, research into computerized fluoroscopy finally led to the availability of commercial DSA units in 1980. The justification for their routine clinical use was the expectation that a simple, peripheral intravenous injection of contrast would allow the arterial tree to be adequately outlined. In particular, it was hoped that a non-selective venous injection of contrast, followed by the assessment of coronary arteries, would supercede selective coronary arteriography.

Compared with conventional methods, DSA offers improved contrast resolution at the expense of spatial resolution. This trade-off is worthwhile since, with improvements in technology, spatial resolution comparable to that achieved in cine angiography can be obtained without loss of the superior conspicuity of DSA. This is illustrated in Figure 6. Unfortunately, intravenous DSA has been the source of much disappointment. Virtually none of its early promise has been realized in terms of anatomical arterial demonstration. Routine clinical use now is limited to screening the major vessels in the thorax and neck. Intra-arterial DSA, on the other hand, has become a stable and viable method for anatomical demonstration, offering much improved contrast resolution, and thus permitting easier identification of smaller vascular structures (Crummy, A.B., Stieghorst, M.F., et al., 1982).

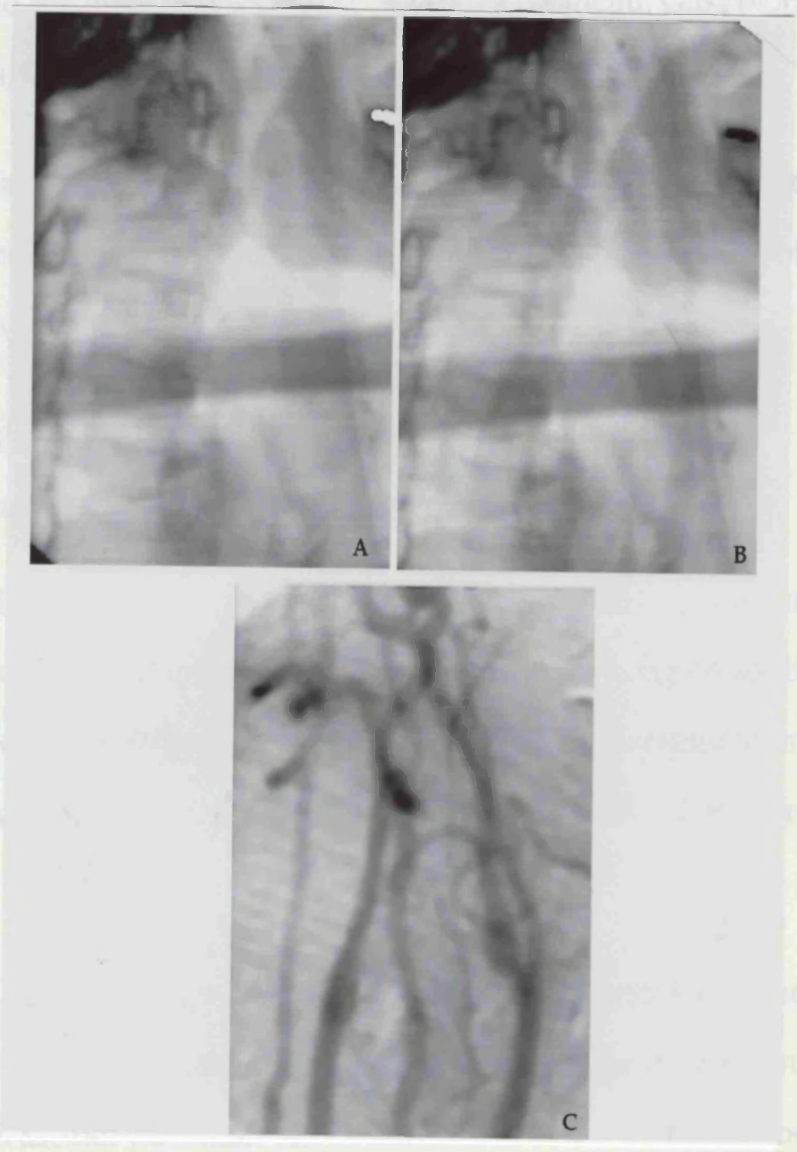

Figure 6. Images A and B are frames obtained before (mask, A) and after (data, B) arrival of contrast in the arteries of the neck. The bottom image, C, is the subtraction of the mask from the data frame. Note how conspicuous the neck vessels have become.

Some improvement of image quality was achieved during intravenous DSA by injecting the contrast into the right atrium, rather than peripherally or in the SVC. Nonetheless, this approach also failed to yield uniformly high quality images of arteries beyond the great vessels and neck vessels (Mancini, G.B., Norris, S.L., et al., 1983; Mancini, G.B., Ostrander, D.R., et al., 1983).

Since digital angiography is a timed sequence of images, the analysis of timing information may be useful in certain circumstances. It is this aspect of the technique which may prove ultimately to be its most valuable contribution.

3.2 Practical Problems with Acquisition

3.2.1 Movement and misregistration

It is obvious that in order for an optimal result to be obtained, movement in the time between the pre-contrast image and the contrast or data image must be eliminated. This is not always possible, and the principle causes of misregistration include respiration, vascular pulsation, peristalsis, and semi-voluntary movement, such as swallowing.

The effects of respiration can be controlled with the cooperation of the patient by asking them to hold their breath for the duration of image acquisition (typically 10-20 seconds). Vascular pulsation can be eliminated at the cost of temporal resolution by ECG gating the acquisition to a fixed point in the cardiac cycle (typically the R wave). Peristalsis can be temporarily suspended by the use of intravenous hyoscine or glucagon (Rabe, F.E., Yune, H.Y., et al., 1982). Artifacts caused by swallowing are a particular problem in neck angiography, but can be minimized with attention to patient comfort and the use of a non-ionic contrast agent.

3.3 Cardiac Imaging with DSA

DSA has been found to be a useful method of anatomical imaging of the chambers of the heart (Mancini, G.B., Higgins, C.B., et al., 1983; Mancini, G.B., Norris, S.L., et al., 1983; Mancini, G.B., Hodgson, J.M., et al., 1985) and, less successfully, has been applied in the assessment of coronary blood flow. The technique involves radiation dosage, as well as a contrast medium load, comparable with that of cine angiography. The duration of the examination is slightly longer, but certainly, ventricular function can be established from a venous approach (Crummy, A.B., Strother, C.M., et al., 1980; Greenbaum, R.A. and Evans, T.R. 1984), with a reduction in patient discomfort. The key to the successful application of DSA in cardiac imaging is patient co-operation. A good quality study allows the utilization of the timing inherent to DSA to provide more extensive information about vascular physiology and may obviate the need for extra investigations and offer the patient a reduction in morbidity.

In terms of cost, DSA is similar to conventional angiography, and indeed most modern angiographic equipment is digital in nature. Since the equipment has a narrow dynamic range, good quality images are obtained only by attention to detail. Film is much more forgiving of even major errors in setup and exposure control; however, overall its use tends to prolong an investigation.

3.4 Current Status of Digital Radiology

In the decade since this work was initiated, digital x-ray imaging methods have become the standard techniques utilized for angiography in all organs. Initial disappointment in the image quality and relatively poor spatial resolution has been replaced by enthusiasm as today's equipment provides all the functionality of earlier film screen combinations while using computerized digital technology. The bulk of angiographic work is performed on digital systems, where subtraction is an option, but not necessarily the one most used. The early emphasis on DSA imaging following an intravenous injection of contrast has been replaced by the more pragmatic, and ultimately sustainable approach of taking advantage of the technology to provide instant acquisition, real-time information review, increased contrast sensitivity and computerized image processing, while recognizing that

often an arterial injection is still necessary to obtain diagnostic angiography. Nevertheless, DSA and unsubtracted digital angiography can, and increasingly do, function as a stand-alone imaging modality. The role of digital angiography has been the focus of a recent report from the AHA (Cardella, J.F., Casarella, W.J., et al., 1994), where details of the optimal environment for use of this technology are presented.

In cardiac imaging, when compared to peripheral vascular imaging, the added issues of pulsation and respiration have decreased the rate of utilization of this technology. However, the need for instant review of the generated images during a procedure, the current standard of care, has propelled the development of cardiac specific digital units. DSA still forms a proportion of the imaging techniques, however, unsubtracted images can also be used in cases where movement introduces unacceptable artefacts. Studies comparing cine angiography with digital angiography have been favourable. With increasing computer power, digital imaging is taking over conventional film based methods. Filmless x-ray imaging is becoming better accepted and angiography, whether or not with subtraction, is part of this trend (Dyet, J.F., Hartley, W., et al., 1992).

CHAPTER 4

DIGITAL SUBTRACTION ANGIOGRAPHY: ITS VALUE IN THE INVESTIGATION OF CARDIOVASCULAR PATHOLOGIES

4.1 The Intravenous Approach

Subtraction angiography has been used for many years to identify subtle vascular structures. A good example of this is the elimination of overlying skull bony density in the investigation of cerebrovascular aneurysm formation. The film-based subtraction technique never became truly routine, simply because it was very time, labour and resource intensive. Nevertheless, there are many circumstances where the application of subtraction, if it were freely and easily available, would be of clinical value. Following are presented a series of DSA case studies which exemplify the quality of imaging data obtainable at different locations in the cardiovascular system. The studies are presented in anatomical order, starting from the venous side of the circulation, through the right side of the heart, the lungs, the left side of the heart and finally the arterial circulation. These cases were selected from a total of 946 patients on whom the author performed DSA; there were 504 neurological, 99 pulmonary, 164 cardiac, 91 abdominal and 88 cardiovascular patients. The case studies presented below were selected to provide a comprehensive set of examples of the value of DSA in demonstrating vascular pathologies in the Great Vessels and pulmonary and cardiac circulations.

4.1.1 Systemic Venous Drainage

Case 1
A 73 year old white female with a 5 year history of sick sinus syndrome requiring a pacemaker, presented with superficial venous congestion over the right side of the neck, exacerbated by bending over. Her initial pacemaker had been placed from a right sided approach. A replacement device and new wire had been inserted from the left side three years later. At the time, the original pacemaker and the proximal portion of the right sided wire were removed. SVC obstruction was clinically suspected and the patient underwent DSA for evaluation.

Contrast, Iopamidol 370 (Bracco Diagnostics, Milan, Italy), was injected at 25 ml/sec for a total of 40 ml, through a 5 Fg straight, multiple side-hole catheter, inserted into the SVC from the right femoral vein. Images were acquired onto a 512 by 512 matrix at 2.5 frames per second. It can be seen from figure 7a that the SVC is patent, but that there is lack of retrograde flow into the right subclavian vein. Further imaging was performed by injection of contrast into the right ante-cubital vein at 10ml/sec for a total of 20 ml. These data showed complete occlusion of the right subclavian vein with collateral flow through the superficial, deep and anterior jugular veins, figure 7b.

Demonstration of the venous circulation is ideally carried out by DSA. With this technique, a simple injection of contrast into an appropriate vein results in superior images of distal venous drainage, and allows easy demonstration of occlusion, filling defects and collateral flow. Upper arm and central vein venography using standard fluoroscopic methods results in larger volumes of contrast utilization yet the image quality is lower compared with DSA. Due to the superior contrast resolution and ability to process the images in real time, Digital techniques have become the standard of practice for vascular imaging.

4.1.2 Right Atrium and Ventricle

Case 2
A 25 year old Indian male presented to his primary physician with a 3 month history of malaise, night sweats and pyrexia. The differential diagnosis lay between TB and a lymphoproliferative disorder. He was referred to his local District General Hospital where he was investigated for pyrexia of unknown origin. No cause for his symptoms was found. While culture for the tubercle bacillus was being awaited the patient was started on triple therapy for TB. His symptoms did not resolve or improve. Further evaluation was undertaken with echocardiography, seeking vegetations as part of bacterial endocarditis. A mass was found in his right atrium and he was sent for venous DSA to evaluate the characteristics and movement pattern prior to surgical removal, figure 8.

Contrast (Iopamidol 370, Bracco Diagnostics, Milan) was injected at 15 ml/sec for a total of 25 ml, through a 5 Fg straight, multiple side-hole catheter, inserted into the right subclavian vein from the right basilic vein. Images were acquired onto a 256 by 256 matrix at 5 frames per second. A large lobulated mass can be seen in the right atrium. Two images are provided which demonstrate that the mass moves during the cardiac cycle. It is attached by a small stalk to the right atrium above the membranous septum close to the tricuspid valve ring. As the mass moves it prolapses through the tricuspid value and partially rotates into the right ventricular outflow tract. This was a benign atrial myxoma. Following successful surgery the patient's symptoms resolved.

Evaluation of the right atrium and ventricle can be ideally undertaken from a venous injection of contrast given proximally. Because the bolus of contrast does not have an opportunity to disperse, low volumes may be given without compromising image quality. The use of subtraction in this case allowed the stalk to be clearly identified. The reduced resolution (256 * 256) compared with case 1 above (512 * 512) allowed a higher framing rate to be used, and thus demonstrated the complex swinging and rotating motion of the intra-atrial myxoma. The data were able to be reviewed immediately at full resolution, thereby allowing a specifically tailored examination to be performed, which answered the surgeon's questions with minimal irradiation and contrast load in this young man.

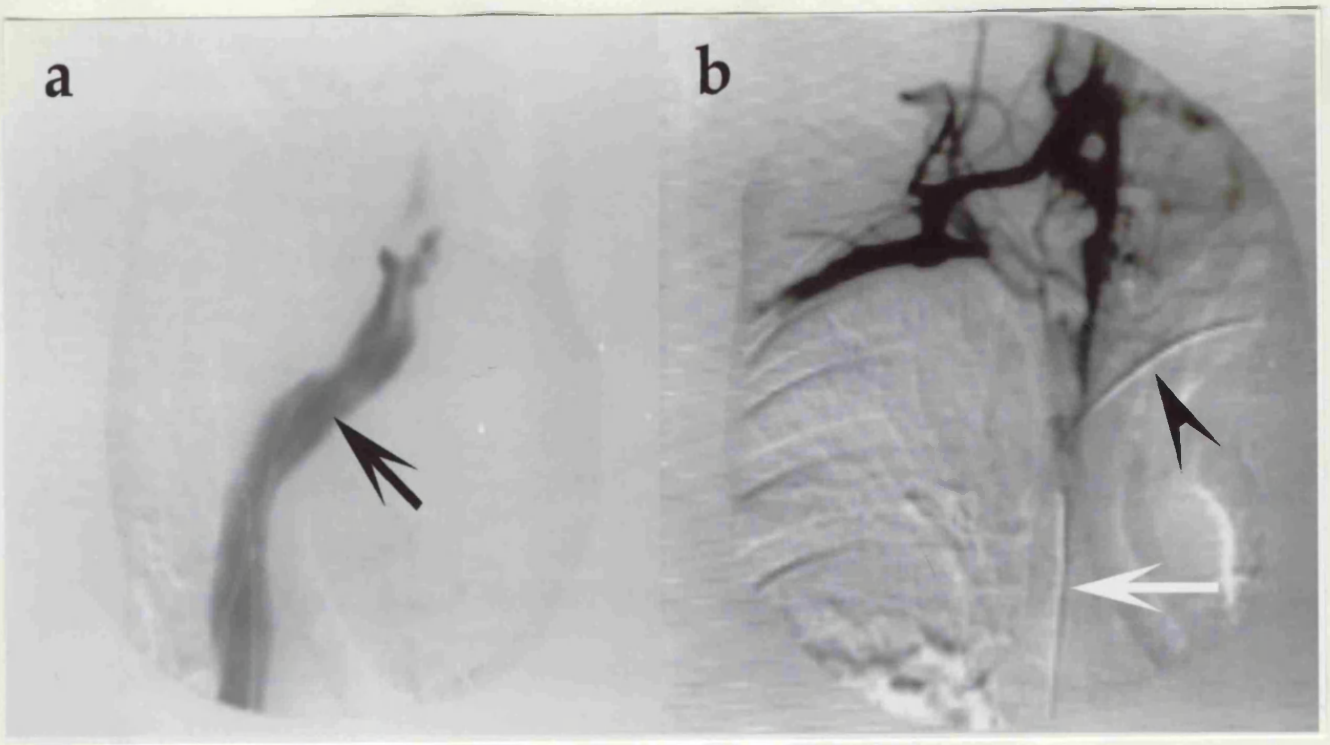

Figure 7. This is an example of superior caval vein thrombosis secondary to a pacing wire. The 5 Fg straight catheter can be seen passing from the IVC, through the right atrium to the SVC (white arrow). The old, right sided pacing wire can be seen in the SVC and right subclavian vein (short black arrow) on the oblique view, the new, left sided wire can be seen in the innominate vein (black arrowhead). Occlusion of the right subclavian vein with jugular collateral flow is evident, the inferior margin of the thrombosis is at the junction of the innominate and right subclavian veins. There are misregistration artifacts adjacent to the ribs caused by limited respiratory movement and hence imperfect subtraction.

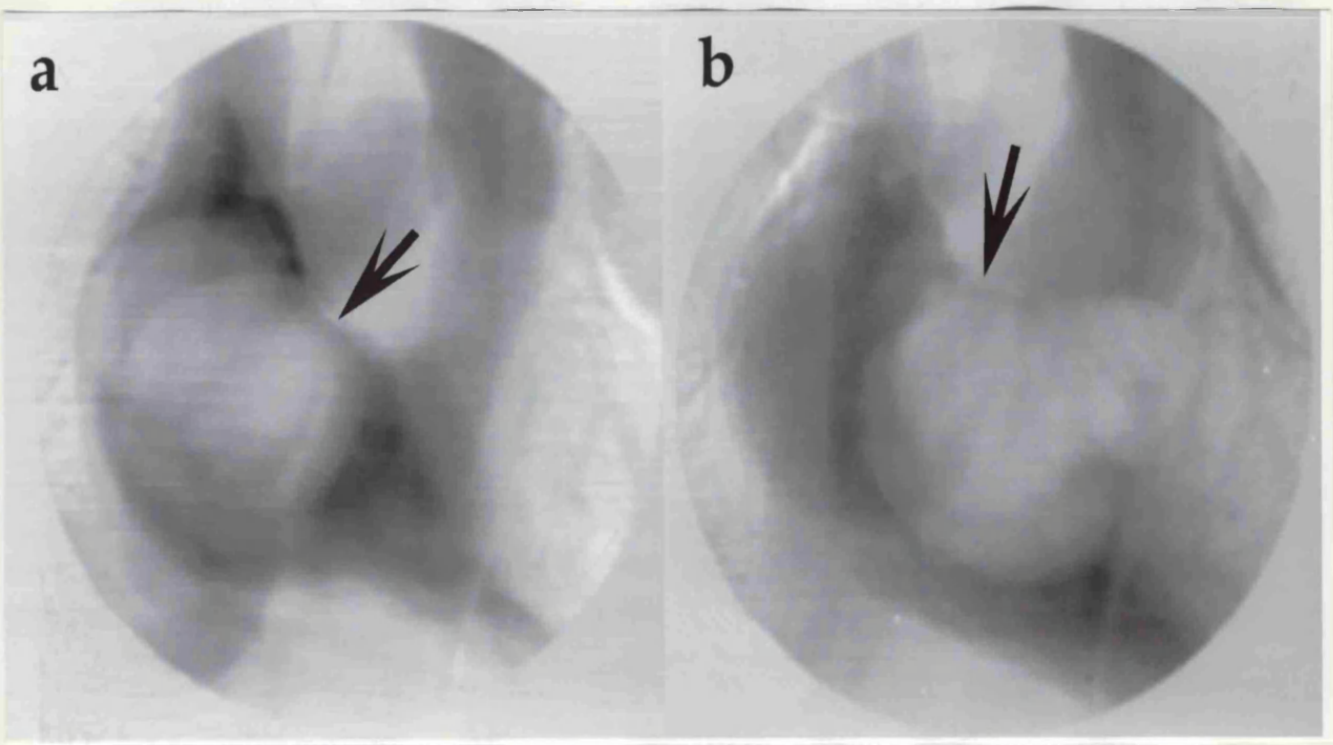

Figure 8. A large filling defect is seen partially to fill the right atrium and prolapse through the tricuspid valve into the right ventricle. The stalk (arrow) attaching the lobulated mass to the right atrium is seen above and close to the tricuspid valve ring, figure 8b. Note how the whole mass rotates around this fulcrum as at the same time as it swings through the valve into the right ventricular outflow tract.

4.1.3 Pulmonary Arteries

Pulmonary arteriography using conventional cut film and selective and super selective catheter placement can be uncomfortable for the patient, risk arrhythmias from right ventricular irritation and be a prolonged examination. DSA following non-selective injection into the SVC of a bolus of contrast was evaluated in the early stages of development of the technique (Saddekni, S., Sos, T., et al., 1984). In addition to being able to demonstrate major and minor discrete emboli, DSA can identify secondary features of embolization, such as reduced parenchymal blush, by virtue of digital manipulation of subtraction and data images to eliminate misregistration between them. Appreciation of the parenchymal phase of contrast passage through the pulmonary vasculature is often difficult with conventional imaging (Slutsky, R.A. and Higgins, C.B. 1983).

Case 3
A 57 year old west Indian male presented to the emergency department with dyspnoea. He was a long standing smoker. On physical examination there was evidence of tachypnoea. No focal signs were elicited and the CXR suggested pulmonary artery prominence without cardiomegaly. The patient underwent pulmonary DSA to exclude embolism.

Contrast (Iopamidol 370, Bracco Diagnostics, Milan) was injected at 25 ml/sec for a total of 40 ml, through a 5 Fg straight, multiple side-hole catheter, inserted into the SVC from the right basilic vein. Images were acquired onto a 256 by 256 matrix at 5 frames per second. Enlargement of the left proximal pulmonary artery can be clearly seen, together with marked bilateral peripheral pruning of the vessels, figure 9. There was no evidence of embolism on this study. The likely cause of these appearances was chronic lung disease associated with smoking.

This case illustrates the value of venous DSA in obtaining diagnostic pulmonary arteriograms without needing to formally catheterize the patient. ECG gating was not used to obtain these images. Instead, multiple pre-contrast images were obtained providing a choice of appropriate mask for individual contrast images, resulting in good subtraction despite cardiac pulsation and respiration. The benefit of this flexibility in choosing a subtraction mask is exemplified in figures 9a and 9b. The difference between them is in the choice of mask, note how the movement artifacts adjacent to the left heart border have been removed in figure 9b, simply by using a mask image from a different part of the cardiac cycle. Such flexibility makes DSA a valuable additional tool in evaluation of pulmonary vascular diseases.

Thus while formal cut film pulmonary angiography remains the gold standard for diagnosis of pulmonary embolism, DSA can often provide sufficient information to

make the diagnosis and allow treatment to proceed. The benefits of this approach are twofold, firstly a non-selective injection of contrast eliminates the need for catheter manipulation through the right ventricle, inherently a procedure with slightly higher risk compared to a basilic vein puncture and SVC catheterization. Secondly, the procedure is potentially more rapid and better tolerated by patients, so that a definitive diagnosis can be made in a highly time efficient manner. Furthermore, formal pulmonary arteriography is not precluded if the initial DSA is non-diagnostic, as modern angiographic equipment often has both capabilities available. In short, if intravenous DSA can give the answer the patient benefits. If, despite DSA, a selective catheter arteriogram is necessary, very little time has been lost by attempting the DSA.

Case 4
A 53 year old white female developed acute chest pain associated with haemotpysis and dyspnoea following routine surgery at an outside institution. Pulmonary embolism was suspected and she was referred for angiography.

Contrast (Iopamidol 300, Bracco Diagnostics, Milan) was injected at 25 ml/sec for a total of 40 ml, through a 5 Fg straight, multiple side-hole catheter, inserted into the IVC from the right femoral vein. Images were acquired onto a 256 by 256 matrix at 5 frames per second, figure 10. Large emboli were identified in both proximal pulmonary arteries. The embolus on the left was seen to prevent perfusion of the upper lobe, while on the right only the upper lobe was perfused. The patient was immediately transferred for thrombolytic therapy.

This case exemplifies the ability of DSA to rapidly obtain diagnostic quality images of the proximal pulmonary arteries from a non-selective injection of contrast. The total study time was less than 15 minutes and no delay was introduced before thrombolysis commenced.

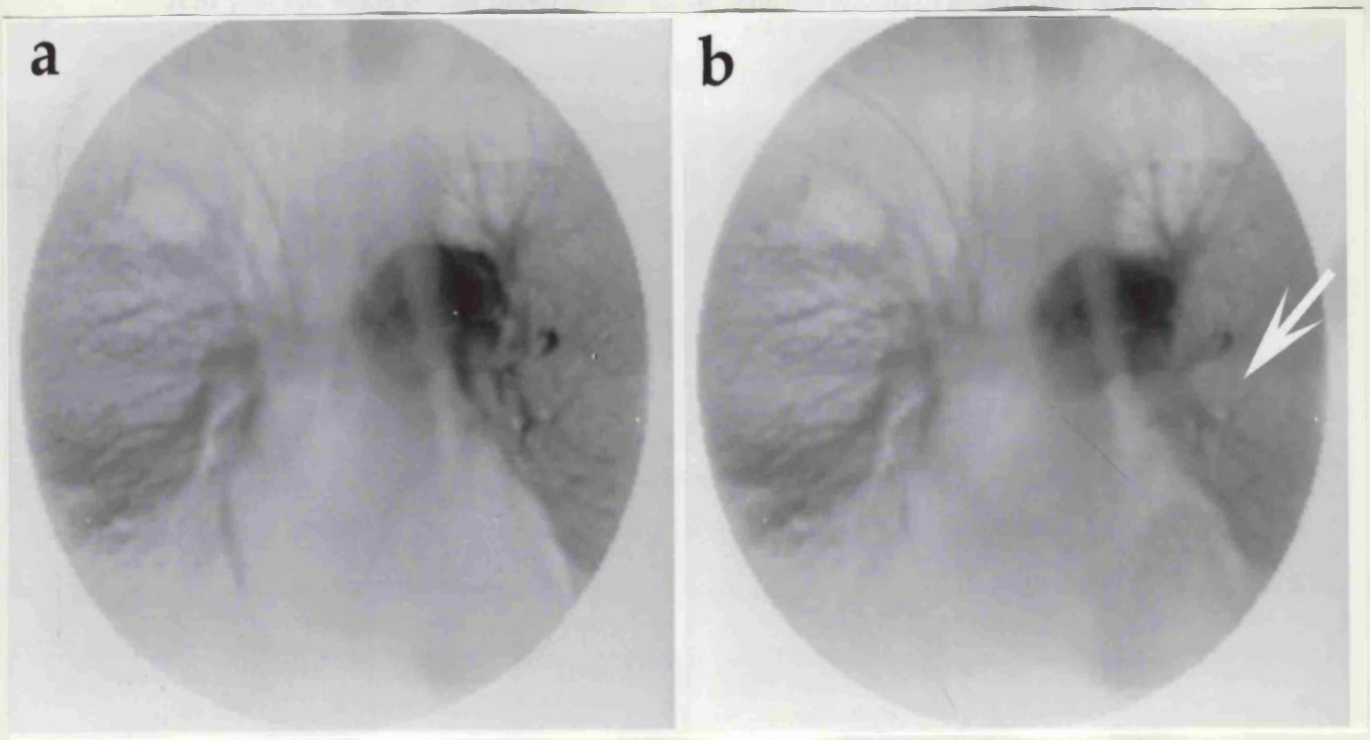

Figure 9. Two images of the same frame using masks from different parts of the cardiac cycle for subtraction. Note how the vessels abutting the left heart border (white arrow) are much more clearly seen in b. This is evident by the loss of the double shadow along these vessels due to motion between the mask and data images observed in a (arrow).

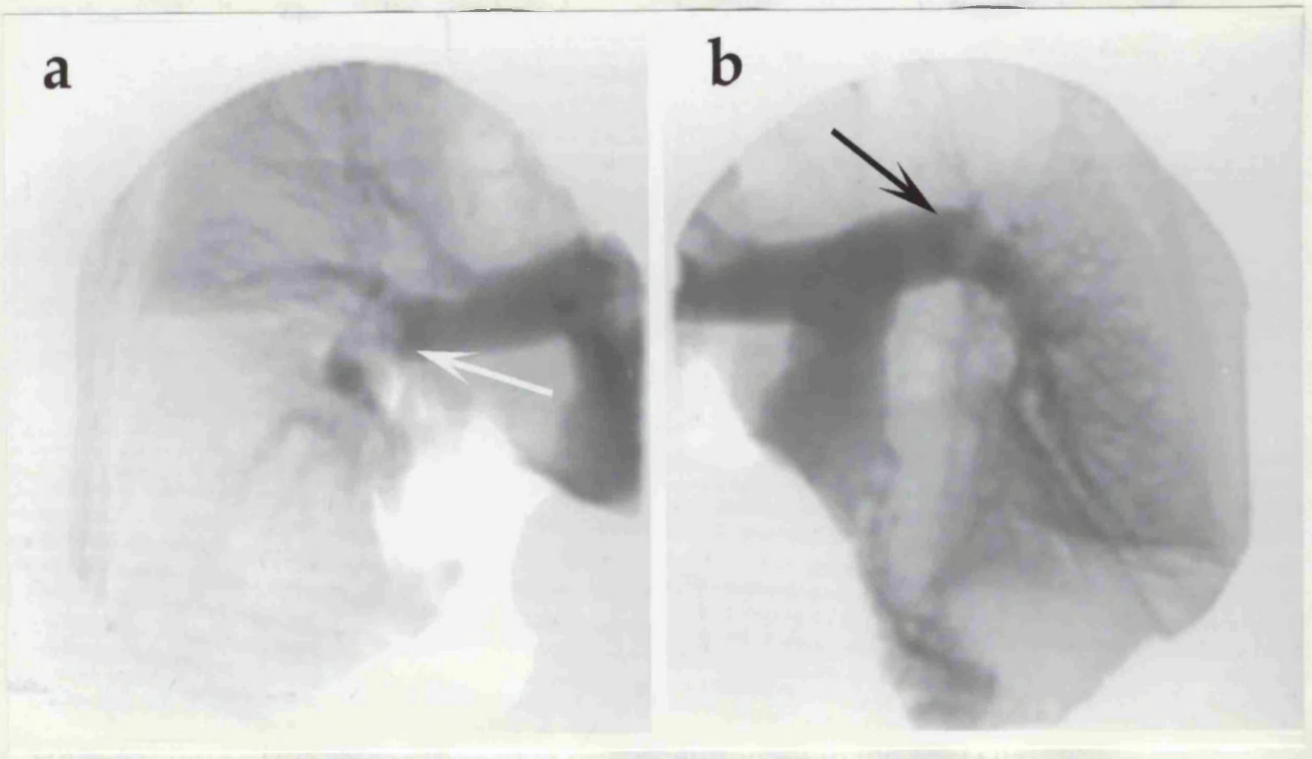

Figure 10. Single DSA images of the right (a) and left (b) proximal pulmonary arteries, showing a right sided pulmonary artery embolus preventing perfusion of the middle and lower lobes (white arrow), and a left sided pulmonary embolus occluding the upper lobe (black arrow).

Case 5
A 31 year old white female presented to her GP with symptoms of progressive dyspnoea. She was a non-smoker. She had used oral contraceptives for approximately 5 years. On examination there was evidence of elevated right ventricular pressure and raised systemic venous pressure. Her chest radiograph showed prominent hila and a working diagnosis of pulmonary arterial hypertension was made. She was referred for DSA as an outpatient, figure 11.

Contrast (Iopamidol 300, Bracco Diagnostics, Milan) was injected at 25 ml/sec for a total of 40 ml, through a 5 Fg straight, multiple side-hole catheter, inserted into the SVC from the right basilic vein. Images were acquired onto a 256 by 256 matrix at 5 frames per second. The prominent proximal pulmonary arteries were clearly seen, together with marked peripheral attenuation. Additionally, there was reduction in lung parenchymal vascular blush in a patchy, non-segmental distribution. These appearances are consistent with primary pulmonary hypertension.

Intravenous DSA may also be used non-emergently to evaluate patients presenting with progressive dyspnoea and no apparent aetiology. DSA can be used as an outpatient procedure with minimal disruption to the patient. In order to evaluate perfusion within lung parenchyma, it is necessary to either ECG gate the acquisition, or to acquire multiple pre-contrast images retrospective gate by matching mask and data images from the same part of the cardiac cycle. Furthermore, in co-operative patients, a good breath-hold can result in excellent subtraction of the ribs. These two manoeuvres successfully applied will result in very good quality pulmonary arteriography. One of the most valuable features of DSA is that all the image data are stored in a computer as individual pixel values and may be manipulated mathematically. The ability to identify vascular structures at different phases of perfusion, together with the accompanying timing information can provide a definitive diagnosis by using parametric and region of interest imaging.

Case 6
A 32 year old white female presented with a history of periodic fever, left sided chest pain and dyspnoea. Chest radiography showed a round mass near the left pulmonary artery. Prior to needle biopsy DSA was undertaken to exclude a vascular lesion, prior to biopsy.

Contrast (Iopamidol 370, Bracco Diagnostics, Milan) was injected at 25 ml/sec for a total of 40 ml, through a 5 Fg straight, multiple side-hole catheter, inserted into the SVC from the right basilic vein. Images were acquired onto a 256 by 256 matrix at 5 frames per second, figure 12. The non-vascular nature of this lesion was confirmed, the biopsy showed carcinoid tumor.

The image in figure 12b is obtained by calculating the maximum intensity in each pixel during the whole acquisition and plotting only this value. Other parameters may be obtained which depend on timing information present in the digitally collected data. This aspect of DSA is further amplified in the next chapter.

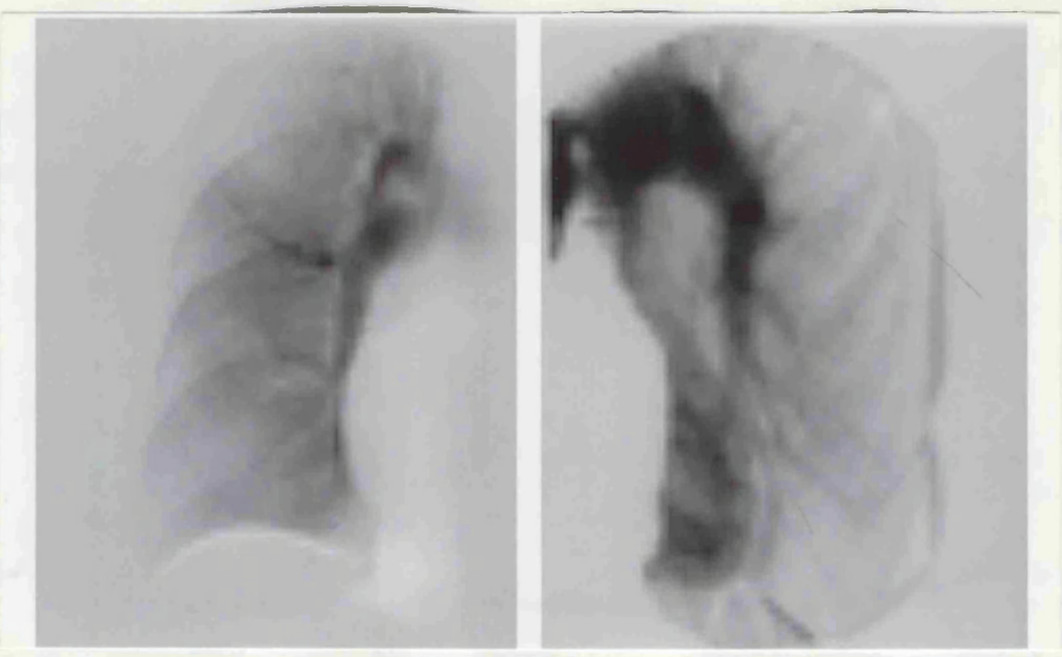

Figure 11. Left and right lung DSA shows marked proximal pulmonary artery hypertrophy with distal tapering and pruning. Note the paucity of perfusion blush in a non-segmental distribution. These findings are strongly suggestive of primary pulmonary hypertension, rather than the sequelae of chronic recurrent thromboembolism. Almost perfect subtraction has been achieved, simply by allowing a long acquisition before contrast to gather a wide choice of mask images to match with individual contrast or data images.

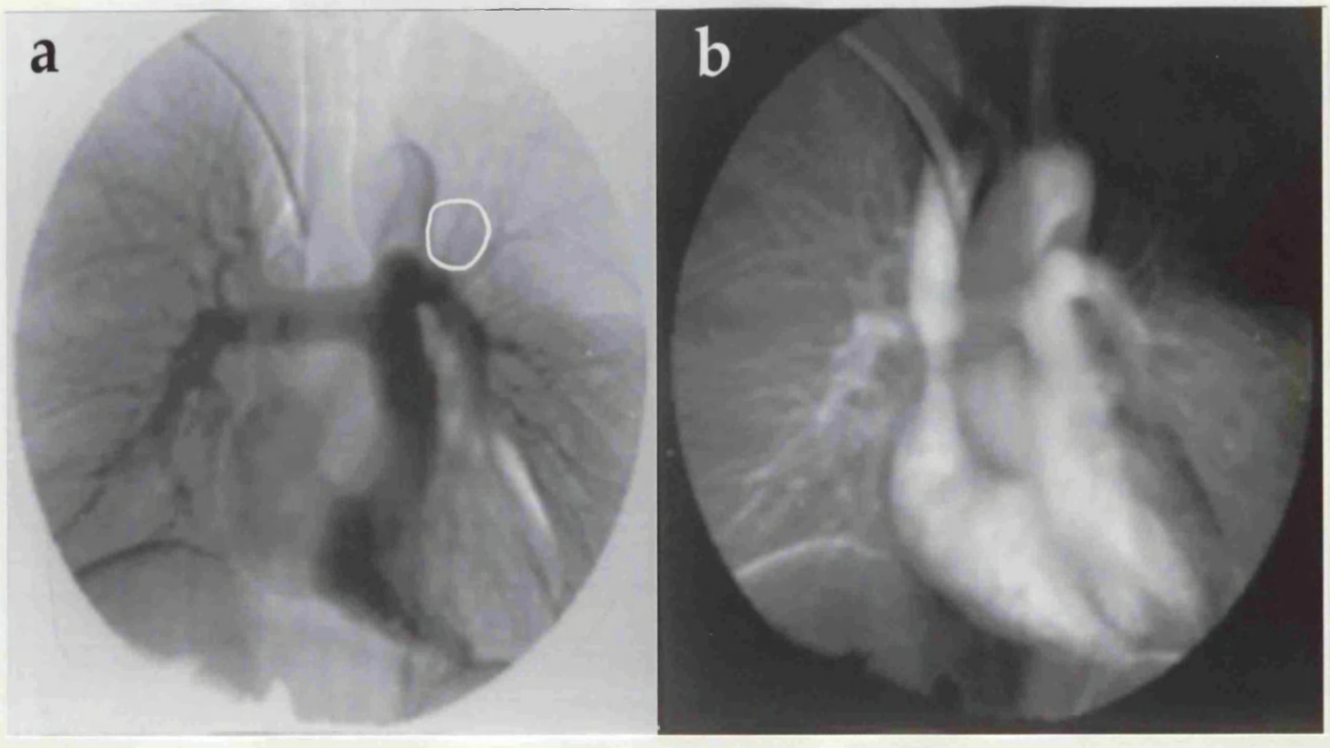

Figure 12. The straightforward subtraction image(a) shows paucity of filling of the left upper lobe vessels. The ROI, (white box) identified the position of the mass on plain film radiography, and can be seen to be separate from the pulmonary arteries. In order to visualize both arterial and venous phases of pulmonary perfusion a collapsed or parametric image can be produced, (b). The non-vascular mass was compressing the left upper lobe artery causing partial obstruction to perfusion.

4.1.4 Pulmonary Vascular Malformations

The nature of DSA is such that it is possible to obtain high resolution images of the peripheral vascular tree of the lungs without selective catheterization. This property is useful in the evaluation of potential vascular malformations. Subsequent treatment can also be provided by using DSA to closely monitor catheter placement and the arterial and venous anatomy comprising the lesion to be treated.

Case 7

A 12 year old white female presented with haemoptysis. Chest radiography showed a suspicious lesion in the right upper zone, with apparent linear structures radiating from the upper hilum to the density. DSA was undertaken to evaluate the lesion.

Contrast (Iopamidol 300, Bracco Diagnostics, Milan) was injected at 20 ml/sec for a total of 25 ml, through a 5 Fg straight, multiple side-hole catheter, inserted into the SVC from the right basilic vein. Images were acquired onto a 512 by 512 matrix at 2 frames per second, figure 13. The presence of an AVM was confirmed and the patient proceeded to embolization.

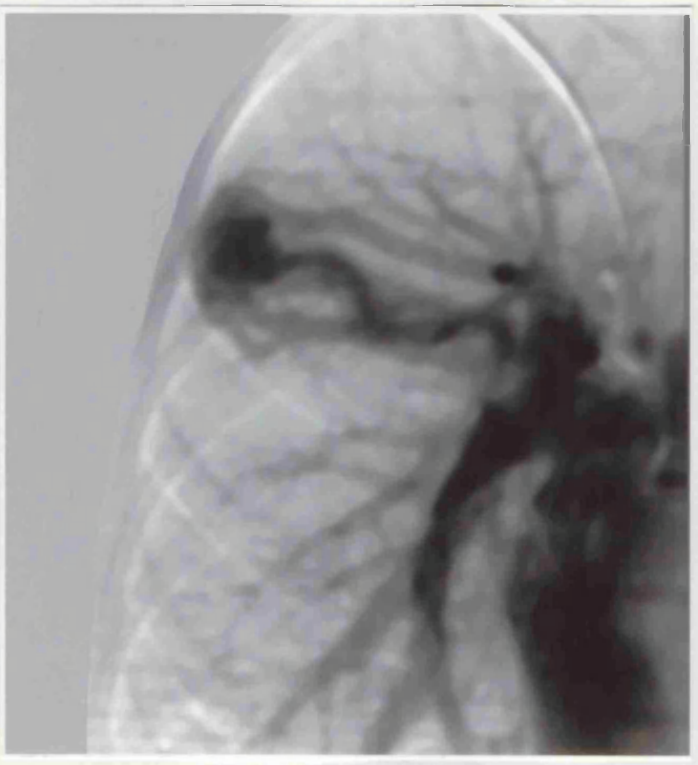

Figure 13. Intravenous DSA shows a right-sided arterio-venous malformation with feeding and draining veins radiating from the upper right hilum.

The availability of DSA spared this young girl a femoral vein puncture and trans-cardiac selective catheterization. The embolization procedure was able to be planned knowing there would be no surprises during its performance. One of the particularly useful features of digital imaging is that the series of images is immediately available for review. This reduces the procedure duration and thereby benefits the patient. The application of DSA to arterial imaging with selective and superselective catheter placement can result in a much reduced dosage of contrast and superb delineation of even tiny vessels.

Case 8
A 47 year old Indian female presented with vague symptoms of intermittent cough and haemoptysis. Chest radiography showed a suspicious lesion in the left lower zone, with linear structures radiating from the hilum to the density. DSA was undertaken to evaluate and demonstrate the anatomy of the lesion.

Contrast (Iopamidol 300, Bracco Diagnostics, Milan, diluted by 50% with physiological saline) was injected at 12 ml/sec for a total of 25 ml, through a 7 Fg curved tip, single side-hole catheter, inserted into the left pulmonary artery from the right femoral vein. Images were acquired onto a 512 by 512 matrix at 2 frames per second, figure 14a. The presence of the AVM was confirmed. Further imaging suggested that the draining vein entered directly into the left atrium. Selective imaging of this draining vein was possible by virtue of a patent foramen ovale, figure 14b. The patient proceeded to embolization which was successfully achieved by using polymer filled balloons to occlude the nidus of the AVM, Figure 15.

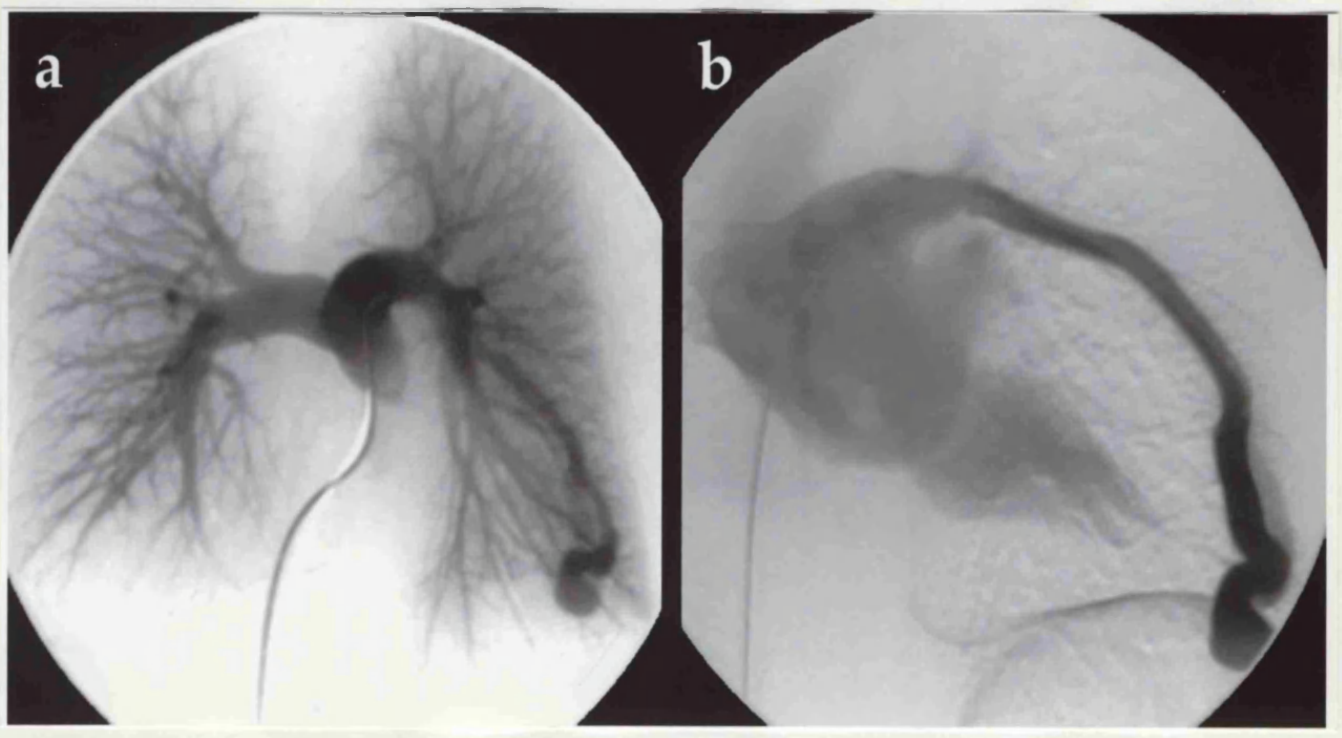

Figure 14. Selective injections into the left pulmonary artery (a) and through a patent foramen ovale into the draining vein of the AVM (b) are shown. The PFO was found incidentally during attempted passage of the catheter into the pulmonary artery.

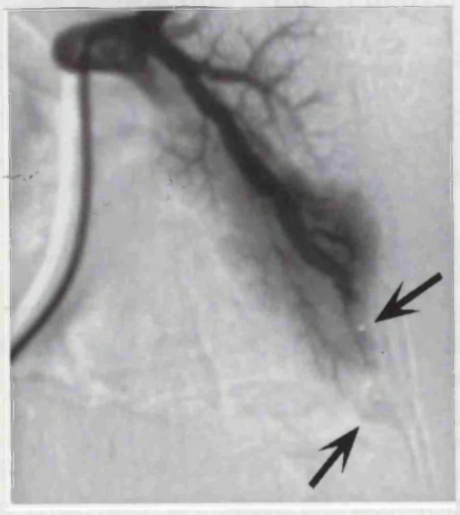

Figure 15. Following balloon embolization the AVM from case 8 is seen to be totally occluded. Two balloons were used, the apex marker of each can be seen as a bright spot in the location of the AVM (black arrows).

4.1.5 Left Ventricle

Evaluation of left ventricular anatomy and function is feasible with DSA. In its passage through the right heart and lungs a contrast bolus spreads out and decreases in apparent density. Without removal of background information such a bolus would not be seen clearly by the time it had reached the left ventricle. However, with DSA, online subtraction is inherent to the technology and good views of the LV may be obtained form an intravenous injection. In patients who have had recent myocardial infarction it may be desirable to avoid a formal arterial catheterization, DSA allows evaluation of the LV with a greater margin of safety.

Case 9
A 68 year old white male presented with chest pain characteristic of a myocardial infarction. ECG confirmed an inferior MI and the patient was admitted to the CCU. He made an uneventful recovery and was moved to the regular ward where mobilization started, on discharge one week later he was well. Six week s following his initial presentation, the patient returned for evaluation and was found to be in severe pulmonary oedema with heart failure. Papillary muscle rupture was suspected, although aneurysm was also a diagnostic possibility. DSA was undertaken to evaluate and demonstrate the anatomy of the LV.

Contrast (Iopamidol 300, Bracco Diagnostics, Milan) was injected at 25 ml/sec for a total of 40 ml, through a 5 Fg straight, multi side-hole catheter, inserted into the SVC from the right basilic vein. Images were acquired onto a 512 by 512 matrix at 2 frames per second, figure 16. Despite the patient's reduced cardiac output, good quality imaging was obtained in the RAO 30° projection. It can be seen that there is a large aneurysmal dilatation arising from the inferior left ventricle. This was successfully treated surgically and the patient returned to an active lifestyle.

The development of an aneurysm or pseudo-aneurysm following myocardial infarction is a well recognised complication. In this case, sufficient data were obtained from IV DSA for surgical repair to be performed without the need for the more invasive arterial catheterization. The total DSA procedure took approximately 15 minutes from beginning to end, and the patient tolerated the study uneventfully.

As IV DSA provides a cine angiogram of the passage of contrast through the left ventricle, there will be images obtained at end-systole and end-diastole. These can be determined either by gating acquisition to the patient's cardiac cycle, yielding individual images at the appropriate times, or by retrospectively choosing maximum and minimum images from a series obtained at a rapid framing rate without gating. The latter method is somewhat easier to implement and retains absolute timing information without the need for knowledge of the heart rate, nor the need for a stable heart rate.

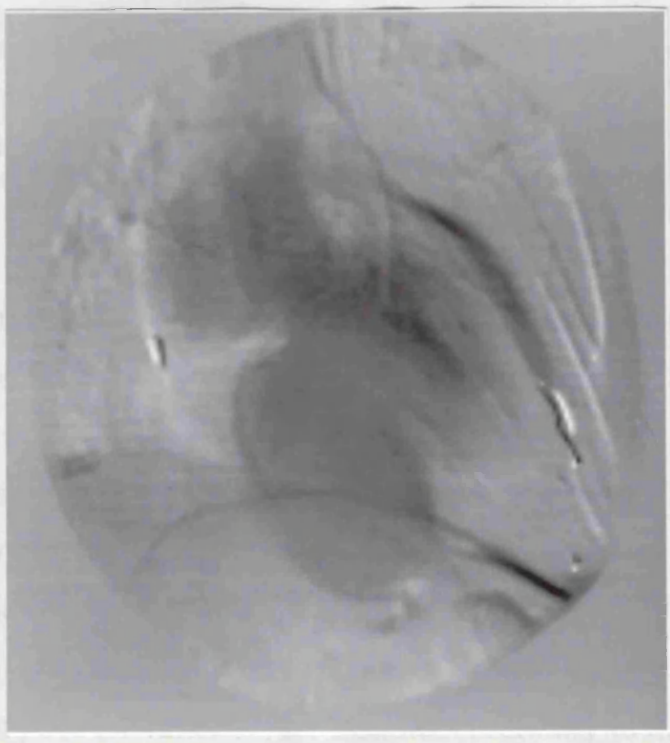

Figure 16. Large inferior left ventricular wall aneurysm demonstrated by IV DSA. This proved to be a pseudo-aneurysm at operation. Resection resulted in resolution of the patient's symptoms.

Case 10

A 71 year old white male presented with chest pain characteristic of angina. As part of his evaluation an IV DSA was performed to determine LV function.

Contrast (Iohexol 350, Nycomed, UK) was injected at 25 ml/sec for a total of 40 ml, through a 5 Fg straight, multi side-hole catheter, inserted into the SVC from the right basilic vein. Images were acquired onto a 128 by 128 matrix at 16 frames per second without prospective ECG gating, figure 17. Good quality imaging was obtained in the RAO 30° projection. End-diastolic and end-systolic frames were identified and contours drawn around the left ventricle. The end-diastolic volume was 170 ml, the end-systolic volume was 47 ml. The resulting ejection fraction was 72%, with a stroke volume of 123 ml These values were obtained by using the area length method of Sandler and Dodge (Sandler, H. and Dodge, H.T. 1968).

The results obtained in case 10 are within normal limits. Current digital cardiac imaging equipment provides these calculations in an automated fashion.

Non-quantitative visual evaluation of left ventricular wall motion is also easily made available by digital data acquisition and review. With an SVC injection of contrast and review of the left ventricle, subtraction is necessary to obtain sufficiently good visualization of the contrast in the LV cavity. This is particularly true in cases with poor LV function, for instance secondary to myocardial infarction.

Case 11

A 73 year old white male was seen in the outpatient department 6 months following an antero-septal myocardial infarction. As part of his evaluation an IV DSA was performed to determine LV function.

Contrast (Iohexol 350, Nycomed, UK) was injected at 25 ml/sec for a total of 40 ml, through a 5 Fg straight, multi side-hole catheter, inserted into the SVC from the right basilic vein. Images were acquired onto a 128 by 128 matrix at 16 frames per second without prospective ECG gating, figure 18. Good quality imaging was obtained in the RAO 30° projection. The presence of severe hypokinesia of the mid and apical portions of the LV is clearly seen. The basal part of the left ventricle was responsible for this patient's cardiac output.

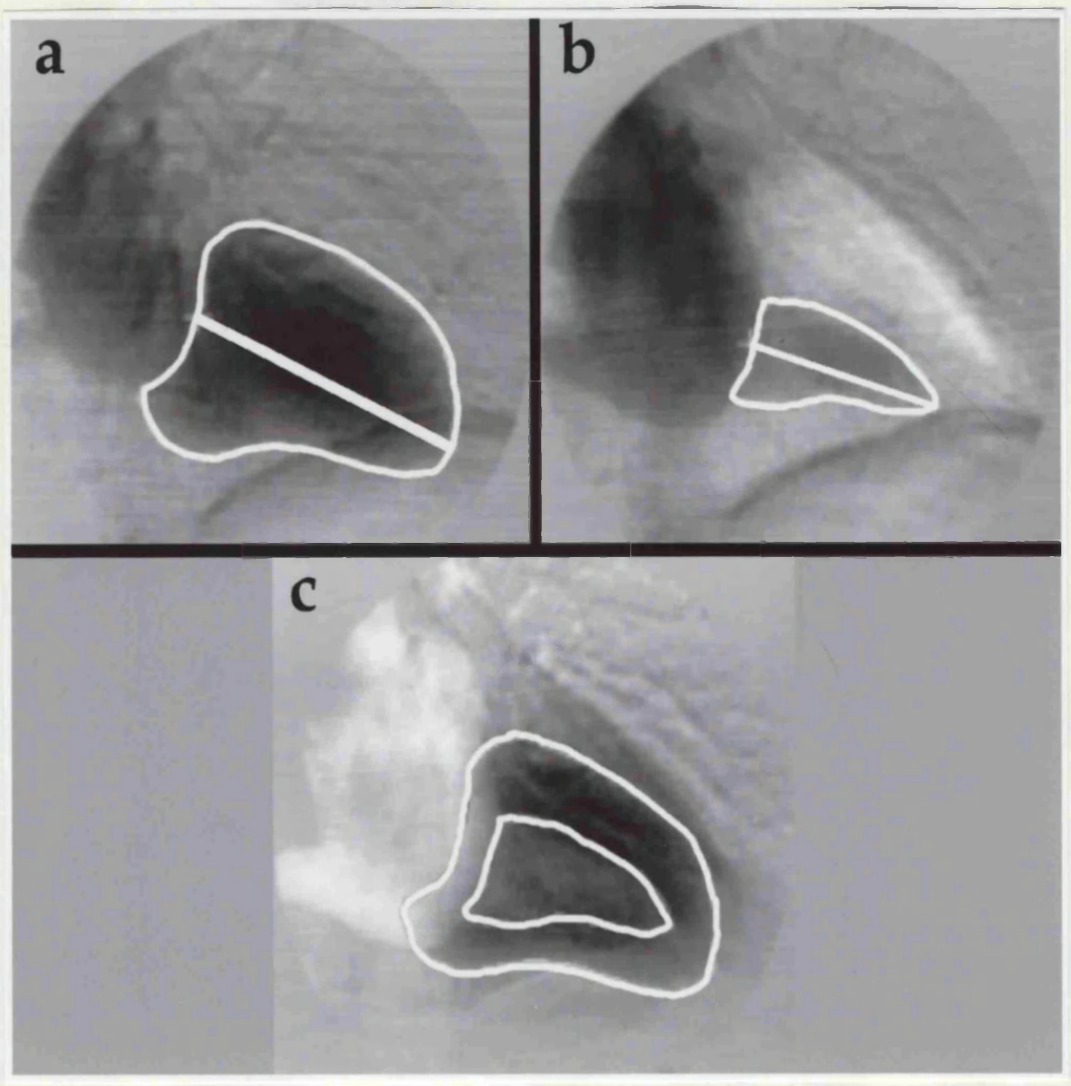

Figure 17. The contours of the left ventricle at end-diastole (a) and end-systole (b) were generated manually, current digital angiographic equipment does this automatically. The calculation of the stroke volume and ejection fraction uses the method of Sandler and Dodge (Sandler, H. and Dodge, H.T. 1968)(Sandler and Dodge 1968). In this case, the two contours have been superimposed electronically for visual interpretation of the movement of the ventricle during contraction (c).

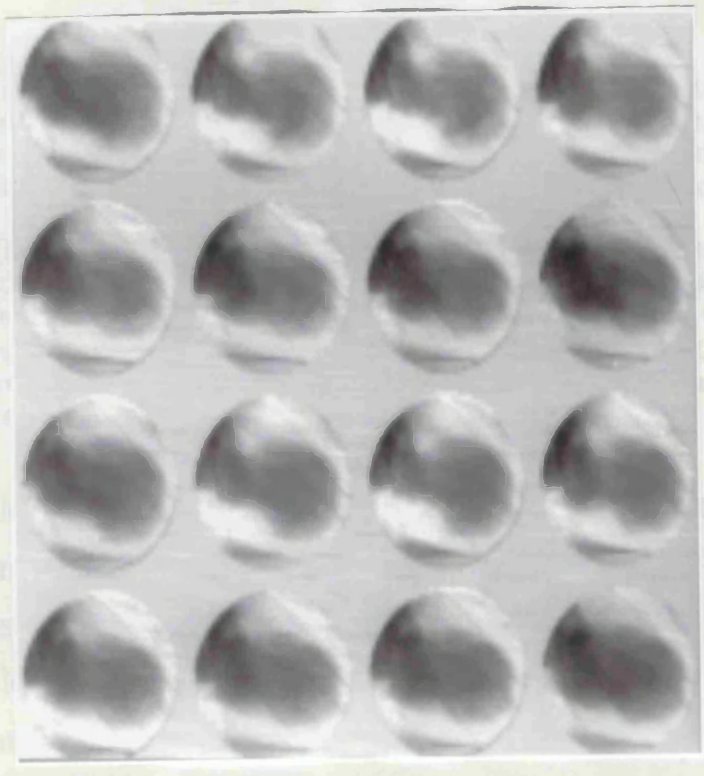

Figure 18. Sixteen consecutive images are presented which encompass the cardiac cycle. Qualitative assessment of ventricular contraction is possible and reveals severe hypokinesia of the apex and mid ventricular myocardium. A little residual contraction is present inferiorly, however this patient relies on basal contraction to produce cardiac output. The quantitative interpretation of such data is discussed in chapter 5.

4.1.6 Great Vessels

Since contrast density is still high in the great vessels, an intravenous injection of contrast material is sufficient to outline structures in this area. DSA is useful in the preoperative evaluation of patients, for instance with potential coarctation, as well as for post-operative follow-up. Often, sufficient information is obtained during an outpatient IV DSA to avoid a more invasive conventional arteriogram .

Case 12
A 24 year old white female presented with hypertension discovered during a routine employment physical. She had hypertension in her right arm, but not in the lower limbs. There was radiofemoral delay between the right arm and right leg, but not between the left arm and right leg. IV DSA was performed to evaluate for aortic co-arctation.

Contrast (Iohexol 350, Nycomed, UK) was injected at 25 ml/sec for a total of 40 ml, through a 5 Fg straight, multi side-hole catheter, inserted into the SVC from the right basilic vein. Images were acquired onto a 512 by 512 matrix at 1 frame per second without prospective ECG gating, figure 19. Good quality imaging was obtained in the LAO 45° projection. The presence of coarctation of the aorta between the left common carotid and left subclavian arteries was demonstrated.

In case 12, while the patient's signs were consistent with coarctation, they were somewhat anomalous, given the most usual form of coarctation beyond the left subclavian artery origin, at the aortic isthmus. DSA was able to identify the correct location of the lesion without conventional angiography. In these patients in order to obtain demonstration of the proximal part of the aorta it may be necessary to perform a brachial artery approach, IV DSA circumvents this need and may be performed on an outpatient basis.

Following surgery periodic monitoring of the coarctation repair site may be usefully performed by using IV DSA. Similarly other aortic surgeries may be monitored without the need for catheter manipulation at or through the site of surgery. While the risk of complication from conventional arteriography is low, the potential complications arising directly from catheter manipulation can be completely avoided by using IV DSA.

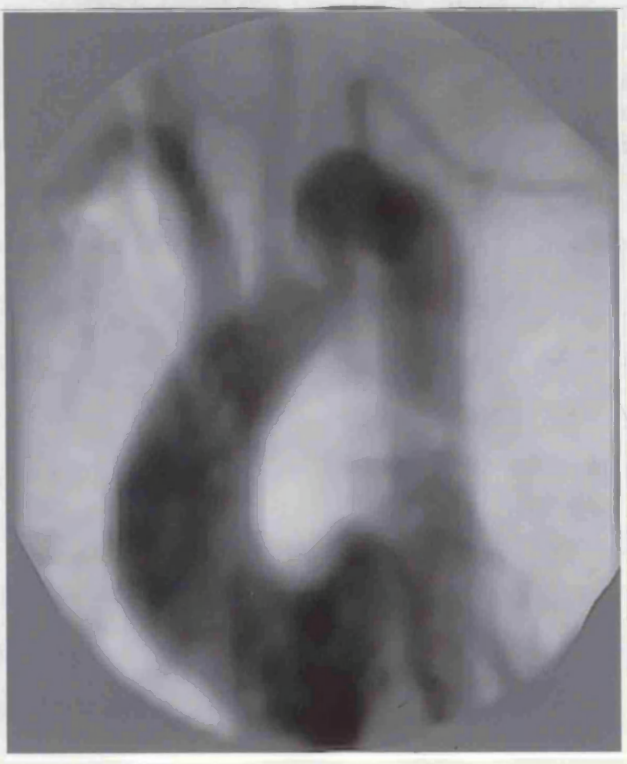

Figure 19. The LAO 45° projection opens out the aortic arch and allows good visualization of the great vessels. Here a coarctation of the aorta can clearly be seen between the left common carotid artery and the left subclavian artery.

Case 13
A 17 year old Indian male had undergone mitral valve replacement for stenosis and simultaneous repair of an aortic isthmus coarctation several years earlier. He presented at routine annual follow-up with symptoms suggesting transient ischaemic attacks. Part of his re-evaluation was to undergo IV DSA to document continued patency of his coarctation repair.

Contrast (Iohexol 350, Nycomed, UK) was injected at 25 ml/sec for a total of 40 ml, through a 5 Fg straight, multi side-hole catheter, inserted into the right atrium from the right basilic vein. Images were acquired onto a 256 by 256 matrix at 2.5 frame per second, figure 20. Good quality imaging was obtained in the LAO 45° projection. The presence of a repaired coarctation of the aorta distal to the left subclavian artery was demonstrated. Also noted was the Starr-Edwards mitral valve replacement, presumed to be the site of vegetations causing the TIA's.

In cases of postoperative infective endocarditis IV DSA may be the most suitable method for confirming the presence of an abscess cavity. Untreated, the mortality from this complication is very high, and early surgical treatment is necessary to obliterate any cavity and remove infected material. No entirely satisfactory technique exists for safe and accurate demonstration of potential abscess formation at the aortic root. IV DSA excludes the possibility of displacement of infected material during arterial catheterization and can often provide sufficient information to plan surgery for treatment of the infection (Hunter, G.J., Thomas, H., et al., 1988a; Hunter, G.J., Thomas, H., et al., 1988b).

Case 14
A 29 year old white female had undergone aortic valvotomy at the age of 12. On this occasion she was admitted with a history consistent with infective endocarditis. Blood cultures grew staphylococcus sanguis. Serial electrocardiograms showed prolongation of the PR interval and an aortic root abscess was suspected. IV DSA was performed to further evaluate the patient.

Contrast (Iohexol 350, Nycomed, UK) was injected at 25 ml/sec for a total of 40 ml, through a 5 Fg straight, multi side-hole catheter, inserted into the right atrium from the right basilic vein. Images were acquired onto a 512 by 512 matrix at 1 frame per second, figure 21. Good quality imaging was obtained in the LAO 40° projection. This demonstrated an outpouching of the aorta at the level of the sinuses of Valsalva, consistent with an abscess cavity. This was surgically removed and the patient made a satisfactory recovery.

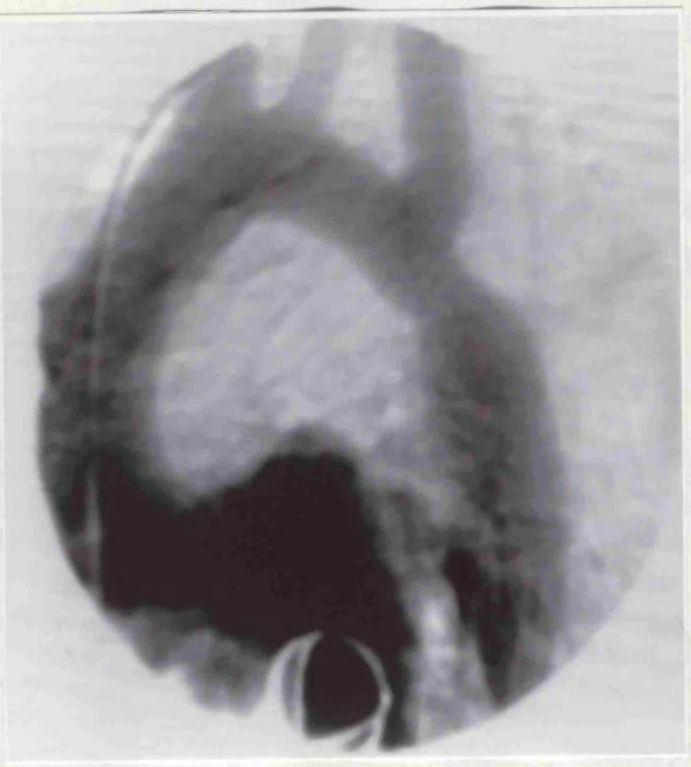

Figure 20. Following repair of a classical coarctation, a good anatomical result is seen. A simple intravenous DSA performed as an outpatient is capable of screening the results of surgery with minimal disruption to the patient. This study was acquired in the LAO 45° projection, and shows no evidence of re-stenosis at the site of coarctation repair.

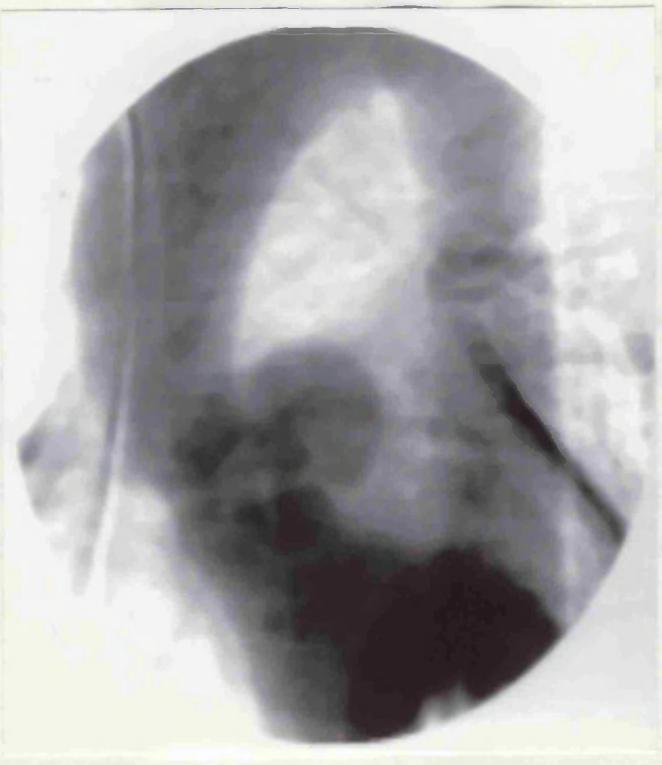

Figure 21. A lengthening PR interval and pyrexia resulted in the IV DSA. Contrast filled outpouching can be seen arising from the left sinus of Valsalva and pointing anterolaterally. This was an abscess cavity which was drained at surgery.

4.1.7 Beyond the Great Vessels

Apart from visualization of large and medium vessels themselves, DSA is able to demonstrate the capillary phase of perfusion. As the capillary phase of tissue perfusion has a relatively low attenuation, it requires subtraction to fully appreciate the extent of the blush. Furthermore, if there is a question of *when* capillary perfusion is occurring, then a timed series of images ,analyzed for time of peak opacification, can yield very important and useful data.

Case 15
A 59 year old white female presented to her GP with a vague history of respiratory symptoms, principally a feeling of inability to take in a good breath. Chest radiography revealed a prominent paratracheal shadow without apparent narrowing of the trachea, figure 22a. IV DSA was performed to further evaluate the patient.

Contrast (Iohexol 350, Nycomed, UK) was injected at 25 ml/sec for a total of 40 ml, through a 5 Fg straight, multi side-hole catheter, inserted into the right atrium from the right basilic vein. Images were acquired onto a 512 by 512 matrix at 1 frame per second, figure 22b. Good quality imaging was obtained in the AP projection. This demonstrated deviation of the innominate artery to the left, with an abnormal capillary blush appearing to be the cause. The location of the blush corresponded to the shadow on plain chest radiography. Analysis of the timing information showed that the mass was being perfused by the systemic circulation, figure 23. At surgery a thymosarcoma was removed, with subsequent resolution of the patient's symptoms.

This case demonstrates how post processing of DSA data can provide information about the relationships of a lesion with respect to different vascular structures. The parametric data can absolutely answer where a lesion is obtaining its blood supply, thus avoiding unexpected surprises during surgery. This latter feature of DSA is only possible because of the digital nature of the underlying image data storage.

In the evaluation of patients pre-CABG, sometimes bruit are heard over the neck. Often this means carotid disease, sometimes the underlying abnormalities are more serious. DSA can provide excellent views of the vessels supplying the upper limbs and head, without the need for arterial catheterization. Such preliminary studies can often be obtained on an outpatient basis, which is more comfortable for the patient and utilizes resources more efficiently.

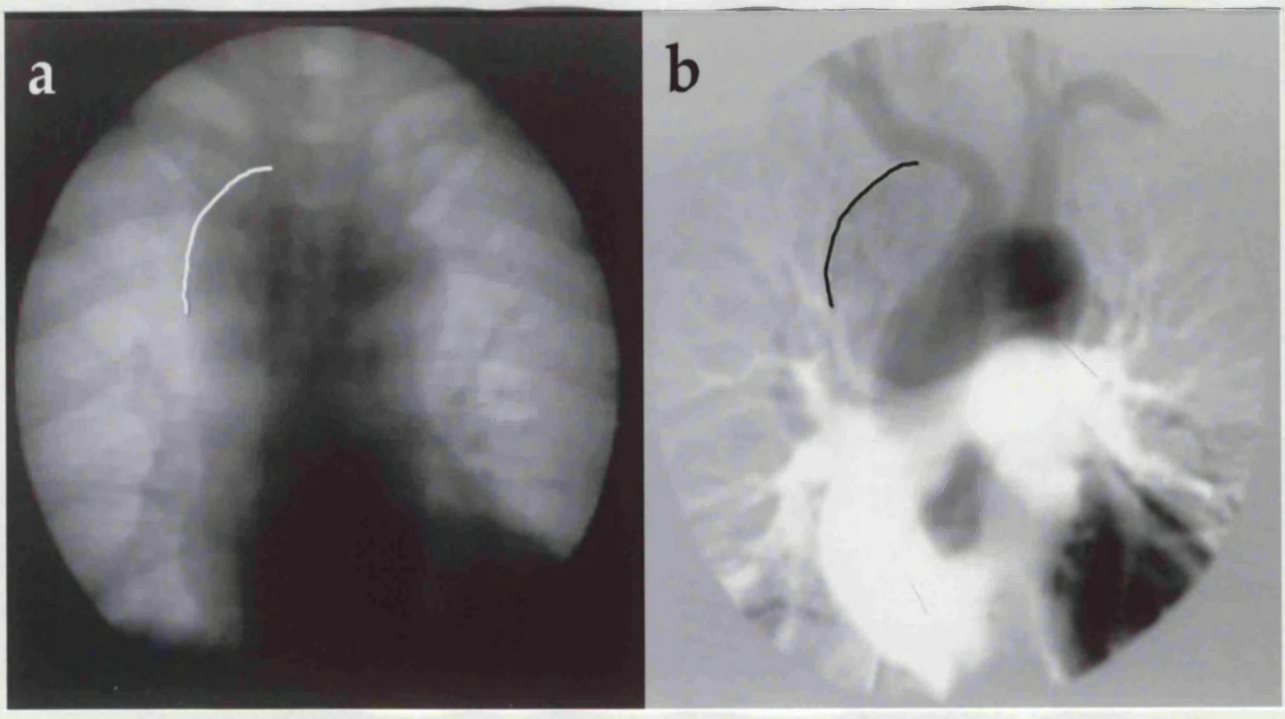

Figure 22. The plain film radiograph (a) shows fullness of the right paratracheal region, the outer margin of the shadow has been marked (white line). The IV DSA image (b) shows deviation of the innominate artery and perhaps a portion of the most proximal right subclavian artery. The DSA image has been produced by using an image from the pulmonary arterial phase of contrast passage as the mask and an image from the systemic arterial phase as the data . Thus pulmonary arterial circulation appears as white, while the systemic arterial circulation appears black. The capillary blush of the paratracheal mass can be clearly seen, the outer margin of the lesion seen on the plain film has been drawn in black.

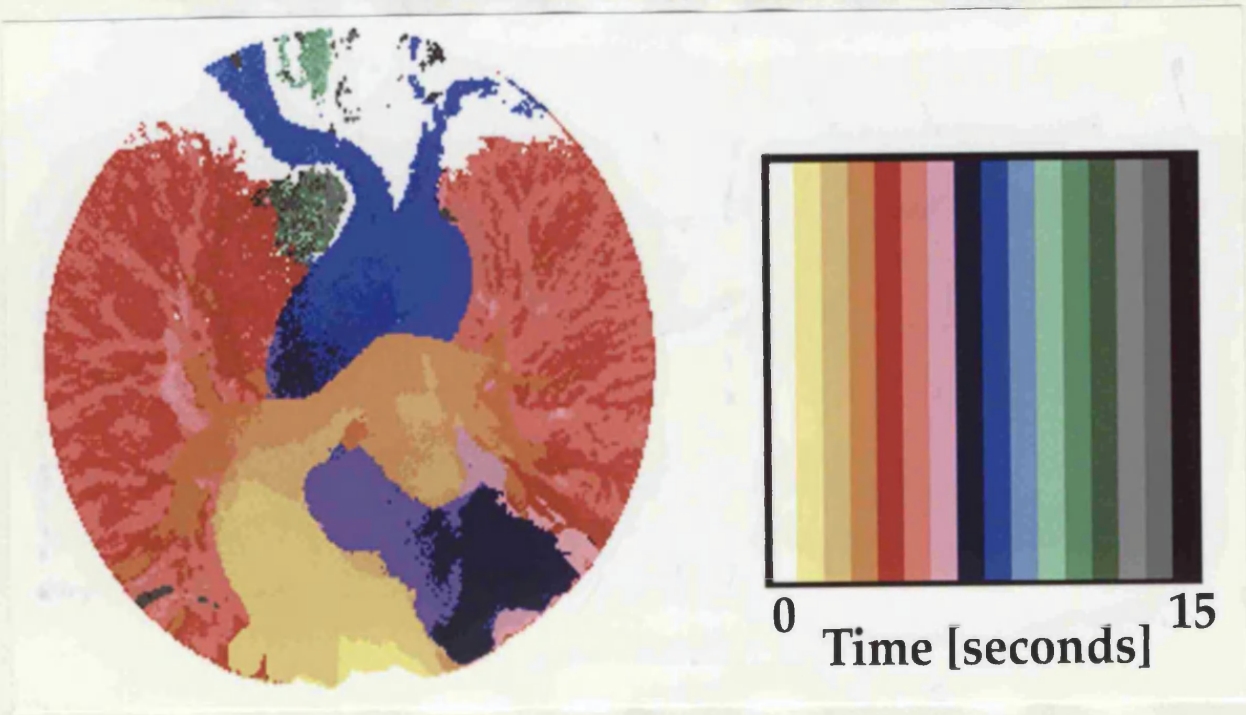

Figure 23. This is a parametric image where each colour in the scale represents 1 second of elapsed time. Notice how the paratracheal mass is predominantly dark green and grey. Thus it was perfused after the aorta (blue). This indicates that the blood supply to this tumour arises from the systemic arterial circulation and not the pulmonary circulation.

Case 16
A 69 year old white male with angina was being evaluated for coronary artery bypass grafting. A bruit was heard over his neck and IV DSA was performed to evaluate the carotid and vertebral circulations.

Contrast (Iohexol 350, Nycomed, UK) was injected at 25 ml/sec for a total of 40 ml, through a 5 Fg straight, multi side-hole catheter, inserted into the right atrium from the left basilic vein. Images were acquired onto a 512 by 512 matrix at 1 frame per second, figure 24. Good quality imaging was obtained in the LAO 40° projection. This demonstrated occlusions of the innominate and right common carotid arteries. The left common carotid was patent, as were both vertebral arteries. The right subclavian artery was perfused by steal from the right vertebral artery.

In some instances, IV DSA may be the only method for evaluating a particular problem. Arterial dissection is one circumstance were IV DSA is particularly useful.

Case 17
A 71 year old white male with angina was undergoing coronary arteriography when it was noticed that passage of one of the catheters had become difficult. Fluorography over the site of resistance suggested that dissection had occurred in the abdominal aorta. The patient was transferred to the DSA suite in order to evaluate the extent of dissection and to ascertain whether or not the renal arteries were involved.

Contrast (Iohexol 350, Nycomed, UK) was injected at 25 ml/sec for a total of 40 ml, through a 5 Fg straight, multi side-hole catheter, inserted into the right atrium from the right basilic vein. Images were acquired onto a 512 by 512 matrix at 1 frame per second, figure 25. Good quality imaging was obtained in the AP projection. This demonstrated the abdominal aortic dissection extending from the right common iliac artery to the right renal artery. It was not clear from the unprocessed images whether or not the origin of the renal artery was involved, so parametric analysis was performed to demonstrate the temporal pattern of delivery of contrast to the aorta, right renal artery and the false lumen, figure 25. This showed that there was not involvement of the renal artery in the dissection and the patient was treated conservatively, there were no long term sequelae.

This case illustrates the value of temporal information in deciding a critical issue where anatomy alone is insufficient to make the diagnosis. Knowing that the renal arteries were not involved in the dissection process, enabled the correct treatment to be started without fear of renal ischaemia or infarction. The alternative would have been unnecessary surgery.

Digital subtraction angiography can be very useful in untangling complex flow patterns, especially when the complexity is as a result of a combination of both temporal and anatomical factors.

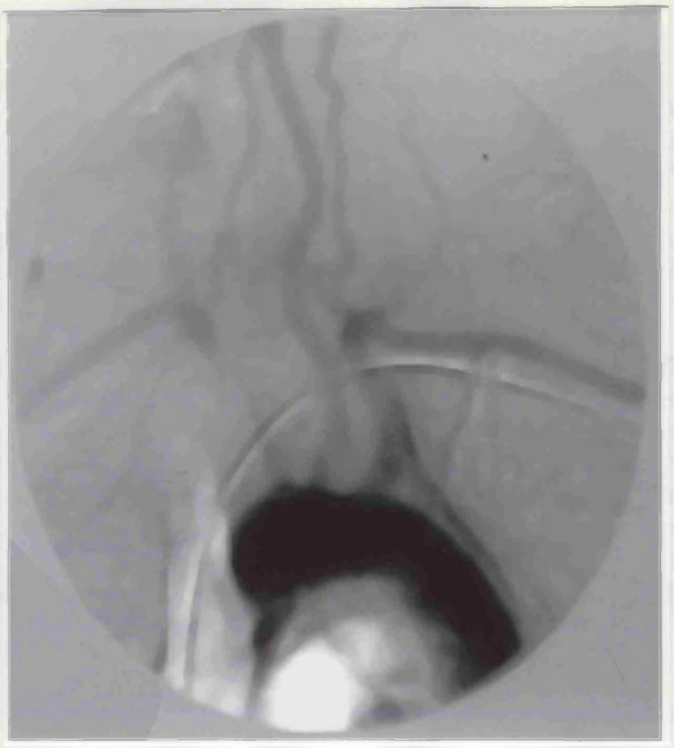

Figure 24 Good subtraction has been achieved with the use of a late mask, appearing as white because it already contains contrast in the right atrium and SVC. The absent right carotid artery can be appreciated, together with occlusion of the innominate artery. There is a narrow, tapering, column of contrast near the origin of the right innominate artery. Disobliteration of this vessel might restore flow to the carotid if it has not been occluded for long. Supply of the right subclavian artery is clearly seen to arise from the right vertebral artery by retrograde flow - subclavian steal. The left vertebral artery is dominant and the left common carotid is normal in calibre.

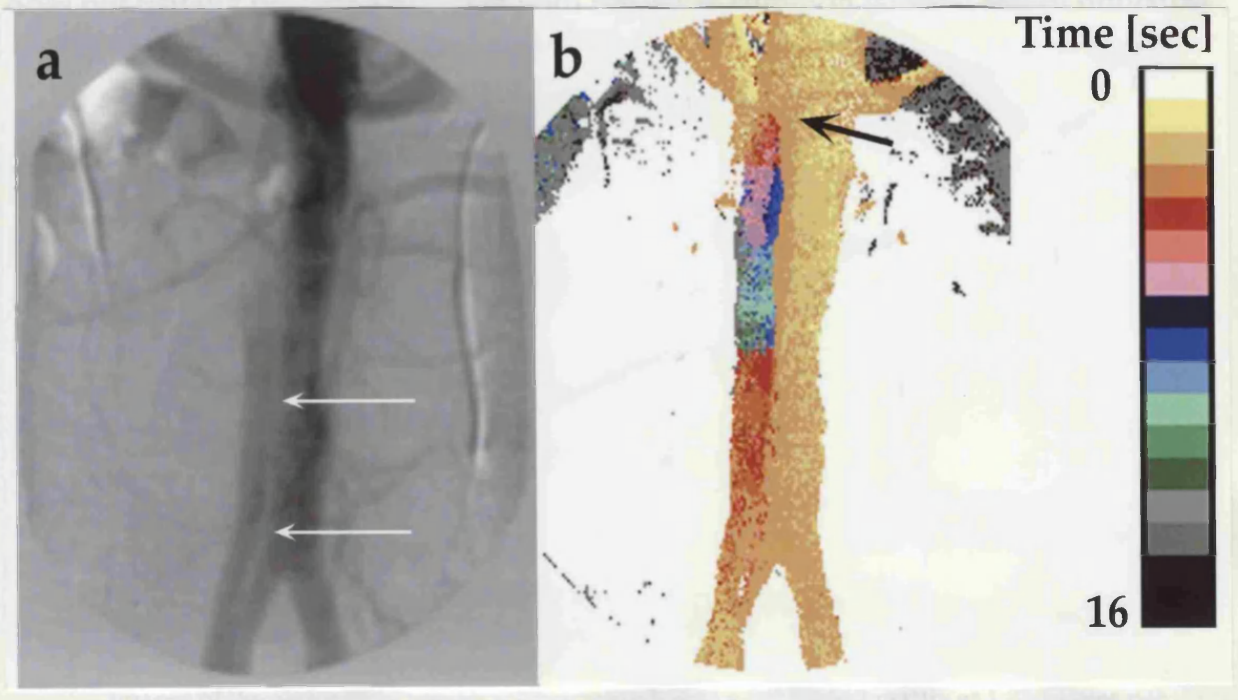

Figure 25. The IV DSA anatomical data is shown in (a). The aortic dissection is clearly seen (white arrows) and extends from the vicinity of the right renal artery to the common iliac artery on the right. Plotting the peak contrast opacification time with a colour scale as shown, indicates that the right renal artery receives its blood from the aorta, before the dissection cavity fills. The dissection cavity fills from below, as expected, but there is also a small amount of filling from above. This is seen as a tiny amount of brown colour at the top of the cavity, whereas the middle portion is red and blue indicating much later perfusion.

Case 18
A 30 year old white male presented with a 5 year history of dyspnoea and occasional wheeze. Recently he had developed breathlessness after strenuous exercise. There was no history of asthma or atopy, and he was a non-smoker. Examination was non-contributory. Pulmonary function tests suggested mild asthma. Routine chest radiography revealed situs solitus. The heart was displaced to the right with rib crowding on the right, consistent with reduced volume of the right hemithorax. There was a soft tissue density band shadow in the mid and lower zones of the right lung. IV DSA was undertaken to evaluate the vascular anatomy.

Contrast (Iohexol 350, Nycomed, UK) was injected at 25 ml/sec for a total of 40 ml, through a 5 Fg straight, multi side-hole catheter, inserted into the SVC from the right basilic vein. Images were acquired onto a 256 by 256 matrix at 2.5 frames per second, figure 26. AP imaging demonstrated an anomalous vein draining the medial aspect of the right lower lung into the inferior caval vein. Analysis of the images also revealed an anomalous systemic artery, arising below the diaphragm and supplying the medial aspect of the lower right lung.

In case 18, a complex case of hypogenetic lung syndrome, the value of timing data is seen by demonstration of the delayed, systemic supply to part of the right lung. It is not practical to obtain such delayed imaging with conventional pulmonary angiography. Furthermore, the contrast concentration in the aorta would be insufficient to confidently identify the anomalous systemic artery without subtraction. An alternative would to perform cine-angiography, however, the lack of subtraction would hamper diagnosis of delayed filling of the anomalous artery.

Many patients with coronary artery disease also have peripheral angiopathy. This does not usually present a problem with regard to common femoral artery puncture and catheter access by way of the iliac vessels and abdominal aorta. Occasionally, however, a femoral pulse may not be palpable. If a femoral pulse is not palpable, then IV DSA to evaluate the abdominal aorta and identify occlusion may prevent unnecessary needle manipulation in the groin. Furthermore, review of priorities pertaining to the arteriopathy may result in resolution of peripheral vascular issues before attempting to investigate and intervene in the coronary vessels.

Case 19
A 67 year old white male presented with angina. On examination he was found to have absent femoral pulses, prior to arterial catheterization he underwent IV DSA to evaluate the condition of his abdominal and pelvic vasculature.

Contrast (Iohexol 350, Nycomed, UK) was injected at 25 ml/sec for a total of 40 ml, through a 5 Fg straight, multi side-hole catheter, inserted into the SVC from the right basilic vein. Images of the abdominal vessels were acquired onto a 512 by 512 matrix at 1.25 frames per second, figure 27. Good quality imaging was obtained in the AP projection. This showed complete occlusion of the aorta below the renal arteries. His vascular status was re-evaluated and he underwent conventional coronary arteriography from a brachial approach.

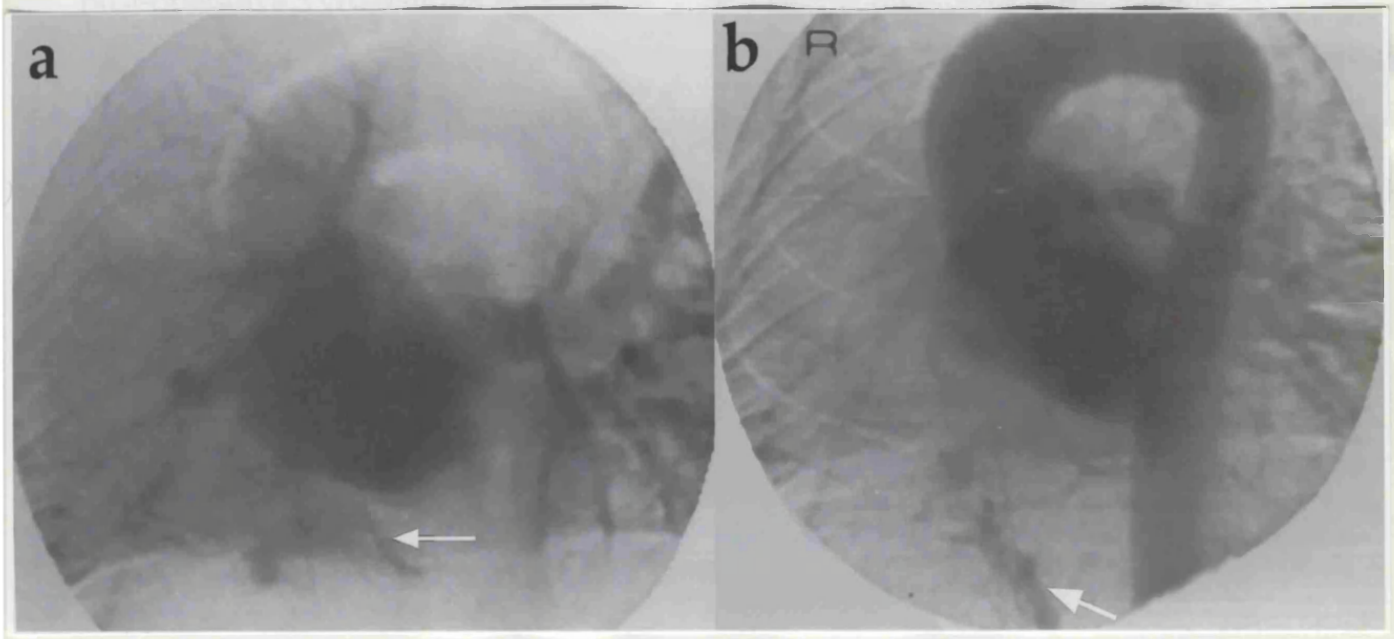

Figure 26. Early (a) and late (b) phases of IV DSA are shown. On the early phase image it is clear that there is anomalous pulmonary venous return to the junction of the IVC and right atrium (arrow). On the late phase however, it can be seen that part of the lung is perfused by systemic blood by way of a vessel arising from the aorta below the diaphragm (arrow). These appearances are part of the spectrum of hypogenetic lung syndrome.

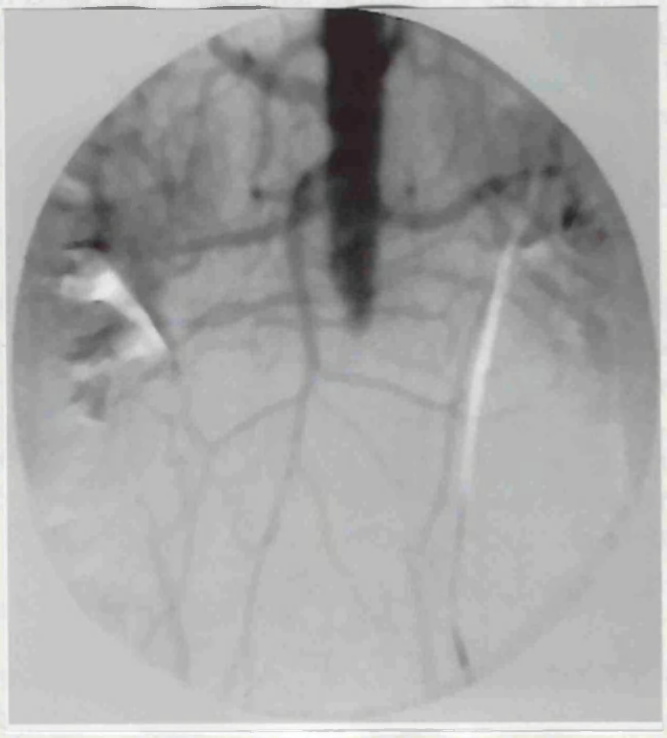

Figure 27. The occluded aorta can be clearly seen, accounting for this patient's lack of femoral pulses. It is useful to have advance warning of these absolute contra-indications to angiography by the femoral approach. In this case this was obtained as an outpatient procedure, permitting subsequent hospitalization and treatment to be better planned.

4.1.8 Visualization of Coronary Artery Bypass Grafts

The number of patients receiving coronary artery bypass graft surgery will continue to increase. The recurrence of symptoms and increased occlusion rate in the second post-operative 5 years emphasize the need for a simple method of assessment of graft patency. A prospective study was undertaken to investigate the use of both intravenous and intra-arterial DSA to evaluate the suitability of DSA for coronary artery bypass graft (CABG) assessment.

Patients and Methods

A total of 26 unselected patients with recurrent chest pain subsequent to CABG surgery were studied. All gave informed consent, and the study was approved by the hospital ethics committee. Sixteen patients underwent ECG gated intravenous DSA, and 10 underwent ECG gated intra-arterial aortic root injection DSA. All patients also underwent conventional cine-angiography with selective graft injection within one week of the DSA studies. Clinical details are summarized in Tables 7 and 8, for the intra-arterial and intravenous studies respectively.

The cine-angiography was performed by using standard methods of catheterization with selective injection of grafts. Intravenous DSA was performed by using a 5 Fg straight, multi side-hole catheter placed in the SVC, with injection of 40 ml of Iohexol 350 (Nycomed, UK) at 25 ml/sec and image acquisition over the aortic root in LAO 35° and RAO 5° projections. Intra-arterial DSA was performed by using a 4 or 5 Fg, 90 cm, eight side-hole pigtail catheter placed in the aortic root with injection of 30 ml of Iohexol 350 (Nycomed, UK) at 15 ml/sec and image acquisition in the LAO 35° and RAO 5° projections. The electrocardiogram and arterial pressure were monitored, and full resuscitatory facilities were at hand. The patients were fully mobile within four hours of the arterial procedure and within 30 minutes for the intravenous procedure.

To minimize misregistration of image data, DSA was performed with the patient in arrested respiration during the image acquisition period. Thus much of the thoracic and pulmonary movements were removed from the data. In order to deal with the effects of cardiac pulsation, image acquisition was gated to the R wave of the patient's electrocardiogram. Images were acquired from a 15 cm field of view onto a 256 by 256 matrix at 8.33 frames per second. The in-plane pixel spatial resolution was 0.6 mm.

Data Analysis

Independent assessment of the cine angiograms and DSA studies was performed by two observers for the intra-arterial studies and three observers for the intravenous studies. Graft patency was noted and compared with the data obtained by cine-angiography. Measures of sensitivity and specificity were obtained, as well as chi squared testing of contingency tables.

Results

Figure 28 is an example of a representative digitally subtracted angiographic frame, together with the cine angiography for patient 1, Table 7. This frame, taken relatively early in the sequence illustrates the digital image quality of this patient's circumflex and LAD grafts. Figure 29 is an example of a representative IV DSA frame, together with the cine angiography for patient 9, Table 7. For the arterial study, there was complete agreement between DSA and conventional cine angiography, that is there were no false positives and no false negative, 100% specificity and sensitivity. Differences emerged however, between the three observers in the interpretation of the IV DSA data and its comparison to conventional cine angiography. These data are summarized in Table 9a. No occluded grafts were identified as patent with IV DSA (100% specificity), but 26/81 patent grafts were not identified and considered occluded (68% sensitivity).

While not the specific focus of the graft visualization studies, assessment of graft vessel run-off was also performed and compared between conventional cine angiography and DSA. In seven of the patients who underwent aortic root injection and DSA there were a total of nine points of disagreement between the two observers assessing the DSA images and a total of six points of disagreement in three patients on the conventional cine angiogram images. These data are summarized in Table 9b. The data demonstrate a tendency for underestimation of the degree of graft vessel run-off when DSA is used for its evaluation. However, in no instance was the degree of disagreement greater than one scoring point (bold figures indicate these occurremces).

It is clear from the images that arterial DSA is superior to IV DSA for the demonstration of graft patency, confirmed by statistical analysis. The arterial studies showed complete agreement with the conventional cine angiograms, while there were difficulties in interpretation and inter observer variation with the IV DSA studies. As a screening procedure, IV DSA may be adequate; however, if patency of inserted grafts is not seen, then formal arteriography will be needed (Hayward, R. and Hunter, G.J. 1985). Indeed as a result of this study, we have abandoned IV DSA in the evaluation of coronary artery bypass grafts. On the other hand, aortic root injection with subtraction is attractive as a replacement for multiple graft hunts. The data also suggest that evaluation of graft vessel run-off is less well performed with aortic root injection and DSA than with conventional selective cine angiography. Based on these findings, non-selective, aortic root injection IA DSA cannot be recommended for the purpose of graft run-off evaluation. Selective injection of the graft would be necessary to achieve satisfactory opacification of poorly filling run-off vessels (Hayward, R. and Hunter, G.J. 1985).

Current angiographic equipment is almost exclusively digital, with subtraction as a feature which can be used when necessary. Enhancements in digital imaging will permit multi-angular subtraction techniques with volumetric reconstruction to be routinely utilized, further reducing angiography duration and risk.

In summary, therefore, DSA has much to offer the angiographer. With the exception of coronary artery graft visualization, IV DSA can supplant more invasive arterial studies. Its ability to be performed as an outpatient procedure is attractive as hospitalization is reduced and there is less risk from a venous puncture than an arterial approach. The introduction of computer controlled image acquisition has also benefitted purely arterial studies. Currently, digital equipment has become standard, offering both conventional arteriography and electronic subtraction in one convenient package.

Table 7

Clinical details of the 10 patients who underwent arterial DSA

Patient	Age (years)	Sex	Coronary Disease	Vessels Grafted	LVEF (%)	Time since Operation
1	46	m	LAD severe Cx severe RCA mild	LAD CxM	57	4 months
2	61	m	LAD severe Cx severe RCA severe	LAD CxM RCA	46	34 months
3	57	m	LAD severe Cx moderate RCA severe	LAD RCA + PDA	-	1 week
4	48	m	LMCA severe LAD blocked RCA severe	LAD CxM RCA + Cx	38	29 months
5	61	m	LAD severe	LAD	61	8 months
6	72	m	LAD severe Cx severe RCA moderate	LAD Cx RCA	49	16 months
7	48	m	LAD blocked Cx mild RCA severe	LAD RCA	-	21 months
8	64	m	LAD blocked Cx severe RCA blocked	LAD CxM RCA	27	73 months
9	52	m	LAD blocked Cx severe RCA blocked	LAD Cx RCA PDA	22	8 years
10	48	m	LAD severe Cx severe RCA severe	LAD Cx RCA	44	8 months

Cx, circumflex artery; LAD, left anterior descending artery;
LMCA left main coronary artery; PDA, posterior descending artery;
RCA, right coronary artery; M, marginal branch; +, jump graft;
LVEF, nuclear cardiology left ventricular ejection fraction;

Table 8

Clinical details of the 16 patients who underwent intravenous DSA

Patient	Age (years)	Sex	Coronary Disease	Vessels Grafted	LVEF (%)	Time since Operation
1	38	m	LAD blocked Cx severe RCA severe	LAD Cx RCA	23	4 months
2	50	m	LAD blocked	LAD	78	11 months
3	40	m	LAD moderate RCA severe	LAD RCA	61	35 months
4	55	m	LAD severe Cx severe RCA blocked	LAD Cx RCA	66	8 months
5	58	m	LAD normal Cx blocked RCA blocked	PDA Cx	48	13 months
6	52	m	LAD blocked Cx severe RCA mild	LAD Cx	53	19 months
7	38	m	LAD blocked Cx severe RCA moderate	LAD Cx	<20	7 months
8	66	m	LAD blocked Cx severe RCA blocked	LAD Cx	18	26 months
9	48	m	LAD severe Cx severe RCA severe	LAD Cx RCA	37	3 years
10	64	m	LAD blocked Cx severe RCA severe	LAD Cx RCA	64	52 months
11	47	m	LAD severe	LAD	68	13 months
12	48	m	LAD blocked Cx severe RCA severe	LAD Cx	57	8 months
13	60	m	LAD severe RCA severe	LAD RCA	47	23 months
14	n/a	m	LAD severe Cx severe RCA severe	LAD Cx RCA	23	> 6 months
15	n/a	m	LAD severe Cx severe RCA severe	LAD Cx RCA	-	> 6 months
16	n/a	f	LAD severe Cx severe RCA severe	LAD Cx RCA	54	> 6 months

Cx, circumflex artery; LAD, left anterior descending artery;
RCA, right coronary artery; PDA, posterior descending artery;
LVEF, nuclear cardiology left ventricular ejection fraction;

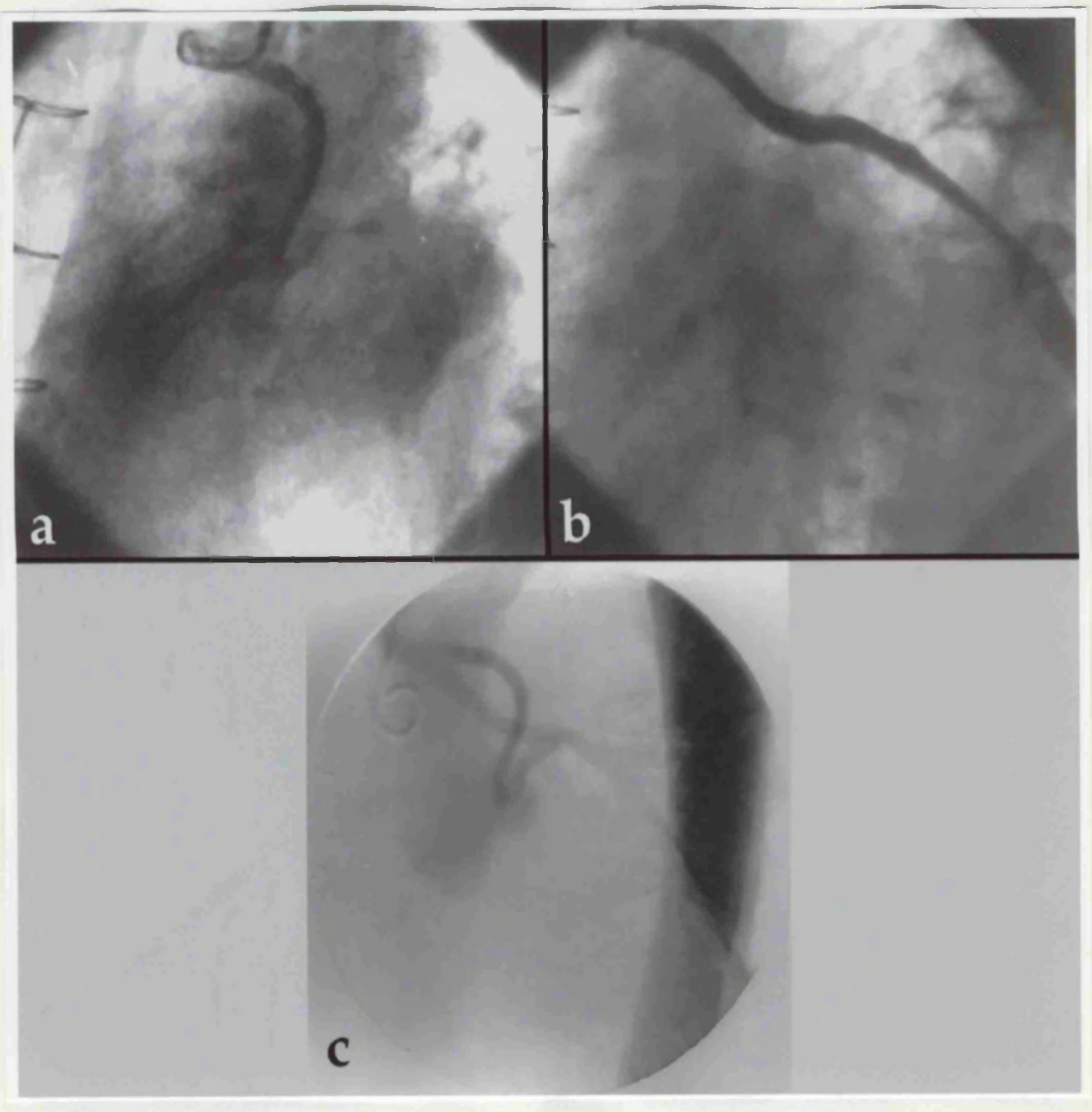

Figure 28. Conventional selective angiograms of the grafts to the LAD (a), and circumflex (b) arteries are shown together with the non-selective arterial DSA image (c). Patency of both grafts is clearly demonstrated by the arterial DSA. These images are from patient 1, table 7.

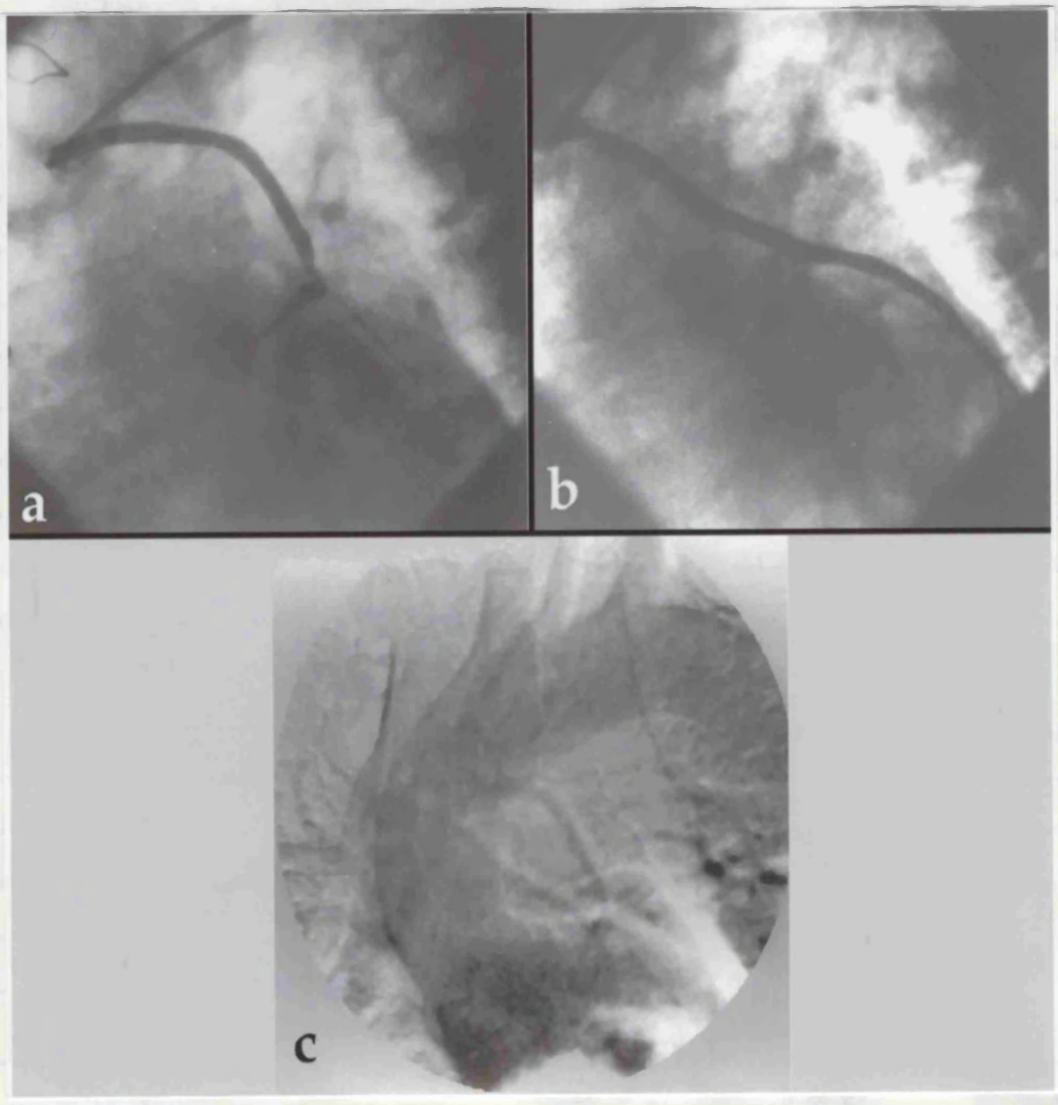

Figure 29. Conventional selective angiograms of the grafts to the LAD (a), and circumflex (b) arteries are shown together with the non-selective IV DSA image (c). Patency of both grafts is seen with IV DSA, however, the quality of the images is far from optimal. As a method for evaluation of graft patency, IV DSA was abandoned in favour of arterial, non-selective DSA. These images are from patient 9, table 8.

Table 9a

Scoring details for the IV DSA data sets

Patient	Assessment by Cine Angiography			Assessment by Physician 1			Assessment by Physician 2			Assessment by Physician 3			Discrepancies		
	RCA	LAD	Cx	RCA	LAD	Cx	RCA	LAD	Cx	RCA	LAD	Cx	RCA	LAD	Cx
1	1	1	1	**0**	1	1	**0**	**0**	1	**0**	**0**	1	3	2	0
2	-	1	-	-	1	-	-	1	-	-	1	-	-	0	-
3	1	1	-	1	**0**	-	1	**0**	-	1	**0**	-	0	3	-
4	1	1	0	1	1	0	1	1	0	1	1	0	0	0	0
5	1	-	0	1	-	0	1	-	0	1	-	0	0	-	0
6	-	1	1	-	**0**	1	-	**0**	1	-	**0**	1	-	3	0
7	-	1	1	-	1	1	-	**0**	1	-	**0**	1	-	2	0
8	0	-	0	0	-	0	0	-	0	0	-	0	0	-	0
9	0	1	1	0	1	**0**	0	1	**0**	0	1	1	0	0	2
10	1	1	1	1	**0**	**0**	**0**	**0**	**0**	0	0	1	2	3	2
11	-	1	-	-	1	-	-	1	-	-	**0**	-	-	1	-
12	-	1	1	-	1	1	-	1	1	-	1	1	-	0	0
13	1	1	-	1	1	-	1	1	-	1	1	-	0	0	-
14	1	1	0	1	1	0	1	1	0	1	1	0	0	0	0
15	1	0	0	1	0	0	**0**	0	0	**0**	0	0	2	0	0
16	1	0	0	1	0	0	**0**	0	0	1	0	0	1	0	0
Totals	9	12	6	8	9	4	5	7	4	6	6	6			
Errors				1	3	2	4	5	2	3	6	0	8	14	4
Grafts Patent	27 of 37			21 of 37			16 of 37			18 of 37					
Discrepancies				6 of 27			11 of 27			9 of 27			26 of 81		
Sensitivity				**68%**											
Specificity				**100%**											

Cx, circumflex artery; LAD, left anterior descending artery; RCA, right coronary artery;
1, inserted graft patent; 0, inserted graft occluded; Bold 0, patent graft scored as occluded

Table 9b

Bypass graft run off independently assessed by two observers who studied selective cine angiograms and non slective DSA acquisitions.

	Conventional Selective Cine Angiography		Digital Subtraction Angiography	
Patient	Assessment by Physician 1	Assessment by Physician 2	Assessment by Physician 1	Assessment by Physician 2
1	**3**	**2**	**3**	**2**
	3	**2**	**3**	**2**
2	3	3	2	2
	3	3	**3**	**2**
3	2	2	2	2
	2	2	2	2
4	2	2	2	2
	1	1	1	1
5	3	3	3	3
6	**1**	**2**	1	1
	1	**2**	2	2
	2	**3**	**2**	**3**
7	2	2	2	2
	3	**2**	**3**	**2**
8	2	2	**2**	**3**
	1	1	1	1
9	3	3	2	3
	3	3	**3**	**2**
10	1	1	1	1
	2	2	2	3
	3	3	3	3
Totals	46	46	45	44

Scoring system: 3, good run off; 2, moderate run off; 1, poor run off.

CHAPTER 5

DIGITAL SUBTRACTION ANGIOGRAPHY: ITS VALUE IN THE DEMONSTRATION OF CARDIOVASCULAR PATHOPHYSIOLOGY

5.1 Introduction

Since Roentgen discovered x radiation in 1896, the application of the technology has been almost exclusively targeted at demonstration of anatomy. The anatomical aspects of DSA have been discussed and exemplified in chapter 4, in addition two instances were described in which functional data were complimentary to the anatomical images, cases 14 and 16. Developing this theme of functional imaging, leads us to the evaluation of cardiac ventricular function from timed sequences of DSA images, characterization of tissue perfusion in terms of time and extent at a capillary level and finally to the measurement of absolute blood flow in large vessels (> 1 mm in diameter). Such functional or physiological techniques are the future of diagnostic imaging. Increasing sophistication in the understanding of disease processes at a cellular or molecular level has resulted in the need for diagnostic studies which can demonstrate abnormalities in tissue function. The reason for this is that alteration in physiological function takes places before changes in anatomy become evident. In some cases there may not even be a change in the anatomy despite extensive damage to functional apparatus within tissues and organs, for example, vasospasm in the vertebral artery following subarachnoid haemorrhage may lead to critical decrease in cerebral perfusion without apparent alteration in CT or MRI appearances of the compromised brain. Digital image acquisition following contrast injection can provide simultaneous anatomical and functional information, thereby allowing the physiology of organ perfusion to be investigated at high spatial and temporal resolution. In this chapter, measurement of left ventricular function and tissue capillary perfusion are presented, in the remainder of the thesis, measurement of absolute blood flow with DSA is described and validated.

5.1.1 Fourier Analysis of the left Ventriculogram

For many years, nuclear medicine techniques have been used to analyze left ventricular motion. Problems associated with this method, however, include super-imposition of chambers on each other, and low spatial and temporal resolutions. Due to the inherent nature of acquisition of DSA images, a good left ventriculogram can be obtained in the standard RAO 30° projection from a right atrial injection using rapid imaging (8.33 frames per second) and high spatial resolution acquisition (1mm in-plane pixel size). ECG gating is not used during such an acquisition.

During the passage of a bolus of contrast through the left ventricle, a reciprocating time density curve may be observed which has two components. There is a high frequency component due to the contraction of the heart, and a low frequency envelope due to the bulk movement of contrast through the left ventricle into the arterial circulation. A series of 16 consecutive images of the left ventricle demonstrating these points is shown in figure 30.

These are the frames acquired during bolus passage of contrast through the left ventricle, they are a subset of the whole acquisition of 140 images in a patient with normal ventricular contraction. If a region of interest is placed over the left ventricle, the changes in contrast density can be demonstrated as a function of time, figure 31. Note the low and high frequency nature of the passage of contrast, the cardiac cycles can be clearly identified superimposed on the washin and washout of contrast in the left ventricle. The 16 images in figure 30 correspond to the three central cycles shown in figure 31.

The technique of phase and amplitude analysis is well established in cardiac nuclear medicine and has been described by many groups in relation to gated blood pool nuclear medicine scans (Walton, S., Ell, P.J., et al., 1982; Houston, A.S. and Macleod, M.A. 1984). A short explanation is, however, pertinent to the present discussion. During a single cardiac cycle, there is ejection of blood from the left ventricle secondary to a systematic contraction of the myocardium. Observing the change in density of contrast in the ventricle during the contraction and relaxation of the myocardium results in the familiar curve shown in figure 32. There are three components of this curve worthy of particular attention, these are the time of

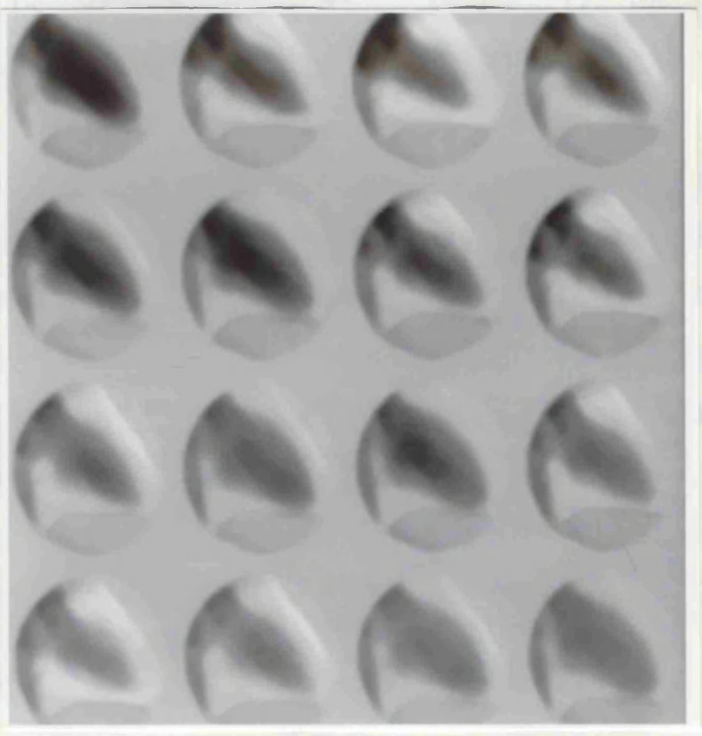

Figure 30. Sixteen images taken from a single cardiac cycle. These correspond to the central cycle shown in Figure 31. The study was acquired in the RAO 30° projection at 8.33 frames per second onto a 256 * 256 matrix from a 15 cm field of view.

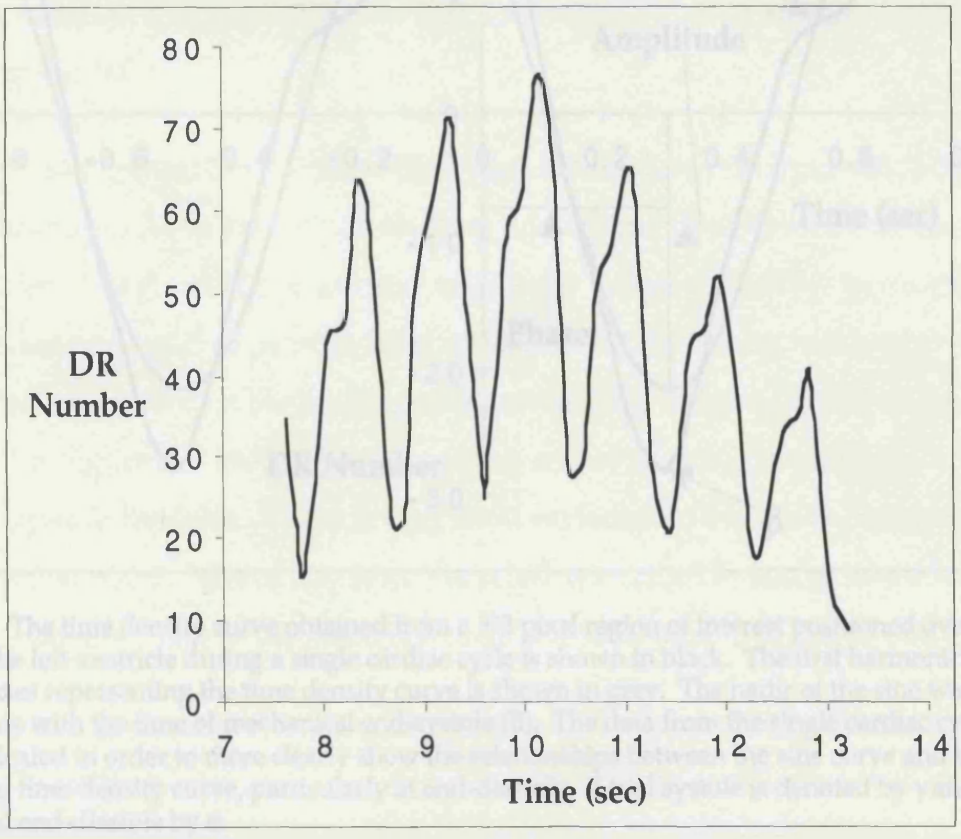

Figure 31. The time density curve obtained from a 3*3 pixel region of interest positioned over the center of the left ventricle is shown. The contrast was injected into the right atrium in order to allow complete mixing and hence a homogenous bolus of contrast to be imaged in its passage through the left ventricle. The framing rate was 8.33 frames per second. Notice the high-frequency components due to cardiac pulsation and the low-frequency envelope as the bolus of contrast passes through the left ventricle. The heart rate is 67 bpm and the ejection fraction is 63.5%.

mechanical end-diastole, the time of mechanical end-systole and the contribution of atrial contraction to ventricular filling. These events are identified in figure 32 as α, β and γ respectively.

Note also that the ventricle does not become completely empty during systole and therefore the time-density curve is always positive and displaced by an arbitrary amount above the abscissa. In order to accept that the observed changes in contrast truly reflect ventricular emptying, it must also be assumed that contrast is admixed homogenously with blood in the left ventricle, and that this concentration does not alter significantly during the observed single cardiac cycle.

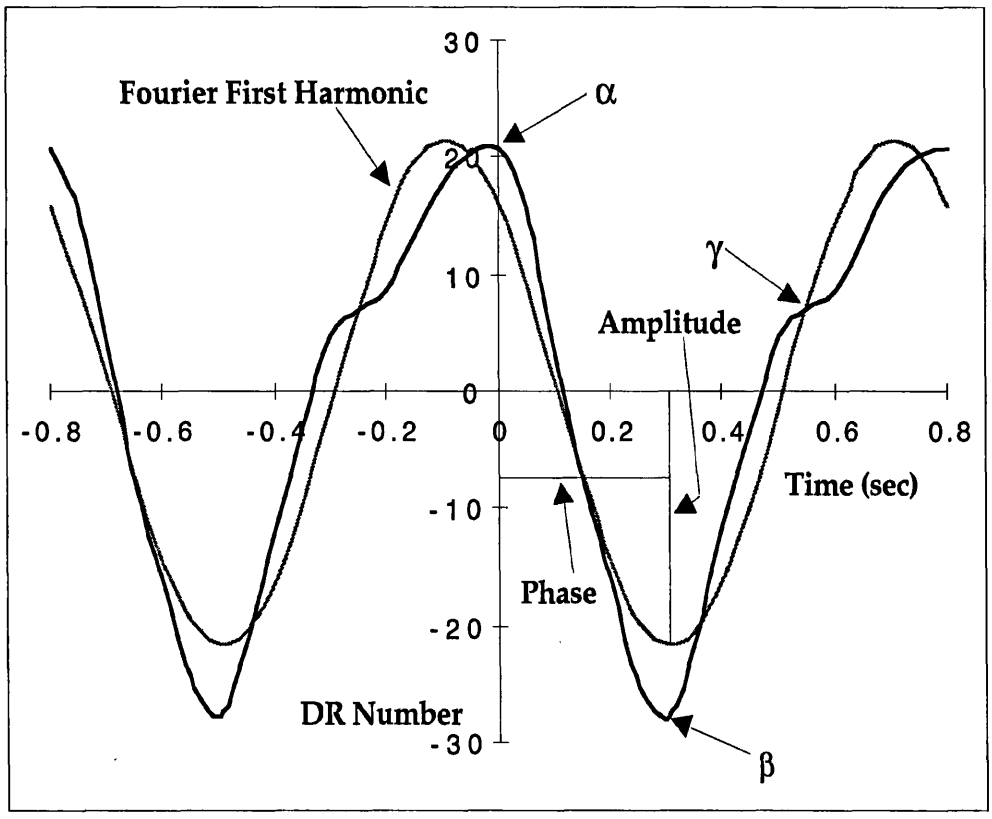

Figure 32. The time density curve obtained from a 3*3 pixel region of interest positioned over the center of the left ventricle during a single cardiac cycle is shown in black. The first harmonic of the Fourier series representing the time density curve is shown in grey. The nadir of the sine wave corresponds with the time of mechanical end-systole (β). The data from the single cardiac cycle have been duplicated in order to more clearly show the relationships between the sine curve and the underlying time-density curve, particularly at end-diastole. Atrial systole is denoted by γ and mechanical end-diastole by α.

This curve may be represented by the sum of a series of sine waves of increasing frequency. Calculating the contributions to the shape of the time-density curve of these sine waves is the technique of Fourier analysis. The zero order component or harmonic corresponds to the mean signal value averaged across a single cardiac cycle. The first harmonic is a sine wave with a single cycle from 0° to 360°, the second harmonic is a sine wave with two cycles from 0° to 360°, and so on. In the present situation, the time-density curve obtained from the left ventricle, from a single cardiac cycle, is constrained to occupy exactly 360°. Each harmonic is characterized by two parameters, the amplitude and phase. These are illustrated in figure 32. The phase angle represents the relative time of end-systole with respect to end-diastole when a single cardiac cycle is considered to occupy 360°, and is about 103° when measured at the apex of the LV. The phase provides information about the timing of contraction, for instance, the timing of atrial contraction, region γ in figure 32, occurs much later than ventricular systole and as such has a higher phase value characterizing it (approximately 210° in this example). The second parameter, the amplitude, reflects the contraction or extent of emptying of the ventricle. It too is a relative number, it is normalized so that the largest value of amplitude observed in a study equals 100.

Taking the single central cycle from the image series shown in figure 31, Fourier analysis was applied to the individual time density curves obtained from each pixel in the image. Images of the phase and amplitude values of the first harmonic were colour coded and used to provide information about the timing and extent of left ventricular contraction in the form of two normalized, relative value images, presented in figure 33. Notice how the phase colour in the left ventricle is uniform from the apex to the base. There is very little variation in the timing of contraction of this normal heart. Notice also how the relative amplitude image is uniform in all regions of the LV. This is the pattern seen in normal phase and amplitude images.

An alternative and somewhat simplified method of presentation of these data may be used. From the phase and amplitude images, the left ventricular outline may be partitioned into 8 overlapping quadrants, starting with the area adjacent to the aortic valve anteriorly, and in a clockwise fashion ending with the area adjacent to the mitral valve inferiorly, figure 34.

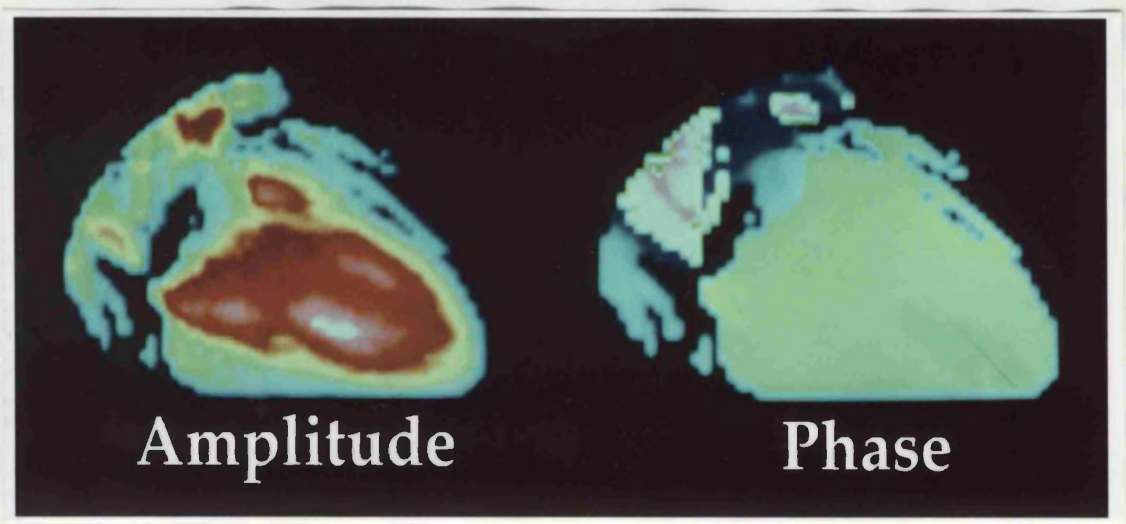

Figure 33. A pair of normal phase (right-hand) and amplitude (left-hand) images. Note the uniform appearance of the left ventricle, seen in the right anterior oblique 30° projection. All parts are contracting simultaneously and evenly, with the greatest amplitude change being in the centre of the ventricle and seen as white going to red.

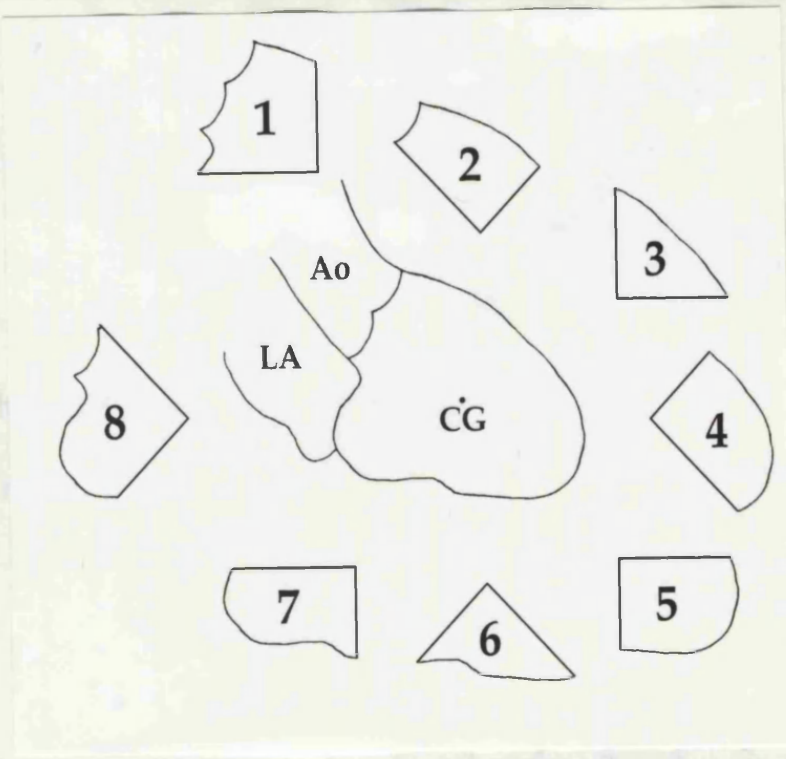

Figure 34. This RAO 30° projection image of the left ventricle, aorta (Ao) and left atrium (LA) has been divided into eight overlapping segments centred at CG, the centre of gravity of the left ventricle. Each of the segments nominally occupies 1/4 of the volume of the ventricle and each segment is rotated by 45° with respect to its neighbours. This scheme reduces the effects of abrupt changes in the data as a result of boundary effects between segments.

The value of phase and amplitude for each of these segments can be individually plotted by region, and compared against normal limits. This method of display is termed a regional parametric plot. The values of regional amplitude and phase for the normal example in figure 33 are given in table 10 and shown in figure 35. The normal ranges presented were obtained from the study described below.

Table 10

Normal ranges for amplitude and phase calculated from table 11, together with the regional values of patient 2. The resulting parametric plot is figure 35.

Amplitude and phase data normalized to 100

	Normal Limits		Patient 2	
Segment	Amplitude	Phase	Amplitude	Phase
1	82	114	92	101
2	90	110	93	100
3	90	110	99	101
4	88	110	100	102
5	89	108	96	104
6	78	109	85	106
7	79	112	85	105
8	80	118	84	104

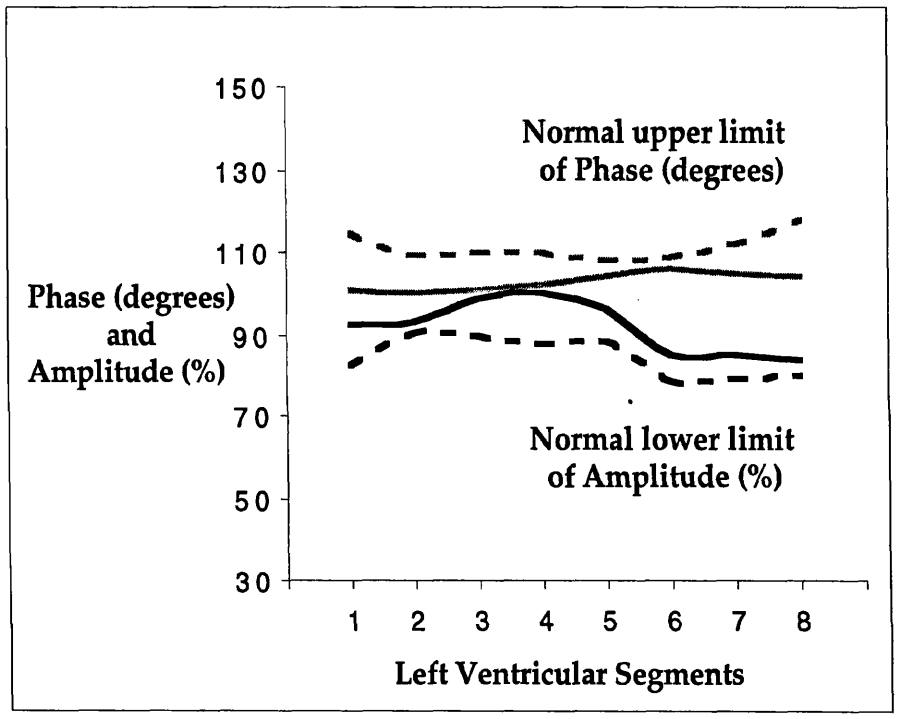

Figure 35. This is a regional parametric plot of the data from patient 2, table 13. There is normal left ventricular function. The upper and lower limits of normality for phase and amplitude are shown as dashed lines; these were obtained from the pooled data of patients with known normal LV function presented in table 11.

These techniques were applied to data from 34 patients with angina, investigated by IV DSA as part of the evaluation of their cardiac status.

Patients and Methods

A total of 34 unselected patients with a history of angina were studied by using IV DSA ventriculography and Fourier phase and amplitude analysis. All gave informed consent, and the study was approved by the hospital ethics committee. Clinical details are summarised in tables 11 and 12 respectively, for the patients who had normal and abnormal ventricular function as assessed by inspection of the left ventriculogram and calculation of the LVEF.

Intravenous DSA was performed by using a 5Fg straight, multi side-hole catheter placed in the SVC, with injection of 40 ml of Iohexol 350 (Nycomed, UK) at 25ml/sec and image acquisition over the left ventricle in an LAO 30° projection. Full resuscitatory facilities were at hand during the procedure. The patients were fully mobile within 30 minutes of the end of the procedure.

To minimize misregistration of image data, DSA was performed with the patient in arrested respiration during the image acquisition period. Thus, much of the thoracic and pulmonary movements were removed from the data. ECG gating was not used. Images were acquired from a 15 cm field of view onto a 256 by 256 matrix at 8.33 frames per second. The in-plane spatial resolution was 0.6 mm per pixel.

Table 11

Clinical details of 12 patients with normal LV function

Patient	Age (years)	Gender	LV Function	Mean Phase	Mean Amplitude	LVEF (%)
1	59	m	Normal	107.88	92.38	78.82
2	57	m	Normal	102.88	91.75	74.57
3	64	m	Normal	108.63	91.38	72.76
4	48	m	Normal	102.75	88.50	60.06
5	37	m	Normal	112.38	88.38	59.55
6	70	m	Normal	110.13	88.00	58.05
7	30	m	Normal	107.88	87.75	57.07
8	45	m	Normal	113.13	87.25	55.14
9	42	m	Normal	106.13	87.13	54.67
10	64	m	Normal	104.38	86.63	52.82
11	55	m	Normal	109.38	86.38	51.91
12	60	m	Normal	105.00	86.00	50.57

Table 12

Clinical details of 22 patients with abnormal LV function

Patient	Age (years)	Gender	LV Function	Mean Phase	Mean Amplitude	LVEF (%)
1	44	m	Anterior Hypokinesia	109.13	86.00	50.57
2	52	f	Inferior akinesia	103.88	85.88	50.13
3	57	m	Inferior hypokinesia	104.25	84.63	45.91
4	59	m	Inferior hypokinesia	104.50	84.50	45.50
5	54	m	Basal hypokinesia	116.63	84.38	45.10
6	51	m	Infero-basal hypokinesia	102.75	83.63	42.75
7	59	m	Mild diffuse hypokinesia	107.00	81.50	36.63
8	39	m	Apical akinesia	109.63	81.13	35.63
9	55	m	Diffuse hypokinesia	103.50	80.38	33.70
10	61	f	Basal hypokinesia	107.13	79.63	31.86
11	67	m	Diffuse hypokinesia	104.38	77.63	27.35
12	38	m	Inferior hypokinesia	101.38	76.88	25.80
13	48	m	Infero-apical hypokinesia	103.00	71.13	23.29
14	47	m	Inferior infarction	117.75	75.50	23.15
15	60	f	Diffuse hypokinesia	110.00	75.50	23.15
16	57	m	Diffuse hypokinesia	111.13	70.75	22.21
17	46	m	Apical akinesia	113.88	70.13	20.50
18	58	m	Infero-apical akinesia	108.75	68.88	17.44
19	42	m	Infero-apical akinesia	111.38	62.00	16.13
20	63	m	Infero-apical akinesia	103.38	67.63	14.79
21	70	f	Apical akinesia	122.63	63.38	13.99
22	57	m	Diffuse hypokinesia	108.38	66.88	13.56

Data Analysis

For each patient the LV angiogram was reviewed and mechanical end-systole and end-diastole were identified as the frames containing the smallest and largest ventricular areas respectively. These frames were then used to obtain a left ventricular ejection fraction by using the method of Dodge and Sheehan (Dodge, H.T. and Sheehan, F.H. 1983). A cine loop of left ventricular contraction was also reviewed and an assessment of regional wall motion performed. The cardiac cycle containing most contrast in the LV was then taken and transferred off-line for Fourier phase and amplitude analysis on the departmental nuclear medicine computer system. The Fourier analysis from those patients considered normal (LV ejection fraction > 50% and no visual dyskinesia on the cine loop) was used to establish values for mean and standard error for phase and amplitude in each of the 8 segments designated. These data were in turn used to establish limits of normality for phase and amplitude in each segment (mean ± 2 standard errors). Phase was normalized such that a single cardiac cycle occupies 360 degrees starting at mechanical end-diastole, and amplitude was normalized such that a value of 100 represented the contraction in the segment with greatest change in contrast between end-diastole and end-systole.

Results

12 of the 34 patients were normal (mean age 53, range 30 to 70 years), based on the dual criteria that LV ejection fraction was more than 50%, and that there was no evidence of regional wall motion abnormality on the cine angiogram. These data are summarized in table 11. The remaining patients (n = 22, mean age 54, range 38 to 70 years), had either visually obvious abnormalities of regional wall motion, or an ejection fraction less than 50%, or both. These data are summarized in table 12. There was no statistically significant age difference between these two groups p = 0.38. The Fourier phase and amplitude values for each overlapping segment are presented in tables 13 and 14 for the normal (n = 12) and abnormal (n = 22) groups respectively.

Table 13

Phase and amplitude details of 12 patients with normal LV function

Amplitude data by segment (normalized to a maximum value of100)

Patient	Segment	1	2	3	4	5	6	7	8	LVEF (%)
1		90	100	100	99	95	76	89	90	78.8
2		92	93	99	100	96	85	85	84	74.6
3		86	86	84	91	98	89	100	97	72.8
4		100	100	87	81	82	88	85	85	60.1
5		100	98	85	91	92	82	77	82	59.6
6		86	95	100	97	91	70	82	83	58.1
7		86	98	100	79	80	88	88	83	57.1
8		100	89	86	83	97	78	73	92	55.1
9		79	93	100	94	91	83	80	77	54.7
10		74	92	100	97	91	80	83	76	52.8
11		82	100	99	90	91	81	75	73	51.9
12		75	81	88	100	99	78	85	82	50.6
Mean		87.5	93.8	94	91.8	91.9	81.5	83.5	83.7	
Standard Error		2.67	1.75	2.06	2.15	1.7	1.62	2.08	1.97	
Mean - 2SE		82.2	90.3	89.9	87.5	88.5	78.3	79.3	79.7	

Phase data by segment (normalized to 0° = 100)

Patient	Segment	1	2	3	4	5	6	7	8	LVEF (%)
1		108	101	100	102	106	116	116	114	78.8
2		101	100	101	102	104	106	105	104	74.6
3		100	100	113	121	116	107	107	105	72.8
4		102	105	103	103	103	105	101	100	60.1
5		100	113	119	115	114	114	113	111	59.6
6		119	110	111	111	106	100	106	118	58.1
7		115	104	100	105	105	103	109	122	57.1
8		129	124	110	104	100	100	113	125	55.1
9		110	103	103	103	103	105	109	113	54.7
10		105	100	101	103	105	105	107	109	52.8
11		118	105	102	101	100	107	117	125	51.9
12		100	101	111	107	102	103	108	108	50.6
Mean		109	106	106	106	105	106	109	113	
Standard Error		2.74	2.06	1.83	1.78	1.43	1.4	1.35	2.39	
Mean + 2SE		114	110	110	110	108	109	112	118	

Table 14

Phase and amplitude details of 22 patients with abnormal LV function

Patient	Segment	1	2	3	4	5	6	7	8	LVEF (%)
1	Amplitude	96	93	77	75	76	78	100	93	50.6
2		83	96	100	87	79	82	83	77	50.1
3		86	100	98	88	83	64	95	63	45.9
4		89	100	95	94	90	71	69	68	45.5
5		62	84	100	94	93	90	81	71	45.1
6		80	80	83	94	100	86	70	76	42.7
7		49	88	100	96	98	90	78	53	36.6
8		84	81	59	60	76	95	100	94	35.6
9		94	91	100	60	60	69	78	91	33.7
10		42	91	100	96	97	94	73	44	31.9
11		100	63	49	71	74	81	87	96	27.3
12		86	98	100	73	53	53	72	80	25.8
13		78	88	100	51	54	62	60	76	23.3
14		90	100	97	77	59	51	62	68	23.2
15		89	88	58	42	49	92	100	86	23.2
16		86	100	89	51	42	56	70	72	22.2
17		98	100	66	39	38	66	77	77	20.5
18		83	100	85	63	61	45	51	63	17.4
19		83	100	88	61	42	34	38	50	16.1
20		90	100	85	50	34	45	64	73	14.8
21		78	71	36	28	34	72	100	88	14.0
22		91	100	71	37	26	43	85	82	13.6
1	Phase	113	107	100	101	106	110	116	120	50.6
2		100	103	104	105	106	105	106	102	50.1
3		104	102	102	100	100	108	110	108	45.9
4		112	104	100	101	102	107	103	107	45.5
5		141	115	100	105	109	111	117	135	45.1
6		107	101	102	102	100	101	102	107	42.7
7		100	100	102	104	108	114	117	111	36.6
8		107	108	117	122	117	100	101	105	35.6
9		100	100	100	110	112	106	100	100	33.7
10		104	104	101	100	102	108	115	123	31.9
11		104	103	106	109	105	105	103	100	27.3
12		101	101	101	101	101	102	102	102	25.8
13		100	101	100	105	103	105	106	104	23.3
14		113	102	100	114	128	126	128	131	23.2
15		103	105	118	126	119	108	100	101	23.2
16		114	110	111	117	113	100	109	115	22.2
17		100	104	108	125	138	128	107	101	20.5
18		104	101	100	101	103	123	125	113	17.4
19		108	101	100	108	117	123	119	115	16.1
20		99	106	106	103	104	104	105	100	14.8
21		102	117	145	147	145	125	100	100	14.0
22		104	102	109	109	117	121	100	105	13.6

The mean minus 2 standard errors for the amplitude and the mean plus 2 standard errors for the phase for each segment are seen in figure 35 as the grey curves bounding the data values. These curves represent the lower limit of normal for amplitude and the upper limit of normal for phase.

All the results are presented in tables 11 through 14, however, two examples are shown in detail. These correspond to patients 14 and 15 in tables 12 and 14. In the case of patient 15, the angiogram on its own is relatively unhelpful, figure 36a, with little evidence of significant contraction. The phase and amplitude images, however, reveal a discrete area of both paradoxical and reduced contraction at the apex, figure 36b. This area of hypo- and dyskinesia is secondary to a focal infarction at the apex of the LV. While the parametric image is quite compelling, a simplified, equally valuable, simultaneous demonstration of the phase and amplitude can also be appreciated on the regional parametric plot shown in figure 36c. From this it can be deduced that the abnormality of function in this patient's left ventricle consists of paradoxical and severely curtailed contraction at the apex.

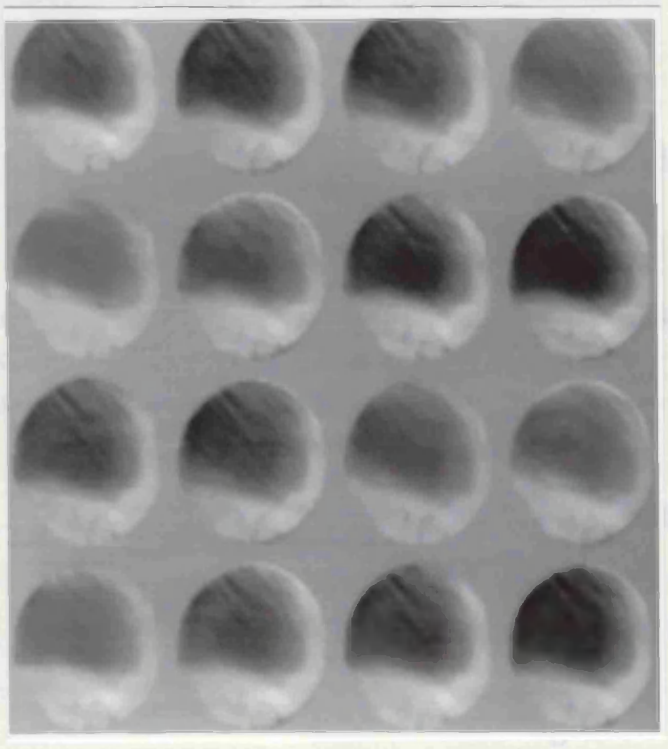

Figure 36a. Sixteen images representing a single cardiac cycle during passage of contrast through the left ventricle. Notice that there is very little apparent movement of the myocardium. It is difficult to interpret the extent and timing of any ventricular abnormality from this image set.

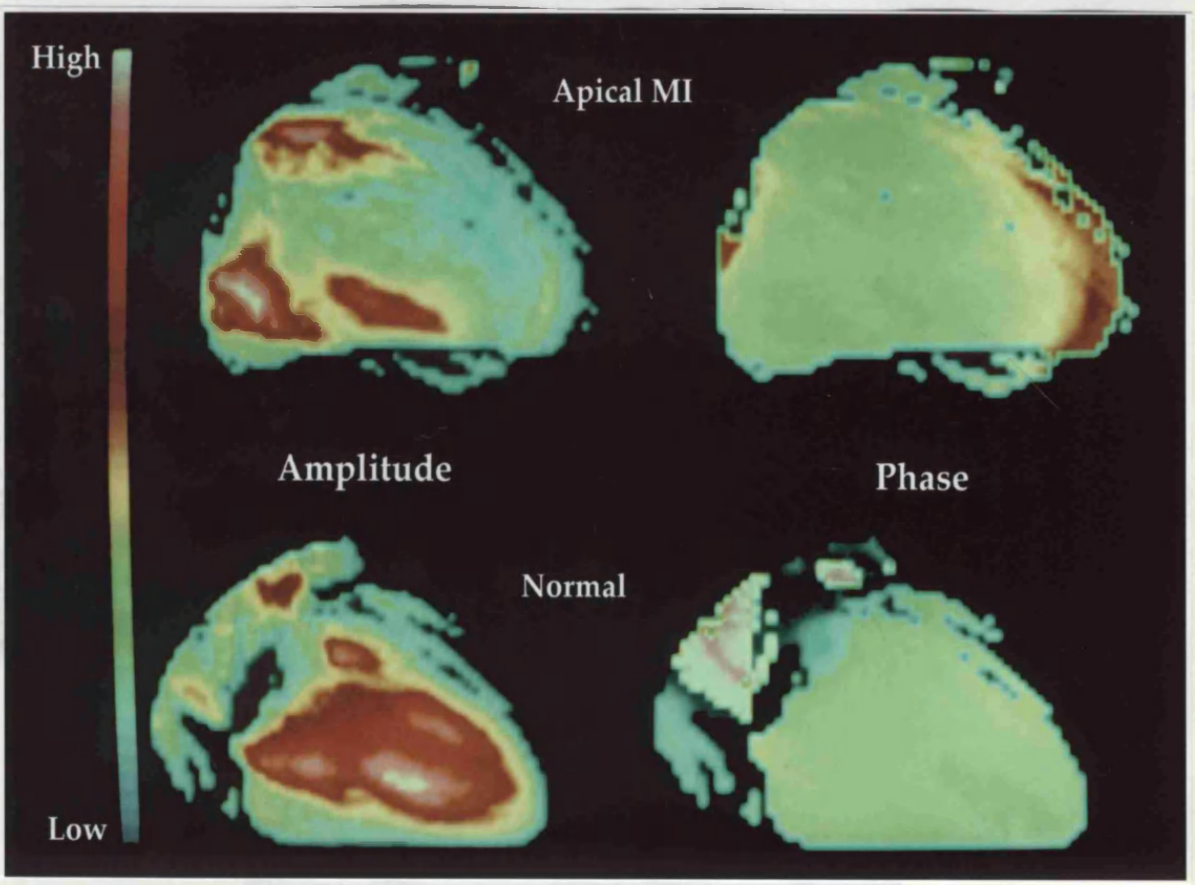

Figure 36b. Phase and amplitude images show that there is both dyskinesia and hypokinesia at the apex, consistent with an apical myocardial infarction. A pair of normal images is presented for reference on the bottom row.

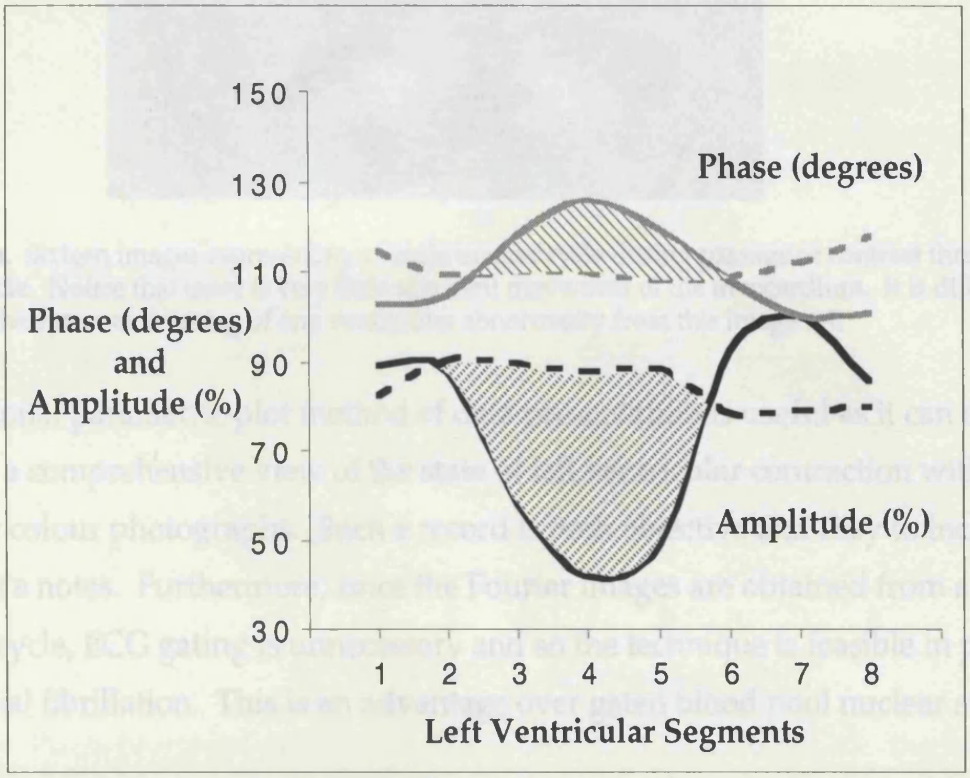

Figure 36c. This is the regional parametric plot of the data from figures 36a and 36b. The upper and lower limits of the normal ranges for phase and amplitude are shown as dashed lines. The segmental values for both phase and amplitude are outside the normal limits in segments 3, 4 and 5. These correspond to the apical abnormality demonstrated in figure 36b. The cross hatched areas represent the extent of phase and amplitude abnormalities.

In the second case, patient 14, the angiogram is again non-contributory, figure 37a. The phase and amplitude images however, reveal that a segment of the inferior wall is akinetic, with some shift of phase in this area, figure 37b. The regional parametric plot also shows the extent of phase delay in this area, figure 37c. This patient suffered an extensive inferior wall infarction 6 months earlier.

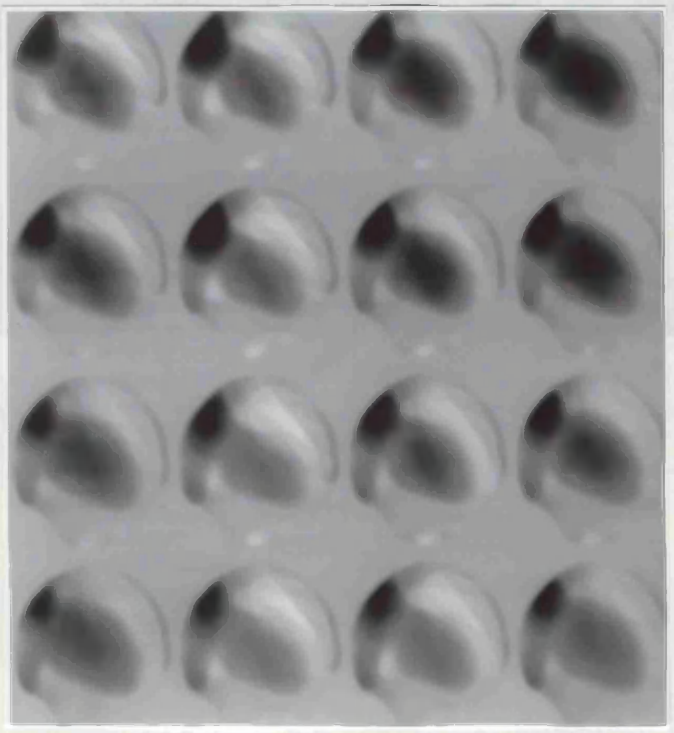

Figure 37a. Sixteen images representing a single cardiac cycle during passage of contrast through the left ventricle. Notice that there is very little apparent movement of the myocardium. It is difficult to interpret the extent and timing of any ventricular abnormality from this image set.

The regional parametric plot method of data presentation is useful as it can easily provide a comprehensive view of the state of left ventricular contraction without the need for colour photographs. Such a record is both objective and easy to include in a patient's notes. Furthermore, since the Fourier images are obtained from a single cardiac cycle, ECG gating is unnecessary and so the technique is feasible in patients with atrial fibrillation. This is an advantage over gated blood pool nuclear studies.

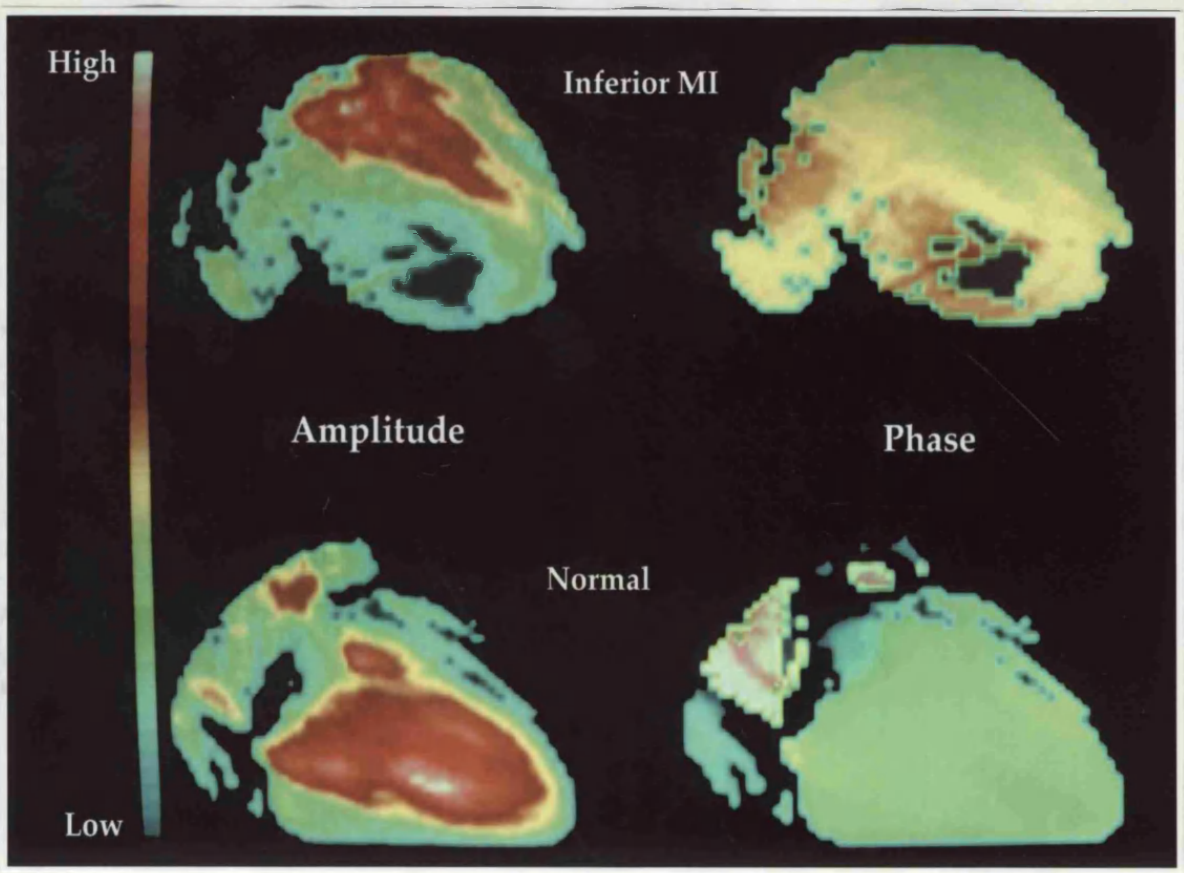

Figure 37b. Phase and amplitude images show that there is both dyskinesia and akinesia involving the infero-posterior myocardial wall, consistent with an posterior myocardial infarction. A pair of normal images is presented for comparison on the bottom row.

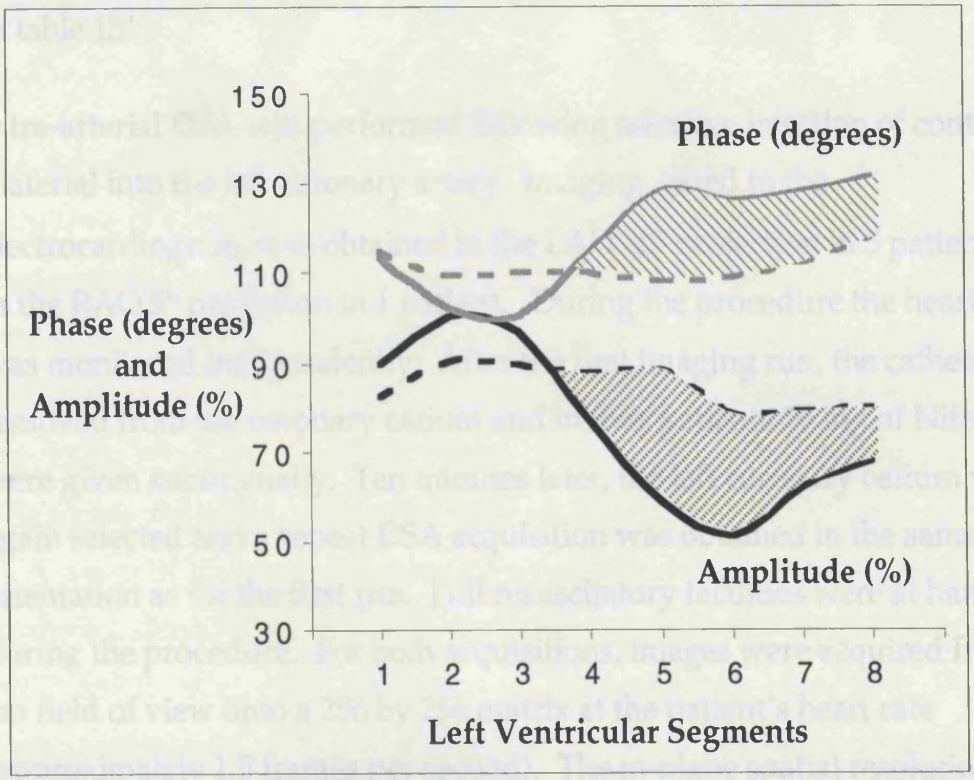

Figure 37c. This is the regional parametric plot of the data from figures 37a and 37b. The upper and lower limits of the normal ranges for phase and amplitude are shown as dashed lines. These lines correspond to the data presented in table 11 and shown in figure 35. The segmental values for both phase and amplitude are outside their respective normal limits in segments 4 through 8. These correspond to the inferior wall abnormality demonstrated in figure 37b. The cross hatched areas represent the extent of phase and amplitude abnormalities.

5.2 Investigation of Coronary Reserve

As coronary artery disease leads to vessel narrowing and reduced myocardial perfusion and flow patients begin to experience angina. In evaluating potential treatments it would be useful to have an objective measurement of myocardial perfusion based on physiological parameters rather than simply relying on anatomical evaluation of vessel dimensions. With this in mind, the group at Ann Arbor (Michigan, USA) used DSA to measure coronary reserve (Vogel, R., Lefree, M., et al., 1984). At the same time, work for this thesis was ongoing and a technique for measuring absolute transit times from the coronary ostium to the myocardium and coronary sinus was developed and implemented (Hunter, G.J. and Hayward, R. 1985). A pilot study was performed to demonstrate the feasibility and validity of the technique; this is presented here.

Patients and Methods

6 unselected patients with a history of chest pain were invited to participate in this preliminary study. All gave informed consent, and the study was approved by the hospital ethics committee. Clinical details are summarised in table 15.

Intra-arterial DSA was performed following selective injection of contrast material into the left coronary artery. Imaging, gated to the electrocardiogram, was obtained in the LAO 30° projection in 5 patients and in the RAO 5° projection in 1 patient.. During the procedure the heart rate was monitored independently. After the first imaging run, the catheter was removed from the coronary ostium and in four patients 10 mg of Nifedipine were given sublingually. Ten minutes later, the left coronary ostium was again selected and a repeat DSA acquisition was obtained in the same orientation as for the first run. Full resuscitatory facilities were at hand during the procedure. For both acquisitions, images were acquired from a 15 cm field of view onto a 256 by 256 matrix at the patient's heart rate (approximately 1.5 frames per second). The in-plane spatial resolution was 0.6 mm per pixel.

Data Analysis

For each patient the passage of contrast through the myocardium and coronary sinus was reviewed. The frame rates were normalized to the ECG and heart rate and yielded uniform data sets with images acquired at known times. Each data set was analyzed using the method described by Hunter et al (Hunter, G.J., Hunter, J.V., et al., 1986). Briefly, for each pixel, the time to half maximum and maximum opacification was calculated after background subtraction. The time differences between the left coronary ostium and the apical myocardium and coronary sinus were measured. A z-test for difference of means was used to show whether or not there was a change in the transit times after Nifedipine.

Results

Four patients had both pre and post Nifedipine acquisitions. In two patients technical factors prevented the second acquisition. The results are summarized in table 15. In all cases there is a decrease in transit time consistent with increased blood flow and thus increased delivery of oxygen and nutrients to the myocardium.

In essence, for each pixel in the matrix, a time-density curve was generated and the appearance time of contrast was color coded. Thus, a color map of myocardial contrast appearance time was obtained. From patient 1 examples of the early and late phases after injection are shown in Figure 38a, with the corresponding arrival-time colour map in Figure 38b. Figure 39a shows the native coronary circulation in the arterial and venous phases of contrast transit found in patient 4. Figure 39b shows the effect of the nifedipine on the arrival-time images. Figures 40a and 40b are a pair of images from patient 3 who has severe atherosclerotic disease; they also show a decrease in perfusion time after nifedipine (Hunter, G.J. and Hayward, R. 1985). In all cases, the heart rate increased after Nifedipine, but the blood pressure remained stable. The post Nifedipine images demonstrate a more rapid delivery of contrast and blood to the myocardium with decreased transit times. These measurements are absolute and provide an objective assessment of the

effects of the drug in individual patients. These examples of functional, physiological imaging outline the value of digital data. Such analysis is difficult with cine film and virtually impossible with cut film. However, further work is necessary to bring these techniques into routine clinical usage.

Table 15

Clinical details and results of arrival time measurement in 6 patients. There is a statistically significant difference between the pre and post Nifedipine data, ($p < 0.001$). After Nifedipine, there is faster transit of blood to the myocardium consitent with increased flow and delivery of nutrients.

Arrival time normalized by heart rate; The left coronary ostium is time = 0

Patien	Age (yrs)	Gender	Presenting Complaint	Conventional Coronary Angiogram	Baseline		Post Nifedipine	
					Heart Rate	Septal Arrival (sec)	Heart Rate	Septal Arrival (sec)
1	28	m	Chest Pain	LAD - Normal Cx - Normal RCA - Normal	88	4.34 ± 0.02	N/A	N/A
2	50	m	Angina	LAD - Severe Cx - Severe RCA - Mild	85	2.66 ± 0.06	N/A	N/A
3	62	m	Angina	LAD - Severe Cx - Moderate RCA - Mild	79	4.77 ± 0.05	88	3.66 ± 0.07
4	57	f	Chest Pain	LAD - Normal Cx - Normal RCA - Moderate	91	4.09 ± 0.03	96	3.02 ± 0.02
5	31	m	Chest Pain	LAD - Normal Cx - Normal RCA - Normal	67	2.32 ± 0.03	69	1.95 ± 0.03
6	55	m	Angina	LAD - Mild Cx - Mild RCA - Normal	82	2.19 ± 0.01	89	1.29 ± 0.02
					Mean ± SEM	3.40 ± 0.09	Mean ± SEM	2.48 ± 0.08

Cx, Circumflex artery; LAD, left anterior descending artery; RCA, right coronary artery;

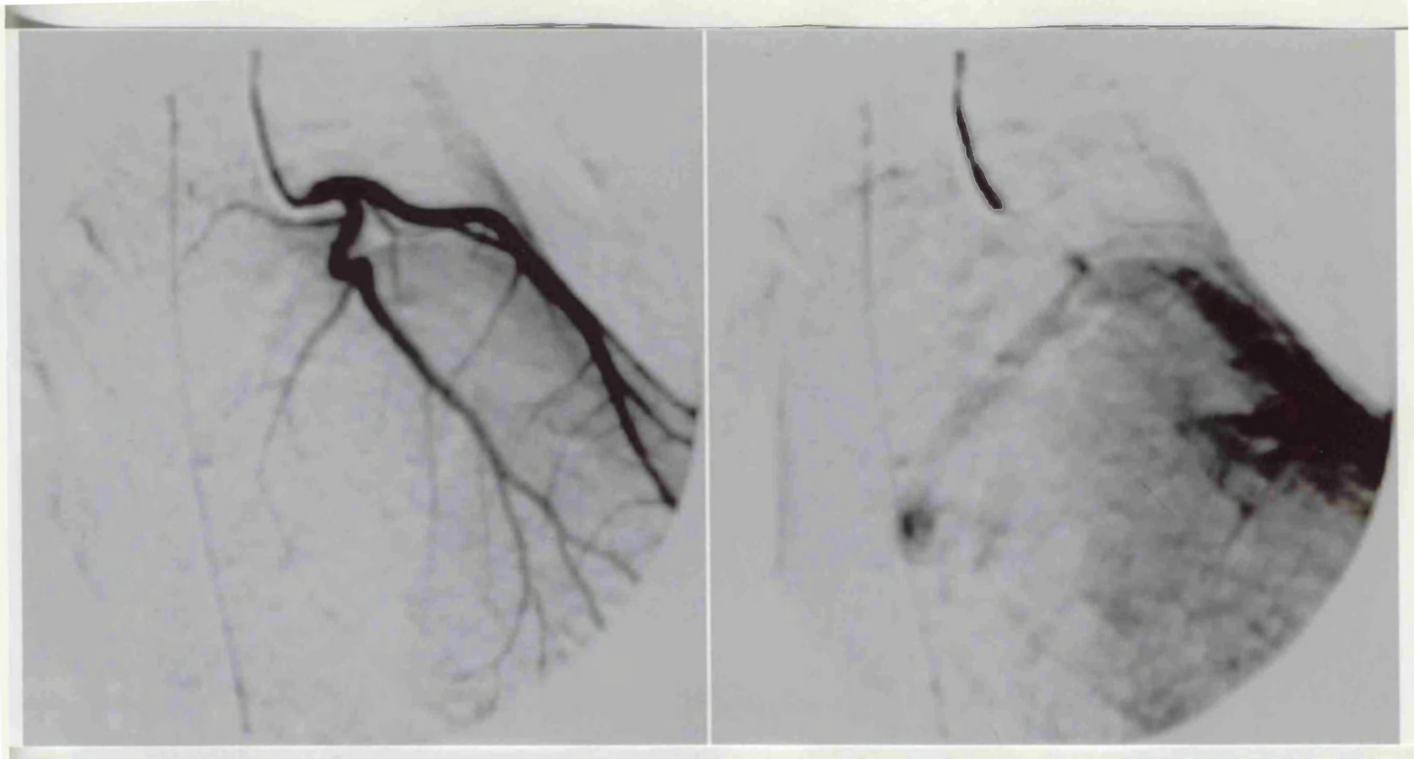

Figure 38a. The early arterial (left) and late venous (right) stages of coronary perfusion. The images were acquired in the RAO 30° projection following injection of 5 ml of iohexol 350 into the left coronary artery. The image sequence acquisition was triggered by the r wave of the electrocardiogram.

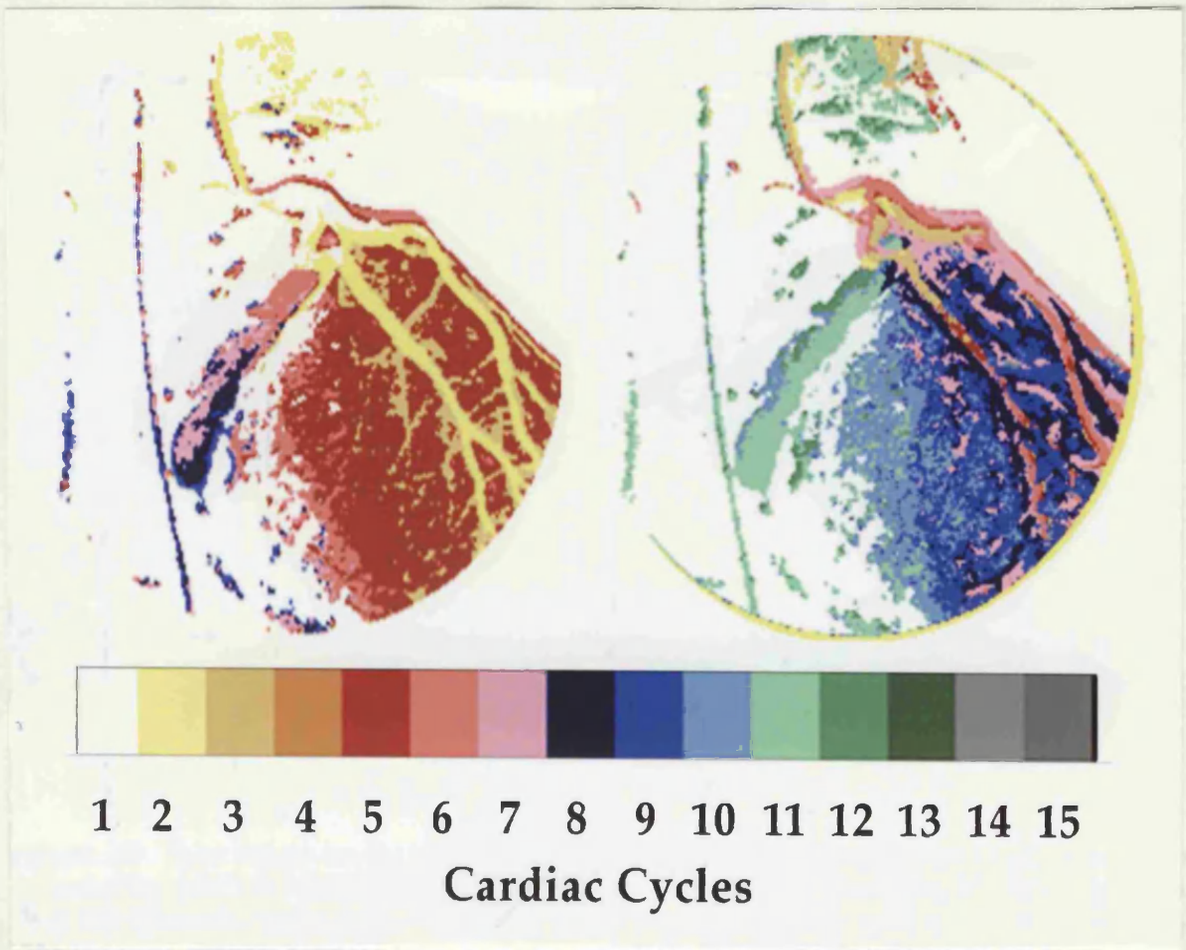

Figure 38b. This is a pair of perfusion images. The right-hand image has been color coded for the time of arrival of contrast in the vasculature, while the left hand image is color coded for the time of peak opacification. The colour scale with respect to the cardiac cycle is illustrated below the images. The colour coding was normalized by the heart rate (= 88 bpm) to yield absolute transit times to the apex and coronary sinus of 4.34 and 5.45 seconds respectively.

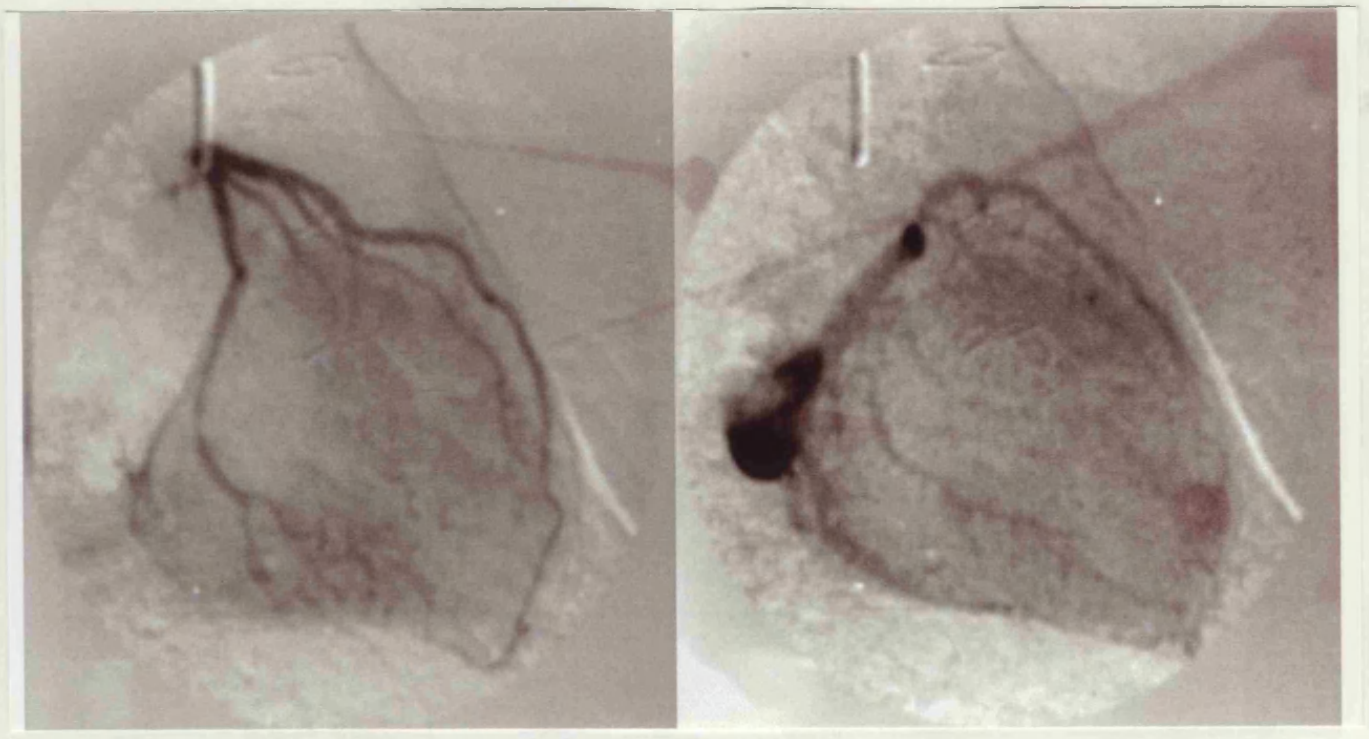

Figure 39a. This is a pair of images in the RAO 30° projection which show the left coronary vasculature in a patient with predominantly right coronary artery disease. The left image outlines the arterial supply and the right image shows the venous drainage of the left ventricular myocardium.

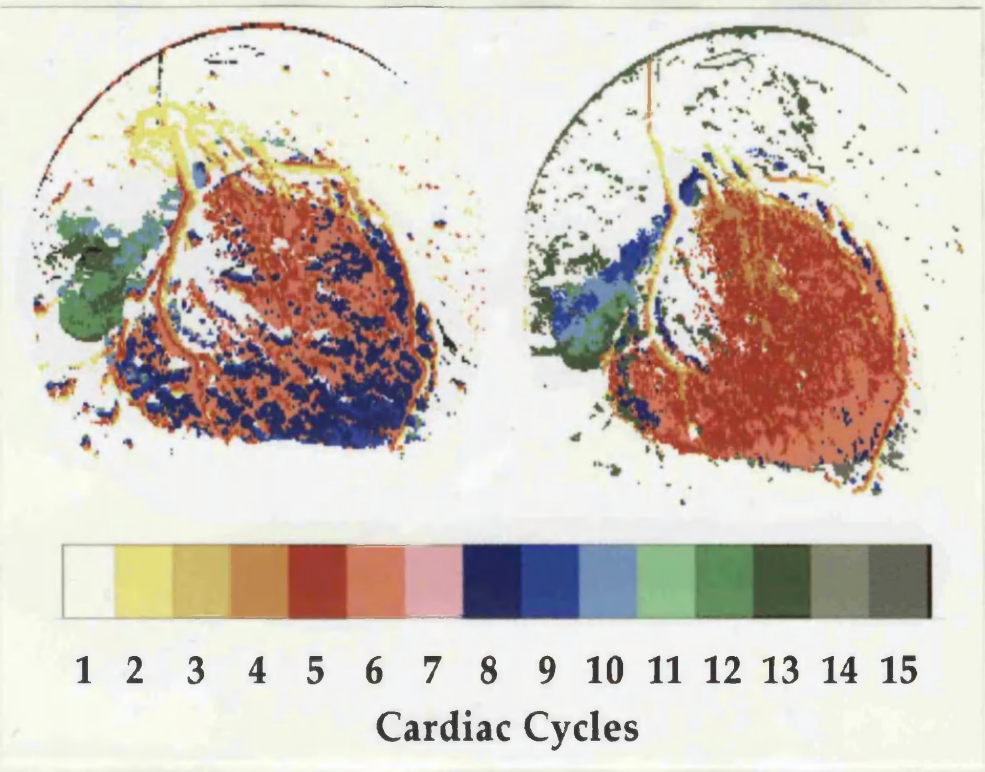

Figure 39b. These images are the result of color flow mapping of the time of arrival of contrast in the vasculature of the left ventricular myocardium. They are taken from two series, of which Figure 39a is an example of the initial series, before and after administration of 10 mg of nifedipine sublingually. The left hand image is from the series before the drug, the right hand image is from the series acquired 10 minutes after the drug was given. Notice the colour shift by about one cardiac cycle to the left, this is particularly easily seen at the apex. This indicates a more rapid delivery of contrast (and, by inference, oxygenated blood) to the myocardium of the left ventricle after the drug. Transit times to the apex before and after Nifedipine were 4.09 and 3.02 seconds respectively, after normalization to the patient's heart rate.

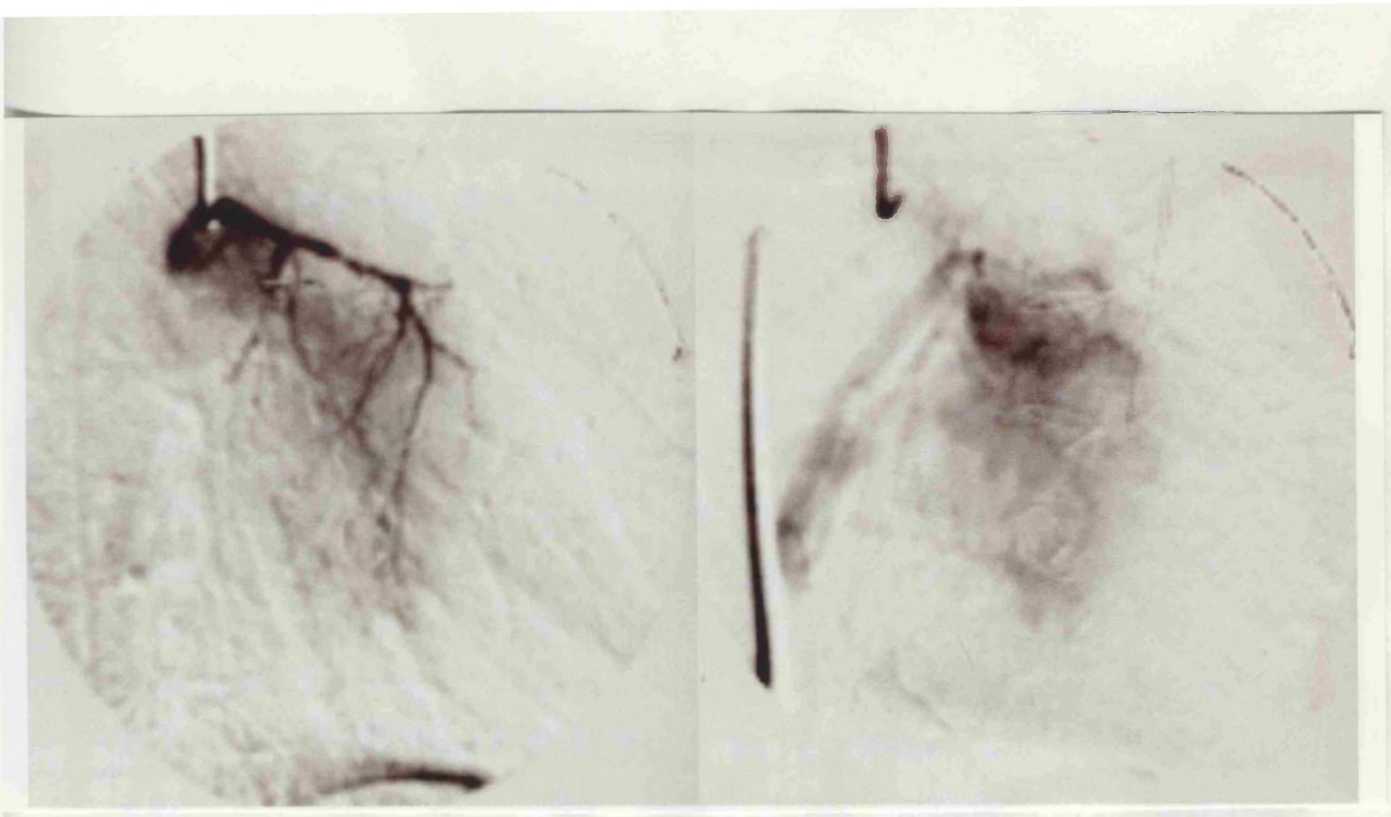

Figure 40a. This pair of images is from the early and late stages of perfusion of the myocardium in a patient with severe left coronary artery disease.

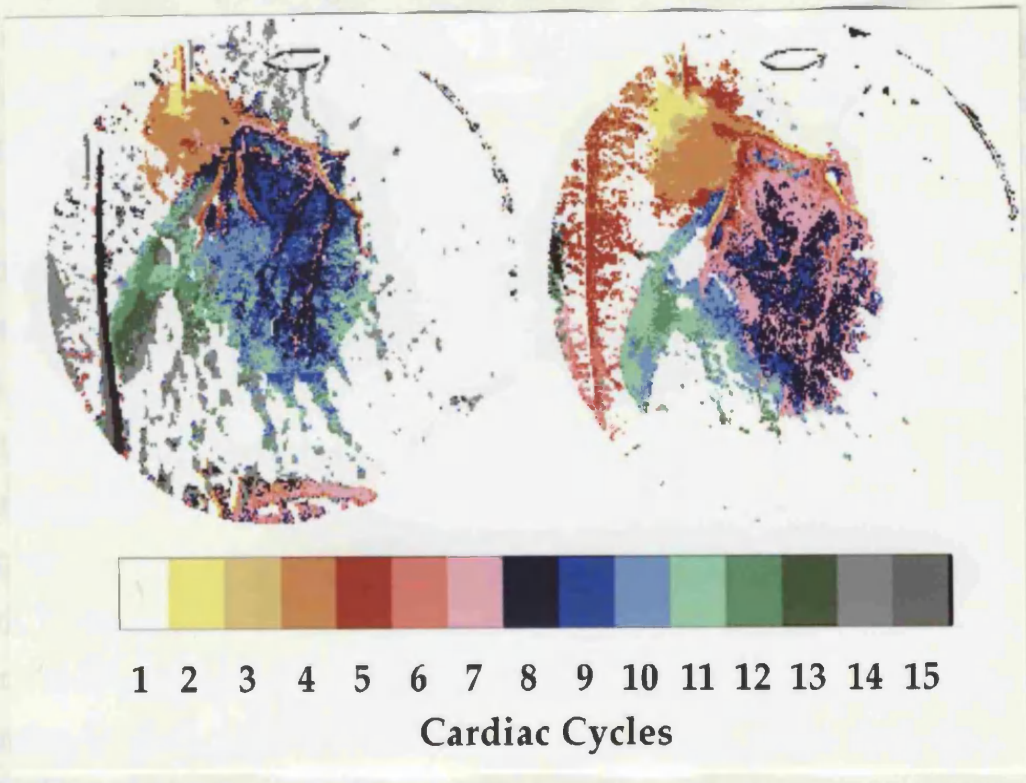

Figure 40b. These are the color flow mapped images from the patient whose vasculature is illustrated in Figure 40a. The left hand image was generated from the initial study acquired before nifedipine was given. The right hand image was generated from the sequence of images acquired 10 minutes after 10 mg of nifedipine had been given sublingually. As with the previous case, notice that there has been an overall shift of about one cardiac cycle in the time of arrival of contrast into the myocardium. The normalized times were 4.77 and 3.66 seconds respectively, before and after the drug.

CHAPTER 6

MEASUREMENT OF BLOOD FLOW BY DENSITOMETRY

6.1 Historical Perspective

By the end of the last century, Stewart had outlined the principles of the dye dilution method for determining blood flow, particularly in relation to cardiac output (Stewart, G.N. 1894; Stewart, G.N. 1897). Thirty years later Hamilton and his co-authors applied and refined the method for use with a bolus injection of dye (Hamilton, W.F., Moore, J.W., et al., 1928). A further thirty years later, the method became established and was accepted into routine clinical practice (Fox, I.J., Brooker, L., et al., 1956). With the advent of routine angiography in the early 1950's, radiographic contrast medium was used as a "dye indicator," with the density of contrast as the time variant parameter. By 1964 several workers had applied this technique with varying degrees of success (Guntert, W. and Zimmer, E.A. 1957; Heuck, F., Anschutz, F., et al., 1963). It was in that year that Wood developed a reliable video densitometer (Wood, E.H., Sturm, R.E., et al., 1964). This instrument performed accurate determinations of radiographic absorption within an arbitrary area of the fluoroscopic television image, and so the dilution of an iodinated contrast medium could be recorded in the circulatory system and used for quantitative measurements. Since that time, many workers have implemented a several techniques utilizing videodensitometry for measuring blood flow in various arteries (Rutishauser, W., Bussmann, W.D., et al., 1970; Bursch, J.H., Johs, R., et al., 1971; Heintzen, P.H. and Pilarczyk, J. 1971; Silverman, N.R., Intaglietta, M., et al., 1973; Erikson, U., Ruhn, G., et al., 1975; Erikson, U., Bjork, L., et al., 1976; Erikson, U., Bjork, L., et al., 1978; Erikson, U., Helmius, G., Pavek, K., et al., 1980; Erikson, U., Helmius, G., Ruhn, G., et al., 1980; Erikson, U., Ruhn, G., et al., 1980; Erikson, U., Helmius, G., et al., 1981; Erikson, U., Helmius, G., et al., 1983). With the advent of DSA, this technique was rapidly pressed into service as a convenient method of performing densitometry (Bursch, J.H., Hahne, H.J., et al., 1981; Bursch, J.H. 1983; Spiller, P., Fischbach, T., et al., 1983; Spiller, P., Schmiel, F.K., et al., 1983; Bateman, W.A. and Kruger, R.A. 1984; Bursch, J.H. 1985; Neuhaus, K.L., Sauer, G., et al., 1986).

Whichever method of densitometric measurement was used, one of two principle means of assessing flow was implemented; either the velocity of flowing blood was measured or the mass of iodine in blood that passed by the detector was used to obtain an estimate of relative flow. There are errors inherent in both these techniques, and these methods of blood flow measurement have not gained worldwide acceptance, being limited to a few centers. Furthermore the bulk of investigation has been conducted with a view to the measurement of coronary artery flow. It may be that a more desirable aim would be to monitor various pharmacological and surgical interventions without necessarily measuring absolute mean forward blood flow.

6.2 Limitations of Video-densitometry

The acquisition and storage method are both prone to noise. Assessment of absolute density values requires logarithmic transformation and correction for beam hardening and scatter. If digitization of cine film is the source of data, then errors related to conditions of film development also influence the results. Various techniques have been developed in an attempt to reduce these variables (Brennecke, R., Bursch, J.H., et al., 1978; Lantz, B.M., Foerster, J.M., et al., 1981).

6.3 Theoretical Benefits of DSA

A well designed, integrated system will produce logarithmically transformed densitometric data where the attenuation of the x-ray beam produced by the iodine in the vessel is linearly related to the mass of iodine in the path of the beam. Although scatter and veiling glare can be controlled and minimized, beam hardening remains by virtue of the polychromatic nature of the x-ray beam. Fortunately, its effects can usually be ignored. However, if the vessel under investigation overlies bone, beam hardening may alter the linear relationship between the mass of iodine in the vessel and the observed attenuation. Such data are non-linear in their behaviour and care must be exercised if quantitative results are to be used for further analysis. Other benefits of DSA over conventional cine-angiography include direct digital storage and reduction of noise in the image. On

the whole, DSA produces already pixelated data in a format for rapid, convenient analysis. The underlying theories in respect of quantitative data analysis apply equally to DSA and to classical video and cine densitometry.

6.4 Mathematical Basis of Blood Flow Measurement

In order to measure a volume flow in absolute units, it is necessary to measure volume and time. The volume information can be deduced from geometrical consideration of the vessel under investigation (Hoornstra, K., Hanselman, J.M., et al., 1980) or by analysis of the density and mass of iodine present (Bursch, J.H., Hahne, H.J., et al., 1981). Timing information is obtained by virtue of a rapid sequence of images acquired at known time intervals and the subsequent measurement of time density curves obtained during the passage of the bolus of iodine contrast material through the region of interest.

6.4.1 The Gamma Variate Curve

6.4.1.1 *Gamma Variate as the Time Density Curve*

When a solution of iodine contrast is injected into a vessel, it becomes diluted with flowing blood and over a period of time mixes with that blood to give a homogenous fluid (axiom 1). The injected iodine does not disperse throughout the blood stream instantaneously and thus the volume and rapidity of the injectate determine the characteristics of the bolus of contrast in its first passage through the region of interest. In this region, iodine concentration $\rho(t)$ will vary as a function of time, initially rising, reaching a peak value and then falling as the bolus passes along the vessel. If a finite mass of iodine, m, is injected, then it can be shown that for a flow of F at the site of injection (Zierler, K.L. 1962):

$$\int_0^\infty \rho(t)dt = m/F \qquad 6.1$$

In a closed situation, such as the circulation, F is the cardiac output and is more usually denoted by Q. Thus 6.1 becomes:

$$\int_o^\infty \rho(t)dt = m/Q \qquad 6.2$$

This is valid for any site of measurement of $\rho(t)$ in the intact circulation, provided axiom 1 holds true. The practical value of this is that if $\rho(t)$ is established in any convenient place, for instance a peripheral artery, it is possible to calculate Q if m is known.

As has been shown in Section 2.2.5 in an ideal case, a grey scale subtracted image yields density or DR numbers proportional to the iodine concentration given by:

$$D \propto (\mu_i \rho_i x) \qquad 6.3$$

Where - μ_i = mass attenuation coefficient for iodine
ρ_i = density /concentration of iodine
x = path thickness
D = density number in arbitrary units

Thus, following an injection of contrast and the passage of the bolus along a vessel through a region of interest, the DR number obtained from that region will vary with time according to:

$$D(t) \propto (\mu_i \rho_i(t) x) \qquad 6.4$$

Integrating both sides gives:

$$\int_o^\infty D(t)dt \propto \int_0^\infty \mu_i x \rho_i(t)dt \qquad 6.5a$$

$$\Rightarrow \int_o^\infty D(t)dt \propto \mu_i x(m/Q) \qquad 6.5b$$

The relationship thus far is merely a proportionality. By introducing a constant K, which represents such intangibles as system amplification, ADC efficiency etc. (Kruger, R.A., Mistretta, C.A., et al., 1981) this proportionality can be converted into an equality:

$$\int_0^\infty D(t)dt \;=\; K\mu_i x(m/Q) \qquad 6.6$$

The expression on the left is the integral over time of the time density curve, ie. the area under the curve. Actual measurement of D(t) is performed by video densitometry or DSA. This is accurate as long as recirculation, noise or background fluctuation does not occur to any significant degree. Inherently our methods of acquisition are noisy; therefore, some form of idealized curve is needed to represent the real data. In 1964 it was shown that an ideal contrast dilution curve could be closely approximated by one of a family of analytical curves, known as gamma-variates (*GV*) (Thompson, H.K., Starmer, C.F., et al., 1964) - axiom 2. These have the mathematical form of:

$$c(t) = ga * (t - ta)^{aa} * e^{-(t-ta)/ba} \qquad 6.7$$

where *aa*, *ba* and *ga* are constants; *t* is time; *ta* is time of first non-zero value (time of arrival) and *c(t)* is the concentration of contrast at time *t*.
Various useful parameters may be inferred from 6.7 that make this relationship amenable to analytical treatment. By convention, $dc/dt = c'$. Differentiating 6.7 with respect to time yields:

$$c' = \left\{aa * ga * (t - ta)^{(aa-1)} * e^{-(t-ta)/ba}\right\} - \left\{\left[ga * (t - ta)^{aa} * e^{-(t-ta)/ba}\right]/ba\right\} \qquad 6.8a$$

Rearranging and eliminating gives:

$$c' = ga * e^{-(t-ta)/ba} * (t - ta)^{aa} * [(aa * ba - (t - ta)^2)/(ba * (t - ta))] \qquad 6.8b$$

Now maximum *c* occurs when c' is zero. That condition is trivially met if g is zero, or alternatively if $t = ta$. Both are irrelevant to the present discussion.
6.8b is also zero if:

$$[aa * ba - (t - ta)]/[ba * (t - ta)] \;=\; 0 \qquad 6.9$$

By rearranging this, it is found that:

$$t_{max} = (aa * ba) + ta \qquad 6.10$$

and $$c_{max} = ga * (aa * ba)^{aa} * e^{-aa} \qquad 6.11$$

The area under this idealized curve is given by:

$$c(t)dt = ga * ba^{(aa+1)}\Gamma(aa+1) \qquad 6.12a$$

where $\Gamma(x)$ is the gamma function:

$$\Gamma(x) = \int_{o}^{\infty} t^{(x-1)} * e^{-t} dt \qquad 6.12b$$

for all $x > 0$

and $$\Gamma(x+1) = x\,\Gamma(x) \qquad 6.12c$$

(Beyer, W.H. 1981). Figure 41 shows a typical gamma variate curve.

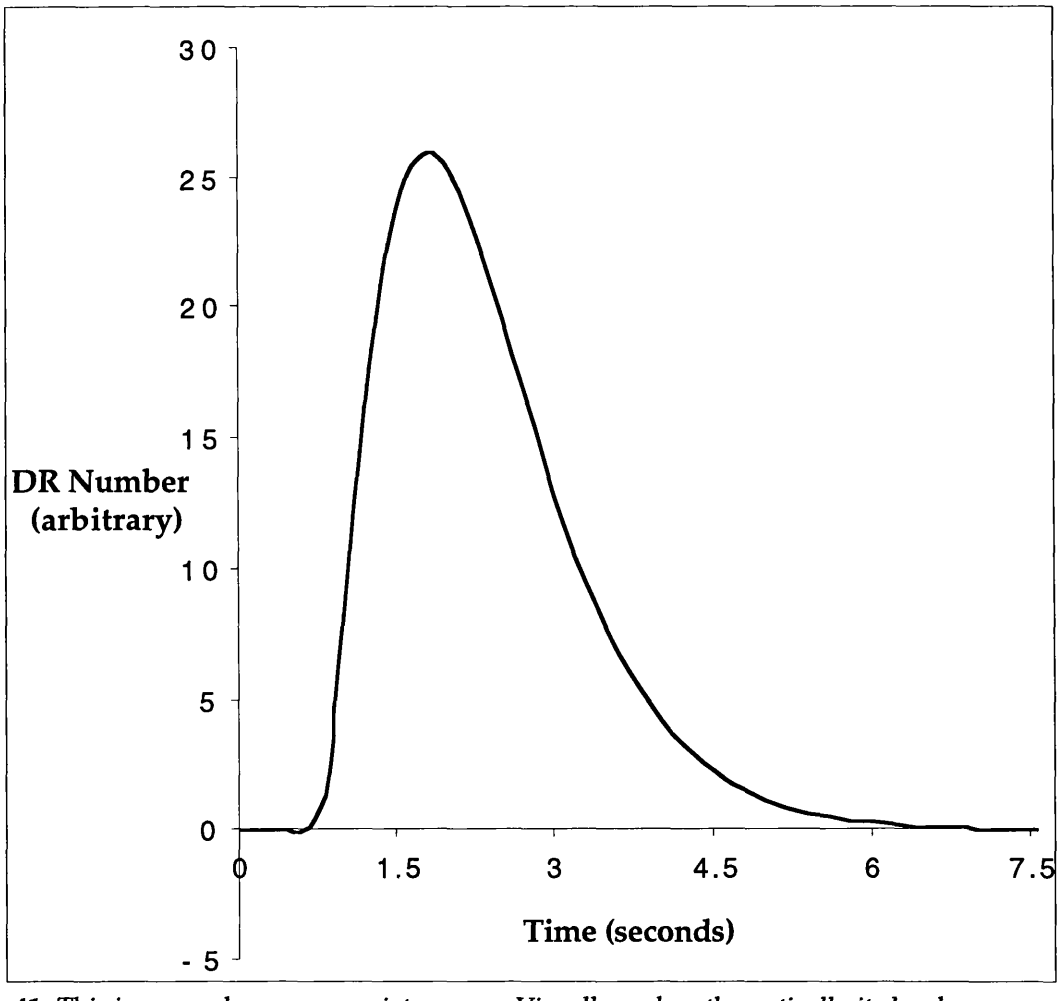

Figure 41 This is a sample gamma variate curve. Visually and mathematically it closely approximates the form of a time-density curve.

This analysis gives a useful, reproducible analytic method for relating timing events to time-density curves obtained at spatially separate points along a vessel. The crucial observation about the gamma variate curve is that it depends on four, and not three, parameters, as is commonly assumed. Mathematically, *ta* is a variable; it is not and should not be treated as a known constant.

6.4.1.2 *Algorithms for Curve Fitting to the Gamma Variate Curve*

The gamma variate curve is non linear. Fortunately it can be linearized by taking logarithms of both sides.

$$Ln(c(t_i)) = Ln(ga) + aa * Ln(t_i - ta) - (t_i - ta)/ba \qquad 6.13$$

This form now lends itself to a straightforward least squares regression that is described in detail in Starmer & Clark (Starmer, C.F. and Clark, D.O. 1970). Review of this paper reveals an unstated assumption which has major ramifications; Starmer & Clark assume that *ta* is known. The linearized least squares method will only work if *ta* is supplied independently, yet under most circumstances there is uncertainty about *ta*. In practice, therefore, any method used to determine the parameters *aa*, *ba* and *ga* must handle provision of *ta* in some objective and defensible fashion. One method that is commonly used in the analysis of Nuclear Medicine data, is to assume that the rising portion of the time density curve is a straight line, and back project this line to its intersection with the time axis, thus giving an estimate of *ta*. If the rising portion of the curve is steep, this method can yield an acceptable estimate for *ta*. However, under most circumstances encountered with video or digital subtraction angiography, the rising portion of the time density curve is not able to be well approximated by a straight line. Thus estimation of *ta* becomes inaccurate as rational decisions about which points to include to determine the best line estimation are subjective. In this thesis an objective technique is described and used.

Equation 6.13 represents the ideal linearized fit of a gamma variate to a set of data points. The criterion used in determining the best fit is that the "sum of the differences on the y axis" squared is a minimum. This minimum value will vary according to different values of *ta* supplied. By a simple iterative technique, the

minimum of the set of possible least squares values is chosen and *ta* established from that equation. This is reproducible, analytic and does not require operator intervention or estimation. A further improvement over the Starmer & Clark algorithm is possible, although computationally it is processor intensive. By using a Simplex method of iterative "down-hill" minima seeking in 5 dimensions, the least squares error can be reduced slightly (Caceci, M.S. and Cacheris, W.P. 1984). Comparison of results from the two approaches, leads to values for t_{max} differing by less than 1%, and this approach has not been used for the data analyses presented here.

6.4.1.3 *Sensitivity to Noisy Data*

Any system of densitometry produces inherently noisy data. DSA is just better than cine film or analogue-video storage, since there are fewer steps between the modulated x-ray beam and the point of analysis. Figures 42 & 44 are pseudo 3-dimensional plots of the images seen in Figure 43 & 45. The image in Figures 42 & 43 is the first image before contrast arrives in the vessel, shown subsequently, in Figure 43. The extent of the noise is obvious. The pattern is random and varies between a DR number of 1 and 3. An image containing contrast is shown from later on in the same sequence in Figure 44. Although the vessel is now outlined, it is clear that some noise is still present: the peak DR numbers are in the order of 20, which translates to a noise level of approximately 10% at peak opacification, and much greater in relation to the DR numbers on the up and down-slopes of the time density curve. To assess how well the gamma variate curve fitting algorithm estimates the true time of flight in the presence of this level of noise, a simple experiment was performed.

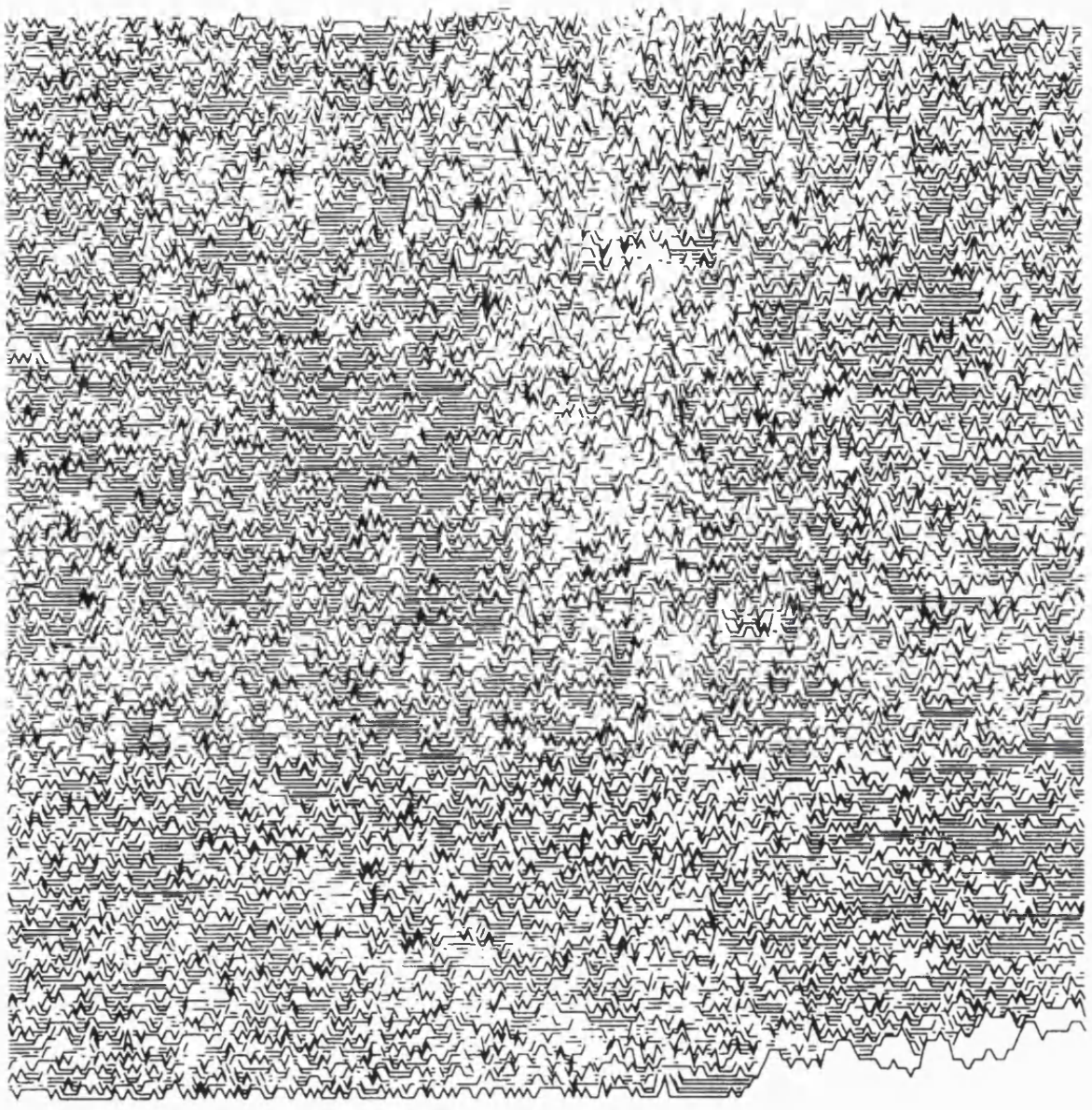

Figure 42 In Figure 43, the DR value in each pixel is represented by an amount of blackness on the film. In order to more easily appreciate subtle differences in DR values between adjacent pixels, the grey scale has been converted into a series of vectors, one for each pixel, extending out of the image plane. Each vector is proportional in length to the DR number of the pixel whose value it represents. In order to see the vectors in a sensible way, a pseudo-3D image is projected at an angle onto the paper and hidden line removal implemented. This yields the projection plot shown. The small peaks represent DR values around 2-3, whilst the flat portions represent a DR value of zero. Notice how noisy the image is. This appreciation of noise does not manifest itself to the same degree when only visual assessment of the image (Figure 43) is undertaken. During mathematical manipulation, however, the noise content is likely to reduce the accuracy of the analysis.

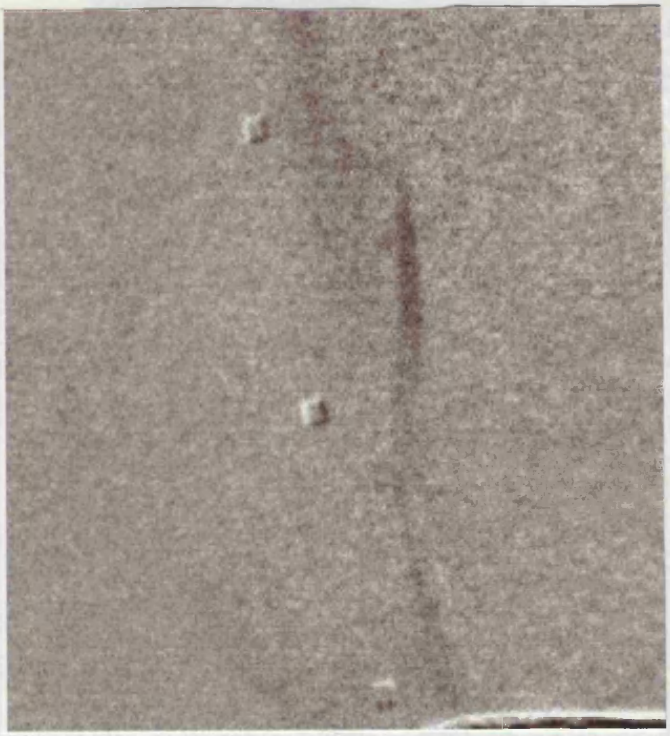

Figure 43. This is a single subtracted frame from a run with inherent background structures removed. Contrast has not yet arrived in the vessel under investigation, a later image from the same series, after contrast has arrived in the vessels is shown in Figure 45 for comparison.

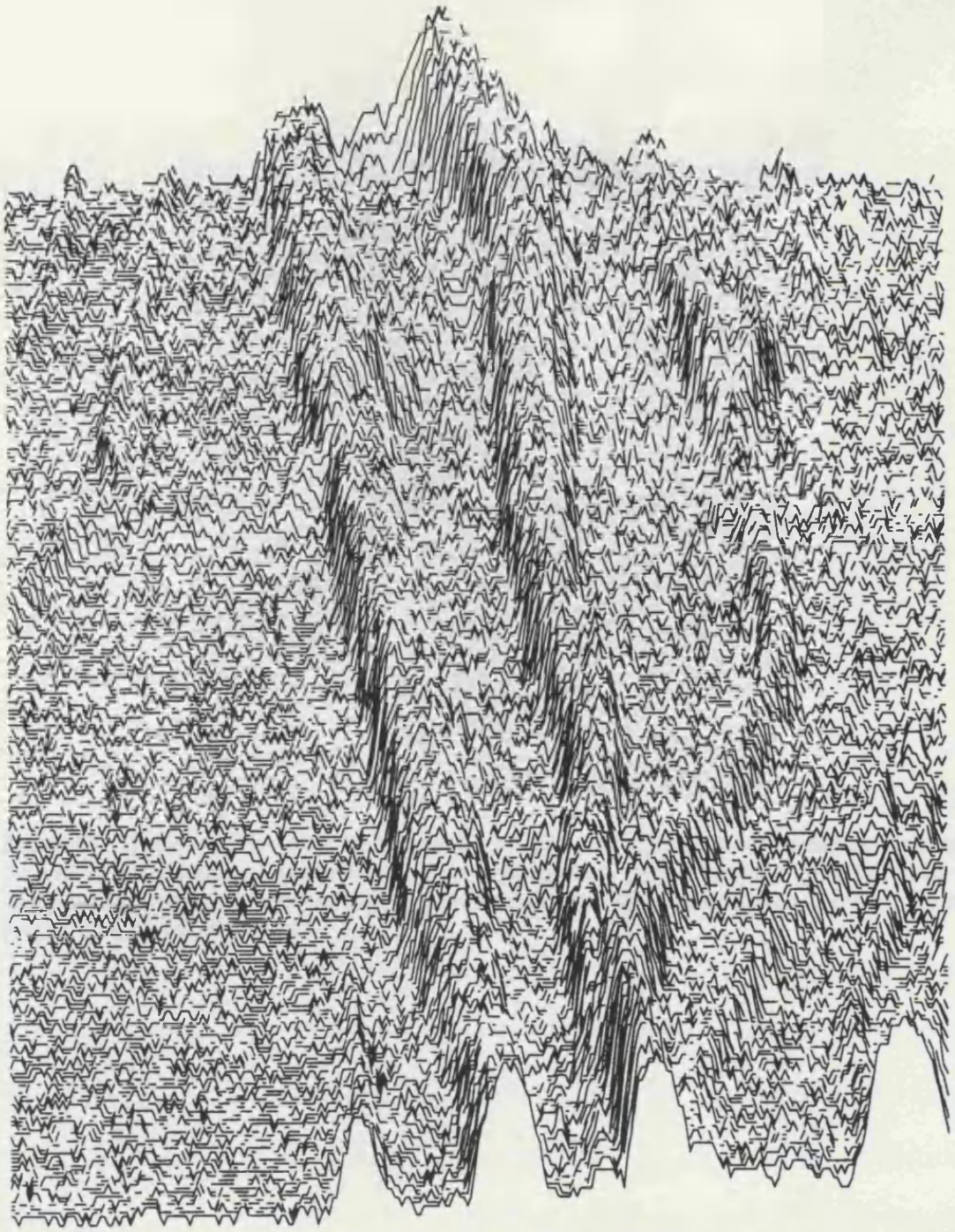

Figure 44. This is a projectional plot of the image in Figure 45. Contrast has now arrived in the vessel under investigation. Notice the considerable impact of noise on the image.

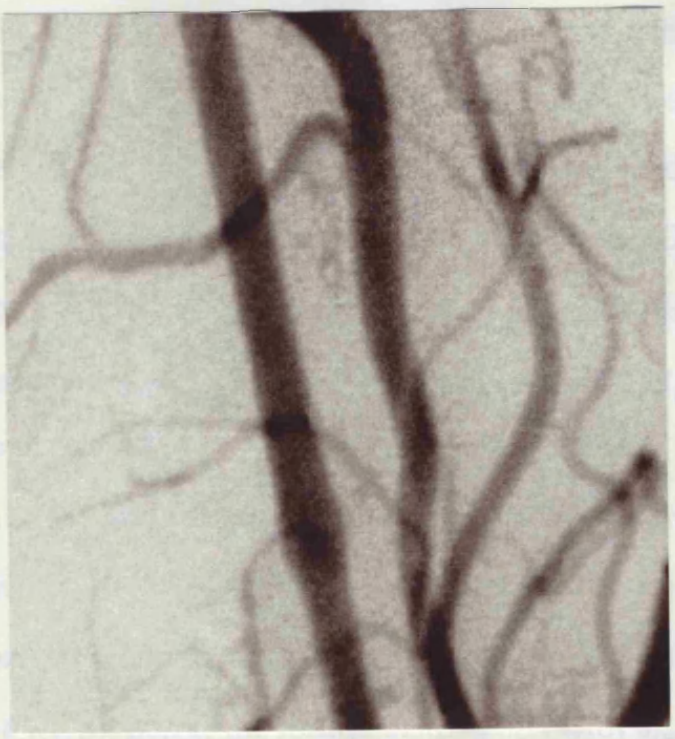

Figure 45. This is the DSA generated frame from a sequence of images where contrast is present in a number of vessels, including the vessel under investigation. Notice how the impact of noise in the image is not particularly evident visually, even though it is quite extensive and obvious from the projectional plot in Figure 44.

Background Theory

In any set, M, of estimated parameters "a" there are uncertainties. During the extraction of parameters there is some true set of values which are unknown to the experimenter; let these be $\underline{a}_{(true)}$. These true parameters are statistically realized along with random measurement errors as a measured data set, $D_{(o)}$ which is known to the experimenter. $D_{(o)}$ is fitted to a postulated model and so a set of parameters is generated $\underline{a}_{(o)}$. Due to noise and other errors $D_{(o)}$ is not a unique realization of $\underline{a}_{(true)}$, rather, it is one of an infinite number of data sets, each of which could have been the one measured. If these are denoted by $D_{(1)}, D_{(2)}, \ldots D_{(i)}, \ldots D_{(\infty)}$, and each one yields a respective parameter set $\underline{a}_{(1)}, \underline{a}_{(2)} \ldots \underline{a}_{(i)}, \ldots \underline{a}_{(\infty)}$, then the sets of $\underline{a}_{(i)}$ occur with some probability distribution in the M – dimensional space of all possible parameter sets $\underline{a}$. The actual measured set $\underline{a}_{(o)}$ is one member drawn from this distribution. Of more use would be knowledge of the difference $\underline{a}_{(i)} - \underline{a}_{(true)}$. This is merely a translation of the former distribution with $\underline{a}_{(true)}$ at the origin. If this distribution were known then all the quantitative uncertainties of the experimental measurement $\underline{a}_{(o)}$ would be known. Whilst it is clearly impossible to know $\underline{a}_{(true)}$, there is a way to estimate the distribution $\underline{a}_{(o)} - \underline{a}_{(true)}$. Although the measured parameter set $\underline{a}_{(o)}$ is not the true one, let us assume that it is not too different and therefore that the shape of probability distribution $\underline{a}_{(i)} - \underline{a}_{(o)}$ is very nearly the same as the shape of the probability distribution $\underline{a}_{(i)} - \underline{a}_{(true)}$. This is not an assumption that $\underline{a}_{(i)}$ equals $\underline{a}_{(true)}$. It is only being assumed that the way in which random errors enter the data and analysis does not vary rapidly as a function of $\underline{a}_{(true)}$, thus $\underline{a}_{(o)}$ can serve as a reasonable surrogate.

Now it is possible to calculate the distribution $\underline{a}_{(i)} - \underline{a}_{(o)}$. Starting with $\underline{a}_{(o)}$, any number of data sets may be simulated. The method is to draw random numbers from an appropriate distribution so as to mimic the measurement errors and noise of the experiment. With such random draws, data sets are constructed with precisely the same number of measured points and precisely the same values of all independent variables as the original $D_{(o)}$ data set. These constructed data sets have

Background Theory

In any set, M, of estimated parameters "a" there are uncertainties. During the extraction of parameters there is some true set of values which are unknown to the experimenter; let these be $\underline{a}_{(true)}$. These true parameters are statistically realized along with random measurement errors as a measured data set, $D_{(o)}$ which is known to the experimenter. $D_{(o)}$ is fitted to a postulated model and so a set of parameters is generated $\underline{a}_{(o)}$. Due to noise and other errors $D_{(o)}$ is not a unique realization of $\underline{a}_{(true)}$, rather, it is one of an infinite number of data sets, each of which could have been the one measured. If these are denoted by $D_{(1)}$, $D_{(2)}$, ... $D_{(i)}$, ... $D_{(\infty)}$, and each one yields a respective parameter set $\underline{a}_{(1)}$, $\underline{a}_{(2)}$ ... $\underline{a}_{(i)}$, ... $\underline{a}_{(\infty)}$, then the sets of $\underline{a}_{(i)}$ occur with some probability distribution in the M – dimensional space of all possible parameter sets $\underline{a}$. The actual measured set $\underline{a}_{(o)}$ is one member drawn from this distribution. Of more use would be knowledge of the difference $\underline{a}_{(i)} - \underline{a}_{(true)}$. This is merely a translation of the former distribution with $\underline{a}_{(true)}$ at the origin. If this distribution were known then all the quantitative uncertainties of the experimental measurement $\underline{a}_{(o)}$ would be known. Whilst it is clearly impossible to know $\underline{a}_{(true)}$, there is a way to estimate the distribution $\underline{a}_{(o)} - \underline{a}_{(true)}$. Although the measured parameter set $\underline{a}_{(o)}$ is not the true one, let us assume that it is not too different and therefore that the shape of probability distribution $\underline{a}_{(i)} - \underline{a}_{(o)}$ is very nearly the same as the shape of the probability distribution $\underline{a}_{(i)} - \underline{a}_{(true)}$. This is not an assumption that $\underline{a}_{(i)}$ equals $\underline{a}_{(true)}$. It is only being assumed that the way in which random errors enter the data and analysis does not vary rapidly as a function of $\underline{a}_{(true)}$, thus $\underline{a}_{(o)}$ can serve as a reasonable surrogate.

Now it is possible to calculate the distribution $\underline{a}_{(i)} - \underline{a}_{(o)}$. Starting with $\underline{a}_{(o)}$, any number of data sets may be simulated. The method is to draw random numbers from an appropriate distribution so as to mimic the measurement errors and noise of the experiment. With such random draws, data sets are constructed with precisely the same number of measured points and precisely the same values of all independent variables as the original $D_{(o)}$ data set. These constructed data sets have

Table 16

Time of flight between the perfect curves 6.14 & 6.15 modulated by varying degrees of noise, using the gamma variate curve fitting method for measurement (correct time = 0.183 secs).

Noise (DR No.)	Time of Flight (seconds)	± SD
0.00	0.189	0.000
0.25	0.188	0.014
0.50	0.187	0.026
1.00	0.188	0.054
1.50	0.191	0.081
2.00	0.196	0.118
2.50	0.204	0.156
3.00	0.250	0.445

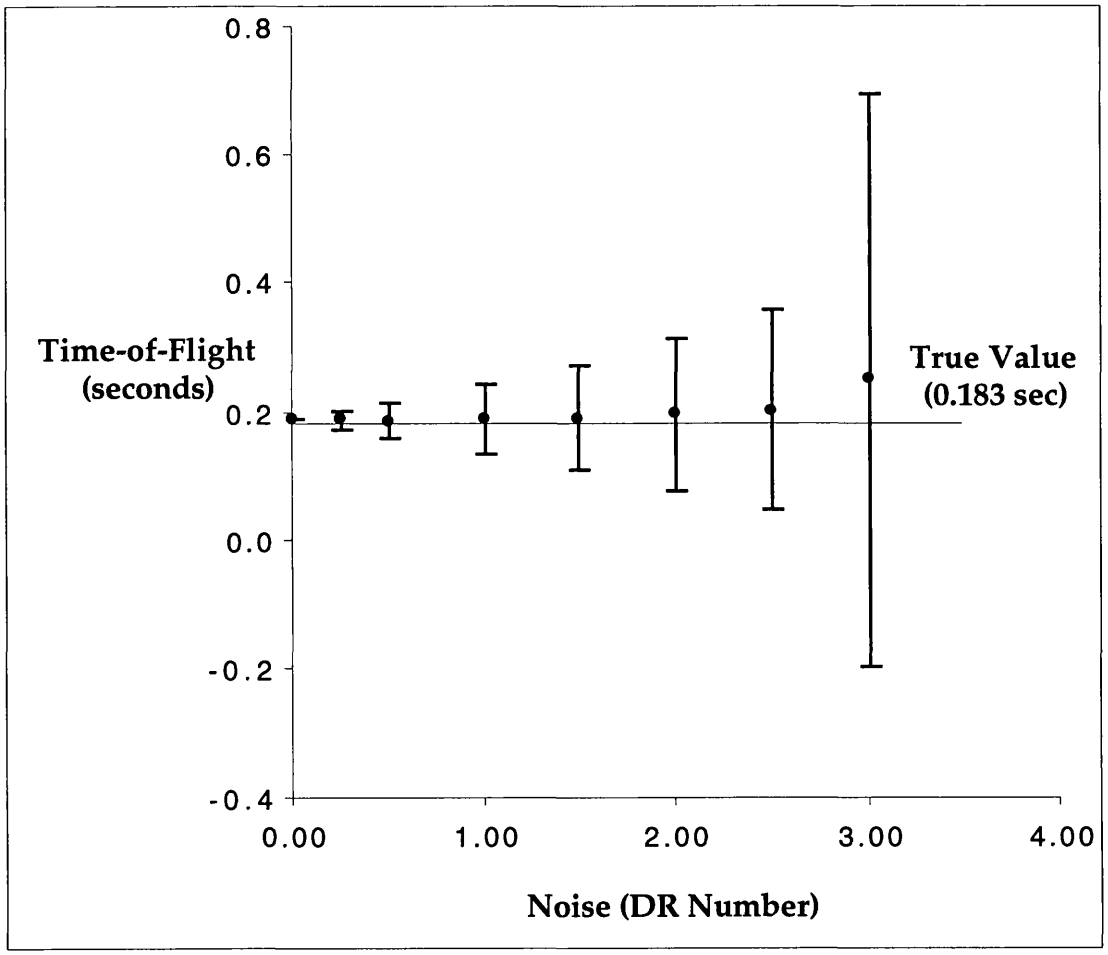

Figure 46. This is a plot of the mean values and standard deviations of a series of calculated times of flight as a function of noise content. The algorithm used to calculate the time of flight is based on gamma variate curve fitting and extraction of parameters from the calculated curves. Notice how estimation of true time of flight becomes successively worse with increasing noise. These data were acquired using Monte-Carlo techniques. The data values are listed in table 16.

That the gamma variate curve to estimate time displacement was suboptimal was recognized by Bursch, who suggested a forward triangle method of determining a fixed point on the data set. He argued that the upslope of the curve was less sensitive to noise and so he used the time to 1/2 maximum opacification as his reference. No curve fitting was necessary for this approach. With this method, the Monte-Carlo experiment yields the results in table 17, and Figure 47. The method is less sensitive to noise and it yields values closer to the true value of 0.1829 seconds but, at a typical level of noise of DR 1.5, the lower and upper 95% confidence limits are 0.05 - 0.31 respectively.

6.4.1.4 *Power Spectrum*

The gamma variate curve used for the Monte-Carlo experiment has been sampled at 2.5 frames per second equivalent. When the Fourier transform of this curve is taken and the power spectrum calculated, there is no significant component of frequencies beyond the 3rd harmonic. This compares favourably with the Fourier transform of real data where there is also little contribution beyond the 2nd harmonic. These data are shown in tables 18 and 19 and Figure 48. On this basis, the gamma variate curve is adequate for modelling contrast time density curves. The limiting factor in its usefulness is the difficulty in determining which gamma variate curve actually achieves the true fit to the experimental data.

Table 17

Time of flight between the perfect curves 6.14 & 6.15 modulated by varying degrees of noise, using the forward triangle method of Bursch for measurement (correct time = 0.183 secs).

Noise (DR No.)	Time of Flight (seconds)	± SD
0.00	0.179	0.000
0.25	0.182	0.011
0.50	0.181	0.021
1.00	0.181	0.042
1.50	0.183	0.065
2.00	0.185	0.085
2.50	0.184	0.105
3.00	0.182	0.129

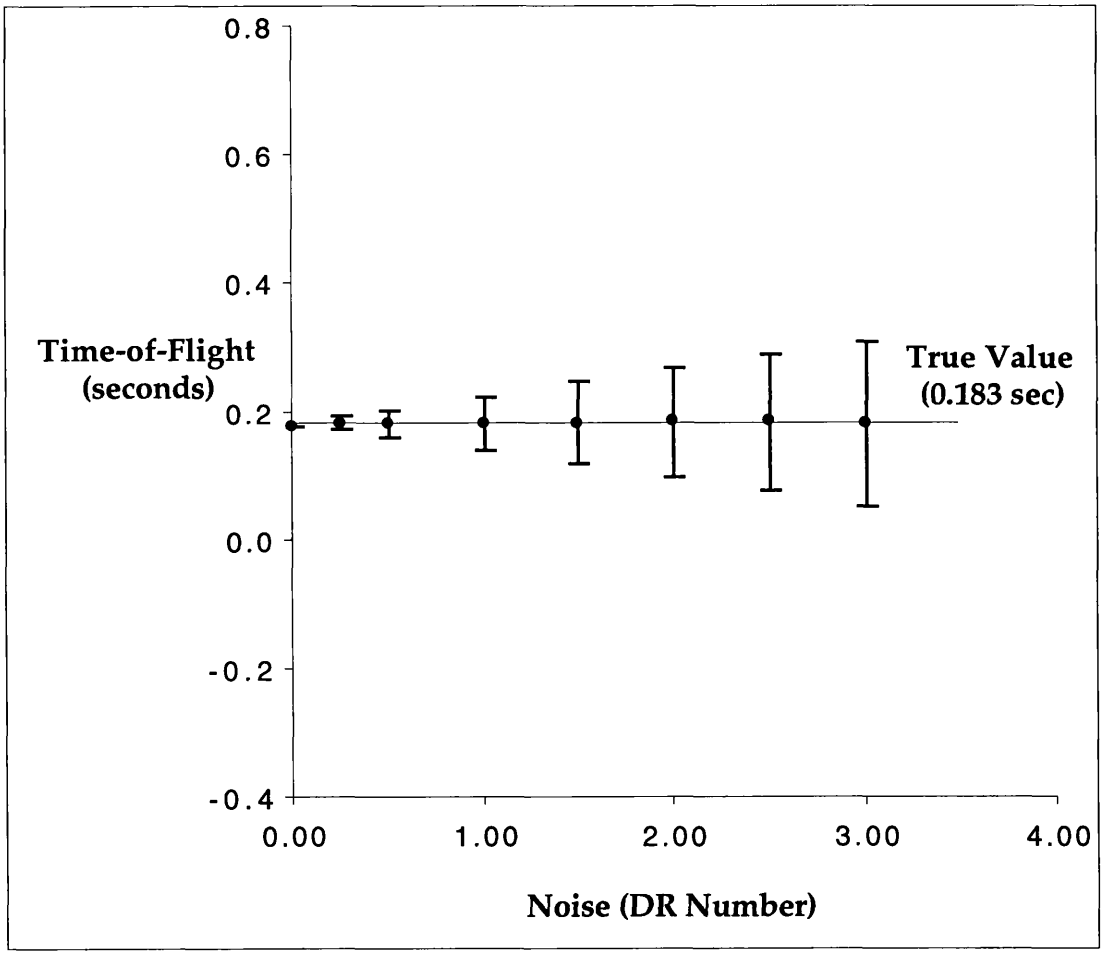

Figure 47. This is a plot of the mean values and standard deviations of a series of calculated times of flight as a function of noise content. The algorithm used to calculate the time of flight is based on the forward triangle method of Bursch. The results are less influenced by noise content when compared with the gamma variate method. These data were acquired using Monte-Carlo techniques. The data values are listed in table 17.

Table 18

Original data with the discrete Fourier transform and the equivalent power spectrum.

Original Time-Density Curve	Fourier Transform		Power Spectrum
	Real	Imaginary	
0.00	13.28	0.00	176.36
0.00	-16.13	-5.83	294.17
0.13	1.51	5.92	37.33
5.84	0.86	-2.10	5.15
16.00	0.38	-0.23	0.20
27.63	0.61	-0.04	0.37
36.76	-0.04	0.23	0.05
37.39	-0.25	0.24	0.12
29.85			
20.92			
13.87			
9.77			
7.98			
6.31			
0.00			
0.00			

Table 19

Gamma variate fit of data in Table 18 with Fourier transform and equivalent power spectrum.

Gamma Variate Density Curve	Fourier Transform		Power Spectrum
	Real	Imaginary	
0.00	13.50	0.00	182.25
0.00	-16.28	-5.53	295.62
0.21	1.95	5.52	34.27
4.63	1.45	-0.73	2.64
16.35	-0.02	-0.49	0.27
29.04	-0.24	-0.04	0.06
35.95	-0.12	0.06	0.02
35.59	-0.06	0.04	0.01
30.27			
23.06			
16.16			
10.61			
6.61			
3.94			
2.26			
1.27			

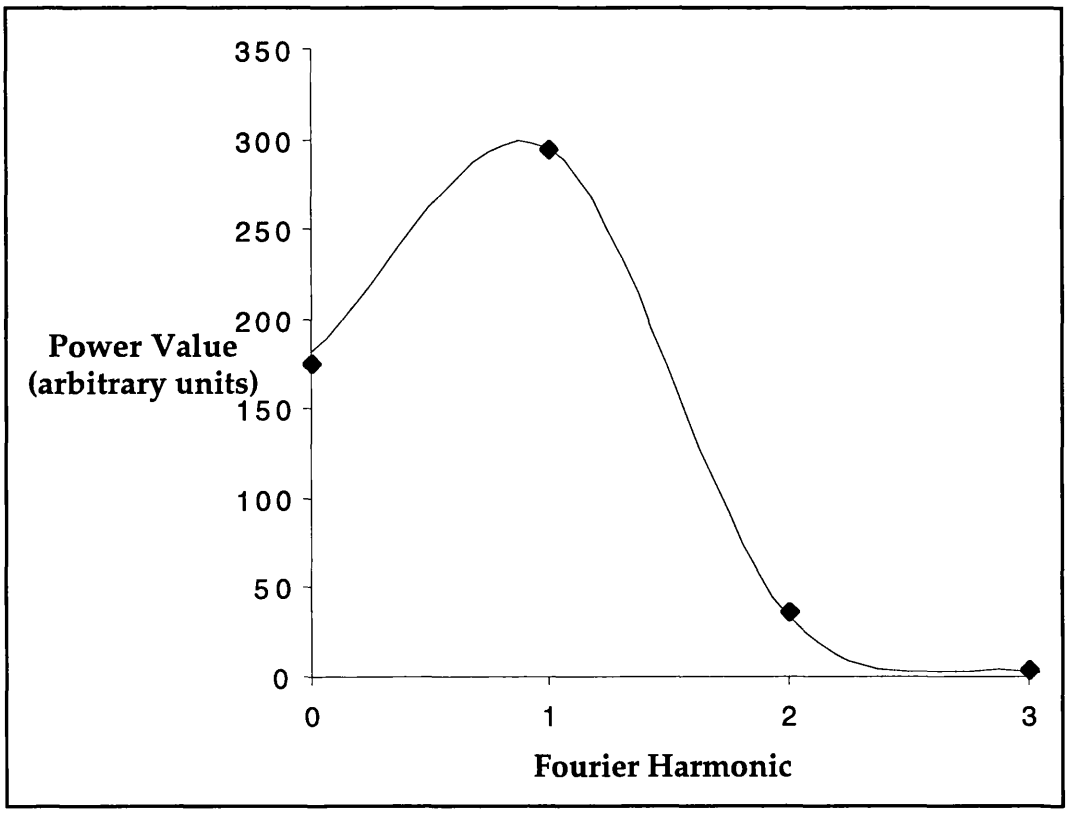

Figure 48. These are the power spectrum curves obtained by Fourier analysis of a real time-density curve and its gamma variate fit. tables 18 and 19 contain the data which are plotted in this graph. Because the power spectrum of the original and its gamma variate fit are very closely matched, the original values are plotted as diamonds and the fitted curve's power spectrum as a solid line. There is no statistically significant difference between the two curves ($p > 0.86$). Less than 1% of the power contribution comes from harmonics above the second, and thus may be ignored.

6.4.2 Vessel cross sectional area estimation

Assessment of volume by geometric methods relies on edge detection of the vessel boundaries; while different methods have been proposed (Kruger, R.A. 1981), a theoretical approach has been adopted here.

6.4.2.1 *Nature of a perfect vessel*

A common assumption is that a blood vessel, specifically an artery, is circular in cross section. This is intuitively obvious and is valid for non-diseased lengths of vessel, down to a size of approximately 1-2 mm. In a noise-free situation, filling a cylinder with an homogenous solution of contrast material and imaging it will yield a transverse density profile, illustrated by Figure 49. This assumes that the vessel itself lies along the lines of pixels making up the matrix. Unfortunately, this is a rare occurrence; generally the vessel will be aligned at an angle to the pixel matrix resulting in distortion of the projection and an elliptical profile to the vessel. The configuration of the ellipse will vary according to the angle between the matrix and the vessel, and also according to the size of the vessel. It is desirable to determine the edge of the vessel. This can be performed in three stages.

1) From a single image, the angle of the vessel with respect to the matrix may be calculated by the least squares method, it will be shown that this is not sensitive to exact knowledge of the boundary.
2) Curve fitting an ellipse to the projected density or DR values along a line of pixels most nearly orthogonal to the long axis of the vessel.
3) Multiplying the fitted ellipse diameter by $\text{Cos}(\theta)$ where θ is the angle between the vessel and the matrix, a corrected diameter may be arrived at.

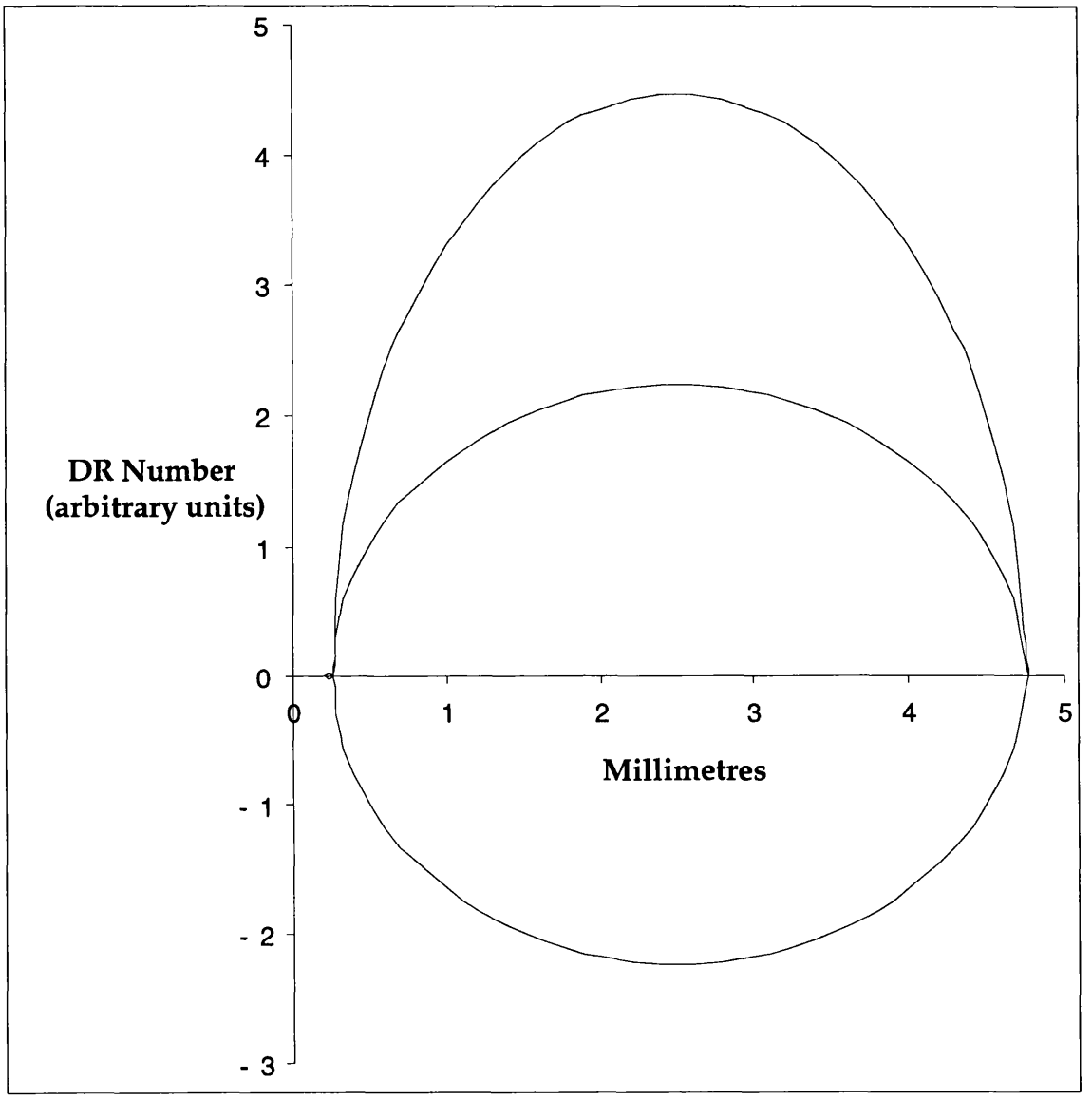

Figure 49. The cross section of a circular vessel becomes elliptic in profile when that vessel is imaged obliquely. The density profile (upper curve) which is generated from such an ellipse (lower curve) is the reflection of the number of molecules of iodine in the path of the beam of x-rays. The generated curve is itself a hemi-ellipse and is the fundamental datum upon which curve fitting is performed, yielding edge and diameter estimations.

6.4.2.2 *Algorithm for edge detection*

Figure 50 is a sample of the DR numbers taken from an artery. The high numbers represent contrast in the lumen. Clearly it is difficult to establish the precise value representing the edge; however, a least squares fit of a straight line through the eights, the nines or the tens gives an angle of inclination of the vessel of 77.6°± 0.21° with respect to the matrix orientation. Indeed, including all of these pixels gives an identical result. There is little problem in determining the vessel inclination with a high degree of confidence; this is the angle θ referred to above.

Table 20 gives the values of the DR numbers from successive frames along a line of pixels across a vessel during the passage of contrast. The first step in fitting an ellipse is to make the assumption that only pixels which exhibit a sinusoidal change in DR number can possibly be within the vessel lumen. This assumption allows the vessel edge to be localized to within 3 or 4 pixels. By plotting the transverse density profile across the vessel, including pixels which are definitely outside the vessel at each end of the profile, and identifying the region of the edges, the following algorithm may be applied.

The general equation of an ellipse is:

$$1 = \{(x - x_o)^2 / a^2\} + \{(y - y_o)^2 / b^2\} \qquad 6.16$$

where a & b are the major and minor axes respectively.

Thus a represents half the diameter of the elliptic section of the vessel centered at x_0, b is the depth of the elliptic section and y_0 is constrained to be zero. In this equation there are thus three unknowns: a Simplex method in 4 dimensions is used to find the least squares fit between the data set and an ellipse that represents the profile of the vessel in this particular projection (Nelder, J.A. and Mead, R. 1965). An example of a single set of data and the fitted ellipse is shown in Figure 51; the data are taken from table 20 Frame 7.

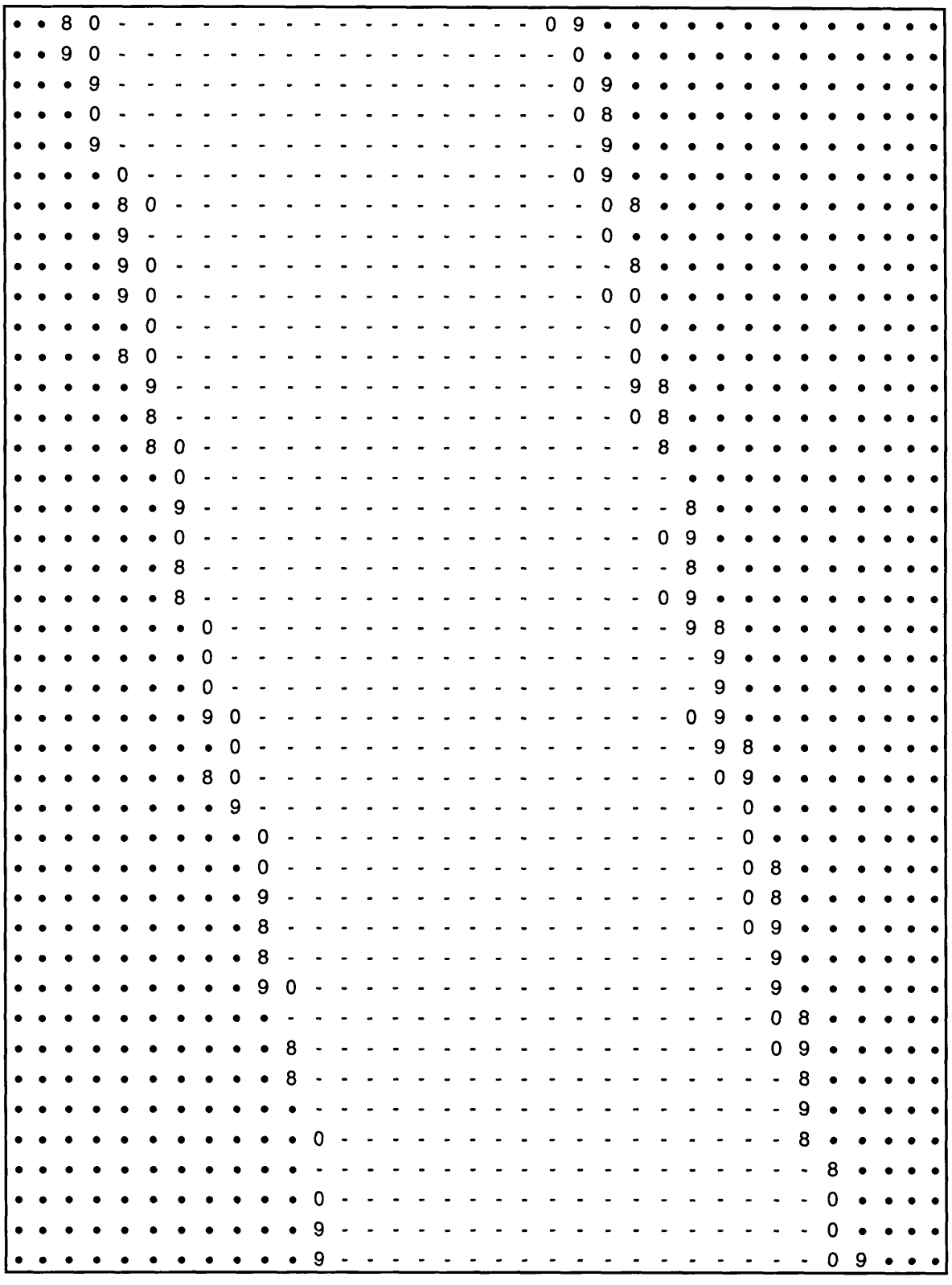

Figure 50. This is a section of vessel under investigation taken from one of the data sets. The digital data from the peak opacification frame is shown. The DR numbers have been converted to symbols: values less than 8 have been replaced by a period, values 8 and 9 are unchanged and 10 has been depicted by 0. Values above 10 have been depicted by a dash. Vessel orientation becomes obvious, with the lumen represented by dashes and the region of the edges, but not necessarily the edges themselves depicted by the numerals. The angulation of this vessel is 77.6° ± 0.21°.

Table 20

Each row represents the density values of pixels in the region of a vessel, such that the margins of the vessel are within the row. Each column represents the DR value of the same pixel in successive frames. As contrast arrives in the vessel so the DR numbers increase and then decrease as the contrast material flows on. By virtue of diffuse tissue perfusion over- and underlying the vessel, there is a small monotonic rise in the DR numbers superimposed on the whole data set. This can be readily appreciated by comparing the average values of pixel DR numbers in frame 1 (0.27) with those in frame 14 (4.92). Only those pixels exhibiting a sinusoidal change over and above this monotonic variation can possibly lie within the vessel. This assumption is the starting point for vessel edge detection.

Fra	DR Numbers																									
1	1	0	0	0	0	0	1	0	0	0	0	0	1	1	0	0	0	0	0	0	0	0	2	1	0	0
2	1	0	0	0	0	0	1	1	0	0	0	0	1	0	0	1	1	0	1	1	0	0	1	0	0	0
3	1	1	1	1	1	2	3	3	2	2	2	2	3	3	2	3	2	1	1	2	2	1	2	1	1	1
4	1	0	1	3	3	5	6	5	4	4	4	5	7	6	6	6	6	4	5	4	3	3	3	2	2	1
5	3	3	4	6	7	9	11	11	9	10	10	11	12	12	10	12	11	9	9	10	8	7	7	5	4	3
6	4	4	7	9	11	13	14	15	13	15	14	15	15	14	15	15	14	13	14	13	12	9	10	6	5	4
7	5	6	8	11	14	16	18	18	16	17	16	17	17	17	16	16	16	16	16	15	14	12	10	8	6	5
8	6	7	9	10	12	14	15	15	14	13	13	13	14	13	13	13	13	12	13	13	12	10	9	6	5	5
9	4	5	7	8	9	11	11	10	9	10	9	10	10	9	10	9	10	10	10	11	9	7	7	5	4	3
10	5	5	6	7	8	8	9	9	7	7	6	7	8	7	7	7	7	7	9	9	6	5	6	4	3	3
11	4	3	5	5	7	7	8	8	6	6	5	6	7	8	6	7	7	8	9	8	7	5	5	4	4	4
12	5	4	5	5	6	7	7	7	6	6	4	5	6	6	5	6	6	7	8	7	7	5	6	5	4	4
13	6	4	6	6	5	6	6	6	4	4	4	5	6	6	6	6	6	5	7	7	5	5	6	5	5	5
14	4	3	4	4	5	5	5	5	4	4	4	5	6	6	5	5	5	5	7	7	6	5	5	6	4	4

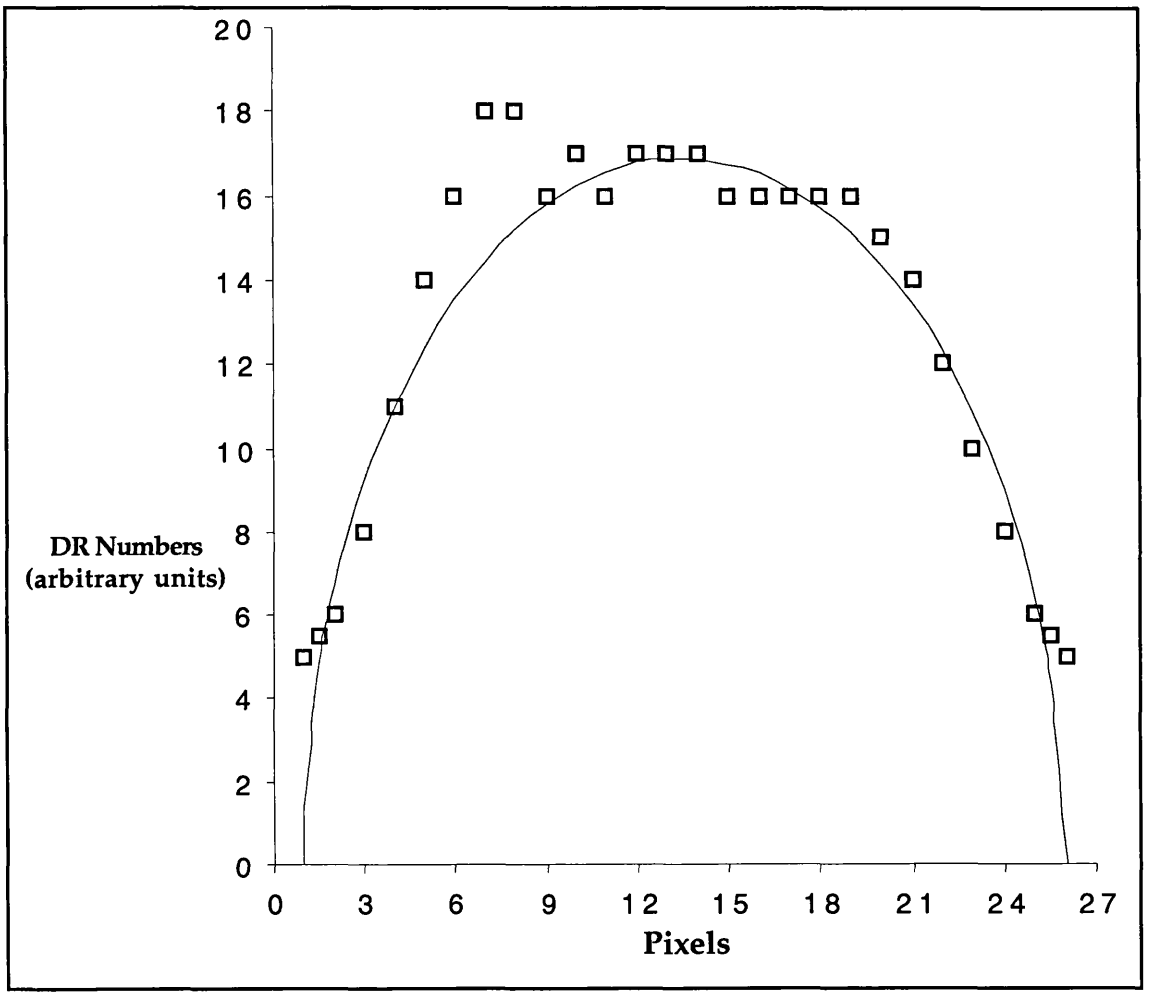

Figure 51. This is a plot of the ellipse (solid line) fitted to the data from frame 7 in table 20 (open squares). The results are displayed in terms of pixels. A least squares method in four dimensions was used taking into account data across the whole field of view. This reduces the impact of local inhomogeneities and allows a reproducible measurement of the vessel diameter to be achieved.

6.4.2.3 *Sensitivity to Noisy Data*

In an ideal situation, data is noise free; this is clearly not the case in reality. Any method of edge detection must be tested for its performance under conditions of varying signal-to-noise ratios. In order to do this a Monte-Carlo experiment was performed on the ellipse fitting method in a similar manner to that used for the gamma variate curve fitting. Points on a perfect ellipse with a major axis of 9 pixels were created mathematically. The simplex curve fitting technique was then implemented with varying amounts of noise added randomly to these perfect ellipse data points. Noise levels up to typical variations in real data (± 2DR numbers) were investigated. The 95% confidence limits on the major axis are seen in to be ± 0.4 pixels, or almost 1 pixel on the diameter. This is a plausible result and allows an estimate of the final error in the vessel diameter, and hence its volume, to be realistically assessed. The results are displayed in table 21.

Table 21

Data points from a perfect vessel with a major axis of 9 pixels and therefore a diameter of 18 pixels were created mathematically. The simplex curve fitting technique was used to estimate the ellipse from which these data originated in a Monte-Carlo experiment. At zero noise levels the technique produces values which are exact. As noise increases, the standard deviation rises. At typical noise levels experienced in real data (2-3 DR numbers) the error on the calculation of the diameter is close to one pixel.

Noise Level (DR Number)	Calculated Diameter Pixels ± 2SD
0.00	18.00 ± 0.00
0.25	17.88 ± 0.10
0.50	17.78 ± 0.18
1.00	17.60 ± 0.36
1.50	17.40 ± 0.52
2.00	17.20 ± 0.80

In summary for this section, a robust method has been presented which enables the edges of the vessel to be identified within 1 pixel, but which tends to under estimate the true edge position by approximately 3%, in the presence of degrees of noise typically encountered in real DSA images.

6.4.3 Time of flight methods

6.4.3.1 *In the time domain*

Time of flight methods of densitometric flow measurement are based on the determination of mean transit time of a contrast bolus between two observation points along a blood vessel, separated by a known or easily measured distance. In order to evaluate the mean time, a contrast density-time curve is obtained and the transit time is defined as the time difference between reference points on both curves, such as the times at which the curves reach their maximum value. This approach has been used by at least one group. However, their results show a consistent 20% overestimation of the mean flow (calculated in an ideal phantom) and insufficient information to reproduce the data (Schmiel, F.K., Huber, H., et al., 1978). Other workers, principally Bursch, have modified the reference point on the time density curve to be half the peak value taken on the upslope, and claim improved accuracy (Bursch, J.H., Hahne, H.J., et al., 1981). Another reference point commonly used is the time of occurrence of the centre of gravity of the curve treated as a solid lamina. Each point on the time density curve has contributions from two principle factors - 1) the mass of iodine in the voxel of which the acquisition pixel forms the face, and 2) noise. The absolute determination of an instantaneous iodine mass which is not stationary, is not possible with pulsed measurement techniques and may lead to an inaccurate estimate of the area under the time-density curve.

Consider a tube and flowing within it is a solution of iodine contrast of fixed and homogeneous density. Consider a means of obtaining an independent reading of the number of iodine molecules within a tiny volume element of that tube. The thickness of iodine alone will determine the number which is to represent the amount of iodine in the beam path. For the purposes of the present discussion, let it be assumed that the measurement device is perfect and gives a noise-free result. If it is switched on for one second it will yield a value I(1). If it is switched on for 10 seconds it will yield a value I(10) which is equal to I(1) - since the contrast is homogenous and of fixed density. There is a difference however, which is hidden to casual acceptance of the above statement. In generating I(10), 10 times as much contrast mass has actually passed the detecting system. The closer the duration of the interrogating measurement is to zero, the nearer to the true value does I(t) approximate, and at the limit when t = 0 - ie. an instantaneous answer, then I(0) is

just the mass of iodine in the beam path divided by the beam's cross sectional area. In our perfect experiment I(0) = I(1) = I(10) = I(∞). If a continuous series of instantaneous measurements were made then integrating over -∞ to +∞ would yield the total mass of iodine which had flowed past during that time. In the real world our measurements are discrete and not instantaneous. The longer the actual moment of measurement the greater the underestimate of total iodine mass based on I(t). In order to correct for this, the velocity of the flowing contrast must be known. Thus the longer is the measuring time in comparison to the mean velocity, the more the measurement will underestimate the true mass of iodine attributed to the value I(t). If the flowing contrast has a variable density - such as the passage of a bolus - then, depending on the pulse width of x-rays producing the Digital Radiography (DR) number, so the total mass of iodine will be underestimated to a lesser or greater extent. It should be noted that this is in addition to the effects of streaming or pooling or pulsatile flow described by Bursch (Bursch, J.H., Hahne, H.J., et al., 1981).

Whichever method is used to establish fixed reference points on the density curves of different regions, a known distance apart, the time between them is a simple calculation, essentially dependent on a direct measurement from the time density curve.

6.4.3.2 *In the frequency domain.*

The time-density curve in the frequency domain is an expression of a mathematical transformation, where, instead of looking at the intensity of the iodine signal, the amplitude of various spectral components of the signal is studied.

6.4.3.2.1 The Fourier transform.

The term "signal" is usually understood to mean a pattern of some kind which is used to convey a message or part of a message. In the present case the DR values obtained from a single region, which when plotted as a function of time give the time-density curve, are part of a signal. A signal waveform is a graphical statement of the way in which (in our case) iodine thickness varies with time. For many purposes, however, it is more helpful to regard the signal as though it were the result of adding together a number of simpler component waveforms. A convenient

method of doing this is the technique of Fourier series expansion, in which the waveform components are sine or cosine waves with varying frequency, amplitude and phase. A display of the amplitudes and phases of the individual sinusoids along the frequency axis, ie. the spectrum of the signal, provides an alternative but just as complete description of the signal in the frequency domain. In this domain however, it is not intuitively recognisable as a time density curve.

In the original time domain we have:
h(t) = the values of the time-density curve at times t.

In the frequency domain we have:
H(f) = the values of amplitude and phase of the component waveforms of h(t) as a function of frequency f.

Clearly these are related. This relationship is the Fourier transform and is defined by:

$$h(t) = \int_{-\infty}^{+\infty} H(f) e^{-2\pi i f t} df \qquad 6.18$$

and $$H(F) = \int_{-\infty}^{+\infty} h(t) e^{2\pi i f t} dt \qquad 6.19$$

If t is in seconds then f is in cycles per second or Hertz. This pair of relationships is valid absolutely only for a continuous signal defined from -∞ to +∞ (in either time or frequency). In the most common situations the function $h(t)$ is sampled in some way at evenly spaced intervals of time. Let Δ denote the time interval between consecutive samples, then the sequence of sampled values may be defined as:

$$h_n = h(n\Delta) \qquad 6.20$$

Where n = -∞.....-3,-2,-1,0,1,2,3,.....+∞

The reciprocal of Δ is the sampling rate, which in the case of DSA is merely the framing rate. For any sampling interval Δ, there is also a special frequency, called the Nyquist critical frequency, given by:

$$fc = 1/2\Delta \qquad 6.21$$

If a sine wave of the Nyquist critical frequency is sampled at its positive peak value then the next sample will be at its negative trough value, the sample after that at its positive peak and so on. In other words critical sampling of a sine wave is two sample points per cycle.

The Nyquist frequency is important for two reasons; if a continuous function, $h(t)$, sampled at an interval of Δ, happens to be band-width limited to frequencies smaller than fc, ie if $H(f)$ = zero for all $|f| > fc$, then the function $h(t)$ is completely determined by its discrete samples h_n. In fact $h(t)$ can be extracted absolutely by the formula:

$$h(t) = \Delta \sum_{n=-\infty}^{+\infty} h_n * [\mathrm{Sin}\, 2\pi fc(t - n\Delta)]/(\pi t - n\Delta) \qquad 6.22$$

This is the mathematical expression of the sampling theorem. In the case of DSA or cine angiography this theorem states that the entire information content of the signal can be recorded by sampling it at a rate $(1/\Delta)$ equal to twice the highest frequency containing any information. However, if the signal is not sampled at or faster than the Nyquist limit, then the information contained in those frequencies above the Nyquist limit is not discarded, but folded into the lower frequencies, distorting the spectrum. This is termed aliasing.

Equations 6.18 and 6.19 are only valid for continuous data. They can be estimated, however, by performing a discrete Fourier transform on the sampled data. Assuming that the signal is described by N sampled values then:

$$h_k \equiv h(t_k)$$

where $t_k = k\Delta$, $k = 0,1,2, \ldots N - 1$ and Δ is the sampling interval.

Let N be an even number. With N data values, only N independent frequencies can be investigated. Therefore, the transform $H(f)$ is only valid at values of f from $-fc$ to $+fc$ and in general:

$$fn = n/N\Delta \text{ and } n = -N/2 \ldots\ldots 0, \ldots\ldots +N/2 \qquad 6.23$$

The extreme values of n in 6.23 correspond exactly to the lower and upper limits of the Nyquist critical frequency range. Approximating the integrals in 6.18 and 6.19 by sums yields:

$$H(f_n) = \Delta \sum_{k=0}^{N-1} h_k * e^{2\pi i k_n / N} \qquad 6.24$$

This is the discrete Fourier transform which maps h_k into H_n.

Now if a Fourier transform is performed on the data of a time density curve a series of complex numbers are obtained. An example of the original data set and its transform is shown in table 18. In 6.24 there is a term $e^{-2\pi i k_n/N}$ where $i = \sqrt{(-1)}$. This is one form of the representation of the circular functions $Cos(\theta)$ and $Sin(\theta)$. My initial statement introducing Fourier methods referred to the representation of a signal by the sum of a series of circular functions. Taking 6.24 and expressing the exponent as circular functions the original signal may be expressed as:

$$h(k_t) = A_0 + (1/N) * \sum_{n=0}^{N-1} X_n * \cos\{(n2\pi k/N) - \phi_n\} \qquad 6.25$$

where $X_n = \sqrt{(A_n^2 + B_n^2)}$ and $\phi_n = tan^{-1}(B_n/A_n)$

X_n = total amplitude,

A_n = amplitude of real component,

B_n = amplitude of imaginary component and

ϕ_n = phase.

The application of the Fourier transform to determine time-of-flight between time-density curves observed at different spatial locations along a blood vessel is valid if certain assumptions are made. These are :

1) That the system is time-invariant and behaves in a linear manner. That is, the mean flow value measured does not depend on when it is measured, and that the flow of blood past the proximal observation point "the input", is the same as the flow of blood past the distal observation point "the output" (Oppenheim, A.V., Willsky, A.S., et al., 1997). In other words, a doubling of flow within the vessel, for a fixed vessel size, will result in a halving of the time-of-flight between the two observation points. This requires that between

the proximal and distal measurement points there are no branches, and that the vessel diameter does not change.

2) That the difference in phase of the first harmonics of the Fourier transforms of the distal and proximal curves is due to a time shift alone.

Assumption 1 can be fulfilled by appropriate choice of measuring locations along a vessel. In the experimental work described in detail in chapter 7, a segment of vessel was chosen such that there were no branches between the proximal and distal measurement locations. The apparent diameter of the vessel between the proximal and distal measurement locations may vary, but remains within the limits of uncertainty imposed by noise in the image (± 1 pixel), and is therefore taken to be unchanging.

Assumption 2 is more difficult to fulfill. In a perfect situation, with assumption 1 completely fulfilled, and no observational uncertainty, the time-density curve observed at the proximal location would not change shape when observed at the distal location. However, in the real world, the distal time-density curve is a partially energy dissipated approximation to the proximal curve. This results in partial re-distribution of the information contained in the harmonics of the proximal curve into higher order harmonics in the distal curve. This dispersion is a complex process, and depends on a number of factors such as friction, viscosity, pulsatility of the vessel and noise introduced into the acquisition and observation system. Thus, the vessel under observation, considered as a system, is not truly linear, but it is time-invariant. However, for short segments of vessel fulfilling assumption 1, the departure from linearity is negligible and manifests itself as measurable differences in the amplitudes of the Fourier coefficients, these differences can be exploited to provide a measure of the error inherent in the actual observation made.

Consider the proximal time-density curve as the reference curve. In terms of its Fourier coefficients the A_0 values represent the mean non-oscillating component of the signal and A_1 and B_1 are the coefficients of the real and complex parts of the first harmonic contributing to the total signal. The first harmonic has a period of exactly the interval over which the Fourier transform is calculated. It is a single cosine wave with an amplitude $(\sqrt{A_1^2 + B_1^2})$ and a phase shift $Tan^{-1}(B_1/A_1)$ in relation to zero time. Fourier analysis of the distal curve yields a similar, but not identical set of

coefficients. The magnitude of the phase difference between the first harmonics of the two curves is due to the time difference between the principal component of the time-density curves ± the phase shift introduced as a result of dispersion of information from the first to higher harmonics. Visual examination of the two curves confirms that they are similar but not the same. Examination of the Fourier coefficients of the first harmonics of both curves also shows that the amplitudes of the first harmonics are similar but not identical. The difference in amplitudes can be used to calculate error limits on the phase difference for each individual pair of curves.

Let r_1 and r_2 be the amplitudes of the first harmonics of the proximal and distal curves respectively. The uncertainty in the phase (θ) of the first harmonic of the distal curve, resulting from a change in its amplitude with respect to the amplitude of the first harmonic of the proximal (reference) curve, can be given by:

$$Tan(\theta) = |r_2 - r_1| / (r_2 + r_1) \qquad 6.26$$

Figure 52 is the Argand diagram of an arbitrary pair of coefficients of the first harmonics of a time-density curve where θ, r_1 and r_2 are as defined above. Straightforward trigonometry yields equation 6.26.

Thus the observed phase difference is due to the phase difference resulting from the time of flight ± an error term determined by the degree of dispersion of the second curve, with respect to the first or reference curve, by the time it reaches the distal observation point. Normalizing the phase difference to 2π radians over $N\Delta$ points allows a true time-of-flight (with appropriate error handling) to be calculated between the two regions of interest from which the curves were generated. This is a novel method of measuring time-of-flight and does not depend on absolute iodine mass, rising slopes of time density curves or other reference points on the curves. Time information is inversely related to frequency and as such it is a logical extension to transform the data into frequency space in a formal analytical fashion in order to extract timing information.

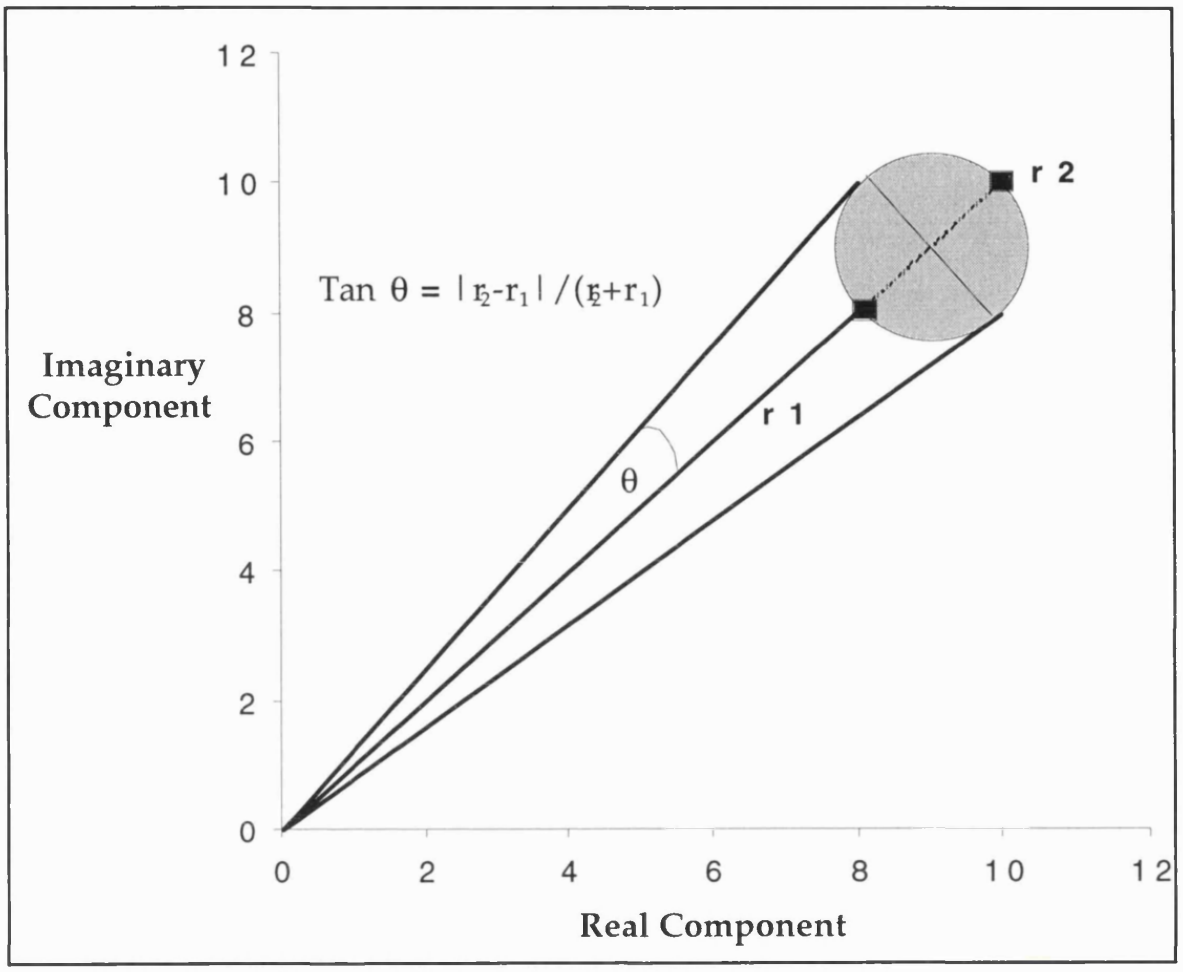

Figure 52. This an Argand diagram of the complex coefficients of the first harmonic of the time-density curve at the proximal (r1) and distal (r2) observation points. The change in amplitude from r1 to r2 results in an uncertainty in the measured phase at the distal observation point of θ°. This uncertainty can be calculated trigonometrically as tan = | r2-r1 | /(r2+r1).

In 1973 an electronic cross correlation technique was described utilising a matched filtering technique (Rosen, L. and Silverman, N.R. 1973), with results from animal experiments that were heavily smoothed and appeared noise free. The method which is presented in this thesis differs substantially from this electronic cross-correlation technique. The following sections address the impact of noise and reproducibility of results.

6.4.3.2.2 Sensitivity to noisy data

As with the GV curve and the forward triangle method, the Fourier transform method of time-of-flight was analysed using the same pair of perfect GV curves previously described (section 6.4.1.3), where the theoretical time-of-flight between them is 0.1829 seconds exactly. Table 22 shows the values obtained using the Monte-Carlo method and figure 53 plots the dependence on noise of the derived value and

Table 22

Time of flight between the perfect curves 6.14 & 6.15 modulated by varying degrees of noise, using the Fourier transform method for measurement (correct time = 0.183 secs).

Noise (DR No.)	Time of Flight (seconds)	± SD
0.00	0.183	0.000
0.25	0.183	0.010
0.50	0.182	0.020
1.00	0.181	0.040
1.50	0.180	0.060
2.00	0.182	0.080
2.50	0.185	0.096
3.00	0.190	0.110

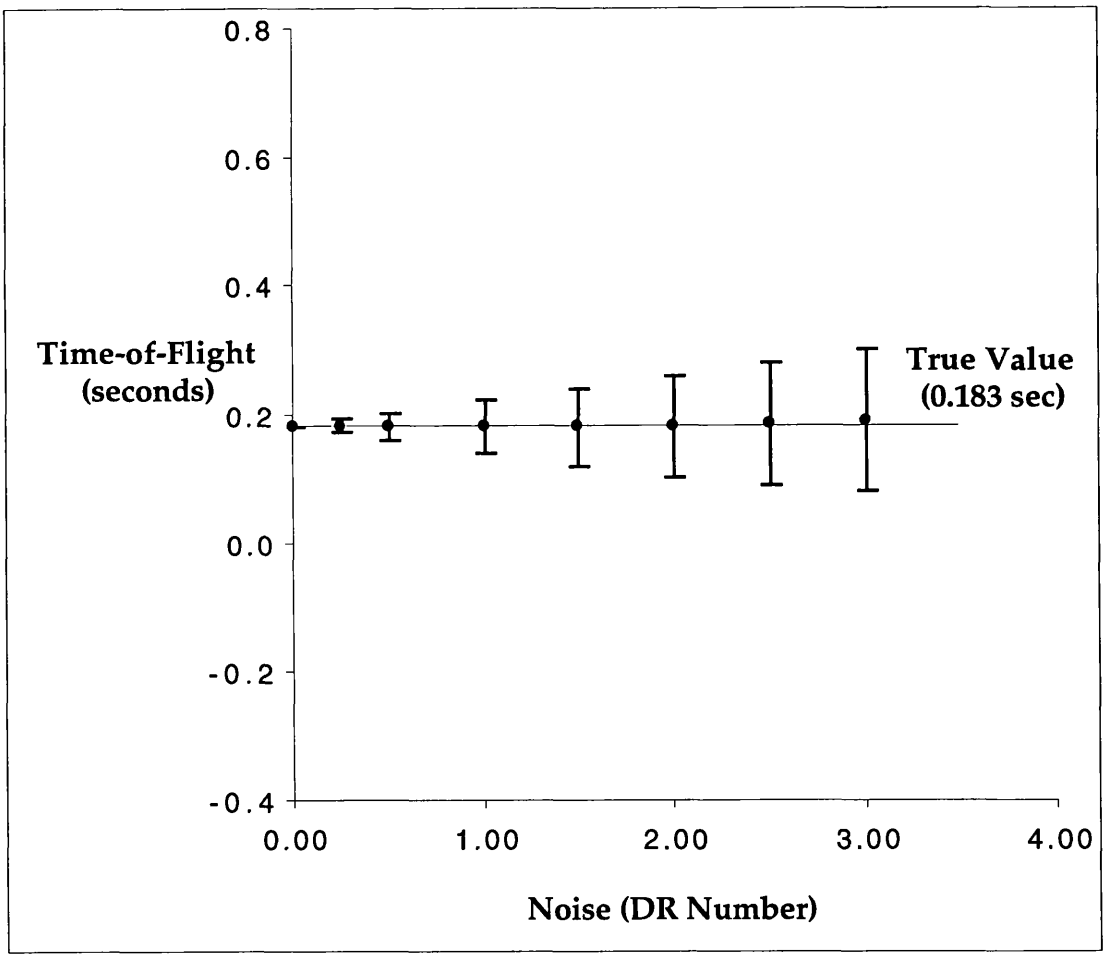

Figure 53. This is a plot of the mean values and standard deviations of a series of calculated times of flight as a function of noise content. The algorithm used to calculate the time of flight is the Fourier method described in the text. The results are far less influenced by noise content when compared with the gamma variate method and offer an improvement even over the forward triangle method of Bursch. These data were acquired using Monte-Carlo techniques. The data are listed in table 22.

standard deviation. At a typical mean noise level of 1.5 - 2.0 DR numbers, the 95% confidence limits are 0.06 - 0.3, which represent an improvement over both the gamma variate and forward triangle methods. Note also that the mean value was consistently within 0.04 seconds of the true value. The conclusion is that the Fourier method is substantially less sensitive to noise within the data than the gamma variate curve method of Hesselink and approximately 20% less sensitive to noise than the forward triangle method of Bursch (Bursch, J.H., Johs, R., et al., 1971; Hesselink, J.R., Chang, K.H., Chung, K.J. and Abbate, L. 1986; Hesselink, J.R., Chang, K.H., Chung, K.J., Abbate, L., et al., 1986).

6.4.3.2.3 Power spectrum of raw data

The concept of a power spectrum has already been alluded to (section 6.4.1.4) without an explanation of the meaning of the term. When the Fourier transform of a discrete set of real values is taken, the result is a set of complex numbers of the form:

$$A_n\, Cos_n(\theta) + iB_n\, Sin_n(\theta) \qquad 6.27$$

The coefficients A_n and B_n are the amplitudes of the real and imaginary components of the frequencies. When these sines and cosines are summed over these frequencies they reconstitute the original data set. The power content of a periodic function $f(t)$ with period T is defined as the mean-square value, given by the expression:

$$\frac{1}{T}\int_{-T/2}^{T/2}|f(t)|^2\,dt \qquad 6.28$$

by Parseval's theorem:

$$\frac{1}{T}\int_{-T/2}^{T/2}|f(t)|^2\,dt = \sum_{n=-\infty}^{\infty}|c_n|^2 \qquad 6.29$$

Where the c_n's are the complex Fourier coefficients of $f(t)$, ie. A_n and B_n.

If $|c_n|^2$ is plotted as a function of n a power spectrum of the original data set is obtained. Thus the proportion that each individual harmonic contributes to the original signal can be determined. This is important because of the sampling theorem, and for evaluation of the noise components of the time-density curves.

Cardiac cine-angiography is usually performed at a rate of 50 frames per second. This translates to a Nyquist limit of 25Hz, which means that there should be no data-containing component in the signal with a frequency greater than 25Hz. The QRS complex of the electrocardiogram occupies of the order of 0.1 seconds ie. it contains information of the order of 10Hz, well within this Nyquist limit. Therefore, to adequately sample an electrocardiogram, 50 frames a second is an unnecessarily high rate. In measuring the mean forward flow of blood along a vessel, we are not concerned with local oscillations in time, rather it is the low frequency envelope which is used to generate the time-density curve. This has a typical time span of between two and ten seconds, depending on other factors such as site of acquisition and age of patient. Taking a worst case figure of a one second bolus, it would be expected to contain frequencies no higher than one Hertz, and thus imaging at two Hertz (two frames per second) is adequate. This is rather surprising in view of the commonly held belief that faster framing rates are mandatory for flow measurement. Of course, this presupposes a relatively noise free signal.

When the power spectrum of a typical DSA time density curve is obtained it can be seen that indeed well over 90% of the information content is present in the first two harmonics only, figure 54, table 23. This implies that at a sampling rate of 2.5 frames per second, the conditions of the sampling theorem have been fulfilled and faster sampling would not have yielded any extra information.

Table 23

Original data from table 18 with the equivalent power spectrum.

Original Time-Density Curve	Harmonic	Power Spectrum
0.00	DC Component	176.36
0.00	First	294.17
0.13	Second	37.33
5.84	Third	5.15
16.00	Fourth	0.20
27.63	Fifth	0.37
36.76	Sixth	0.05
37.39	Seventh	0.12
29.85		
20.92		
13.87		
9.77		
7.98		
6.31		
0.00		
0.00		

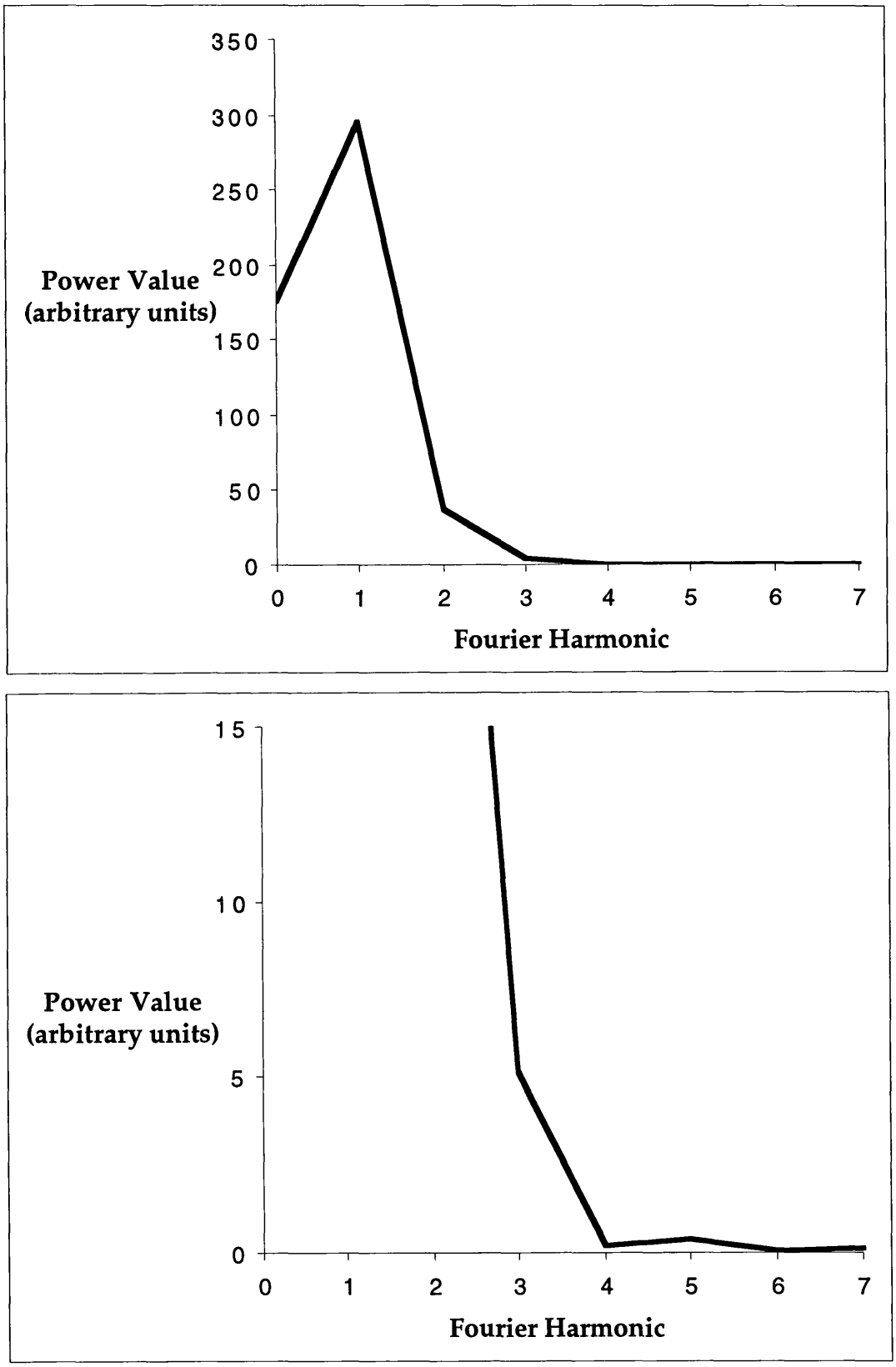

Figure 54. The top curve shows the whole power spectrum of an observed time-density curve obtained by Fourier analysis and Parseval's theorem. Table 23 contains the data which are plotted in this graph. More than 90% of the information content is contained in the first two harmonics. Thus, a sampling rate of just 2.5 frames per second is adequate to define the curve correctly. The bottom curve shows detail of harmonics 3 through 7.

6.4.3.2.4 Noise and its meaning in the frequency domain

Looking at the work of Bursch and others (Bursch, J.H., Johs, R., et al., 1971; Rosen, L. and Silverman, N.R. 1973), the literature contains many examples of apparently relatively noise free time density curves. There is usually little or no discussion as to the manner in which noise content in the data is handled. Furthermore, frame dependent evaluation of background tissue perfusion is inconsistently treated with the favoured approaches being a) to not mention how it is done at all, or b) to take an area adjacent to the sampling window and to use that for background correction (Schmiel, F.K., Huber, H., et al., 1978).

A simple method of background correction is proposed. Before the arrival of contrast in a pixel, the only visible signal is due to inherent background. After passage of the bolus, there is additional signal present due to iodine accumulation in the under- and over-lying tissue. This later signal will, in general, be greater than the initial value. If an adjacent pixel away from the vessel is studied, then to a first order approximation, the background accumulation is a straight line joining the first and last points. The slope of this line will be similar but different for every pixel studied. It appears reasonable therefore, to use the actual region of interest under study as the source of data for background subtraction, and to interpolate between the before-and-after iodine values and to subtract the appropriate amount from each point on the acquired time density curve. This has been done for all the analyses discussed so far, and all the results should be considered in the light of the data being unsmoothed but background (not noise) subtracted.

When a power spectrum is obtained from such a background subtracted time density curve, it is seen to be dominated by the first two harmonics, table 23. While there is some power at higher frequencies, these correspond to signals which are rapidly changing and are likely to be due to noise. Figure 55 shows the arrival of the contrast bolus in the distal part of the vessel, but in the bottom left hand part of the picture there are many tiny sharp peaks - these are due to the inherent noise in the image and they have characteristic frequencies which are at the high end of the spectrum generated by Fourier transformation. Thus using Fourier transform analysis, time-of-flight can be calculated and noise removal performed. Fourier transform methods allow direct analysis of the data with no need for smoothing or data-bounding.

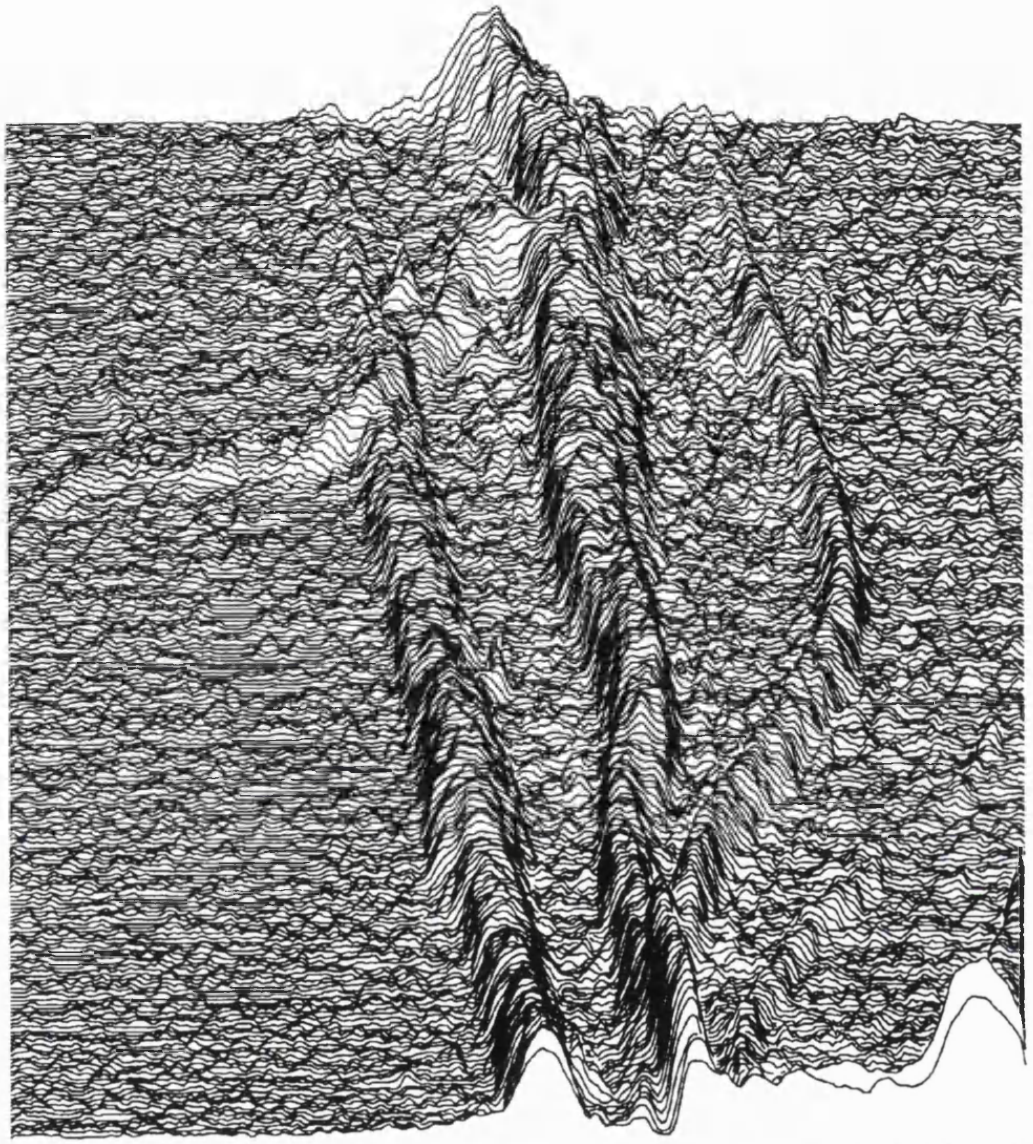

Figure 55. This is a projectional plot of an image frame from a DSA acquisition, after logarithmic transformation and pre-contrast "mask" image subtraction. The structures in relief in the centre of the image are blood vessels containing iodine contrast material. The advancing edge of the contrast bolus can be made out as the vessels cross. The data has been smoothed once with a binomial weighted nine point smooth purely for the purposes of illustration. The bottom left of the image has multiple small peaks in an area devoid of major blood vessels. These peaks are due to the inherent random noise associated with image acquisition.

6.4.3.3 *Comparison of the Fourier transform with other methods.*

Table 24 summarises the comparison between three methods of measuring time-of-flight. In principle, with perfect data, each method is equally valid. In the real world the Fourier method is less sensitive to noise present in the curves. The gamma variate method is sensitive to noise as well as extraneous decisions, such as which points to use in fitting to the curve. It is the least satisfactory. The forward triangle method improves on the gamma variate, but uses averaged and smoothed data - it is not as robust as the Fourier method.

6.4.4 Flow in rigid tubes

6.4.4.1 *Laminar flow*

Flow of a fluid in a cylindrical tube is described by the Poiseuille equation which states that the pressure drop along a pipe is proportional to the length of the pipe, the rate of flow and to the viscosity, and is inversely proportional to the fourth power of the radius. If contrast is injected into a liquid flowing under these circumstances it is seen that the liquid in the axis of the tube is moving much faster than that at the wall and that the front of the contrast assumes a parabolic shape. The reason for this is that the particles of the liquid are flowing in a series of laminae parallel to the sides of the tube and the fluid in contact with the wall is stationary, with each successive lamina slipping against the viscous friction of the lamina outside it. This is laminar flow. Figure 56a is a projection image of the front of the bolus of contrast; compare it with figure 56b where the contrast has filled the whole vessel - the appearance of the parabolic shape of the advancing bolus is apparent.

6.4.4.2 *Turbulent flow*

If the rate of flow through a tube is continuously increased, there comes a point when the resistance to flow increases sharply. Contrast injected at this stage into the stream shows that the fluid is mixing across the tube and that the fluid is no longer moving regularly along the line of flow but is following a more or less random path across the tube in addition to its main forward movement. This type of flow is termed turbulent. This classical differentiation between laminar flow and turbulent flow holds absolutely only for steady flow in a rigid tube. There are intermediate stages of instability in a liquid which become relevant to pulsatile flow in the arteries of a living animal.

Table 24

Comparison of the operational characteristics of the three methods of time-of-flight measurement.

	Fourier Transform	Gamma Variate	Forward Triangle
Single Pixel Resolution	Yes	No	No
Smoothing Needed	No	Yes	Yes
Background Removal	Yes	Yes	Yes
Automatic Noise Removal	Yes	No	No
Sensitivity to Noise	Low	High	Moderate

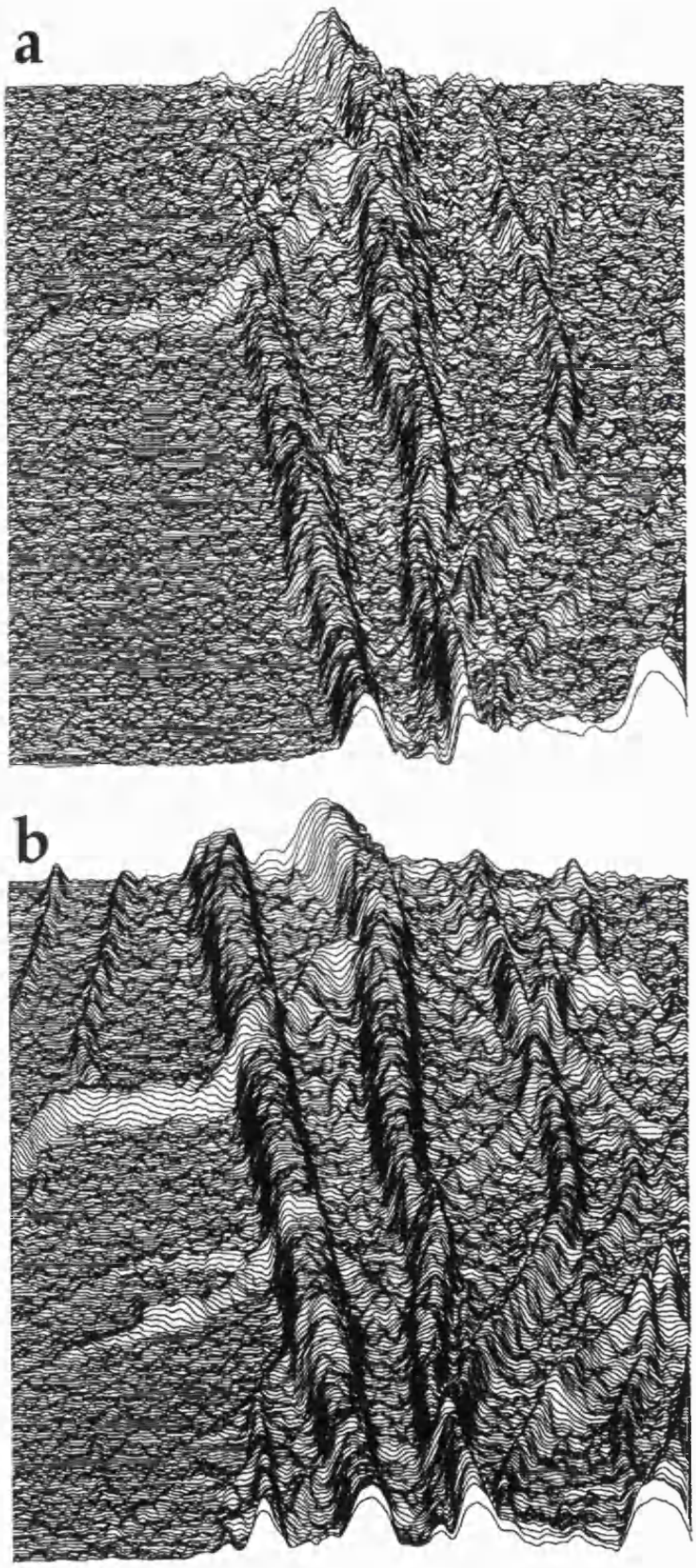

Figure 56. Two projectional images are shown; the top image is early in the sequence as the bolus of contrast is beginning to fill the vessels, the bottom image is at a time point when the whole of the vessel is full of contrast. The advancing front of the bolus in its parabolic form is clearly demonstrated in the top image.

6.4.4.3 *Poiseuille's equation*

Poiseuille was a physicist and also a physician who wanted to apply the results of his investigations to the understanding of the circulation of blood. He therefore chose capillary sized tubes but, as no method of preventing coagulation of blood was known at that time he had to use water as a test liquid; this was fortunate because blood flowing in capillaries shows anomalous properties of viscosity which would have altered his results. The theoretical treatment and derivation of the equation for flow in a cylinder is attributed to Hagenbach and Wiedeman in 1860, with a more complete derivation attributed to Lamb in 1890 (Lamb, H. 1932).

Consider a cylinder of length L and radius R. Consider also within this cylinder a coaxial cylindrical liquid shell of thickness dr with an inner radius of r. Let the velocity v, be parallel to the axis of the cylinder and be a function of the distance, r, from that axis. If the pressures at each end of the cylinder are respectively $P1$, $P2$, then the net normal pressure on the end of the cylinder is:

$$F_p = (P1 - P2) * 2\pi * r * \delta r \qquad 6.30$$

The retarding force on the inner surface will now be:

$$F_{visc} = -\frac{\partial}{\partial r}(\mu * \frac{\partial v}{\partial r} * 2\pi rL)\ \delta r \qquad 6.31$$

where μ is the viscosity.
In a stable situation these are equal and therefore:

$$(P1 - P2)2\pi r\delta r = -\frac{\partial}{\partial r}(\mu * \frac{\partial v}{\partial r} * 2\pi rL)\ \delta r \qquad 6.32$$

rearranging this gives:

$$\frac{\partial}{\partial r}(r * \frac{\partial v}{\partial r}) = -(P1 - P2)r/\mu L \qquad 6.33$$

integrating with respect to r gives:

$$\frac{\partial v}{\partial r} = -\{(P1 - P2)r/2\mu L\} + \{A/r\} \qquad 6.34$$

where A is a constant of integration. At the axis $r = 0$ and $\frac{\partial v}{\partial r} = 0$, therefore $A = 0$.

Integrating again yields:

$$v = -\{(P1 - P2)r^2 / 4\mu L\} + B \qquad 6.35$$

and at $r = R$, and $v = 0$, B is given by:

$$B = (P1 - P2)R^2 / 4\mu L \qquad 6.36$$

$$\Rightarrow \quad v = (P1 - P2)(R^2 - r^2) / 4\mu L \qquad 6.37$$

This is an equation of a parabola where v is zero at R (the edge of the cylinder) and v is a maximum at the axis (v_{axial}). In order to determine volume flow it is necessary to determine the volume of the paraboloid which has this parabola as its profile, ie. the volume of the solid of revolution;

let Q = volume flow, then:

$$Q = \int_0^R 2\pi v r \delta r \qquad 6.38$$

but from equation 6.37 v is known and therefore:

$$Q = \{2\pi(P1 - P2)/4\mu L\}\int_0^R (R^2 - r^2) r dr \qquad 6.39$$

$$\Rightarrow \quad Q = (P1 - P2)\pi r^4 / 8\mu L \qquad 6.40$$

Equation 6.40 is Poiseuille's equation. In the case of DSA, pressure is not measured, rather a velocity measurement is obtained. The average velocity across the vessel($\overline{v}$) is given by:

$$\overline{v} = (P1 - P2)R^2 / 8\mu L \qquad 6.41$$

at the axis we also have both v_{axial} and $r = 0$, taken together with 6.37 this yields:

$$v_{axial} = (P1 - P2)R^2 / 4\mu L \qquad 6.42$$

therefore:

$$v = v_{axial} / 2 \qquad 6.43$$

Now Q, the integrated flow from 6.40 can be expressed in terms of velocity using 6.41:

$$Q = \bar{v}\pi R^2 \qquad 6.44$$

which in turn leads to:

$$Q = v_{axial}\pi R^2/2 \qquad 6.45$$

Equation 6.45 has no dependence on pressure and v_{axial} can be measured and hence mean flow calculated. This derivation has been made with the following assumptions:

1. The liquid is homogenous and has the same viscosity at all rates of flow.
2. The liquid does not slip at the wall.
3. The flow is laminar.
4. The flow is steady, without acceleration or deceleration
5. The tube is long compared with the region under study.
6. The tube is rigid.

Blood is a suspension of particles in a liquid. However, under circumstances where the tube in which it is flowing is large compared with the particle size, it behaves like a classical Newtonian fluid. The critical size for an artery is 0.5 mm in diameter. For the purposes of the present study, blood flowing in arteries of 4 - 10mm in diameter can be treated as a homogenous fluid and under conditions of mixing with iodine contrast, the mixture may still be considered a Newtonian fluid. Condition 2 is crucial to Poiseuille's law and has been shown to be valid for blood in vessels (Whitmore, R.L. 1967a; Whitmore, R.L. 1967b; Whitmore, R.L. 1967c). Condition 3 is met in all vessels with sufficiently steady flow - this is true for all but the largest arteries, such as the ascending aorta, where during forward motion, flow is transiently turbulent. Condition 5 is met for the cases under study. Condition 4 is clearly not met, since there is pulsatile flow in arteries due to the nature of the heart beat. The result of the failure of condition 4 is dealt with in the next section. Condition 6 is not true in the circulation, since arteries are elastic in nature and expand slightly during the increase in pressure generated by the heart in systole. The expansion, however, is minimal compared with the diameter and in terms of any practical measurement an artery may be considered to be rigid, at least when taken over a short length.

6.4.4.4 *Bessel functions in the real world*

Since flow is not steady in the circulation, condition 4 does not hold, and Poiseuille's law does not apply. The velocity profile will not be of the same form as is present in steady state laminar flow. Nonetheless it will be shown that if only mean forward flow is considered, then Poiseuille's law can be applied to its measurement. Expanding equation 6.33 gives:

$$\frac{\partial^2 v}{\partial r^2} + \frac{1}{r}\frac{\partial v}{\partial r} + (P1 - P2)/\mu L = 0 \qquad 6.46$$

This is valid where *P1* and *P2* don't vary instantaneously. If *z* is the direction of the axis of the vessel then *(P1 - P2)/*μL is now correctly written as:

$$P1 - P2 = \frac{\partial p}{\partial z} \qquad 6.47$$

and as velocity changes with time equation 6.46 is not equal to zero but in general gives:

$$\frac{\partial^2 v}{\partial r^2} + \frac{1}{r}\frac{\partial v}{\partial r} + \frac{1}{\mu}\frac{\partial p}{\partial z} = \frac{\rho}{\mu}\frac{\partial v}{\partial t} \qquad 6.48$$

Where ρ is the density of the liquid and μ is its viscosity. This equation was derived by Womersley, (Womersley, J.R. 1955). If it is assumed that the pressure change may be approximated by a simple harmonic motion then:

$$\frac{\partial p}{\partial z} = Ae^{i\omega t} \qquad 6.49$$

Where $i = \sqrt{(-1)}$ and $\omega = 2\pi f$

6.48 reduces to:

$$\frac{\partial^2 v}{\partial r^2} + \frac{1}{r}\frac{\partial v}{\partial r} - \frac{\rho}{\mu}\frac{\partial v}{\partial t} = -\frac{A}{\mu}e^{i\omega t} \qquad 6.50$$

let $v = ue^{i\omega t}$, then 6.50 becomes:

$$\frac{\partial^2 u}{\partial r^2} + \frac{1}{r}\frac{\partial u}{\partial r} - \frac{\rho i\omega}{\mu} = \frac{A}{\mu} \qquad 6.51$$

This is a form of Bessel's equation with the solution appropriate to the boundary conditions:

$$u = \frac{A}{i\omega\rho}\{1 - (J_0[r\sqrt{i^3}\sqrt{\omega\rho/\mu}])/(J_0[R\sqrt{i^3}\sqrt{\omega/\mu}])\} \qquad 6.52$$

Where $J_0[]$ is a Bessel function of the first kind of zero order. The quantity $R\sqrt{\omega\rho/\mu}$ is non-dimensional and is related to the Reynolds number of the fluid. It may be conveniently expressed as:

$$\alpha = R\sqrt{\omega\rho/\mu} \qquad 6.53$$

Substituting α and $y = r/R$ in 6.52 yields:

$$v = \frac{AR^2}{i\mu\alpha^2}\{1 - (J_0[\alpha y\sqrt{i^3}])/(J_0[\alpha\sqrt{i^3}])\} \qquad 6.54$$

This gives the instantaneous velocity of that lamina present at a fraction of the distance (y) from the axis of the tube. Equation 6.54 appears to be very different to equation 6.37. It will be shown that in fact under certain circumstances 6.54 reduces exactly to 6.37.

To solve 6.54 for flow is quite complicated and has been performed by a number of authors (Lambossy, P. 1952; Womersley, J.R. 1957). Summarizing the treatment by Womersley,

let: $J_0[\alpha y\sqrt{i^3}] = M_0[y]e^{i\theta_0}$ and $J_0[\alpha\sqrt{i^3}] = M_0e^{i\theta_0}$

If $A\,e^{i\omega t}$ is written in modulus and phase form and the real part alone is considered, then 6.54 reduces to:

$$v = \frac{M}{\omega\rho}[Sin(\omega t - \phi) - (M_0[y]/y)Sin(\omega t - \phi - \delta_0)] \qquad 6.55$$

Where $Ae^{i\omega t} = MCos(\omega t - \phi)$ *and* $\delta_0 = \theta_0 - \theta_0[y]$.

Now at the boundary , ie. when $r = R$ and $y = 1$, this reduces to, $v = 0$, which is the same as for the steady flow situation. Womersley compressed 6.55 further by writing

$h_0 = M_0[y]/M_0$ and

$M_0' = \sqrt{1 + h_0 - 2h_0 Cos(\delta_0)}$ and $Tan\, E_0 = h_0 Sin(\delta_0)/(1 - h_0 Cos(\delta_0))$

Thus 6.55 becomes:

$$v = (M/\omega\rho) M_0' Sin(\omega t - \phi + E_0) \qquad 6.56$$

by substituting 6.53 this in turn yields:

$$v = (MR^2/\mu)(M_0'/\alpha^2) Sin(\omega t - \phi + E_0) \qquad 6.57$$

In this way the velocity profiles of the various laminae at points within a vessel are calculated. In terms of flow though, it is necessary to integrate 6.57 across the vessel. This gives a volume flow of:

$$Q = \frac{\pi R^2 A}{i\omega\rho} \{1 - (2J_1[\alpha\sqrt{i^3}])/(\alpha\sqrt{i^3}\, J_0[\alpha\sqrt{i^3}])\} e^{i\omega t} \qquad 6.58$$

Where $J_1[]$ is a Bessel function of the first kind and order 1. Womersley went on to substitute the terms in square brackets with $[1\text{-}F_{10}]$ and tabulated this function (Womersley, J.R. 1957). By substituting $[1\text{-}F_{10}]$ with its modulus and phase values, M_{10} and E_{10} are generated analogously to the treatment above. This yields:

$$Q = \frac{\pi R^4}{\mu} M \frac{M_{10}'}{\alpha^2} Sin(\omega t - \phi + E_{10}) \qquad 6.59$$

As ω tends to zero and E_{10} tends to 90°, so $\frac{M_{10}'}{\alpha^2}$ tends to 1/8, and

$M Sin(\omega t - \phi + E_{10})$ tends to $M Cos(\omega t - \phi)$ which is just $(P1 - P2)$.

Therefore, in the limit, Poiseuille's equation is recovered.

In order to calculate the flow components of a pressure waveform, Fourier transformation of equation 6.59 is performed. It will be remembered that the value A_0 for the discrete Fourier transform represents the mean value of the signal under consideration. In the case of 6.59, A_0 is just the condition where $\omega = 0$, $E_{10} = 90°$ and so on; this reduces equation 6.59 back to:

$$Q = \pi R^4(P1 - P2)/8\mu L$$

and in turn to:

$$Q = v_{axial}\pi R^2/2$$

Thus the statement made in relation to 6.54 is proven. If the only component of a pulsatile waveform of interest is the mean forward flow, then equation 6.54 reduces to Poiseuille's equation and we can consider the system as being of steady flow in a rigid tube. This is precisely the situation that pertains to densitometric methods of flow measurement - with one important provision. The framing rate must be slow enough to filter out the high frequency cardiac pulsations. As has been seen above (section 6.4.3.2.3), a framing rate of between 2.5 and 5.0 frames per second is sufficient to fulfil this condition.

6.4.5 Flow in arteries

From the above exposition, therefore, it may be deduced that measurement of the mean forward flow in real arteries can be achieved by applying equation 6.45. I have discussed a method of acquiring R (the vessel radius) and a novel method of acquiring v (volume). As long as the true axial velocity is measured, then equation 6.45 is valid.

CHAPTER 7

VERIFICATION OF DIGITAL SUBTRACTION ANGIOGRAPHY DATA

7.1 *In Vivo* Experiments

In chapter 6 the detailed theory for measuring bulk blood flow in an artery has been described using three methodologies. Two of these, the gamma variate technique and the Bursch forward triangle technique, have been described and published previously, while the Fourier analysis technique is novel and forms part of this thesis. In summary, each method uses the passage of iodinated contrast material along a blood vessel to simultaneously determine the time of travel of the contrast between two points chosen along the vessel, and the volume of the vessel between those chosen points. The volume determination utilizes cartesian geometry and trigonometry with an external reference scale in order to calculate the circular cross sectional area of the artery at the chosen points and the distance between them. The calculation of time displacement between the chosen points potentially can yield different answers depending on the method used. In the situation where there is no uncertainty in the observed time-density curve, it was shown through Monte Carlo simulation in chapter six that the three methods yield similar results close to the true answer; these data are summarized in tables 16, 17 and 22. However, in the presence of noise, the Fourier method yielded more consistent results with a lower standard deviation than either the gamma variate or Bursch forward triangle technique. In order to confirm that this finding is applicable over a physiological range of blood flow values in vivo, a series of experiments in Yorkshire pigs was performed. The requirement for such an animal model of blood flow is the ability to create a variety of a stable flow rates in a large vessel and for each of these flow rates to be able to be measured simultaneously using an independent gold standard technique and the DSA techniques. In the implemented pig model, the common carotid artery was used to provide DSA data sets at a variety of stable flow rate values. As the electromagnetic (EM) flow probe is considered the gold standard technique for measuring arterial blood flow (Rutishauser, W., Bussmann, W.D., et al., 1970; Calvert, M.H., Pullan, B.R., et al., 1975; Hackbarth, W., Bircks, W., et al., 1980). EM flow probe data were collected simultaneously, starting before each DSA

data acquisition and continuing after the bolus of contrast had passed through the vessel. Flow was determined from the DSA data using gamma variate, Bursch forward triangle and Fourier methods and compared with the gold standard flow values recorded during the passage of the contrast bolus using the EM flow probe.

7.1.1 Methods

7.1.1.1 *Animal Model*

Following approval from the Office for Laboratory Animal Research, OLAR, a common carotid flow model was implemented in seven Yorkshire pigs. Each animal was fasted for 48 hours, and premedicated through an intramuscular injection of a mixture of ketamine (10mg/kg), xylazine (50mg/kg), atropine (0.05mg/kg), and butorphanol (0.1mg/kg). An ear vein was then cannulated, and α-chloralose solution (6gm in 800ml of saline) infused to achieve full anaesthesia. Lignocaine spray was applied to the larynx, and the animal intubated. After transfer to the imaging suite, the animal was connected to a mechanical ventilator and paralysed using gallamine (1.5mg/kg).

Deep anaesthesia was maintained by continuous infusion of the α-chloralose solution, titrated to the animal's reflexes, heart rate, and blood pressure. Femoral venous and arterial lines were established for fluid hydration and pressure monitoring, respectively. ECG leads were attached to the thorax to monitor the heart rate and rhythm. Physiological parameters (ECG and BP) were continuously monitored throughout the experiment.

The left common carotid was exposed by the careful dissection and retraction of overlying muscles and other tissues. Any branches present were ligated and divided. Two freely adjustable ties were looped around the vessel, one proximal to the measurement zone and one distal. At the end of this procedure, a segment of artery, approximately 5cm long, with no branches and free of surrounding tissue, was available for study. The vessel's external diameter was visually assessed to be suitable for a 3.5mm EM flow probe.

An electromagnetic flow probe system was used (Statham Instruments, Inc. Oxnard, California, Model no. SP2202) with a 3.5 mm section probe. This size was

found to be a suitable fit in all the animals, and was connected to the amplifier equipment. The flow probe was covered with gauze swabs and soaked in normal-saline in order to facilitate completion of the earthing part of the circuit.

A 5Fg straight catheter, with tantalum bands spaced at 2 cm intervals, was placed alongside the dissected section of artery and closely applied to it. The distal tie was used to temporarily occlude the vessel under study and thus to provide a zero flow situation which was then used to calibrate the computer controlled digital recording device to give a digital reading of +32768. Prior to each run, the zero reading was recorded to compensate for any fluctuations in the amplifier due to temperature change or electronic drift. Once the initial setup was complete, the settings were locked in position and remained constant throughout the whole series of experiments. Repeated check of the zero setting at the beginning and end of each experiment revealed no changes. The output of the EM flow probe amplifier was connected to a digitizer which recorded the voltage following amplification at a rate of exactly 50 samples per second with a precision of 16 bits, resulting in a 0.003% error in this measurement. Absolute time markers were generated independently by using a very high accuracy crystal oscillator (RS data, London U.K., stock number 301-858), whose output served to provide reference ticks at exactly 5 msec intervals (200 Hz). These reference ticks were used to trigger digitization of the EM flow probe data at 50Hz and the ECG data at 200Hz.

A 5Fg pigtail catheter was introduced from the right femoral artery through a previously placed arterial sheath and advanced until it lay in the ascending aorta, just above the aortic valve. Catheter position was selected to ensure the even mixing of contrast with blood prior to its arrival in the region under the study.

The DSA equipment was a Toshiba Digital Fluorography System DFP 60A, (Toshiba Corporation Medical Systems Division, Tokyo, Japan), with a maximum framing rate of 5 frames per second, acquired on a 1024 * 1024 imaging matrix, with a field of view (FOV) of 4.5 cm.

The animal was manoeuvred beneath the image intensifier with the vessel under investigation in the centre of the field. Exposure factors were chosen to utilize the full dynamic range of the image intensifier and TV imaging chain. An FOV of 4.5 cm was used for all experiments.

The procedure for each DSA run was identical, in particular, image magnification was not altered between DSA runs acquired at different flow rates in the same animal. The output from the EM flow probe was continuously monitored by the galvanometer integrated with the flow probe amplifier. Starting from a baseline stable flow rate in the region of interest, a single acquisition cycle consisted of the following steps; 1. Flow in the artery was modified by variable, partial occlusion of the vessel using the tie proximal to the probe. 2. Once a new stable flow rate was achieved, digitization and storage of the flow probe data was started. 3. DSA acquisition commenced and approximately 5 seconds later, 15 ml of iohexol 350 (Sterling-Winthrop, USA), were injected into the aorta through the pigtail catheter at 15 ml/sec using a calibrated power injector (Medrad, Inc., USA). The passage of the bolus of contrast was imaged through the region of interest, simultaneously with the output of the flow probe and the ECG. The imaging parameters used were a field of view of 4.5 cm, 5 frame per second acquisition rate and a 1024 by 1024 acquisition matrix. 4. At the end of this acquisition the partially occluding tie was released and baseline flow in the artery was re-established. The steps from 1 to 4 were repeated several times, each time with a different flow rate being present in the vessel under investigation. At the conclusion of the last cycle in the experiment, the digital data were transferred to a Macintosh workstation (Apple Computer, Cupertino, California, USA) for subsequent analysis.

The animals were sacrificed by pentobarbitone injection and incinerated by OLAR. In the last pig studied, immediately after lethal injection, 250 ml of blood were collected into an anticoagulated container and used to calibrate the flow meter system.

7.1.1.2 *Calibration of Flow Probe Data*

The segment of artery used for the *in vivo* acquisition of EM flow probe data in the last animal studied was removed for subsequent, *in vitro* flow probe calibration. The flow probe was placed around this vessel segment and connected to the amplifier in exactly the same manner as during the *in vivo* experiment. A rotary pump was used to produce pulsatile flow through this vessel of the blood collected at the end of the last experiment. A series of flow rates were measured simultaneously by using the

3.5 mm EM flow probe and a measuring cylinder and stopwatch. The manual measurements were reproducible to within 0.1ml, and the times to within 0.1 sec. The haematocrit of the blood was found to be 51%, normal for the pig. A calibration line of EM flow value (in arbitrary units) against manually calculated flow was constructed and used for subsequent conversion of EM flow values to real flows in millilitres per second.

7.1.1.3 *Data Analysis and Flow Calculation*

Once the calibration line for the flow probe system was determined, the data collected from all the experiments were analysed. The output of the EM flow probe had been digitized and electronically recorded during DSA acquisition. For each DSA run, for each animal, the signal from the flow probe was normalized by subtraction of the baseline, zero flow value determined before and during the experiment. A design characteristic of the Model SP2202 Statham EM flow probe system is an internal electronic feedback loop which automatically corrects for baseline drift secondary to factors such as changing temperature of the electronics, changes in voltage supply and changes in electrical current draw from the power circuit supplying the amplifier. The net result of this design is to obviate the need for continuous adjustment and re-checking of zero flow, baseline EM amplifier output, This stability of the zero flow setting of the measuring system was demonstrated explicitly in animal two, before and after each flow rate was achieved and measured. In the remaining animals, the zero flow, baseline value was confirmed to be unchanged at the beginning and end of the series of data acquisitions only.

For each set of data, corresponding to a different flow rate, the EM flow probe and DSA data were analyzed separately. For the EM flow probe, the flow present in the vessel during the passage of contrast was obtained by first taking the mean signal output value of the EM flow probe during passage of contrast through the vessel under study and subtracting from this the baseline zero flow value. Then, this baseline subtracted value was converted to absolute flow in ml/sec by using the previously determined calibration line.

For the DSA data the following series of steps 1 to 11 was performed. 1. The raw images were logarithmically transformed using the technique described in section 2.2.5 of chapter two. 2. Logarithmically transformed pre contrast images were averaged to yield a subtraction mask. 3. This mask was then subtracted from each image in the series. 4. From this digitally subtracted series, the frame or image with maximum opacification in the carotid vessels was identified. Regions of interest were placed in the centre of the vessel, one proximally and one distally. 5. From each of these interrogation regions, a time density curve, being the result of the passage of contrast along the vessel, was obtained from the whole image series. 6. The distance between the interrogation regions of interest was measured by using the 2 cm spacing of the tantalum bands on the catheter alongside the vessel as a reference distance. 7. At each of the interrogation locations the vessel profile orthogonal to its long axis was obtained from the frame with maximum contrast opacification of the vessel, 8. An ellipse function was fitted to this profile as described in detail in section 6.4.2 in chapter 6. 9. Once the distance between and cross sectional areas for the proximal and distal interrogation points was know, the volume of the vessel between these points was calculated. 10. For the proximal and distal time density curves, gamma variate, Bursch forward triangle and Fourier methods were applied to calculate a time of flight between the interrogation points. Details of these methods are presented in chapter 6 in sections 6.4.1 and subsections 6.4.1.2 and 6.4.1.3 respectively for the gamma variate and Bursch forward triangle, and section 6.4.3 and subsection 6.4.3.1 and 6.4.3.2 for the Fourier method. In summary, gamma variate functions were fitted to the time density curves and the difference in time between the peaks of these fitted curves used as the time of flight. For the Bursch forward triangle method, the maximum value of the density curve was found, then half this value was calculated. The time at which this half-max value occurred was used as a reference time point and the difference between these reference half-max time points on the proximal and distal curves was used as the time of flight between the proximal and distal interrogation points. Finally, Fourier transforms of both curves were obtained. The phase difference between the first harmonics of these Fourier transforms was converted into a time difference using knowledge of the image framing rate and the inherent mathematical properties of Fourier analysis. Namely, if the Fourier transform is calculated over 16 data points, the first harmonic will have 2 π radians corresponding to one cycle or 3.2 seconds,

when an acquisition rate of.5 frames per second is used to record the images. 11. Once the time of flight and volume is known, the flow in ml/sec may be determined for each of the three analysis methods. These 11 steps were repeated for each image data acquisition run.

Once all the flow data were calculated, regression analysis was performed between the EM flows and flows from each of the other three methods. Statistical advice was obtained from the departmental statistician.

7.1.2 Results

Calibration Curves

Figure 57 is the output recorded from the EM flow probe for the calibration run at a flow of 5.62 ml/sec. Similar curves were obtained from the other runs and in total there were 9 calibration runs with known flows from 2.79 to 6.51 ml/sec. After baseline subtraction, the mean probe values were used to generate a calibration line converting the recorded arbitrary units to values of flow in ml/sec. These data are summarized in table 25, and the calibration line is plotted in figure 58. The calibration equation was:

$$\text{Flow} = (0.00219 * \text{Probe value}) - 0.14314$$

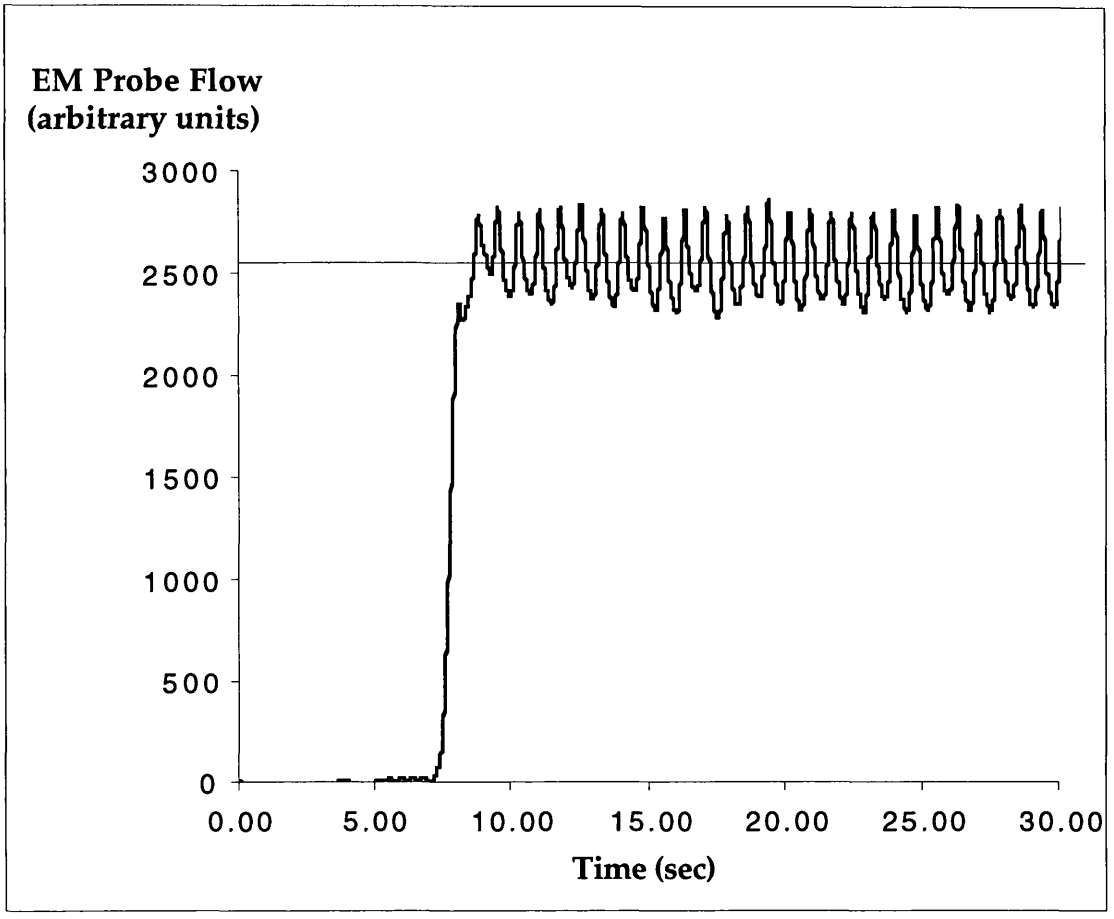

Figure 57 The flow probe output from a single calibration run (pump setting 50) with the calculated mean value of (2552.3 ± 11.3). This corresponded to a flow of 5.62 ml/Sec. The other data sets were similar, yielding the values in table 25.

Table 25

Calibration details for the 3. 5mm EM flow probe, the final calibration line was Flow (ml/sec) = (0.00219 * Probe value) – 0.14314.

Pump Setting	Volume ± 0.5 (ml)	Time ± 0.1 (sec)	Flow ± SD (ml/sec)	Probe Value ± SD (arbitrary units)
70	84.00	12.91	6.51 ± 0.09	2827 ± 28
65	88.50	14.29	6.19 ± 0.08	2766 ± 26
60	81.00	12.99	6.24 ± 0.07	2834 ± 27
55	90.00	15.62	5.77 ± 0.07	2561 ± 24
50	89.00	15.85	5.62 ± 0.07	2552 ± 26
45	67.00	14.55	4.60 ± 0.04	2017 ± 26
40	89.05	23.99	3.71 ± 0.03	1675 ± 23
35	78.05	25.67	3.04 ± 0.03	1287 ± 24
30	68.00	24.38	2.79 ± 0.03	1220 ± 25

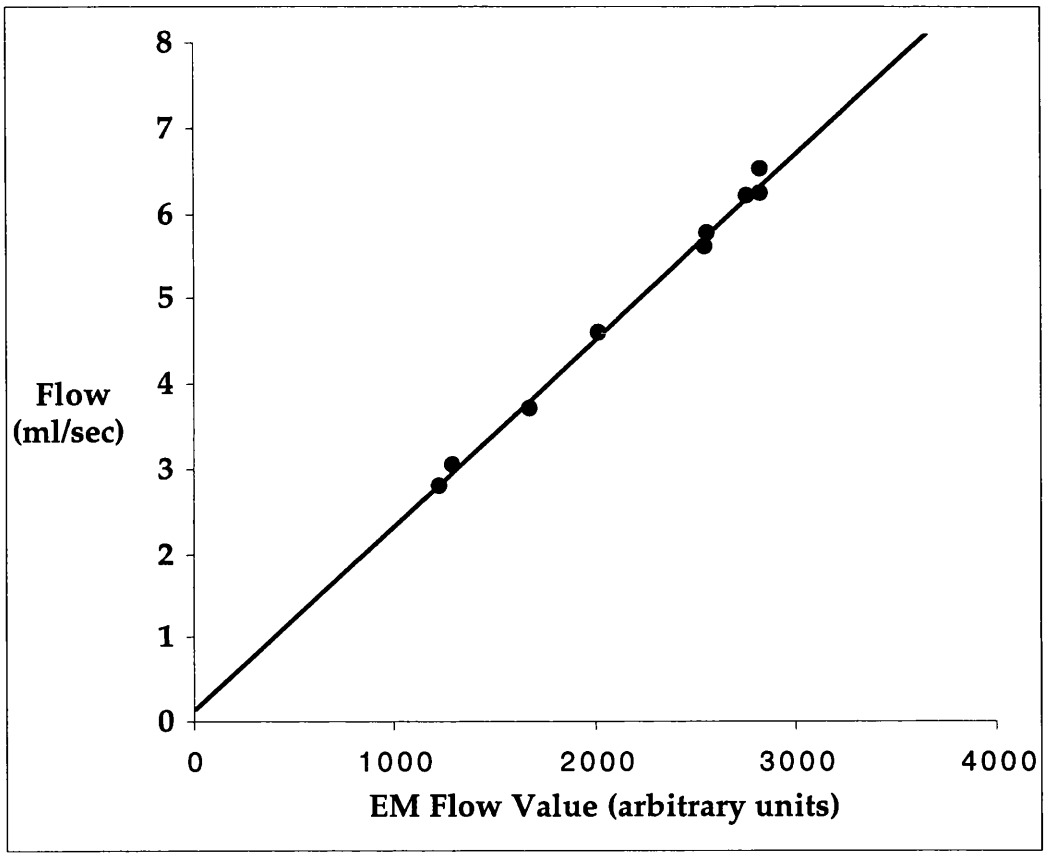

Figure 58 Calibration least squares line. Flow = (0.00219 * Probe value) – 0.14314

DSA flow rates

A series of images from animal 2 are shown in figure 59. These images were obtained by logarithmic transformation followed by baseline subtraction. The figure shows a sequence of frames as contrast arrives and leaves the vessel under investigation. Figure 60 is a single frame taken from animal 2 at peak opacification of the left common carotid artery. The banded catheter utilized for calibration is seen adjacent to the vessel (black arrows), as is the flow probe (open arrow). The proximal and distal sampling sites are also marked. The vessel profiles and time-density curves at these locations are shown in figure 61. Superimposed on the vessel profiles are the fitted curves used to generate vessel cross-sectional areas. The method for determining these dimensions has been described in detail in Chapter 6, section 6.4.2. The pixel dimensions were obtained by measuring the distance in pixels between the 2cm bands on the sizing catheter and converting the value to mm. In this instance, at this magnification, the pixel size was 0.123mm. The distance between the proximal and distal sampling points was measured and found to be 5.66cm. The volume of blood between the sampling points was thus calculated to be 1.06ml, based on a mean radius of 2.44mm and length of 5.66cm. A summary of the calculations for this particular data set is presented in table 26. Next, the time of flight between the sampling points was calculated using the Fourier, Gamma variate and Bursch forward triangle methods as previously described. These values were 0.202, 0.0497 and 0.117 seconds, yielding flow values of 2.61, 10.6 and 4.5 ml/sec respectively. Table 27 summarizes the data and its Fourier analysis for the time-density curves shown in figure 61. Figure 62 shows the these time-density curves with their associated first harmonics normalized to a peak of 90, for the purposes of display only. The phase shift is evident from the curves.

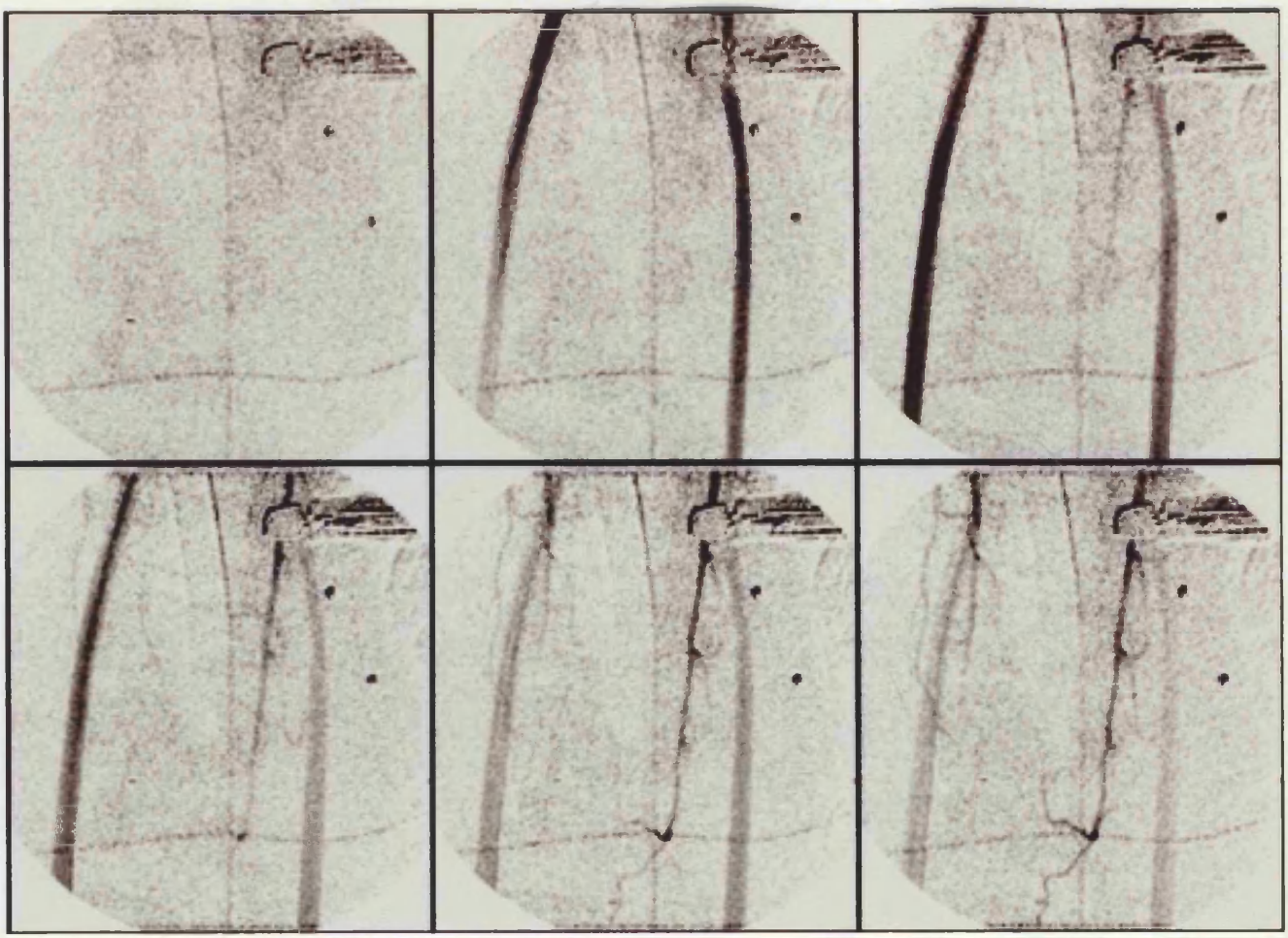

Figure 59 This is a series of images showing the arrival and washout of contrast from the left common carotid artery in animal two. The head of the animal is at the bottom of the image.

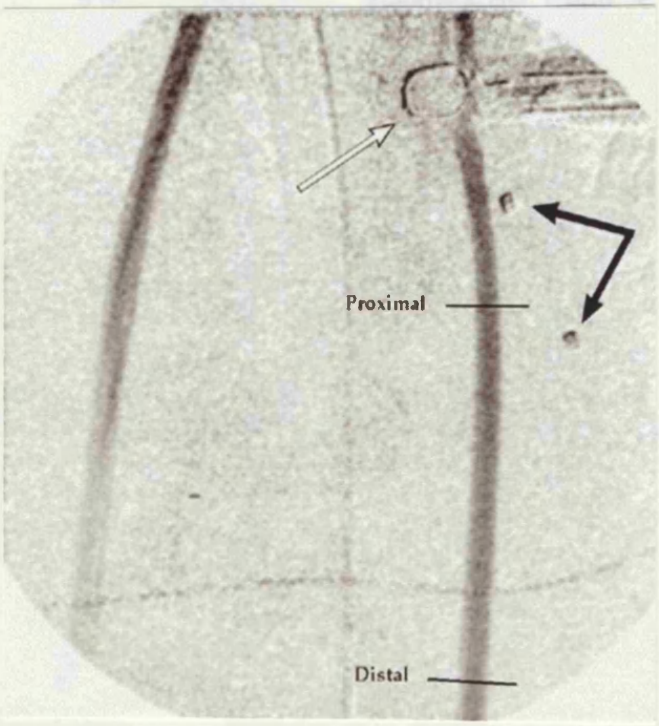

Figure 60 This the frame with maximum opacification in the left common carotid artery from animal 2. The 2cm bands on the sizing catheter are indicated by solid arrows, and correspond to 162.6 pixels, the pixel dimension is therefore 0.123mm. The proximal and distal locations along the artery are marked with the profiles and Time Density curves plotted in figure 61.

Table 26

Vessel profiles for proximal and distal locations with numeric values necessary to calculate flow between these two locations.

Pixel	Density Profile Proximal	Distal	Pixel Dimension = 0.123 mm		
0	-24		Start x	626	
2	15		Start y	356	
4	24				
6	0		End x	606	
8	-20		End y	816	
10	10				
12	19		Distance	460.435	pixels
14	14			56.633	mm
16	27	19			
18	73	8			
20	105	2	Proximal Vessel Location		
22	111	-7			
24	77	34	Radius	2.373	mm
26	80	55	Area	17.693	mm2
28	111	73			
30	79	116			
32	74	88	Distal Vessel Location		
34	80	80			
36	68	64	Radius	2.499	mm
38	49	88	Area	19.617	mm2
40	71	58			
42	93	41	Volume ± SD	1.056 ± 0.52	ml
44	55	68			
46	56	74			
48	20	103			
50	24	83			
52	-9	96			
54	-8	74			
56		50			
58		32			
60		15			
62		16			
64		1			

Table 27

Time density curves together with their Fourier analyses for data shown in figure 63. The time of flight was 0.202 seconds. The Bursch and gamma variate values were 0.124 and 0.053 seconds respectively. Calculated flow values were 2.61, 4.25 and 10 ml/sec respectively, versus the EM gold standard of 2.26 ml/sec.

Proximal

Image	DR Number	Fitted Curve	Fourier coefficients Real	Fourier coefficients Imaginary	Phase (radians)	Time (sec)
0	2.059	0	354.14			
1	-2.549	0	-153.3	-170.6	0.839	0.427
2	-0.417	0	-74.38	113.14		
3	4.25	0	75.22	41.46		
4	3.275	0	24.47	-49.37		
5	4.951	4.51	-53.94	-31.14		
6	68.676	70.61	-15.98	19.22		
7	86.681	80.59	15.56	-17.37		
8	54.873	62.59	3.94			
9	41.956	41.24				
10	28.706	24.78				
11	18.147	14.05				
12	11.887	7.64				
13	13.407	4.04				
14	4.789	2.08				
15	3.157	1.06				
16	7.25	0.53				
17	2.549	0.26				
18	0.377	0.13				
19	6.804	0.06				
20	14.951	0.03				

Distal

0	-1.033	0	367.45			
1	-4.566	0	-207.7	-98.04	0.441	0.225
2	4.711	0	-1.72	121.6		
3	-0.934	0	69.38	-18.85		
4	-3.079	0	-9.51	38.42		
5	5.684	0	-16.84	31.12		
6	19.171	0	28.04	13.53		
7	79.401	79.31	4.63	-30.26		
8	69.118	69.32	-24.68			
9	54.132	54.59				
10	42.336	41.18				
11	30.408	30.35				
12	21.283	22.04				
13	15.099	15.84				
14	14.717	11.3				
15	8.368	8.02				
16	3.125	5.66				
17	3.908	3.98				
18	2.789	2.79				
19	2.079	1.96				
20	6.658	1.37				

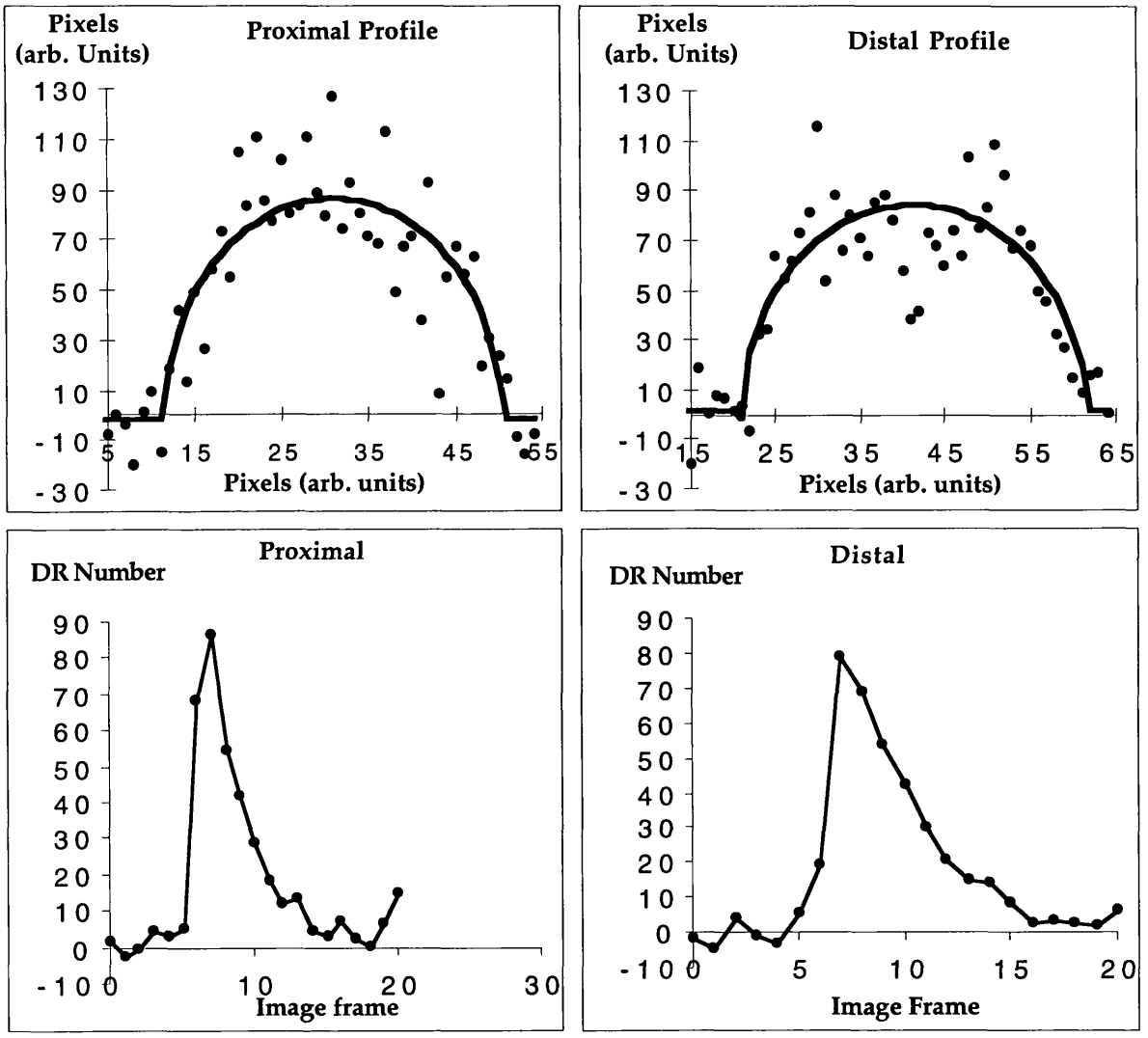

Figure 61 These are the curves corresponding to the locations marked on figure 60. The fitted vessel profiles are also shown in the top two images. The framing rate for acquisition was 5 frames per second onto a 1024 by 1024 matrix.

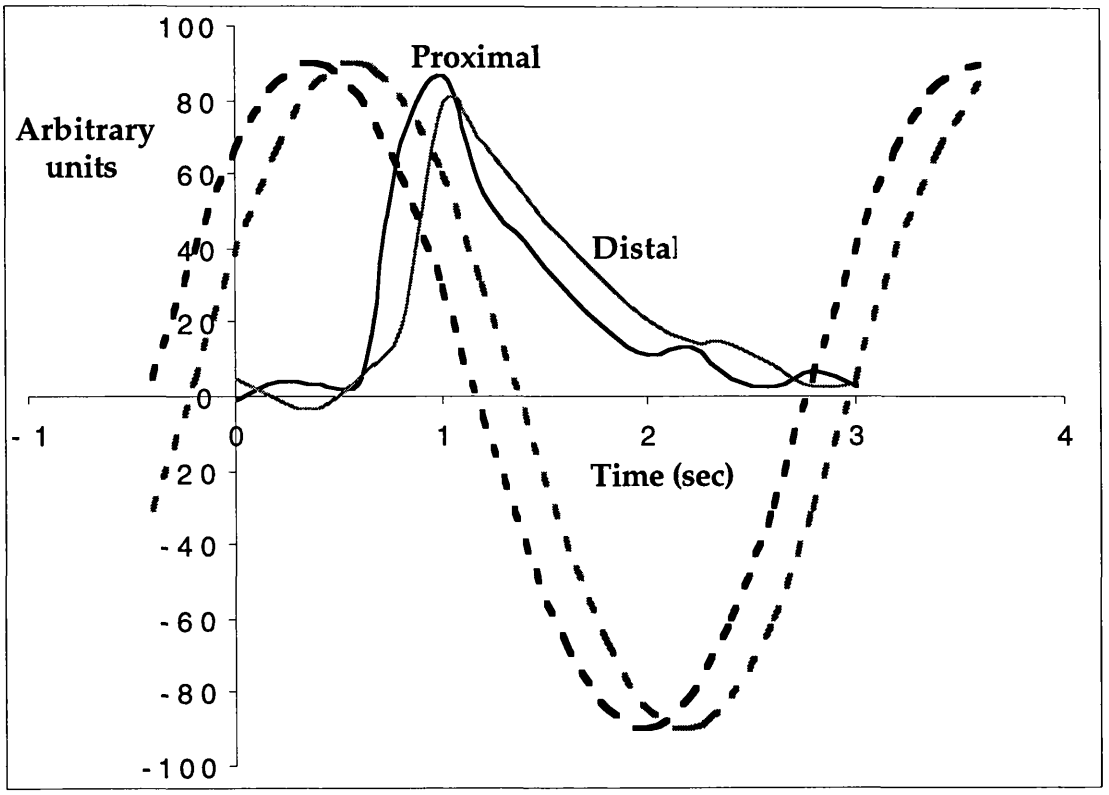

Figure 62 These are the original Time density curves corresponding to the locations marked on figure 60 and for which the data are given in table 27. The first harmonics of each of these are also plotted. The phase shift is clearly evident and represents a time difference of 0.202 seconds.

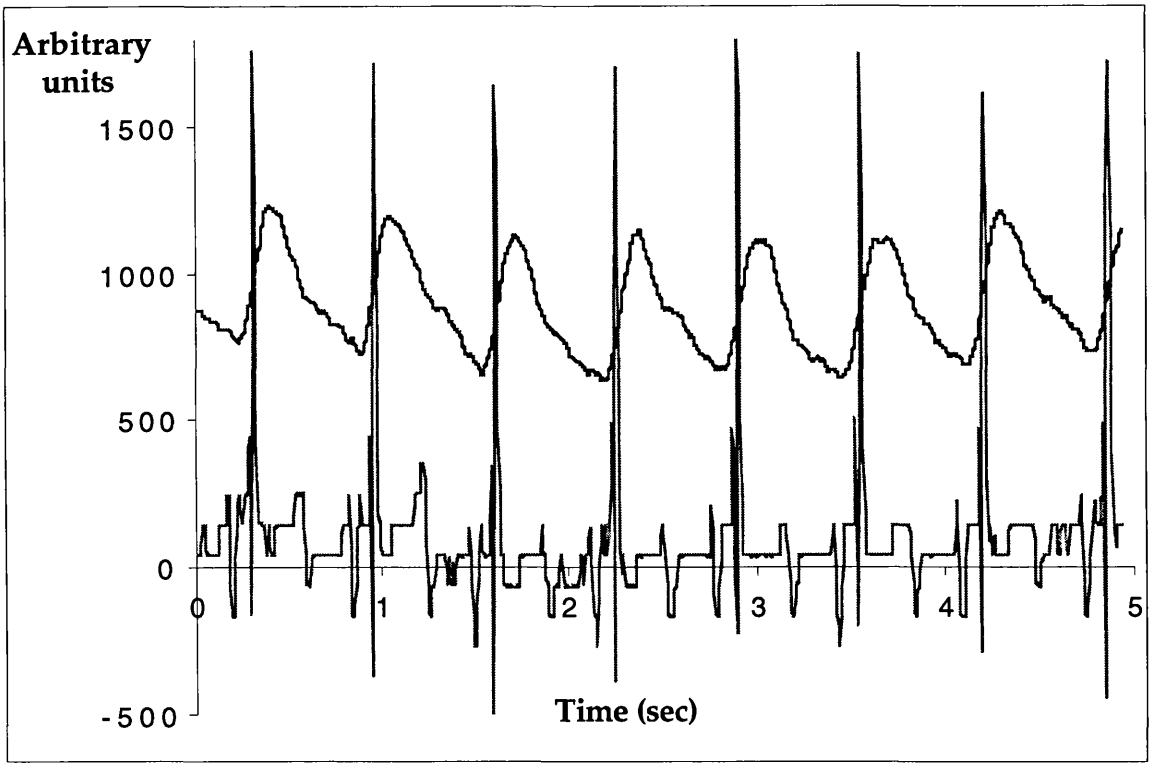

Figure 63 a This is the flow probe output and ECG recorded during the DSA run shown in figures 59 to 62. The heart rate was 92 BPM. The relationship between the flow wave and the ECG is clearly seen. The ECG values have been normalized to fit on the same graph as the probe output. The calculated flow in this instance was 2.26 ml/sec.

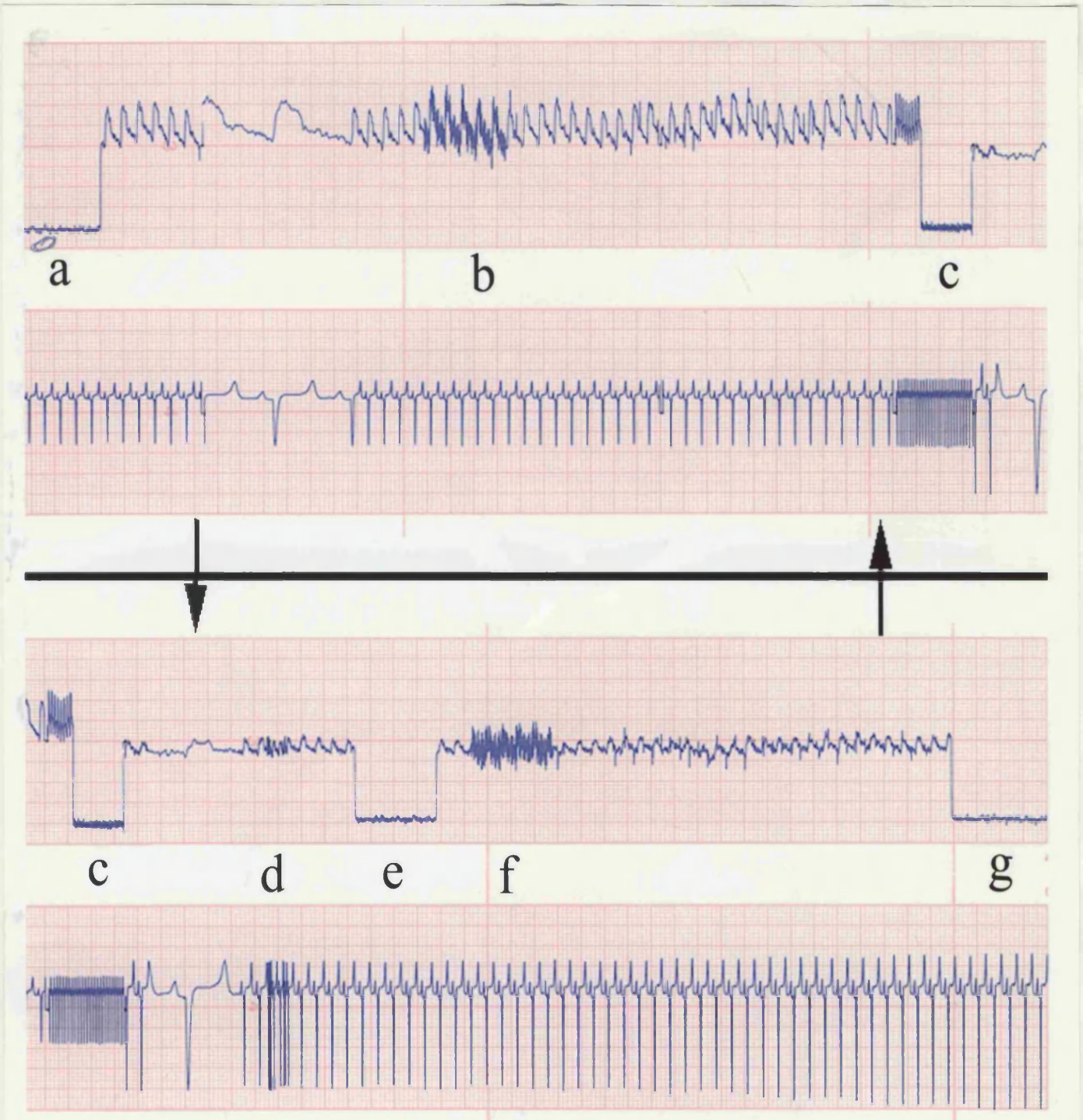

Figure 63 b This is part of the analogue chart recorder output for animal 2 showing the ECG and raw flow probe amplifier signal; the overlap points are shown by the black arrows. The zero flow situation is present in regions a,c,e and g and can be seen to be stable during the experiment. The ECG is also stable with no evidence of cardiovascular stress.

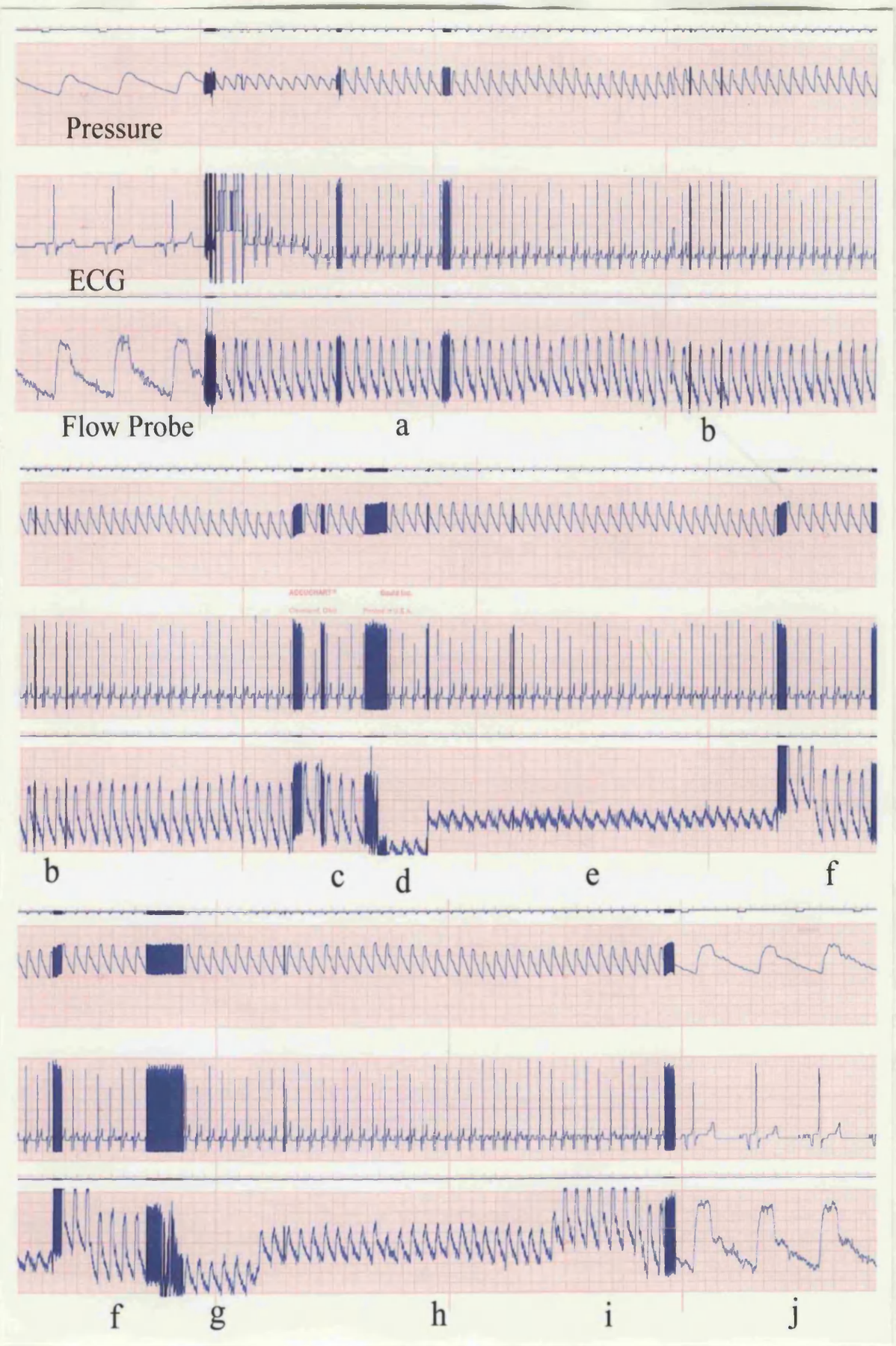

Figure 63 c This is part of the analogue chart recorder output for animal 3 showing pressure, ECG and flow probe amplifier signal. Regions a, b, c and j represent stable 100% flow through the vessel under investigation. Regions e and h represent different degrees of partial occlusions resulting in decreased flow rates compared to the unoccluded situation. Regions d and g represent the manipulation of the vessel necessary to achieve a new degree of partial occlusion and thus a new flow rate. Regions f and i represent release of the partial occlusion. The ECG remained stable during the experiment, as did the blood pressure.

EM Flow Probe Results

An example of the digitally recorded output from one run taken from animal 2 is shown in figure 63a. The output of the flow probe recorded during these DSA data is presented in tables 26 and 27. The ECG tracing obtained at the same time is also presented. The flow value obtained from these data was 2.26ml/sec. Figure 63b shows part of the output of the analogue chart recorder during the series of experiments performed on animal 2; the overlap points are marked by the black arrows. Before and after each run, the zero flow point of the EM probe was recorded. This corresponds to regions a, c, e and g. As can be seen from the strip recording, the baseline is stable during the whole experiment. As is also evident form the strip recording, the animal's heart rate and configuration of the ECG remained stable during the experiment. Regions b, d and f correspond to the passage of the contrast bolus through the flow probe; this can be seen as a slight, transient distortion of the signal resulting from the different conductivity value of blood and contrast material. Varying gains were used to record the ECG during sections b and f, resulting in different amplitudes at these times.

Figure 63c is part of the analogue chart recording from animal 3 showing pressure, ECG and raw EM flow probe signal output. It can be seen that the pressure during the experiment was stable with no evidence of alteration during the data acquisition runs or manipulation of the vessel. Similarly the ECG remained stable with no alteration in heart rate or configuration to suggest cardiovascular stress. Regions a, b, c and j represent stable 100% flow through the vessel under investigation. Regions e and h represent different degrees of partial occlusions resulting in decreased flow rates compared to the unoccluded situation. Regions d and g represent the manipulation of the vessel necessary to achieve a new degree of partial occlusion and thus a new flow rate. Regions f and i represent release of the partial occlusion. It should be noted that immediately following release of occlusion, there is a transient increase in flow through the vessel which rapidly returns to the baseline 100% stable values.

The DSA and flow probe analyses were applied to all data sets (n = 36) resulting in a complete data set consisting of the EM probe flow value and corresponding flows calculated with the Fourier, gamma variate and Bursch forward triangle methods.

These results are presented in table 28. Figures 64, 65 and 66 respectively show the correlation curves between the EM flow probe data and the Fourier, gamma variate and Bursch forward triangle methods for calculating flow. It is clear that the Fourier method is superior with a coefficient of determination (R^2) of 0.99 ($p < 0.001$) compared to values of 0.24 and 0.20 for the gamma variate and Bursch techniques. For the Fourier method the line of regression is not significantly different from the line of identity ($p > 0.8$), while this is not the case for the other methods.

7.1.3 Discussion

The aim of this experimental work was to verify that the proposed Fourier methodology for measuring bulk blood flow in arteries from DSA data yielded results consistent with those obtained at the same time using an EM flow probe gold standard measurement technique. The experimental work was successfully completed and analyzed. Review of the regression lines for the three methods demonstrates that the results for the Fourier method are all within the 95% confidence limits of the line of identity and that for the other two methods, there is a wide variability with poor correlation between the EM flow probe values and the calculated flows. The Fourier method produces consistent results over the range of flows encountered clinically in vessels of this size, and could replace either of the other methods for performing such evaluations of bulk flow.

Table 28

These are the values for flow obtained for all animals, presented by method.

Animal	EM Probe Flow (ml/sec)		Digital Subtraction Angiography Flows (ml/sec)					
			Fourier		Gamma Variate		Bursch	
	Mean	SEM	Mean	SEM	Mean	SEM	Mean	SEM
1	2.358	0.008	2.736	0.240	2.016	0.175	0.653	0.057
2	5.479	0.049	5.038	1.171	2.392	0.154	2.003	0.129
	4.555	0.053	4.805	0.413	14.829	0.691	4.396	0.205
	2.263	0.011	2.609	0.302	10.632	0.536	4.522	0.228
	4.048	0.023	3.823	0.982	5.503	0.280	5.204	0.265
3	3.733	0.014	3.889	0.841	0.776	0.212	2.254	0.616
	2.727	0.007	2.518	0.545	1.062	0.077	1.489	0.109
	1.390	0.007	1.210	0.284	0.202	0.074	0.121	0.044
	0.868	0.007	0.816	0.347	0.065	0.010	0.059	0.009
4	12.490	0.041	12.538	0.562	3.515	0.158	4.217	0.189
	6.065	0.041	6.245	0.364	4.883	0.186	14.548	0.554
	4.820	0.024	4.552	1.220	0.520	0.027	1.065	0.055
5	7.504	0.018	7.236	0.821	9.284	0.863	30.169	2.803
	7.136	0.019	7.445	0.808	10.394	0.709	13.380	0.912
	7.166	0.026	7.260	0.709	5.181	0.346	6.343	0.424
	5.232	0.029	5.449	0.718	8.803	0.764	12.833	1.114
	5.718	0.033	5.770	0.463	6.123	0.480	7.667	0.601
	5.149	0.034	5.212	0.742	5.340	0.457	8.923	0.763
	3.632	0.018	3.830	0.408	4.358	0.383	3.970	0.349
	3.362	0.015	3.393	0.373	5.050	0.438	5.546	0.481
	2.617	0.012	2.565	0.250	2.652	0.236	3.416	0.304
	1.501	0.007	1.600	0.152	1.498	0.139	1.524	0.141
	0.807	0.004	0.752	0.143	0.343	0.035	0.303	0.031
6	3.123	0.011	3.235	0.519	2.532	0.235	8.227	0.764
	3.154	0.035	3.212	0.319	5.190	0.447	5.796	0.499
	2.888	0.042	2.887	0.445	3.619	0.308	4.085	0.347
	2.647	0.036	2.029	0.272	2.905	0.251	3.601	0.311
	2.542	0.037	2.107	0.700	3.248	0.288	3.261	0.289
	2.223	0.020	2.511	0.321	2.617	0.227	2.557	0.222
	1.127	0.023	1.213	0.313	0.906	0.081	0.989	0.088
	1.629	0.009	1.380	0.341	1.397	0.126	1.326	0.119
	0.525	0.006	0.808	0.091	0.129	0.012	0.233	0.022
7	2.594	0.009	2.695	0.834	0.178	0.025	0.153	0.022
	1.890	0.005	1.795	0.645	0.597	0.082	0.624	0.086
	1.227	0.004	1.373	0.389	0.968	0.166	19.521	3.353
	1.106	0.003	1.043	0.428	1.383	0.210	1.771	0.268

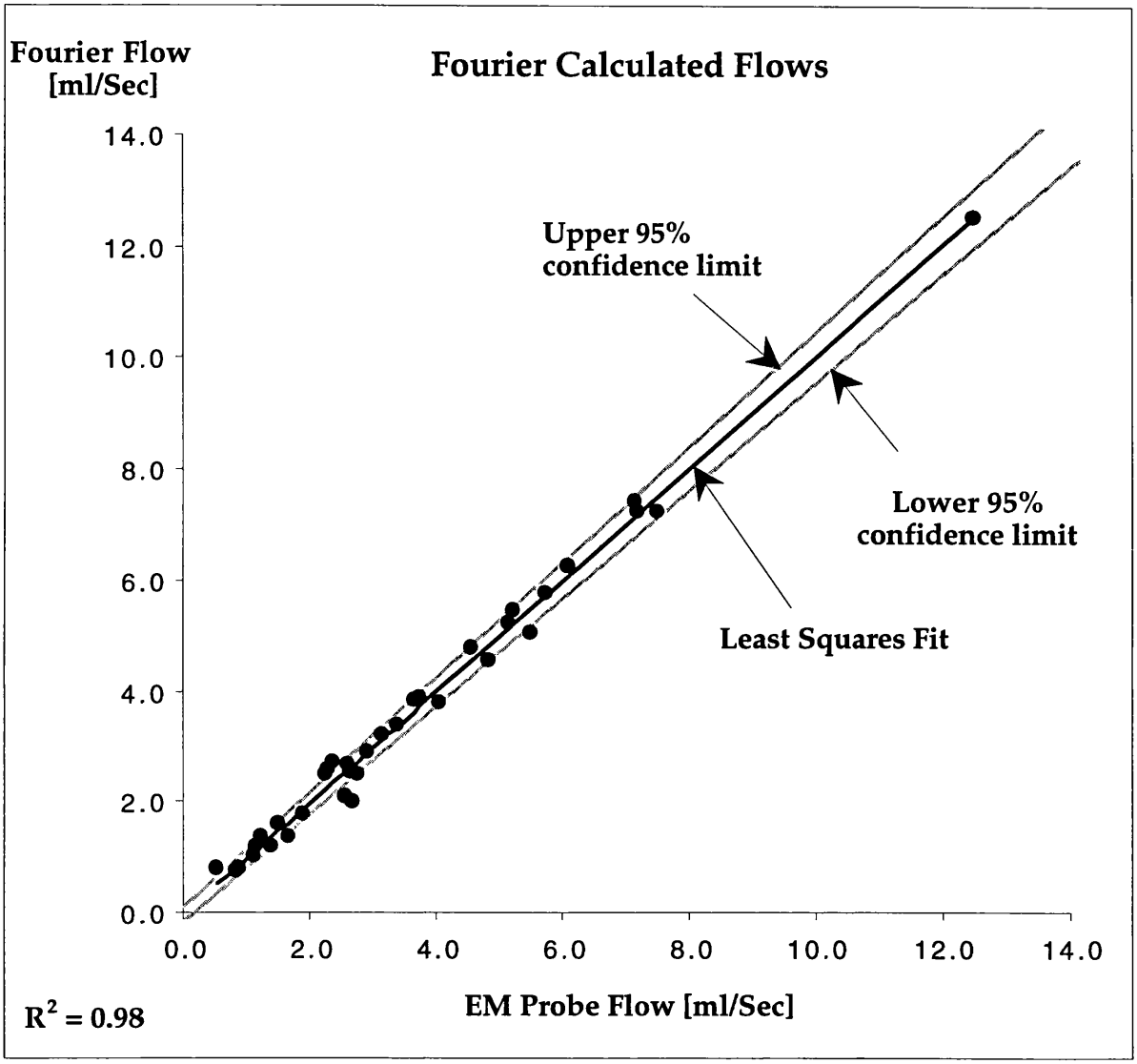

Figure 64. This is the regression of the EM flow probe "gold standard" against the Fourier transform method of volume flow extraction. The data are given in table 28. The coefficient of determination is $R^2 = 0.98$, and the slope of the line is 1.0022 with a p value of < 0.001. That is the line of regression is not significantly different from the line of identity.

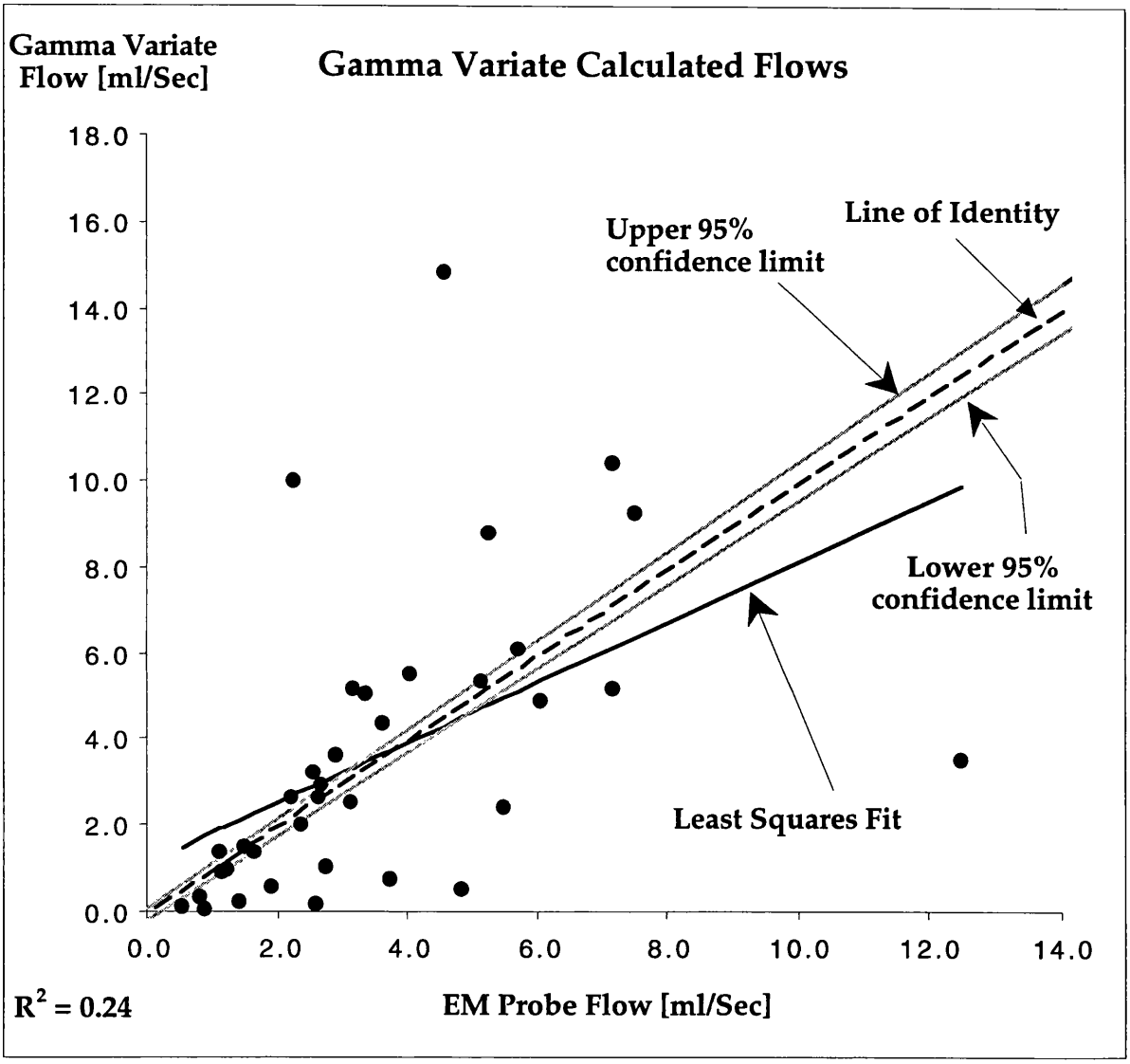

Figure 65. This is the regression of the EM flow probe "gold standard" against the gamma variate method of volume flow extraction. The data are given in table 28. The coefficient of determination is $R^2 = 0.24$, and the slope of the line is 0.70 with a p value of > 0.2. That is the line of regression is significantly different from the line of identity.

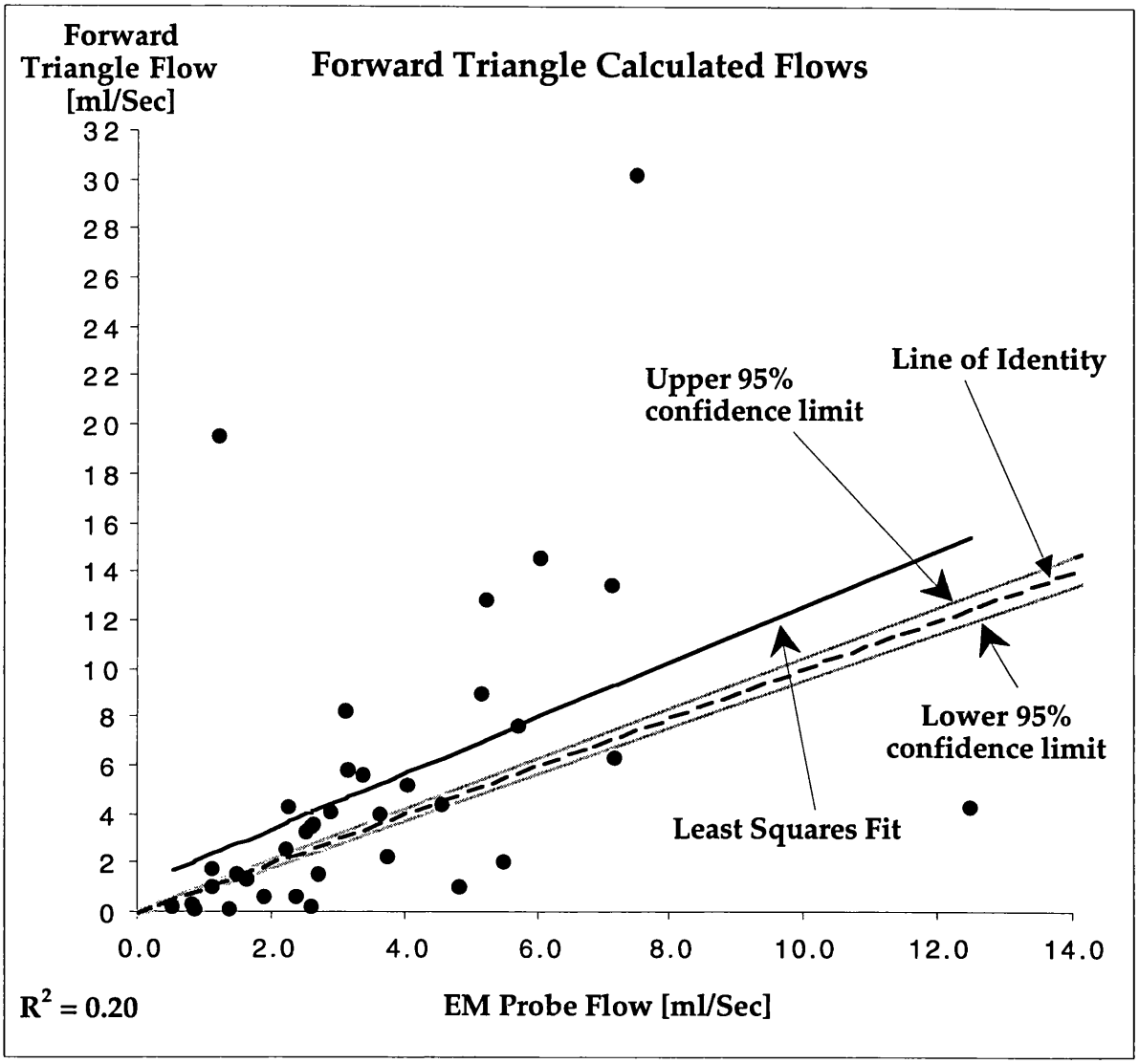

Figure 66. This is the regression of the EM flow probe "gold standard" against the Bursch forward triangle method of volume flow extraction. The data are given in table 28. The coefficient of determination is $R^2 = 0.20$, and the slope of the line is 1.15 with a p value of > 0.5. That is the line of regression is significantly different from the line of identity.

CHAPTER 8

SUMMARY, DISCUSSION AND CONCLUSIONS

8.1 Summary

In a worldwide context, DSA has reached an equilibrium in its deployment. Conventional vascular equipment has been replaced by digital systems, which have become the standard for routine use. The separation between intravenous and intra-arterial routes of introduction of contrast into the circulation has become more firmly established. For routine clinical cardiovascular work, arterial digital acquisition is now the norm, and the intravascular approach is used only in a few specific instances. The reasons for the benefits of DSA have been described in chapters 1 and 2, and basically are due to the increased contrast conspicuity available. This allows lower volumes of contrast to be given, with attendant improvement in patients' safety and comfort. By and large, the practical problems associated with routine DSA imaging are well recognised, and methods to minimize or exclude them have been developed, as discussed in chapter 3. Chapter 4 illustrates the main areas where intravenous DSA provides good quality imaging, and places the cardiac aspects of this acquisition methodology into perspective in relation to nuclear medicine and conventional cardiac cine angiography. Chapter 5 exemplifies the functional imaging features of DSA, while Chapter 6 discusses densitometric methods used to measure blood flow and proposes an improved technique for this purpose. Chapter 7 validates this method in an animal model.

8.2 Discussion

8.2.1 Clinical applicability of DSA

Considering the case of the veins draining into the right atrium, only a venous injection will give the highest image quality. This observation can be extended to the right atrium and right ventricle, with little argument about its efficacy. The benefits of imaging the pulmonary circulation following a right atrial injection of contrast are, however, still open for debate. Compared with selective pulmonary artery injection and cut film acquisition, the need for both ECG gating and some form of respiratory control make pulmonary digital *subtraction* angiography a

significantly more difficult procedure. If a non-subtracted, low resolution acquisition method is used, such as cine film, then DSA can be compared favourably. The principal problem with pulmonary DSA is movement misregistration. If this is either solved (by gating and respiratory control), or bypassed (by rapid acquisition > 10 frames/sec), then vascular detail and added information about capillary perfusion becomes available. In some centres, conventional cut film pulmonary angiography has been superceded by high resolution (1024 * 1024 matrix) digital acquisition without subtraction. Further improvements continue to be made; some centres are now acquiring images at 2048 * 2048 resolution. However, subtraction angiography is of substantial value during interventional procedures in the lung, eg. arteriovenous malformation (AVM) embolization, when used with superselective, subsegmental levels of contrast injection. Under these circumstances, very low volumes of dilute contrast are still able to give unparalleled detail of the very fine structure of an AVM and the lung tissue surrounding it. With the ability to construct a map of the relevant vessels to guide subsequent placement (road-mapping) of balloons or coils, DSA has found a really practical use in this field.

There is a polarization of views regarding the value of DSA in the assessment of the left ventricle. On the one hand, a direct intra-arterial injection of a low volume of contrast into the left ventricular cavity can give some information about wall motion and geometric ejection fraction. The opposing view holds that this approach leads to insufficient mixing between blood and contrast to define ventricular contours accurately, and hence provides poor data for wall motion and ejection fraction studies. This lack of homogeneity certainly hampers objective assessment of ventricular function. The alternative is to inject contrast into the right atrium and allow mixing to occur in the right ventricle and lungs; by the time the contrast and blood mixture reaches the left ventricle, it is homogenous. This allows good definition of the left ventricular anatomy and simultaneously permits the assessment of ventricular dynamics on the basis of timed changes in density measurements. One criticism of this latter approach is that cardiac and respiratory movement can be a problem. Certainly ECG gating and voluntary respiratory control are useful methods for removing misregistration. In my experience, however, voluntary respiratory control alone is sufficient to give good quality image series, especially if a fast framing rate is used to acquire the data. Chapters 4 and 5

show examples of the quality of left ventriculograms that can be obtained under these circumstances, even in patients who are quite ill and have compromised ventricular function. It should be noted at this point that no form of DSA can be expected to yield good quality images if there is poor cardiac output, or valvular regurgitation at any level. Another benefit of the homogeneity of the contents of the left ventricle lies in the feasibility of assessment of parametric data. Nuclear cardiology utilizes Fourier analysis and paradox imaging in order to quantify the timing and extent of ventricular contraction. As blood pool imaging is usually undertaken in the LAO projection to separate the right and left ventricles, it is not directly comparable to the conventional cine angiogram investigation. Digital subtraction imaging, however, separates the right and left ventricles in time rather than space. This allows a conventional RAO 30° projection to be used and analysed. Examples of left ventricular parametric imaging are shown in chapter 5. As can be seen, the data are of good quality and high resolution. Nevertheless the techniques have not gained support amongst clinicians. This is probably due to the lack of adequately validated software, and the necessarily time consuming nature of the preparation for analysis. The equivalent nuclear medicine studies are clinically just as useful and certainly more easily and cheaply obtained. If the spatial resolution is of paramount importance, however, then intravenous DSA is unsurpassed and does allow the RAO 30° projection favoured by cardiologists.

Whilst intravenous DSA ventriculography has become largely acceptable, investigation of the coronary circulation by the intravenous route remains virtually unacceptable. There is too much complex movement of each coronary artery to yield a satisfactory view of the coronary tree following an injection of contrast into the right atrium. If, however, coronary bypass grafts are being visualised, then under some circumstances, sufficiently good views maybe obtained by this route to allow screening for patency to take place. However, as section 4.1.5 demonstrates, an aortic root injection with DSA imaging provides so much better anatomical detail that any argument in favour of the intravenous approach is doomed. When coupled with the ability to perform day-case, small catheter angiography, there can be little doubt that the correct screening test for graft patency is DSA with aortic root injection, although proponents of real-time cine-CT or MR angiography may disagree.

Although graft patency can adequately be assessed by non-selective injection of contrast, conventional selective techniques are required to define native coronary artery morphology. The benefit in using DSA is that it provides a timed series of images from which additional physiological information may be gathered. The passage of contrast through the myocardium can be studied in terms of rate and extent. Neither of these physiological data are easily available from conventional cine angiography. This is because there are inconsistencies in cine film data. In itself, cine film provides a cheap, perfectly adequate record of the anatomy of the coronary circulation, sufficient for routine clinical use. If more detailed analysis is necessary, then digitization of the film must be undertaken. Since the densities on the film depend on the exposure, developer concentration, developer temperature, development time and type of film used, linear data is almost impossible to extract reliably. Nonetheless, the extraction of such density data has been undertaken by many groups, but the measurements which are realised have wide variations and significant errors inherent within them (Bursch, J.H., Johs, R., et al., 1971; Bursch, J.H., Heintzen, P.H., et al., 1974; Erikson, U., Lindgren, P.G., et al., 1977; Brennecke, R., Bursch, J.H., et al., 1978; Hoornstra, K., Hanselman, J.M., et al., 1980; Lantz, B.M., Foerster, J.M., et al., 1980a; Lantz, B.M., Foerster, J.M., et al., 1980b; Alderman, E.L., Berte, L.E., et al., 1981; Bursch, J.H., Hahne, H.J., et al., 1981; Erikson, U., Helmius, G., et al., 1981; Bursch, J.H. 1983; Bursch, J.H., Hahne, H.J., et al., 1983; Dodge, H.T. and Sheehan, F.H. 1983; Erikson, U., Helmius, G., et al., 1983; Kruger, R.A., Bateman, W., et al., 1983; Bogren, H.G. and Bursch, J.H. 1984; Bursch, J.H. 1985; Bursch, J.H., Hahne, H.J., et al., 1985; Haude, M., Brennecke, R., et al., 1990).

Digital subtraction angiography with its well defined and well behaved characteristics has been used in several centres for the assessment of myocardial flow reserve and perfusion dynamics. In particular, the effects on these parameters of pharmacological or surgical interventions have been studied. The ability to assess these effects objectively allows unbiased conclusions about treatment efficacy to be reached. The methods of analysis are still time consuming, however, and in general are limited to research projects rather than applied in routine clinical practice. Section 5.2 outlines a simple study which demonstrated changes in myocardial transit times following sublingual vasodilator intervention. As more objective methods for assessing drug effect become mandatory, DSA imaging, combined with

analysis of vascular dynamics, may prove to be a satisfactory means of fulfilling these requirements.

8.2.2 Blood flow measurement

The whole issue of blood flow measurement has been investigated for over 3 decades by many groups all over the world. Of the many problems inherent in extracting blood flow data, perhaps the two most serious are: i) estimation of true vessel dimensions; and ii) establishing true, noise free, density-time curve data. The historical background and limitations of non-DSA data are described and placed into context in sections 6.1 and 6.2. Section 6.3 suggests the benefits of DSA and this leads on to a synopsis of the mathematics necessary to measure volume blood flow. Fundamental to all methodologies of x-ray flow measurement is the change in x-ray attenuation as a mixture of iodine contrast and blood flows through a vessel. Whether or not the vessel is straight, curved, branching, or singular, only the local changes in attenuation are available for analysis. The statistical nature of x-ray imaging inevitably leads to an inherent variability in the data recorded. In some instances this variation is substantial. For instance, a cine record, without subtraction, contains more noise than an equivalent DSA record. In any event, the attenuation or density-time curves are far from perfect. These then require fairly complex analysis of the data in order to extract desired parameters. Unfortunately, these parameters - usually a time measurement and a geometric measurement - are deceptive in the ease of their extraction.

Examining a record of a DSA run with a contrast/blood mixture entering a vessel, reaching peak attenuation, and leaving the field of view gives an impression of time events which seem very obvious. The problem with such subjective interpretation is that we integrate and smooth the data without our active knowledge. Such a subjective assessment of flow phenomena disintegrates when objective measurements are made of density or attenuation data. In order to extract meaningful results from noisy, imperfect data, recourse has to be made to mathematical techniques. The key values of interest are a displacement and a time. Together, these give a velocity. To convert this to volumetric flow, a geometric measurement of vessel dimensions is necessary. Implicit in the latter is the assumption that arteries have a circular cross section. This is not always true, for

instance in the region of an atheromatous plaque. For the purposes of the current discussion, these complications have been ignored. Once a density-time curve has been extracted from a region of interest placed over the vessel, two methods of volume flow measurement become feasible. The flaw in the approach which integrates the area under such a curve and calculates flow from that, has been discussed in section 6.4.3.1. The alternative approach depends on three measurements: distance, vessel diameter, and time. Each of these has an error associated with its value. However, unlike the problem of exposure timing with the integration technique, these errors are capable of being estimated. Thus they can be accounted for and minimised. A significant portion of this thesis is devoted to a description of the methodology for the accurate assessment of these errors during measurement.

Of the three parameters, distance is trivially simple in its measurement and has only a small error associated with it. Vessel diameter is more complex and difficult to assess accurately. A reproducible method has been described in section 6.4.2 which uses all the available information to reduce the possible error. Perhaps not surprisingly, the ability to define an edge is limited to about 1/2 a pixel. Therefore the cross sectional diameter can, at best, be defined to within 1 pixel; despite the wish for better resolution, it has been shown that, in the presence of significant levels of noise, ± 1 pixel is the best that can be expected. The last measurement - time - is the most fraught. As has been demonstrated, an inordinate amount of effort has gone into perfecting a reproducible method for timing the movement of contrast along a blood vessel. The fundamental problem with making this measurement is *noise*. If the density-time curves were perfect and, by implication, noise-free, all the available methods would work equally well. This has been shown by reference to a perfect data-set and discussed and illustrated in chapter 6, figs 46, 47, and 53. With real data, even obtained under artificially ideal circumstances, there is a significant element of random noise. Until this point, the term 'noise' has been used rather loosely to mean the effects of quantum mottle, electronic noise in the imaging chain, imperfect focussing within the image intensifier, TV signal variability, quantization limits, patient movement (both voluntary and involuntary), and limited inhomogeneity in the mixing of blood and contrast.

A review of the available methods for time parameter extraction revealed that techniques of curve fitting to smoothed and bounded data together with visual estimation were the most commonly employed. The results were found to be variable, even unreliable at times; this lack of reliability is further compounded by our inability to recognise its occurrence. This thesis proposes an approach to the measurement of time by moving into the frequency domain through the use of Fourier methods and subsequent measurement of time differences as phase shifts between density-time curves. This approach has been described and its behaviour analysed under noisy conditions using mathematical modelling methods. These same methods have been used to investigate and objectively quantify the robustness of the more traditional means of timing parameter extraction, namely, gamma variate curve fitting and forward triangle estimation of reference points on density-time curves. The Fourier method appears to be more robust and less subjective than either of the other methods, at least in theoretical data in the presence of varying amounts of random noise. Clearly, whilst of interest, such a pure mathematical treatment raises questions of applicability under clinical conditions.

In order to validate, and indeed compare, the various techniques with Fourier methods, in vivo experiments were undertaken using farm pigs. The accepted gold standard for volume flow measurement has been a properly calibrated electromagnetic flow meter. Such a device was used and the measurements obtained from it directly. Since the animals were anaesthetised, and there was complete control over their respiration and movement, these sources of potential error were largely eliminated. In patients, however, such controlled circumstances are not usually present during routine DSA and, under normal clinical conditions, the potential for error would be somewhat greater. Nevertheless, the experimental data still provide a useful testing ground for the different methods of parameter extraction. After all, if under ideal conditions one or the other method fails, it can hardly be expected to work under the less ideal circumstances found in clinical practice. After analysis, the results are encapsulated in 3 graphs, figures 64, 65 and 66. As can be seen, the non-Fourier methods yield erratic values and reflect the problems identified in the theoretical section of this thesis. The proposed Fourier method (chapter 6) was shown to be consistent in its ability to yield a volume flow measurement accurately. Recently, the technique has been applied for the measurement of flow in the vertebro-basilar artery in animals with induced

subarachnoid haemorrhage. Its application in similar studies in patients might prove useful for clinical management. The Fourier method coupled with the edge detection algorithm has the potential to give the most reliable results in research for validating the use of drugs with cardiovascular effects.

8.3 Conclusion

Digital subtraction angiography adds an extra dimension to simple anatomical imaging of vascular structures, in that it provides timing information making analysis of physiological properties possible (Pijls, N.H., Uijen, G.J., et al., 1990). As a result, simultaneous assessment of structure and function becomes possible. This thesis proposes and validates a novel Fourier Transform based analysis method for calculation of blood flow from a DSA data set.

With increasing computer power, the implementation of physiological DSA techniques have become feasible for both routine clinical use and also as a tool for the evaluation of pathophysiological phenomena related to myocardial perfusion (Schuhlen, H., Eigler, N.L., et al., 1994; Vassanelli, C., Menegatti, G., et al., 1995; Haude, M., Caspari, G., et al., 1997). These dynamic perfusion analyses from DSA data are becoming increasingly important in the study of cardiovascular disease as as they permit simultaneous evaluation of anatomy and physiology (Felder, L.M., Hess, O.M., et al., 1992; Rother, T., Duck, H.J., et al., 1992). Studies in man are being carried out to fully assess the impact of DSA based methods for tissue blood flow and perfusion measurement and to define their proper role in patient management (Simon, R., Herrmann, G., et al., 1990; Pijls, N.H., Aengevaeren, W.R., et al., 1991; Haude, M., Caspari, G., et al., 1997). DSA has matured as a technology, and currently enjoys the respectability of an established main stream imaging modality. High quality anatomical information as well as good physiological data are simultaneously available in the cardiovascular system through this technique.

Bibliography

Alderman, E.L., Berte, L.E., Harrison, D.C., Sanders, W. (1981). "Quantitation of Coronary Artery Dimensions Using Digital Imaging Processing." Society of photo optical instrumentation engineers 314(273): 273-278.

Ameuille, P., Ronneaux, G., Hinault, V., Desgre, A., Lemoine, J.M. (1936). "Remarques Sur Quelques Cas D'arteriographia Pulmonaire Chez L'homme Vivant." Bulletine et memoires de la Societe Medicale des hospitaux de Paris. 52: 79.

Arnold, V., Eisenberg, H., Borger, D. (1981). "Digital Video Angiography System Evaluation." Applied Radiology 10: 81-90.

Bateman, W.A., Kruger, R.A. (1984). "Blood Flow Measurement Using Digital Angiography and Parametric Imaging." Medical Physics 11(2): 153-157.

Beyer, W.H. (1981). Crc Standard Mathematical Tables. 27 ed. Boca Raton, Florida: CRC Press.

Bogren, H.G., Bursch, J.H. (1984). "Digital Angiography in the Diagnosis of Congenital Heart Disease." Cardiovascular & Interventional Radiology 7(3-4): 180-191.

Brennecke, R., Bursch, J.H., Heintzen, P.H. (1978). Improvements in Videodensitometric Measurement Techniques. In: Heintzen, P.H., Bursch, J.H., editors. Roentgen Video Techniques for Dynamic Studies of Structure and Function of the Heart and Circulation. Stuttgart: Georg Thieme; p. 15-22.

Bursch, J.H., Johs, R., Kirbach, H., Schnurer, C., Heintzen, P.H. (1971). Accuracy of Videodensitometric Flow Measurements. In: Heintzen, P.H., editor. Roentgen, Cine and Videodensitometry. Stuttgart: Georg Thieme; p. 119.

Bursch, J.H., Heintzen, P.H., Simon, R. (1974). "Videodensitometric Studies by a New Method of Quantitating the Amount of Contrast Medium." European Journal of Cardiology 1(437).

Bursch, J.H., Hahne, H.J., Brennecke, R., Gronemeier, D., Heintzen, P.H. (1981). "Assessment of Arterial Blood Flow Measurements by Digital Angiography." Radiology 141: 39-47.

Bursch, J.H., Hahne, H.J., Brennecke, R., Eicker, C., Heintzen, P.H. (1983). Arterial Blood Flow Analysis by Digital Angiography. In: Heintzen, P.H., Brennecke, R., editors. Digital Imaging in Cardiovascular Radiology. Stuttgart: Georg Thieme; p. 115-123.

Bursch, J.H. (1983). "Use of Digitized Functional Angiography to Evaluate Arterial Blood Flow." Cardiovascular & Interventional Radiology 6(4-6): 303-310.

Bursch, J.H., Hahne, H.J., Heintzen, P.H. (1985). "Functional Imaging of Blood Flow." Annales de Radiologie 28(2): 183-188.

Bursch, J.H. (1985). "Densitometric Studies in Digital Subtraction Angiography: Assessment of Pulmonary and Myocardial Perfusion." Herz 10(4): 208-214.

Caceci, M.S., Cacheris, W.P. (1984). "Fitting Curves to Data." Byte 9(5): 340-362.

Calvert, M.H., Pullan, B.R., Bone, D.E. (1975). "A Simple Method for Measuring the Frequency Response of an Electromagnetic Flowmeter." Medical & Biological Engineering 13(4): 592-594.

Cardella, J.F., Casarella, W.J., Deweese, J.A., Dorros, G.M., Gray, J.E., Katzen, B.T., Laragh, J.H., Levin, D.C., Marks, V.M., Nickoloff, E.L. (1994). "Optimal Resources for the Examination and Endovascular Treatment of the Peripheral and Visceral Vascular Systems. Aha Intercouncil Report on Peripheral and Visceral Angiographic and Interventional Laboratories." Cirulation 89(3): 1481-1493.

Castellanos, A., Pereiras, R., Garcia, A. (1937). "La Angiocardiographia Radio-Opaca." Archivos de la Sociedad de estudios Clinicos de Habana 31: 523-596.

Cellis, A.S. (1946). "Angiocardiographia. Not a Preliminar Sobre Un Metodo Personal." Revista Medica del Hospital General 8: 1101-1110.

Cournand, A., Ranges, H.A. (1941). "Catheterisation of the Right Auricle in Man." Proceedings of the Society of Experimental Biology and Medicine 46: 462-466.

Crummy, A.B., Strother, C.M., Sackett, J.F., Ergun, D.L., Shaw, C.G., Kruger, R.A., Mistretta, C.A., Turnipseed, W.D., Lieberman, R.P., Myerowitz, P.D., Ruzicka, F.F. (1980). "Computerized Fluoroscopy: Digital Subtraction for Intravenous Angiocardiography and Arteriography." American Journal of Roentgenology 135(6): 1131-1140.

Crummy, A.B., Stieghorst, M.F., Turski, P.A., Strother, C.M., Lieberman, R.P., Sackett, J.F., Turnipseed, W.D., Detmer, D.E., Mistretta, C.A. (1982). "Digital Subtraction Angiography: Current Status and Use of Intra-Arterial Injection." Radiology 145(2): 303-307.

Davisson, C.M. (1965). Chapter 2. In: Siegbahn, K., editor. Alpha, Beta and Gamma Ray Spectroscopy. Amsterdam: North-Holland.

Dodge, H.T., Sheehan, F.H. (1983). "Quantitative Contrast Angiography for Assessment of Ventricular Performance in Heart Disease." Journal of the American College of Cardiology 1(73): 73-81.

Dos Santos, R., Lamas, A.C., Caldas, J.P. (1931). Arteriographie Des Membres Et De L'aorte Abdominale. In. Paris: Masson et Cie.; p. 11.

Dotter, C., Steinberg, I., Temple, H. (1949). "Automatic Roentgenray Roll-Film Magazine for Angiocardiography and Cerebral Arteriography." American Journal of Roentgenology 62: 355-358.

Dyet, J.F., Hartley, W., Cohen, A.R., Aber, C.B. (1992). "Digital Cardiac Imaging - the Death Knell of Cineangiography?" British Journal of Radiology 65(777): 818-821.

Erikson, U., Ruhn, G., Wolgast, M. (1975). "Measurement of Total and Regional Renal Blood Flow by Means of a Videodensitrometric Method." Scandinavian Journal of Urology & Nephrology.

Erikson, U., Bjork, L., Cullhed, I., Enghoff, E., Ruhn, G. (1976). "Videodensitometry in the Diagnosis of Aortic Incompetence." Acta Radiologica: Diagnosis 17(3): 361-368.

Erikson, U., Lindgren, P.G., Lofroth, P.O., Ruhn, G., Wolgast, M. (1977). "Measurements of Total and Regional Renal Blood Flow by Videodensitometry." Acta Radiologica: Diagnosis 18(2): 225-234.

Erikson, U., Bjork, L., Cullhed, I., Enghoff, E., Nordgren, L., Ruhn, G. (1978). "Left Ventricular Function Evaluated by Videodensitometry in Patients with Coronary Heart Disease." Acta Radiologica: Diagnosis 19(5): 737-746.

Erikson, U., Helmius, G., Pavek, K., Ruhn, G. (1980). "Videodensitometry and Thermodilution for Measuring Left Ventricular Function." Acta Radiologica: Diagnosis 21(5): 621-625.

Erikson, U., Ruhn, G., Bjork, L. (1980). "Videodensitometry in Angiography." Medicamundi 25(4): 4-8.

Erikson, U., Helmius, G., Ruhn, G., Aberg, T. (1980). "Determination of Pulmonary Blood Flow by Videodensitometry." Bulletin Europeen de Physiopathologie Respiratoire 16(5): 663-670.

Erikson, U., Helmius, G., Hennig, K., Johansson, L., Enghoff, E., Ruhn, G. (1981). "Determination of Myocardial Blood Flow by Videodensitometry. A Preliminary Report." Rofo: Fortschritte auf dem Gebiete der Rontgenstrahlen und der Nuklearmedizin 135(4): 404-406.

Erikson, U., Helmius, G., Ruhn, G., Sawada, S. (1983). "Measurement of Regional Lung Blood Flow by Videodensitometry." Acta Radiologica: Diagnosis 24(3): 195-199.

Evans, R.D. (1968). Chapter 3. In: Attix, F., Roesch, W.C., editors. Radiation Dosimetry, Volume 1. New York: Academic Press.

Felder, L.M., Hess, O.M., Vassalli, F., Jiang, Z., Grimm, J., Krayenbuhl, H.P. (1992). "[Digital Subtraction Angiography for the Assessment of Myocardial Perfusion]." Schweiz Rundsch Med Prax 81(43): 1277-1280.

Finby, N. (1964). Intravenous Aortography. In: Scholinger, R.A., Ruzicka, F.F., editors. Vascular Roentgenology. New York: Macmillan Co.; p. 329-342.

Forssmann, W. (1929). "Die Sondierung Des Rechten Herzens." Klinische Wochenschrift 8: 2085-2087.

Forssmann, W. (1931). "Uber Kontrastdarstellungen Der Hohlen Des Lebenden Rechten Herzens Und Der Lungenschlagader." Munchener Medizinische Wochenschrift 78: 489-492.

Fox, I.J., Brooker, L., Hesseltine, D.W., Wood, E.H. (1956). "A New Dye for Continuous Recording of Dye Dilution Curves in Whole Blood Independent of Variations in Blood Oxygen Saturation." Circulation 14(937): 937-938.

Franck, O., Alwens, W. (1910). "Kreislaufstudien Am Roentgenschirm." Munchener Medizinische Wochenschrift 78: 489-492.

Gidlund, A. (1949). "New Apparatus for Direct Cineroentgenography." Acta Radiologica 32: 81-88.

Greenbaum, R.A., Evans, T.R. (1984). "Investigation of Left Ventricular Function by Digital Subtraction Angiography." British Heart Journal 51(2): 163-167.

Guntert, W., Zimmer, E.A. (1957). "Grundlagen Fur Die Messung Der Stromungsgeschwindigkeit Des Blutes Mittels Einer Roentgenkymographischen Messmetode." Cardiology (supplement 7).

Hackbarth, W., Bircks, W., Politz, B., Korfer, R., Schmiel, F.K., Spiller, P. (1980). "[Videodensitometric and Electromagnetic Flow Measurements in Aorto Coronary Bypass Grafts (Author's Transl)]. [German]." Rofo: Fortschritte auf dem Gebiete der Rontgenstrahlen und der Nuklearmedizin 132(5): 554-560.

Hamilton, W.F., Moore, J.W., Kinsman, J.M., Spurling, R.G. (1928). "Simultaneous Determination of Pulmonary and Systemic Circulation Times in Man and of Figure Related to Cardiac Output." American Journal of Physiology 84: 338-344.

Haschek, E., Lindenthal, O. (1896). "Ein Beitrag Zur Praktischen Verwertung Der Photographie Nach Roentgen." Wiener Klinische Wochenschrift 9: 63-64.

Haude, M., Brennecke, R., Erbel, R., Lang, M., Deutsch, H.P., Renneisen, U., Meyer, J. (1990). "Parametric Assessment of Myocardial Perfusion During Interventional Cardiac Catheterization by Means of X-Ray Densitometry-Short-and Long-Term Results." International Journal of Cardiac Imaging 5(2-3): 183-190.

Haude, M., Caspari, G., Baumgart, D., Spiller, P., Heusch, G., Erbel, R. (1997). "[New Developments in Parameter-Oriented Roentgen Densitometry Perfusion Analysis within the Scope of Heart Catheter Studies]." Herz 22(2): 72-86.

Hayward, R., Hunter, G.J. (1985). "Digital Subtraction Angiography in Coronary Artery Bypass Graft Assessment: Clinical Applicability." British Heart Journal 54(4): 357-361.

Heintzen, P.H., Pilarczyk, J. (1971). Videodenistometry with Contoured and Controlled Windows. In: Heintzen, P.H., editor. Roentgen- Cine- and Videodensitometry. Stuttgart: George Thieme; p. 56.

Hesselink, J.R., Chang, K.H., Chung, K.J., Abbate, L., Goodsitt, M. (1986). "Flow Analysis with Digital Subtraction Angiography: 2. Acquisition and Accuracy of Transit-Flow Measurements." Ajnr: American Journal of Neuroradiology 7(3): 427-431.

Hesselink, J.R., Chang, K.H., Chung, K.J., Abbate, L. (1986). "Flow Analysis with Digital Subtraction Angiography: 1. Description of a Simplified Flow Model." American Journal of Neuroradiology 7(423): 423-426.

Heuck, F., Anschutz, F., Schwartzkopf, H.J. (1963). "Ein Roentgenkinematographisches Verfahren Zur Quantitativen Bestimmung Des Blutstromvolumens." Roefo 98(428): 428-438.

Hoornstra, K., Hanselman, J.M., Holland, W.P., De Wey Peters, G.W., Zwamborn, A.W. (1980). "Videodensitometry for Measuring Blood Vessel Diameter." Acta Radiologica: Diagnosis 21(2A): 155-164.

Houston, A.S., Macleod, M.A. (1984). A Comparitive Review of Methods of Obtaining Amplitude/Phase and Related Images for Gated Cardiac Studies. In: Deconick, F., editor. Information processing in medical imaging (8th conference); The Hague: Martinus Nijhof.

Hunter, G.J., Hayward, R. (1985). Myocardial Perfusion: An Assessment by Digital Subtraction Angiography. In: British Cardiac Society.; London, U.K.

Hunter, G.J., Hunter, J.V., Brown, N.J. (1986). "Parametric Imaging Using Digital Subtraction Angiography." British Journal of Radiology 59(697): 7-11.

Hunter, G.J., Thomas, H., Treasure, T., Sturridge, M.F., Swanton, R.H. (1988a). "Demonstration of the Ascending Aorta in Infective Endocarditis by Intravenous Digital Subtraction Angiography [See Comments]." British Heart Journal 60(3): 252-258.

Hunter, G.J., Thomas, H., Treasure, T., Sturridge, M.F., Swanton, R.H. (1988b). "Demonstration of the Ascending Aorta in Infective Endocarditis by Intravenous Digital Subtraction Angiography." British Heart Journal 60(252): 252-258.

Knoefel, P.K., Huang, K.C. (1956). "The Biochemorphology of Renal Tubular Transport: Iodinated Benzoic Acids." Journal of Pharmacological exp. Therapy 117(307): 307-316.

Kruger, R.A. (1981). "Estimation of the Diameter of and Iodine Concentration within Blood Vessels Using Digital Radiography Devices." Medical Physics 8(5): 652-658.

Kruger, R.A., Mistretta, C.A., Riederer, S.J. (1981). "Physical and Technical Considerations of Computerized Difference Imaging." IEEE transactions on Nuclear Science 28: 205-211.

Kruger, R.A. (1982). Basic Physics of Computerized Fluoroscopy Difference Imaging. In: Digital Subtraction Arteriography: An Application of Computerized Fluoroscopy. Chicago: YearBook Medical Publishers; p. 16-21.

Kruger, R.A., Bateman, W., Liu, P.Y., Nelson, J.A. (1983). "Blood Flow Determination Using Recursive Processing: A Digital Radiographic Method." Radiology 149(1): 293-298.

Lamb, H. (1932). Hydrodynamics. Cambridge: Cambridge University Press.

Lambossy, P. (1952). "Oscillations Forcees D'un Liquide Incompressible Et Viscueux Dans Un Tube Rigide Et Horizontal. Calcul De La Force Frottement." Helvetica Physiologica Acta 8(209): 209-227.

Lantz, B.M., Foerster, J.M., Link, D.P., Holcroft, J.W. (1980a). "Determination of Relative Blood Flow in Single Arteries: New Video Dilution Technique." Ajr. American Journal of Roentgenology 134(6): 1161-1168.

Lantz, B.M., Foerster, J.M., Link, D.P., Holcroft, J.W. (1980b). "Angiographic Determination of Cerebral Blood Flow." Acta Radiologica: Diagnosis 21(2A): 147-153.

Lantz, B.M., Foerster, J.M., Link, D.P., Holcroft, J.W. (1981). "Regional Distribution of Cardiac Output: Normal Values in Man Determined by Video Dilution Technique." American Journal of Reontgenology 137(5): 903-907.

Magni, G.A. (1954). "Technical Problems in Rapid Serial Radiography." Acta Radiologica (suppl) 116: 638-648.

Mancini, G.B., Ostrander, D.R., Slutsky, R.A., Shabetai, R., Higgins, C.B. (1983). "Intravenous Vs. Left Ventricular Injection of Ionic Contrast Material: Hemodynamic Implications for Digital Subtraction Angiography." American Journal of Roentgenology 140(3): 425-430.

Mancini, G.B., Norris, S.L., Peterson, K.L., Gregoratos, G., Wildmann, T.F., Ashburn, W.L., Higgins, C.B. (1983). "Quantitative Assessment of Segmental Wall Motion Abnormalitites at Rest and after Atrial Pacing Using Digital Intravenous Ventriculography." Journal of the American College of Cardiology 2(1): 70-76.

Mancini, G.B., Higgins, C.B., Norris, S.L., Slutsky, R.A. (1983). "Cardiac Imaging with Digital Subtraction Angiography." Cardiovascular & Interventional Radiology 6(4-6): 252-262.

Mancini, G.B., Hodgson, J.M., Legrand, V., Bates, E.R., Aueron, F.M., Lefree, M.T., Smith, J.S., Beauman, G.J., Vogel, R.A. (1985). "Quantitative Assessment of Global and Regional Left Ventricular Function with Low-Contrast Dose Digital Subtraction Ventriculography." Chest 87(5): 598-602.

Nelder, J.A., Mead, R. (1965). "A Simplex Method for Function Minimization." Computer Journal 7(308).

Neuhaus, K.L., Sauer, G., Krause, H., Tebbe, U. (1986). Videdensitometric Measurement of Coronary Flow. In: Just, H., Heintzen, P.H., editors. Angiocardiography, Current Status and Future Developments. Berlin: Springer Verlag; p. 383-388.

Oppenheim, A.V., Willsky, A.S., Nawab, S.H. (1997). Signals and Systems. 2nd ed. Upper Saddle River, New Jersey: Prentice Hall.

Pijls, N.H., Uijen, G.J., Hoevelaken, A., Pijnenburg, T., Van Leeuwen, K.L., Fast, J.H., Bos, H.S., Aengevaeren, W.R., Van Der Werf, T. (1990). "Mean Transit Time for Videodensitometric Assessment of Myocardial Perfusion and the Concept of Maximal Flow Ratio: A Validation Study in the Intact Dog and a Pilot Study in Man." Int J Card Imaging 5(2-3): 191-202.

Pijls, N.H., Aengevaeren, W.R., Uijen, G.J., Hoevelaken, A., Pijnenburg, T., Van Leeuwen, K., Van Der Werf, T. (1991). "Concept of Maximal Flow Ratio for Immediate Evaluation of Percutaneous Transluminal Coronary Angioplasty Result by Videodensitometry [See Comments]." Circulation 83(3): 854-865.

Pullan, B.R. (1981). Digital Radiology. In: Moores, B.M., Parker, R.P., Pullan, B.R., editors. Physical Aspects of Medical Imaging. London: John Wiley and Sons Ltd.

Rabe, F.E., Yune, H.Y., Klatte, E.C., Miller, R.E. (1982). "Efficacy of Glucagon for Abdominal Digital Angiography." Ajr. American Journal of Roentgenology 139(3): 618-619.

Reynolds, R.J. (1935). "Cine-Radiography." American Journal of Roentgenology and Radium Therapy 41: 1-17.

Robb, J.P., Steinberg, I. (1938). "A Practical Method of Visualisation of the Chambers of the Heart and the Great Blood Vessels in Man." Journal of clinical investigation 17: 507.

Robb, J.P., Steinberg, I. (1939a). "Visualisation of the Chmabers of the Heart, the Pulmonary Circulation and the Great Blood Vessels in Man: A Practical Method." American Journal of Roentgenology and Radium Therapy 41: 1-17.

Robb, J.P., Steinberg, I. (1939b). "Visualisation of the Chambers of the Heart, the Pulmonary Circulation and the Great Vessels in Heart Disease." American Journal of Roentgenology and Radium Therapy 42: 14-36.

Roehrig, H., Nudelman, S., Capp, M.P., Frost, M.M. (1977). "X-Ray Image Intensifier Video System for Diagnostic Radiology." Society of photo optical instrumentation engineers 127(216): 216-225.

Roehrig, H., Lum, B., Fisher, D. (1979). "Digital Method to Evaluate the Noise of X-Ray Image Intensifiers." Society of photo optical instrumentation engineers 206(135): 135-145.

Roentgen, W.C. (1895). "Uber Eine Neue Art Von Strahlen. Vorlaufige Mittheilung." Sitzungsbericht, Physikalische, Medizinische Gesellschaft Wurzburg 137: 132-141.

Rosen, L., Silverman, N.R. (1973). "Videodensitometric Measurements of Blood Flow Using Crosscorrelation Techniques." Radiology 109(2): 305-310.

Rother, T., Duck, H.J., Neugebauer, A., Lobe, M. (1992). "[Densitometry Determination of Coronary Flow Rates Using Digital Subtraction Angiography (Dsa). Methods, Multiple Examinations and Interobserver Comparison]." Z Gesamte Inn Med 47(7): 291-298.

Rutishauser, W., Bussmann, W.D., Noseda, G., Meier, W., Wellauer, J. (1970). "Blood Flow Measurement through Single Coronary Arteries by Roentgen Densitometry. I. A. Comparison of Flow Measured by a Radiologic Technique Applicable in the Intact Organism and by Electromagnetic Flowmeter." American Journal of Roentgenology, Radium Therapy & Nuclear Medicine 109(1): 12-20.

Saddekni, S., Sos, T., Sniderman, K.W., Srur, M., Bodner, L.J., Kneeland, J.B., Cahill, P.T. (1984). "Optimal Injection Technique for Intravenous Dsa." Radiology 150: 655-659.

Sanchez, P.J. (1943). "The Cranial Seriograph and Its Utility in Neurologic Radiology for Cerebral Angiography." Surgery 13: 661-666.

Sandler, H., Dodge, H.T. (1968). "The Use of Single Plane Angiocardiograms for the Calculation of Left Ventricular Volume in Man." American Heart Journal 75(3): 325-334.

Schmiel, F.K., Huber, H., Neuhaus, K.L., Spiller, P. (1978). Densitometric Measurement of Coronary Blood Flow. Methodical Improvements. In: Heintzen, P.H., Bursch, J.H., editors. Roentgen Video Techniques for Dynamic Studies of Structure and Function of the Heart and Circulation. Stuttgart: Georg Thieme; p. 49-55.

Schuhlen, H., Eigler, N.L., Whiting, J.S. (1994). "Digital Angiographic Impulse Response Analysis of Regional Myocardial Perfusion. Detection of Autoregulatory Changes in Nonstenotic Coronary Arteries Induced by Collateral Flow to Adjacent Stenotic Arteries." Circulation 89(3): 1004-1012.

Shaw, C.G., Ergun, D.L., Myerowitz, P.D., Van, L.M., Mistretta, C.A., Zarnstorff, W.C., Crummy, A.B. (1982). "A Technique of Scatter and Glare Correction for Videodensitometric Studies in Digital Subtraction Videoangiography." Radiology 142(1): 209-213.

Sicard, J.A., Forestier, J. (1923). "Injection Intravasculaire D'huile Iodee Sous Controle Radiologique." Comptes Rendus de societe de Biologie (Paris) 88: 1200-1202.

Silverman, N.R., Intaglietta, M., Tompkins, W.R. (1973). "A Videodensitometer for Blood Flow Measurement." British Journal of Radiology 46(548): 594-598.

Simon, R., Herrmann, G., Amende, I. (1990). "Comparison of Three Different Principles in the Assessment of Coronary Flow Reserve from Digital Angiograms." Int J Card Imaging 5(2-3): 203-212.

Sjogren, S.E., Fredzell, G. (1953). "Apparatus for Serial Angiography." Acta Radiologica 40: 361-368.

Slutsky, R.A., Higgins, C.B. (1983). "Analysis of the Pulmonary Circulation Using Digital Intravenous Angiography." Radiology 146: 219-221.

Spiller, P., Fischbach, T., Jehle, J., Lauber, A., Politz, B., Schmiel, F.K., Loogen, F. (1983). "[Reliability of Digital Subtraction Angiocardiography for the Evaluation of Left Ventricular Function and Physical Stress]. [German]." Zeitschrift fur Kardiologie 72(11): 681-687.

Spiller, P., Schmiel, F.K., Politz, B., Block, M., Fermor, U., Hackbarth, W., Jehle, J., Korfer, R., Pannek, H. (1983). "Measurement of Systolic and Diastolic Flow Rates in the Coronary Artery System by X-Ray Densitometry." Circulation 68(337): 337-347.

Starmer, C.F., Clark, D.O. (1970). "Computer Computations of Cardiac Output Using the Gamma Function." Journal of Applied Physiology 28(2): 219-220.

Stewart, G.N. (1894). "Researches on the Circulation Time in Organs and on the Influences Which Affect It." Journal of Physiology 15: 1-89.

Stewart, G.N. (1897). "Researches on the Circulation Time and on the Influences Which Affect It; Iv. The Output of the Heart." Journal of Physiology 22: 150-183.

Thompson, H.K., Starmer, C.F., Whalen, R.E., Mcintosh, H.D. (1964). "Indicator Transit Time Considered as a Gamma Variate." Circulation Research 14(502): 502-515.

Vassanelli, C., Menegatti, G., Molinari, J., Zanotto, G., Zanolla, L., Loschiavo, I., Zardini, P. (1995). "Maximal Myocardial Perfusion by Videodensitometry in the

Assessment of the Early and Late Results of Coronary Angioplasty: Relationship with Coronary Artery Measurements and Left Ventricular Function at Rest." Cathet Cardiovasc Diagn 34(4): 301-310; discussion 311-302.

Vogel, R., Lefree, M., Bates, E., O'neill, W., Foster, R., Kirlin, P., Smith, D., Pitt, B. (1984). "Application of Digital Techniques to Selective Coronary Arteriography: Use of Myocardial Contrast Appearance Time to Measure Coronary Flow Reserve." American Heart Journal 107: 153-164.

Von Lichtenberg, A., Swick, M. (1929). "Klinische Prufung Des Uroselectans." Klinische Wochenschrift 8: 2089-2091.

Walton, S., Ell, P.J., Jarritt, P.H., Swanton, R.H. (1982). "Phase Analysis of the First Pass Radionuclide Angiocardiogram." British Heart Journal 48: 441.

White-Grodstein, G. (1957). Photon Interaction Cross Sections by Element. Washington DC: National Bureau of Science.

Whitmore, R.L. (1967a). "The Flow Behaviour of Blood in the Circulation." Nature 215(97): 123-126.

Whitmore, R.L. (1967b). "Interaction Forces in Blood." Bibliotheca Anatomica 9: 240-245.

Whitmore, R.L. (1967c). "A Theory of Blood Flow in Small Vessels." Journal of Applied Physiology 22(4): 767-771.

Womersley, J.R. (1955). "Method for the Calculation of Velocity, Rate of Flow and Viscous Drag in Arteries When the Pressure Gradient Is Known." Journal of Physiology 127: 553-563.

Womersley, J.R. (1957). "An Elastic Tube Theory of Pulse Transmission and Oscillatory Flow in Mammalian Arteries." Wright Air Development Center Technical Report 56: 614.

Wood, E.H., Sturm, R.E., Sanders, J.E. (1964). "Data Processing in Cardiovascular Physiology with Particular Reference to Roentgen Videodensitometry." Proceedings of the Mayo Clinic 39: 849.

Ziedses Des Plantes, B.G. (1935). "Subtraktion. Eine Roentgenographische Methode Zur Separaten Abbildung Bestimmter Teile Des Objekts." Fortschritte auf dem Gebiete der Roentgenstrahlen und der Nuklearmedizin. 52: 69.

Zierler, K.L. (1962). "Theoretical Basis of Indicator Dilution Methods for Measuring Flow and Volume." Circulation Research 10: 393.